Boron Removal Effect in p-type Silicon Sensors

Dissertation

zur Erlangung des Doktorgrades
des Fachbereichs Physik
der Universität Hamburg

vorgelegt von Chuan Liao
aus Hamburg

Hamburg 2023

Gutachter der Dissertation:	Prof. Dr. Erika Garutti Dr. Micheal Moll
Gutachter der Disputation:	Prof. Dr. Robin Santra Prof. Dr. Erika Garutti Prof. Dr. Peter Schleper Dr. Jörn Schwandt Dr. Michael Moll
Datum der Disputation:	13.09.2023
Vorsitzender des Prüfungsausschusses:	Prof. Dr. Robin Santra
Vorsitzende des Promotionsausschusses:	Prof. Dr. Günter H. W. Sigl
Leiter des Fachbereichs Physik	Prof. Dr. Wolfgang J. Parak
Dekan der Fakultät für Mathematik Informatik und Naturwissenschaften:	Prof. Dr.-Ing. Norbert Ritter

Declaration on oath

I hereby declare in lieu of oath that I have written this dissertation myself and that I have not used any auxiliary materials or sources other than those indicated.

Hamburg, 17-07-2023

Chuan Liao

Signature of the doctoral student

Ich versichere, dass dieses gebundene Exemplar der Dissertation und das in elektronischer Form eingereichte Dissertationsexemplar (über den Docata-Upload) und das bei der Fakultät (zuständiges Studienbüro bzw. Promotionsbüro Physik) zur Archivierung eingereichte gedruckte gebundene Exemplar der Dissertationsschrift identisch sind.

hamburg 17/07/2023	Chuan Liao
Ort, Datum	Vorname und Nachname, Unterschrift

I, the undersigned, declare that this bound copy of the dissertation and the dissertation submitted in electronic form (via the Docata upload) and the printed bound copy of the dissertation submitted to the faculty (responsible Academic Office or the Doctoral Office Physics) for archiving are identical.

hamburg 17/07/2023	Chuan Liao
Place, Date	*First name and surname, signature*

Abstract

Silicon detectors operated at collider experiments like for instance the Large Hadron Collider at CERN, experience radiation damage due to the intense flux of charged and neutral particles through them. In the innermost part of the detector, the particle fluence can reach up to $\Phi_{\text{eq}} = 3.5 \times 10^{16}$ cm^{-2}.

To increase radiation tolerance, the silicon sensors currently developed for the LHC detectors upgrade are boron-doped p-type silicon, in contrast to the n-type sensors currently in operation. In addition to planar pixel sensors, also devices with an additional gain layer, under the name of Low Gain Avalanche Detectors (LGADs), will be employed in the upgraded LHC detectors. These devices feature a p-type layer with higher boron concentration than in the bulk of p-type sensors.

This work focuses on one particular radiation damage effect in p-type silicon sensors known as the boron removal effect. This effect is characterized by the removal of boron dopants from their lattice sites, causing them to lose their acceptor properties. The boron removal effect is particularly significant for p-type silicon sensors. For example, the reduction in gain value observed in LGADs after radiation exposure is commonly attributed to the deactivation of boron dopants during the initial irradiation. This effect is closely associated with radiation-induced defects.

In general, the types of bulk defects induced by radiation, whether point-like or cluster-related, can vary depending on the type of radiation. For example, both hadrons and leptons can induce either defect type, but leptons are more likely to introduce point defects, while high-energy photons only generate point-like defects. The properties of these defects are determined by their components, i.e. the elements that make up the defect, and these elements strongly depend on the concentration of dopants and impurities like Oxygen or Carbon.

In this work, diodes with different dopants and impurities concentrations (boron, oxygen and carbon) were studied after being exposed to three different types of radiation (23 GeV protons, 5.5 MeV electrons and ^{60}Co γ-ray). The microscopic techniques of Thermally Stimulated Current (TSC) and Thermally Stimulated Capacitance (TS-Cap) were employed to characterize radiation-induced defects, especially focusing on B_iO_i (boron interstitial and oxygen interstitial) and C_iO_i (Carbon interstitial and Oxygen interstitial) defects. The presented results include the analysis of defect concentrations, energy levels within the band gap, and their charged states at room temperature. The changes in macroscopic properties, such as leakage current and space charge density, after irradiation, are evaluated through current-voltage (I–V) and capacitance-voltage (C–V) measurements, respectively. To assess the impact of microscopic defects on macroscopic properties, isothermal annealing experiments at a temperature of 80 °C with varying annealing times, and isochronal annealing experiments for a duration of 15 minutes with varying annealing temperatures up to 300 °C have been performed. In the end, the devel-

opment of the boron removal rate with initial doping concentration, irradiation fluence (for different radiation sources) and impurities are presented and discussed together with the radiation-induced defects in chapter 6-8. Besides that, the annealing behaviour of B_iO_i including the candidate state of B_iO_i after it anneals out is given.

Kurzfassung

Im Zuge des Ausbaus des Large Hadron Collider (LHC) am CERN zum High Luminosity LHC (HL-LHC) mit einer instantanen Spitzenluminosität von etwa $7,5 \times 10^{34}$ cm^{-2}s^{-1} werden auch die Siliziumspur-Systeme der Experimente aufgerüstet, um dem extrem intensiven Strahlungsfeld mit Fluenzen von bis zu $\Phi_{\mathrm{eq}} = 3,5 \times 10^{16}$ cm^{-2} für die innerste Schicht der Pixel-Detektoren gewachsen zu sein. Insbesondere werden die neuen Sensoren, die derzeit entwickelt werden, aus Bor-dotiertem p-Typ-Silizium hergestellt im Gegensatz zu den vorhandenen n-Typ-Detektoren, um eine höhere Strahlungstoleranz zu erreichen.

Diese Arbeit konzentriert sich auf einen speziellen Strahlungsschadenseffekt in p-Typ-Siliziumsensoren, der als "Boron removal" Effekt bekannt ist. Dieser Effekt zeichnet sich durch die Entfernung von Bor-Dotierungsatomen von ihren Gitterplätzen aus, wodurch sie ihre Akzeptoreigenschaften verlieren. Der "boron removal" Effekt ist besonders signifikant für p-Typ-Siliziumsensoren, insbesondere im Fall von Low-Gain Avalanche Detektoren (LGADs). Die beobachtete Verringerung des Verstärkungswerts bei LGADs nach Strahlenexposition wird üblicherweise auf die Deaktivierung von Bor-Dotierstoffen während der anfänglichen Bestrahlung zurückgeführt. Dieser Effekt ist eng mit strahleninduzierten Defekten verbunden.

Im Allgemeinen können die Arten von Volumendefekten, die durch Strahlung verursacht werden, je nach Art der Strahlung variieren, ob es sich um Punktdefekte oder Cluster-Defekte handelt. Zum Beispiel können sowohl Hadronen als auch Leptonen beide Arten von Defekten verursachen, aber Leptonen neigen eher dazu, Punktdefekte zu generieren. Die Eigenschaften dieser Defekte werden durch ihre Bestandteile bestimmt, d.h. die Elemente, aus denen der Defekt besteht, und diese Elemente hängen stark von der Konzentration Konzentration der Dotierung und von Verunreinigungen im Silizium Material wie Sauerstoff oder Kohlenstoff ab.

In dieser Arbeit wurden drei Gruppen von Dioden nach Exposition von verschiedenen Arten von Strahlung untersucht. Die erste Gruppe, die 23 GeV Protonen ausgesetzt war, bestand aus EPI-Dioden mit Bor-Dotierungskonzentrationen im Bereich von 6×10^{12} bis 1×10^{15} cm^{-3} und wurde mit einer Fluenz von $\Phi_{\mathrm{p}} = 7 \times 10^{13}$ cm^{-2} bestrahlt. Die zweite Gruppe, die 5,5 MeV Elektronen ausgesetzt war, umfasste sowohl EPI-Dioden als auch Cz-Dioden mit derselben Bor-Dotierungskonzentration von 1×10^{15} cm^{-3}, aber die Fluenz variierte von $\Phi_{\mathrm{e^-}} = 1 \times 10^{15}$ bis 6×10^{15} cm^{-2}. Die dritte Gruppe, die ^{60}Co-Gammastrahlenbestrahlung ausgesetzt war, bestand aus FZ-Dioden mit einer Bor-Dotierungskonzentration von $3,5 \times 10^{12}$ cm^{-3}. Die Dosis variierte von $D = 0,1$ bis 2 MGy. Die Konzentrationen der Hauptverunreinigungen, Sauerstoff und Kohlenstoff, wurden durch die Wachstumstechniken (Czochralski (Cz), Float Zone (FZ) und Epitaxie (EPI)) und die Herstellungsprozesse der Sensoren bestimmt.

Zur Charakterisierung strahleninduzierter Defekte wurden die mikroskopischen Techniken der Thermisch Stimulierten Strommessung (TSC) und der Thermisch Stimulierten

Kapazitätsmessung (TS-Cap) eingesetzt. Dabei lag der Fokus insbesondere auf den B_iO_i-Defekten (Bor-Interstitial und Sauerstoff-Interstitial) sowie den C_iO_i-Defekten (Kohlenstoff Interstitial und Sauerstoff Interstitial). Die präsentierten Ergebnisse umfassen die Analyse der Defektkonzentrationen, der Energielevel innerhalb der Bandlücke und ihrer geladenen Zustände bei Raumtemperatur. Die Veränderungen der makroskopischen Eigenschaften wie Leckstrom und Raumladungsdichte nach Bestrahlung werden jeweils durch Strom-Spannungs-(I-V)- und Kapazitäts-Spannungs-(C-V)-Messungen bewertet. Um den Einfluss mikroskopischer Defekte auf makroskopische Eigenschaften zu beurteilen, wurden isothermale Ausheilungsexperimente bei einer Temperatur von 80 °C mit variierenden Ausheilzeiten sowie isochronale Temperungen für eine Dauer von 15 Minuten pro Temperaturschritt bis zu einer Temperatur von 300 °C durchgeführt.

摘要

欧洲核子中心最近提出了对其大型粒子对撞机进行升级的计划，即将其升级为高亮度大型粒子对撞机。该升级计划旨在使其瞬时峰值光度达到7.5×10^{34} $\mathrm{cm}^{-2}\mathrm{s}^{-1}$。为了适应这一升级，硅探测器系统也需要提升其抗辐射性能，以应对高达$\Phi_{\mathrm{eq}} = 3.5 \times 10^{16}$ cm^{-2}的年等效中子通量。因此，为了具备强大的抗辐射特性，新型的p型硅传感器正在快速发展，以满足系统升级的需求。

本文重点研究了p型硅传感器中的一种重要辐射破坏效应，即硼移除效应。该效应表现为硼掺杂原子由于粒子的撞击而离开其原本的晶格位置，导致其失去了作为受主的特性。在p型硅传感器中，硼移除效应尤为显著，特别是在低增益雪崩探测器(Low Gain Avalanche Detectors (LGADs))中。在辐射初期，观察到的增益值降低通常被归因于硼移除效应。而该效应与辐射诱导的缺陷密切相关。

通常情况下，由辐射引起的体缺陷可以根据大小分为点缺陷和缺陷簇，而缺陷的大小则取决于辐射的类型。一般而言，强子和轻子能够同时诱导这两种类型的缺陷，但轻子更容易诱导点缺陷。而高能光子只会产生点缺陷。缺陷的性质也与其构成元素的种类有关，而这取决于掺杂元素和杂质如氧和碳。

因此，本研究针对三组p型硅二极管在受到不同辐射后的性能变化进行了研究。第一组二极管暴露在能量为23 GeV的质子辐射环境中，所有二极管都采用外延单晶硅制备，包括不同硼掺杂浓度的二极管（范围从6×10^{12}到1×10^{15} cm^{-3}）。所有二极管都经受了相同的辐射通量：$\Phi_{\mathrm{p}} = 7 \times 10^{13}$ cm^{-2}。第二组二极管暴露在能量为5.5 MeV的电子辐射环境中，包括具有相同硼掺杂浓度(1×10^{15} cm^{-3})的外延单晶硅和直拉单晶硅二极管。同时，它们经受了不同的辐射通量：$\Phi_{\mathrm{e^-}} = 1 \times 10^{15}$到$6 \times 10^{15}$ cm^{-2}。第三组二极管暴露在^{60}钴-伽马射线辐射环境中，所有二极管都由浮区单晶硅制备，具有相同的硼掺杂浓度(3.5×10^{12} cm^{-3})，但经受的辐射剂量不同($D = 0.1$到2 MGy)。主要杂质（即氧和碳）的浓度由生长技术（直拉(Cz)，浮区（FZ）和外延（EPI））以及器件制造过程决定。

为了表征辐射诱导的缺陷，特别是$\mathrm{B_iO_i}$（间隙硼原子和间隙氧原子）和$\mathrm{C_iO_i}$（间隙碳原子和间隙氧原子), 本文利用热刺激电流（TSC）和热刺激电容（TS-Cap）。所呈现的结果包括缺陷浓度、带隙内能级以及它们在室温下的带电状态的分析。辐照后，二级管宏观性质（如漏电流和空间电荷密度）的变化分别通过电流-电压（I-V）和电容-电压（C-V）测量进行评估。为了评估微观缺陷对宏观性质的影响，本文进行了在80 °C温度下持续时间不同的等温退火实验，以及在不同的退火温度（高达300 °C）下进行的等时退火实验，持续时间为15分钟。

廖川(张家界)

2023年

Contents

1 Introduction

1.1 HL-LHC and Silicon Sensors

The world's largest particle accelerator, the Large Hadron Collider (LHC) at European Organization for Nuclear Research (CERN) in Geneva, started operations in 2008. Some of today's most fundamental open questions about the structure of matter are addressed by the four LHC-Experiments, the Compact Muon Solenoid (CMS), A Toroidal Lhc ApparatuS (ATLAS), the Large Hadron Collider Beauty (LHC-B) and A Large Ion Collider Experiment (ALICE). The High-Luminosity Large Hadron Collider (HL-LHC) project aims to crank up the performance of the LHC to increase the potential for discoveries after 2029. The objective is to increase the integrated luminosity by a factor of 10 beyond the LHC's design value.

In the two general-purpose experiments, CMS and ATLAS, silicon sensors are installed inside a magnetic field close to the interaction points. Electromagnetic and hadronic calorimeters follow them. Muon systems are installed in the outermost region of the detector. The demand for the silicon sensors in the innermost part of the detector is the tracking of traversing charged particles and their vertices with high accuracy. This information makes it possible to obtain momenta and charge and sometimes the particle ID.

In HL-LHC experiments, silicon sensors faced several challenges. One of these challenges is that these sensors were required to cope with extraordinary high particle rates of up to 200 p–p collisions per bunch crossing. For this purpose, new types of silicon sensors were developed e.g. Low Gain Avalanche Detectors (LGADs) with high precision timing ($\leq$ 50 ps) and position resolution (few hundred µm) [2, 3]. Besides that, for other requirements, new types of sensors are developed e.g. High Voltage CMOS devices (HV CMOS) for the inner tracking detectors [4, 5, 6, 7, 8, 9], as well as the new pixel and strip devices.

The main challenge of these sensors is the degradation of their performance due to the induced defects by the expected high radiation field. Figure 1.1 demonstrates the expected 1 MeV neutron equivalent particle fluence as a function of the distance to the interaction point. It can be observed, that the total fluence decreases towards larger radii. Furthermore, the total fluence has contributions from different particles, mostly dominated by pions up to 15 cm radius, followed by a nearly constant background of backscattered neutrons.

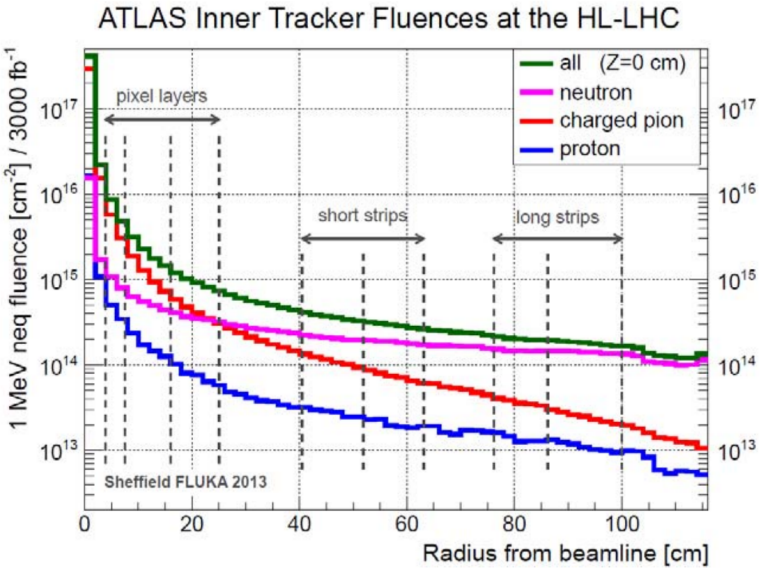

Figure 1.1: Expected fluences of particles in the inner tracker of the ATLAS detector at HL-LHC for an integrated luminosity of 3000 fb^{-1}. Figure taken from [1].

1.2 Boron Removal Effect

The degradation of n-type silicon sensors after irradiation was detail investigated in the past decades [10, 11, 12, 13, 14], which leads nowadays to the use silicon sensors in high energy physics experiments being manufactured on boron-doped (p-type) silicon. The degradation of the performance of these sensors is due to the induced defects by the expected high radiation field. For instance, the charged defects at room temperature (e.g. E30K, H40K, B_iO_i, H140K, H152K and I_P) [15, 16, 17, 18] cause changes of the space charge density (N_{eff}). The deep defects (e.g. vacancy related traps such as V_2 and V_3) [19] lead to the degradation of charge collection efficiency (CCE) and an increase of dark current. In general, the formed defects can be classified into two categories by their corresponding size: cluster-related or point-like defects. The formation of these two types of defects depends on the energy of irradiating particles.

One of the important degradations of p-type silicon sensors is caused by the boron removal effect. The schematic of the boron removal effect can be found in Fig. 1.2. As can be seen here, this effect has three main processes: I, Lattice silicon atom (Si_s) was knocked out by incident particle and Si_s got recoil energy and turns to interstitial silicon (Si_i); II, Si_i diffusion in the bulk and impact on lattice boron atom (B_s); III, B_s was knocked out Si_i and turns to interstitial boron (B_i) and finally captured by interstitial oxygen (O_i), formed boron interstitial and oxygen interstitial complex defect B_iO_i. The B_iO_i is normally assumed to be a point-like defect, thus, the formation of B_iO_i could be dependent on the energy of the incident particles.

For specific incident particles, the non-ionization energy loss (NIEL) in silicon sensors with different impurity concentrations is assumed to be the same. However, the formation of defects can be very dependent on the impurities. This means that the formation of

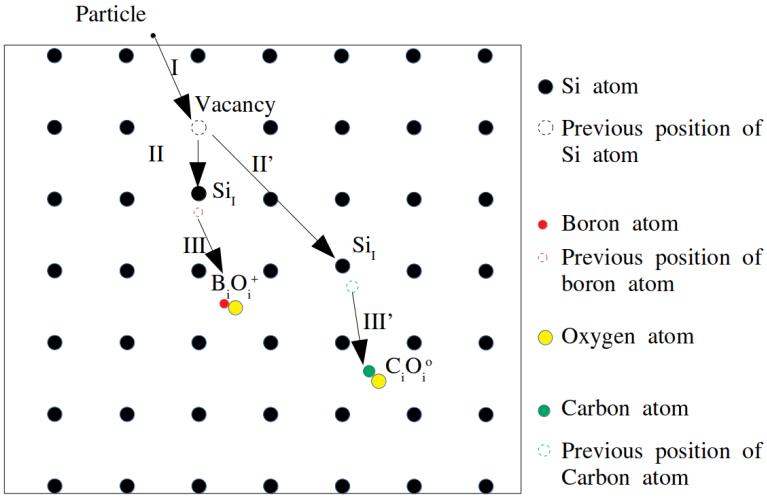

Figure 1.2: Schematic of boron removal effect in p-type silicon sensor. The symbols and procedures of this effect (I-III) were indicated in the figure.

B_iO_i is affected by impurities in silicon. For example, a possible way to reduce boron removal is a co-implantation of carbon into the gain layer of LGADs [3]. The assumed mechanism behind this effect is the competition between the displacement of substitutional boron (B_s) and substitutional carbon (C_s) by primary silicon interstitials (Si_I) into interstitial positions (B_i) and (C_i), respectively. Both interstitial atoms are mobile at room temperature and can react with different impurities, ending up e.g. in the formation of B_iO_i or C_iO_i defects [15, 20, 21, 22, 23, 24]. Although both defects have donor states in the bandgap of silicon, the B_iO_i act as a trap for electrons while the C_iO_i is a hole trap. At room temperature (RT) the B_iO_i is positively charged and its concentration affects the effective space charge density (N_{eff}) while C_iO_i is in a neutral charge state with no influence on N_{eff}. The C_iO_i defect has an energy level in the lower half of the bandgap of silicon, with an activation energy of 0.36 eV and temperature-dependent capture cross sections for holes and electrons [24]. On the other hand, the B_iO_i defect is a coulombic center having an energy level in the upper half of the silicon bandgap with an activation energy depending on the electric field, experimentally determined to be between 0.24 and 0.26 eV [23], and independent on temperature capture cross sections of 1×10^{-14} cm^2 for electrons and 1×10^{-20} cm^2 for holes [15, 22].

1.3 Content of Thesis

To investigate the boron removal effect in silicon sensors, in this work, three groups of diodes were studied after being exposed to different types of radiation. The first group, exposed to 23 GeV protons, consisted of EPI-diodes with boron doping concentrations ranging from 6×10^{12} to 1×10^{15} cm^{-3} and irradiated with a fluence value of $\Phi_p = 7 \times 10^{13}$ cm^{-2}. The second group, exposed to 5.5 MeV electrons, included both EPI-diodes and Cz-diodes with the same boron doping concentration of 1×10^{15} cm^{-3}, but the fluence

varied from $\Phi_{e^-} = 1 \times 10^{15}$ to 6×10^{15} cm^{-2}. The third group, exposed to ^{60}Co γ-ray irradiation, consisted of FZ-diodes with a boron doping concentration of 3.5×10^{13} cm^{-3}. The dose varied from $D = 0.1$ to 2 MGy. The concentrations of the main impurities, oxygen and carbon, were determined by the growth techniques (Czochralski (Cz), Float Zone (FZ), and Epitaxial (EPI)) and device manufacturing processing.

This work highly involved semiconductors physics, detector performance and radiation damage. Thus, in chapter 2 the fundamental knowledge of silicon material will be introduced and followed by detector physics of silicon in chapter 3. In chapter 4, the radiation damage will be introduced. The experimental detail will be introduced in chapter 5 including irradiation facility, macroscopic (I–V, C–V) measurements, microscopic (Thermally Stimulated Current and Capacitance) measurements and additional theory about their defect filling processes and thermally stimulated signal formation. The studies of this work will be presented in chapter 5 to 7, following the sequence of diodes irradiated by 23 GeV protons, 5.5 MeV electrons and ^{60}Co γ-rays and with individual introduction and its conclusion. In the end, chapter 8, the final conclusion and outlook will be given.

2 Fundamental Knowledge of Silicon Materials

2.1 History of Silicon

Silicon, discovered by Jöns Jacob Berzelius in 1823, is the second most abundant solid element on earth after oxygen. Its transformations from SiO_2 to poly-crystal silicon and single-crystal silicon have led to new technologies, transistors, sensors, and microchips. As the one of important sensors-silicon detectors, including CMOS, CCDs, SiPMs, and LGADs, have become crucial for applications in cameras, medical imaging detectors, X-ray detection, astronomy, and high energy physics experiments.

This chapter will cover the manufacturing processes of silicon, including extracting it from complex materials and producing polycrystalline and single-crystal silicon (see Fig. 2.1). The properties of single-crystal silicon will also be discussed, such as its crystal structure, and physical characteristics as a semiconductor, including doping, bandgap, *p*-*n* junction, and other electrical properties.

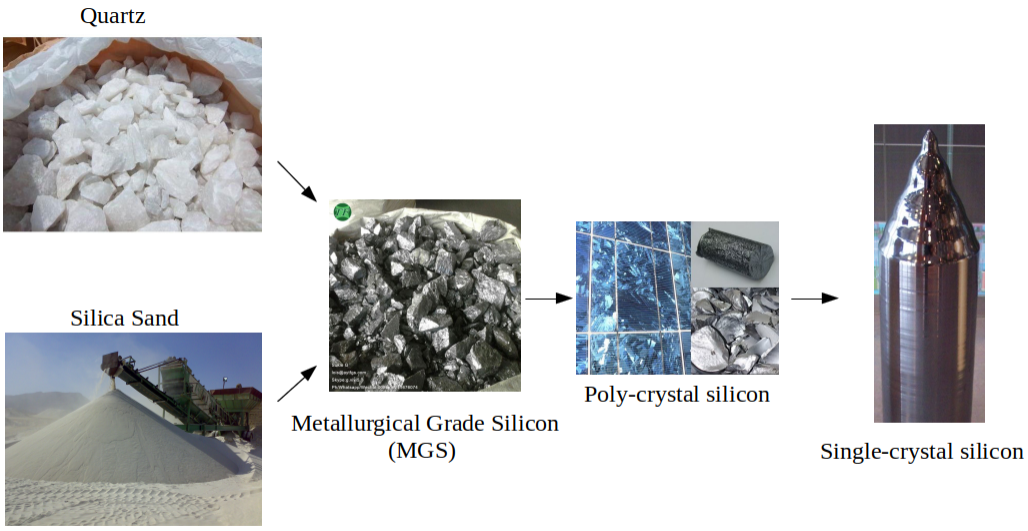

Figure 2.1: The development of silicon materials. Pictures were taken from [25, 26, 27, 28, 29].

2.2 Silicon Processing

This study investigated silicon grown using three different techniques: Czochralski (Cz), Float Zone (FZ), and Epitaxial (EPI). These are also the primary techniques used for growing silicon and will be introduced in this section.

2.2.1 Poly-Crystal Silicon

Quartz and sand, which are mainly composed of SiO_2, can serve as raw materials for obtaining pure silicon. The extraction process involves heating quartz or pure sand in a furnace at around 1780 °C, leading to the isolation of main impurities such as Al_2O_3 and Fe_2O_3. The remaining liquid is purified silicon that is about 99% pure, and the solids that form from this liquid are called Metallurgical Grade Silicon (MGS).

To obtain higher purity silicon, the MGS undergoes a process where it is exposed to hydrogen chloride (HCl) gas at 300 °C, generating the gas Trichlorosilane ($SiHCl_3$). The gas is repeatedly distilled along with H_2 and then passed over the surface of a silicon rod at 900-1100 °C, which results in the deposition of silicon on the rod. This process produces polycrystalline silicon with impurity concentrations below 10^{13} cm^{-3} [30].

2.2.2 Single-Crystal Silicon

Polycrystalline silicon has crystal boundaries that can trap drifting charges. Thus, making single crystal silicon is necessary for silicon detectors.

Czochralski (Cz) Silicon

The Cz method, named after J. Czochralski in 1918 [31], involves pulling a single crystal out of a melt. This method was employed and developed to produce single crystal silicon by Teal and Little in 1950 [32]. A schematic of the Cz method can be seen in Fig. 2.2.

The method involves three main components: the holder (consisting of the crucible susceptor and SiO_2 crucible), the growing pillar (seed holder, seed, crystal neck, and single-crystal silicon pillar), and the rotation mechanism (consisting of two parts rotating in opposite directions). The entire process takes place in an inert gas environment. It should be noted that the silicon melt reacts with the SiO_2 crucible and forms SiO. While more than 99% of the SiO is driven out as a gas, the rest remains in the final silicon pillar [33]. Additionally, some of the gaseous SiO reacts with the carbon on the surface of the melt ($SiO + 2C \rightarrow SiC + CO$), introducing carbon into the final silicon pillar. The details of rotation speeds and how to use rotation to control the reaction rate in the melt have been discussed in previous studies [34, 35, 36].

The main impurities in Cz silicon are oxygen and carbon, with typical concentrations of around $10^{17} - 10^{18}$ cm^{-3} and 1×10^{16} cm^{-3}, respectively [38, 39]. Two well-known defects in Cz silicon are thermal double donors (TDD) and shallow thermal donors (STD), both

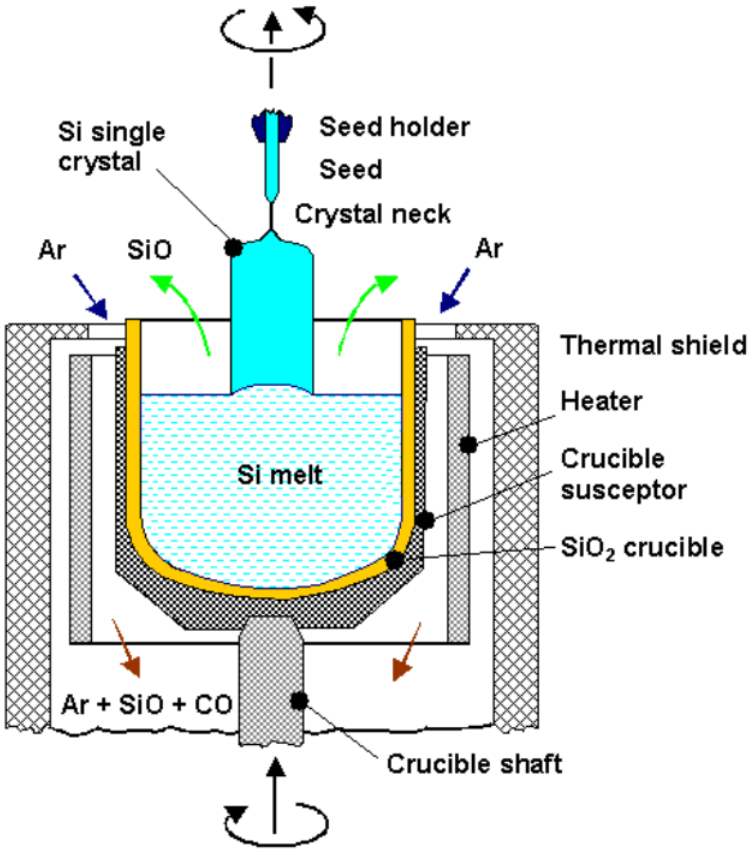

Figure 2.2: Czochralski method [37].

of which are related to oxygen [33, 40, 41, 42, 43]. In high radiation fields, oxygen can act as a trap centre and traps other impurities formed the defects, such as B_iO_i [15, 20] and C_iO_i [24], as well as for vacancy-formed shallow acceptor trap e.g. VO [20, 24, 44, 45]. Oxygen can also act as a pinning point in the material, restricting the movement of dislocations and trapping metal impurities in the crystal, ultimately strengthening the crystal. Furthermore, the oxygen-related complexes improve the thermal stress resistance of the material.

The "Magnetic Field Applied Cz" (MCz) [46] and "Continuous Cz" (CCz) [47] methods have been developed in addition to the standard Cz method, but they are not relevant to this work.

While the presence of oxygen and carbon can enhance the radiation hardness of detectors, these two impurities can also form defects (e.g. TDD (Thermal Double Donor), V_2O [18] and C_iO_i) that can significantly degrade the performance of silicon detectors (increase leakage current, reduce charge collection efficiency (CCE)) dependence on the defect concentration. Therefore, despite the development of other methods such as Cz, MCz, and CCz, Float Zone silicon remains the primary material for silicon detectors due to its high purity and low impurity concentration.

Float Zone (FZ) Silicon

The Float Zone growth technique was developed by Henry Theuerer in 1955 at Bell Labs [48]. This method is used to produce extremely pure silicon by avoiding interaction with the SiO_2 crucible. The schematic of the FZ method is presented in Fig. 2.3.

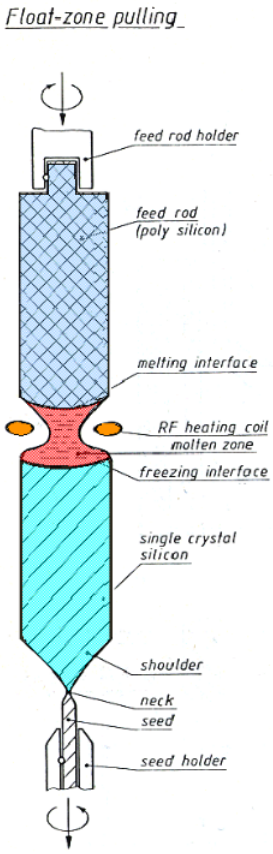

Figure 2.3: Float Zone method [37].

The FZ method is similar to the Cz method in equipment and principle, but instead of pulling a single crystal from melted silicon in a SiO_2 crucible, the FZ method uses the molten interface between the polycrystal and single crystal to grow a silicon pillar. RF heating regions are used to melt the polysilicon, and a single-crystal silicon pillar is formed by freezing the melted silicon on the interface.

In summary, FZ silicon has much lower oxygen and carbon concentrations compared to Cz silicon, typically below 5×10^{15} cm^{-3} [11]. It can be grown without any substance except ambient gas, which allows for precise control of impurity concentrations. To grow n- or p-type silicon, the PH_3 or B_2H_6 is included in the gas environment. However, the diameter of silicon pillars is limited due to heating constraints. More information about the critical parameters for the reactions involved can be found in the literature [34, 11].

The thermal distribution during crystal growth can result in non-uniform distributions of impurities, such as boron and phosphorus. This is particularly true for phosphorus due to its high diffusion coefficient. To address this issue, neutron transmutation doping

(NTD) can be used. NTD involves transforming a portion of the ^{30}Si to ^{31}P through neutron transmutation reactions [49]. However, this process also generates radiation damage in the wafer. Thus, the wafer is annealed at 800 °C to activate the implanted Phosphorus and reduce irradiation-induced defects [11].

Epitaxial (EPI) Silicon

Epitaxial silicon wafers were first developed in 1966 and achieved commercial acceptance by the early 1980s [50]. The most widely used method of growing silicon is vapour-phase epitaxy (VPE). The EPI diodes investigated in this work are grown by this method. In VPE, the silicon crystal grows on a Cz-silicon substrate under a special gas environment (Si Cl_4, SiH_2Cl_2, $SiHCl_3$, and SiH_4). $SiCl_4$ is the most commonly used gas for growing single-crystal silicon wafers. The general reaction for growing a wafer is:

$$SiCl_4(gas) + 2H_2(gas) \xrightarrow{1200\ ^\circ C} Si(Soild) + 4HCl(gas) \tag{2.1}$$

However, at this temperature, another reaction is also introduced:

$$SiCl_4(gas) + Si(Soild) \xrightarrow{1200\ ^\circ C} 2SiCl_2(gas) \tag{2.2}$$

Thus, the concentration of $SiCl_4$ is a critical parameter for growing wafers. The typical growth rate for VPE is approximately 1 µm/min [51]. Dopants are introduced by PH_3 or B_2H_6. More information on epitaxial silicon wafer growth can be found in [51].

EPI-silicon's impurities are substrate-dependent, with Cz-silicon leading to higher levels of oxygen and carbon than FZ silicon, particularly near the Cz interface. However, its uniform dopant distribution is useful for studying radiation damage, while its reduced thickness improves detector time resolution.

After discussing the topics in the previous sections, the process of producing a single crystal is introduced, along with both the advantages and disadvantages of using silicon detectors. The common concentrations of oxygen and carbon in silicon are presented in Table 2.1. The manufacturing and processing of the detectors will be discussed in chapter 3. In the following section, the features of silicon will be presented.

Table 2.1: Impurities information (Epitaxial wafer is growth on Czochralski)

Growth Techniques	Czochralski (Cz)	Float Zone (FZ)	Epitaxial (EPI) [52]
Oxygen $[O_i]$ (cm^{-3})	1×10^{18}	5×10^{15}	1×10^{17}
Carbon $[C_i]$ (cm^{-3})	1×10^{16}	5×10^{15}	2×10^{15}

2.3 Features of Silicon

2.3.1 Silicon Crystal

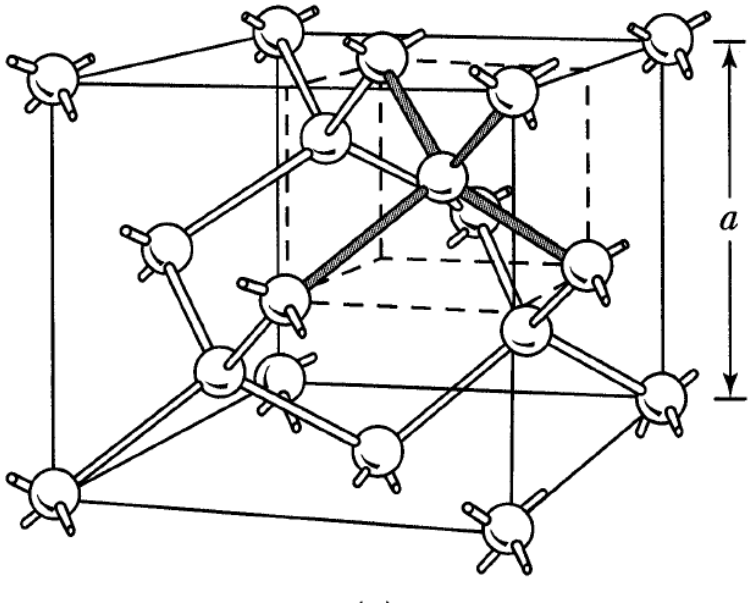

Figure 2.4: The conventional unit cell of the diamond lattice with lattice constants a, the dashed line marked in the figure is the tetrahedral structure of closest neighbours in the silicon lattice.

The schematic of the silicon crystal is presented in Fig. 2.4, which is the so-called conventional unit cell of a diamond lattice. The cell is repeated in all three dimensions and forms an overall crystal lattice in the end. At room temperature, the single silicon atoms covalent bonded (sp^3 hybridization) with another four silicon, with the same angle 109.5° and lattice constant $a = 5.43$ Å. The periodic arrangement of the unit cell results in two interpenetrating Face-Centered-Cubic (FCC) Bravais lattices. As mentioned in section 2.2 all single-crystal silicon grows on seeds, thus orientations and properties of the surface of seeds are critical factors for silicon wafers, which, in turn, affects the performance of produced sensors. To analyze the crystal and the related properties, typically Miller indices $< h,\ k,\ l >$ were used to define the various planes in the crystal:

$$\vec{g}_{hkl} \quad = \quad h\vec{b}_1 + k\vec{b}_2 + l\vec{b}_3 \tag{2.3}$$

where $< h,\ k,\ l >$ indicates a normal to the planes on the basis of the primitive reciprocal lattice vectors (PRLV). The reciprocal lattice vectors along three different dimensions are denoted by $\vec{b}_i$ (for $i = 1,\ 2,\ 3$) and are defined by the three primitive lattice vectors (PLV) $\vec{a}_i$ (for $i = 1, 2, 3$), if the lattice sites of the unit cell can be described by $\vec{R}_{m,n,p} =$

$m\vec{a}_1 + n\vec{a}_2 + p\vec{a}_3$ with integers m, n, and p:

$$\vec{b}_1 = 2\pi \frac{\vec{a}_2 \times \vec{a}_3}{\vec{a}_1 \cdot (\vec{a}_2 \times \vec{a}_3)} \tag{2.4}$$

$$\vec{b}_2 = 2\pi \frac{\vec{a}_1 \times \vec{a}_3}{\vec{a}_2 \cdot (\vec{a}_1 \times \vec{a}_3)} \tag{2.5}$$

$$\vec{b}_3 = 2\pi \frac{\vec{a}_1 \times \vec{a}_2}{\vec{a}_3 \cdot (\vec{a}_1 \times \vec{a}_2)} \tag{2.6}$$

In principle, there are several ways to select the basis of PLV. In general, the $\vec{a}_{1,2,3}$ (for $i = 1, 2, 3$) of FCC cells were given by four bases (0, 0, 0) with:

$$\vec{a}_1 = \frac{a}{2}(0,\ 1,\ 1) \quad \vec{a}_2 = \frac{a}{2}(1,\ 0,\ 1) \quad \vec{a}_3 = \frac{a}{2}(1,\ 1,\ 0) \tag{2.7}$$

and the following reciprocal lattice vectors are:

$$\vec{b}_1 = \frac{2\pi}{a}(-1,\ 1,\ 1) \quad \vec{b}_2 = \frac{2\pi}{a}(1,\ -1,\ 1) \quad \vec{b}_3 = \frac{2\pi}{a}(1,\ 1,\ -1) \tag{2.8}$$

Single crystal silicon typically grows along the $< 1,\ 0,\ 0 >$ orientation. The periodic arrangement of atoms in the crystal creates a periodic potential. The potential $V(\vec{x})$ in the crystal can be expressed as a Fourier transform, which relates the reciprocal lattice and direct lattice through a Fourier series. This approach can be used to calculate the bandgap.

2.3.2 Bandgap

The band describes the energy level where free carriers (both electrons and holes) can stay, and its density is a commonly used concept in semiconductor physics to describe the density of states. This is derived from the wavefunction (Ψ) in the Schrödinger equation [53]:

$$[-\frac{\hbar^2}{2m}\nabla^2 + V(\vec{x})]\Psi = E(\vec{k})\Psi \tag{2.9}$$

the potential $V(\vec{x})$ is mentioned in section 2.3.1. m is the mass and it will be replaced by the effective mass m^* for semiconductor physics. The quantity $E(\vec{k})$ represents the energy that is allowed to exist at wavevector $\vec{k}$, which defines the energy band. The periodic distribution of potential in the crystal results in the Bloch function, which describes how the wavefunction can be expressed as [54]:

$$\Psi(\vec{x}, \vec{k}) = u(\vec{x}, \vec{k})e^{i\vec{k}\cdot\vec{x}} \tag{2.10}$$

where $u(\vec{x}, \vec{k})$ also follows the periodicity requirement. Finally, the position-dependent energy level called the bands, of semiconductors and insulators was calculated with the

Tight Binding Model (TBM) [55]. The energy bands in different solids explained the difference in conductivity between metals, semiconductors, and insulators. The obtained difference in the nearby two bands is the so-called band gap.

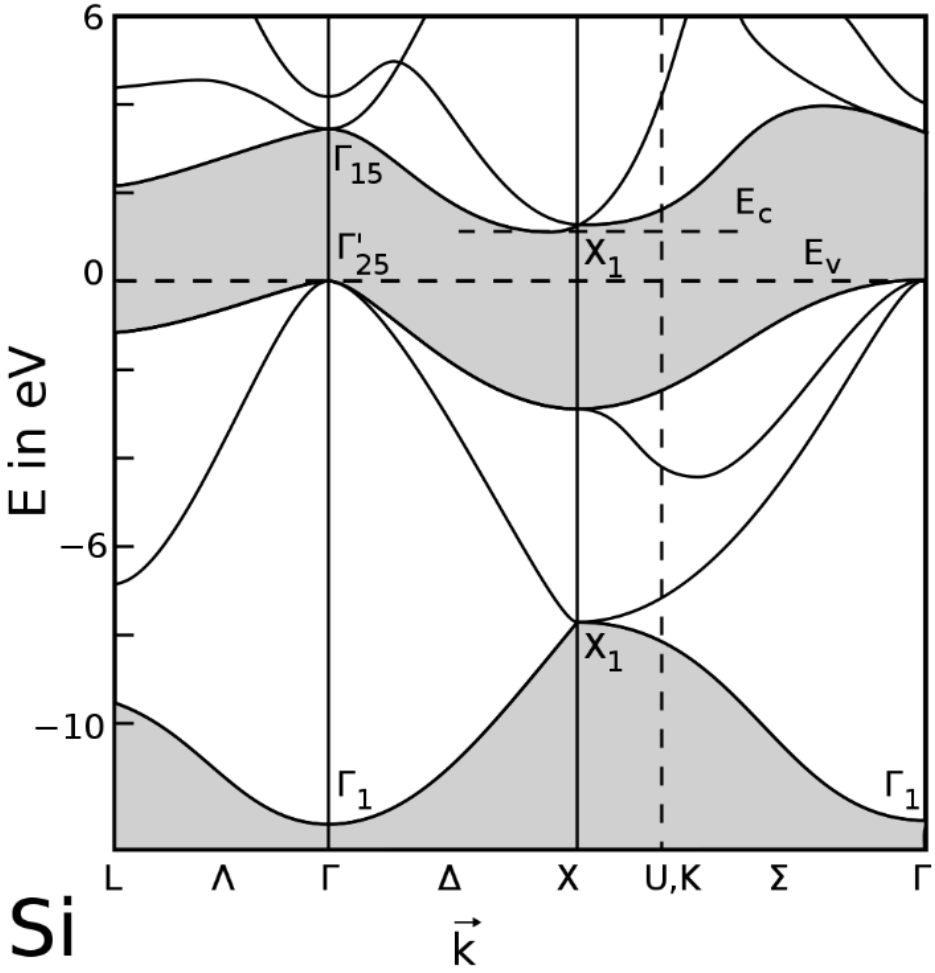

Figure 2.5: Band gap structure for silicon at 300 K given by pseudopotential method [56] with TBM [57]. The momentum $\vec{\Gamma}$ and $\vec{X}$ correspond to reciprocal lattice sites. Where E_C and E_V indicated the lowest point of the conduction band and the highest point of the valence band respectively, generally the band gap is given by the difference of these two values i.e. $E_C - E_V = 1.12$ eV.

In summary, the electrical properties of solids are determined by the minimum difference between the energy of the highest band where the states are filled by electrons and the nearby band where the states are empty. The filled band is called the valence band, and the other is the conduction band. In metals, the conduction and valence bands overlap, which means that all outer electrons can move in the crystal. However, in semiconductors and insulators, the conduction and valence bands do not overlap, and their properties are determined by the difference between the edges of conduction and the edges of valence bands, which are usually called "bandgap". The bandgap can explain several electric properties of silicon, such as temperature-dependent conductivity and photo-current. In the following sections, the band gap structure will be simplified by considering only the

difference between the minimum level of conduction bands and the maximum level of valence bands, and the position-dependent energy level will be ignored (see Fig. 2.7).

2.3.3 Intrinsic Silicon and Non-Intrinsic Silicon

Silicon without impurities or dopants is defined as intrinsic silicon. However, in fact, silicon will be doped by the number of elements for application. Two commonly used elements for doping silicon are boron and phosphorus. In order to form four bonds in the lattice, boron will capture one electron from the valence band and the left one empty state that can move freely in the valence band which is a so-called hole. The boron in the lattice site is lattice boron or substitutional boron, and it has one negative charge at room temperature (B_s^-). Elements like boron are the so-called acceptor (p-type). On the contrary, phosphorus will release one electron into the conduction band and form a lattice phosphorus with one positive space charge, which is the donor (n-type). Their properties strongly relate to radiation detector properties e.g. distribution of the electric field, leakage current, and the formation of defects.

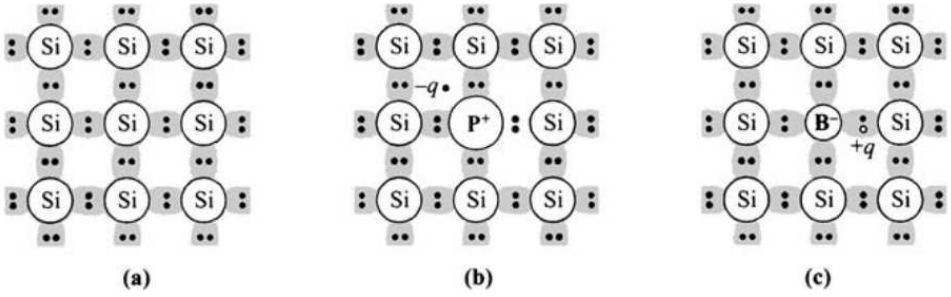

Figure 2.6: Three basic bond pictures of a semiconductor. (a) Intrinsic Si. (b) n-type Si with donor (phosphorus). (c) p-type Si with acceptor (boron). Taken from [35].

Carrier Concentration and Fermi Level

The carrier concentration and Fermi level had already been discussed in reference [35, 58]. The relevant equation used in this work is the expression of the density of states in conduction band N_C and in valence band N_V:

$$N_{C,V} = 2\left(\frac{2\pi m^*_{de,dh} k_B T}{h^2}\right)^{3/2} \tag{2.11}$$

where k_B is the Boltzmann constant, $m^*_{de,dh}$ are the density-of-states effective masses in the conduction and valence bands, h is the Planck constant and T is temperature. In this work, the $N_{C,V}$ is given by [59]:

$$N_{C,V} = 2.540\,933 \times 10^{19} \times \left(\frac{m^*_{de,dh}}{m_0}\right)^{3/2} \left(\frac{T}{300}\right)^{3/2} \text{ cm}^{-3} \tag{2.12}$$

where m_0 is the electron rest mass. Detail can be found in [59].

Mobility

The mobility of electrons (μ_e) and holes (μ_h) is related to the scattering caused by lattice atoms and can be characterized by the mean free time ($\tau_{m,e,h}$) or mean free path ($\lambda_{m,e,h} = \tau_{m,e,h} \cdot v_{th,e,h}$) [35]:

$$\mu_{e,h} = \frac{q_0 \tau_{m,e,h}}{m^*_{de,dh}} = \frac{q_0 \lambda_{m,e,h}}{\sqrt{3 k_B T m^*_{de,dh}}} \tag{2.13}$$

with taking into account the formula:

$$\lambda_{m,e,h} = v_{th,e,h} \tau_{e,h}, \qquad v_{th,e,h} = \sqrt{\frac{3 k_B T}{m^*_{de,dh}}} \tag{2.14}$$

where q_0 is the elementary charge and $v_{th,e,h}$ is the thermal velocity. $\mu_e \approx 1450\ \mathrm{cm}^2/(\mathrm{V} \cdot \mathrm{s})$ and $\mu_h \approx 450\ \mathrm{cm}^2/(\mathrm{V} \cdot \mathrm{s})$ at room temperature. In the following chapter the $v_{th,e,h}$ is used to analysis data, which given by [59]:

$$v_{th,e,h} = v_{0th,e,h} \sqrt{\frac{T}{300}}, \qquad v_{0th,e} = 2.042 \times 10^7 \mathrm{cm/s},\ v_{0th,h} = 1.562 \times 10^7 \mathrm{cm/s} \tag{2.15}$$

The drifting velocity (v) of free carriers is an important parameter for inducing a signal in the detector, which was determined by mobility with electric field E [60]:

$$v_{e,h} = \frac{\mu_{e,h} E}{\left(1 + \left(\frac{\mu_{e,h} E}{v_s}\right)^i\right)^{1/i}} \tag{2.16}$$

where i is 1 for holes and 2 two for electrons, and the drifting direction is parallel to the field. The saturation velocity v_s at room temperature is given by [35]:

$$v_s = \sqrt{\frac{8 E_p}{3 \pi m_0}} \approx 10^7 \mathrm{cm/s} \tag{2.17}$$

where E_p is the optical-phonon energy that can be found in [35].

Besides drifting velocity, the conductivity (σ) or the resistivity (ρ) are also determined by mobility and free carrier concentration:

$$\sigma = \frac{1}{\rho} = q_0(\mu_e n + \mu_h p) \tag{2.18}$$

where the n and p are the free charge carrier concentration. In general, it was assumed to equal the doping concentration before irradiation $N_{\mathrm{eff},0}$ (or effective space charge density before irradiation). Thus, this equation is used to $N_{\mathrm{eff},0}$ for diodes presented in Table 6.1

with $\mu_h \approx 450\ \mathrm{cm}^2/(\mathrm{V}\cdot\mathrm{s})$. Another method to measure $N_{\mathrm{eff},0}$ and effective space charge density N_{eff} will be discussed in chapter 3.

Recombination

Up to now, two assumptions for electron and hole recombination were proposed and had been discussed in [35] (band-to-band) and [61] (Shockley-Read-Hall recombination).

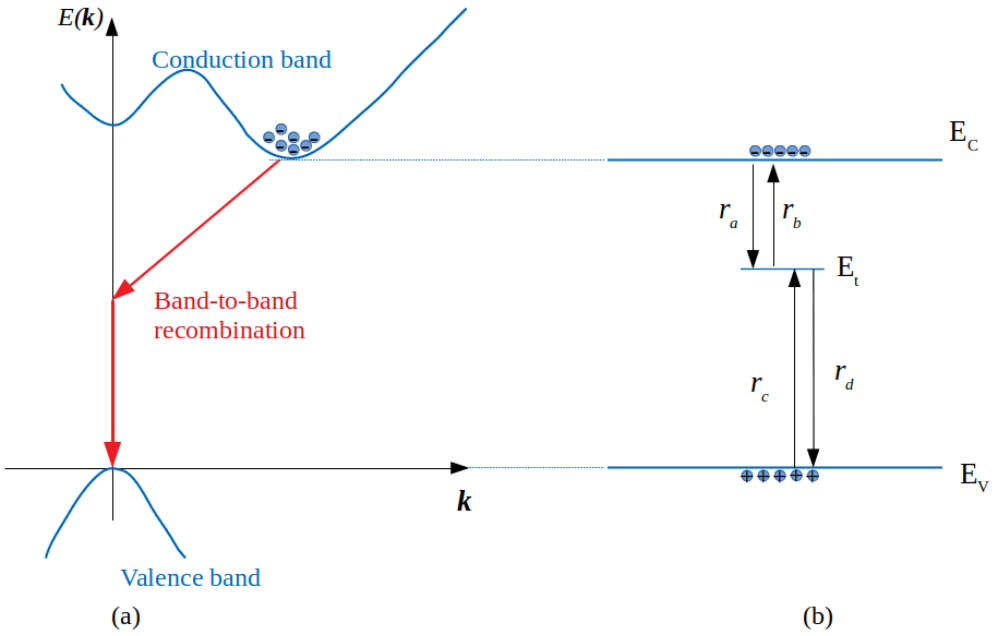

Figure 2.7: 2-D schematic of recombination in silicon. (a) Band-to-band recombination, (b) SRH recombination, E_C and E_V are the edges of the conduction and valence band respectively, E_t is trap level. r_a capture rate of electrons concentration, r_b emission rate of electrons concentration, r_c capture rate of holes concentration, and r_d emission rate of holes concentration.

The band-to-band recombination indicates the direct transition of electrons between the conduction and valence band. Silicon is an indirect-bandgap semiconductor(See Fig. 2.5 and 2.7). The transitions not only relate to the changes of energy but also require the electron to change its momentum. Thus, the recombination procedure in silicon is dominated by SRH. The disorder or impurities create energy levels in the band gap and assists the recombination, which is described by four recombination procedures $r_{a,b,c,d}$ (see Fig. 2.7(b)) [61]:

$$r_a = c_n n p_t, \quad r_b = e_n n_t, \quad r_c = c_p p n_t, \quad r_d = e_p p_t \tag{2.19}$$

where $c_{n,p}$ is the capture coefficient for electrons or holes respectively (with unit $\mathrm{cm}^{-3}\mathrm{s}^{-1}$), the $e_{n,p}$ is the emission rate for electrons or holes (with unit s^{-1}), n_t or p_t are the density of trap levels occupied by electrons or holes and those two follow the relation: $N_t = n_t + p_t$. The calculation for n_t and p_t need to discuss for specific situations, which will be

discussed in detail in chapter 5. Considering the thermal equilibrium, the emission rate is equal to the capture rate [61]:

$$e_{n,p} = c_{n,p} N_{C,V} \exp\left(\pm \frac{E_t - E_{C,V}}{k_B T}\right) \tag{2.20}$$

and the capture coefficient was defined by the capture cross section σ and $v_{th,e,h}$ [61]:

$$c_{n,p} \;=\; \sigma_{n,p} v_{th,e,h} \tag{2.21}$$

For some cases e.g. light injection or irradiated ionization, the built-up equilibrium will be affected and a new equilibrium will be built again. Those procedures involve parameters transition rate (U) and carrier lifetime (τ), which was defined by:

$$U = \frac{\delta n'}{\tau} \tag{2.22}$$

Where the $\delta n'$ is the induced free carriers. The derivation of U and τ are discussed by W. Shockley in detail [61]. Such results given by $U = r_a - r_b$ or $U = r_c - r_d$ with assumption that constant carriers injection:

$$U = \frac{\sigma_n \sigma_p v_{th,e} v_{th,h} N_t (pn - n_i^2)}{\sigma_n v_{th,e}\left(n + n_i \exp\left(\frac{E_t - E_i}{k_B T}\right)\right) + \sigma_p v_{th,h}\left(p + n_i \exp\left(\frac{E_i - E_t}{k_B T}\right)\right)} \tag{2.23}$$

For the level of the trap close to mid-gap, the τ in p-type or n-type silicon was given [61]:

$$\tau_n = \frac{1}{\sigma_n v_{th,n} N_t}, \qquad \tau_p = \frac{1}{\sigma_p v_{th,p} N_t} \tag{2.24}$$

respectively. Equation 2.24 indicates the carrier's lifetime increases with trap concentration, which explains the degradation of the detector performance after irradiation.

3 Silicon Detector

As a detector, radiation-induced charges in silicon must be converted into an electronic signal and distinguished from the dark current. Therefore, a p-n junction under reverse bias is commonly used for detector applications. In this case, a semiconductor-semiconductor contact provides a uniform electric field, while a metal-semiconductor contact applies bias and facilitates to readout signal.

This chapter will discuss the metal-semiconductor and semiconductor-semiconductor contacts, and present the electrical properties of one-dimensional silicon detectors, including electric field, potential, current, and capacitance. Additionally, the operation of silicon detectors involving the Shockley-Ramo theory, the detector system on the accelerator, and different types of detectors will be demonstrated.

3.1 p-n Junction and Metal-Semiconductor Contact

3.1.1 p-n Junction

As mentioned before, boron or phosphorus doping turns intrinsic silicon into p- or n-type silicon. Once this is achieved on the same wafer, it forms the so-called p-n junction. As described in Fig. 3.1, the free charge carriers will diffuse from each side, and the negative or positive space charges on the left (B_s^- or P_s^+) will form a field that restricts the diffusion of free charge carriers. Eventually, diffusion will reach the thermal equilibrium condition, and the formed field is a so-called built-in field.

In the case without carrier injection and applied bias, considering the thermal equilibrium condition, the potential of the built-in field ϕ_{bi} can be given by $\phi_{bi} = \frac{k_B T}{q_0} \ln\left(\frac{N_D N_A}{n_i^2}\right)$ [35].

3.1.2 Metal-Semiconductor Contact

Similar to the case of semiconductor-semiconductor contact, when two materials touch, the bandgap bends, and a field similar to the built-in field is introduced into the silicon bulk. For detector applications, typically a metal is connected to a low-resistivity layer (p^+ or n^+, where N_A or $N_D > 10^{19}$ cm^{-3}) that is also referred to as an ohmic contact. In this case, the field between the metal and semiconductor can be neglected. In some references, these contacts are also called electrodes.

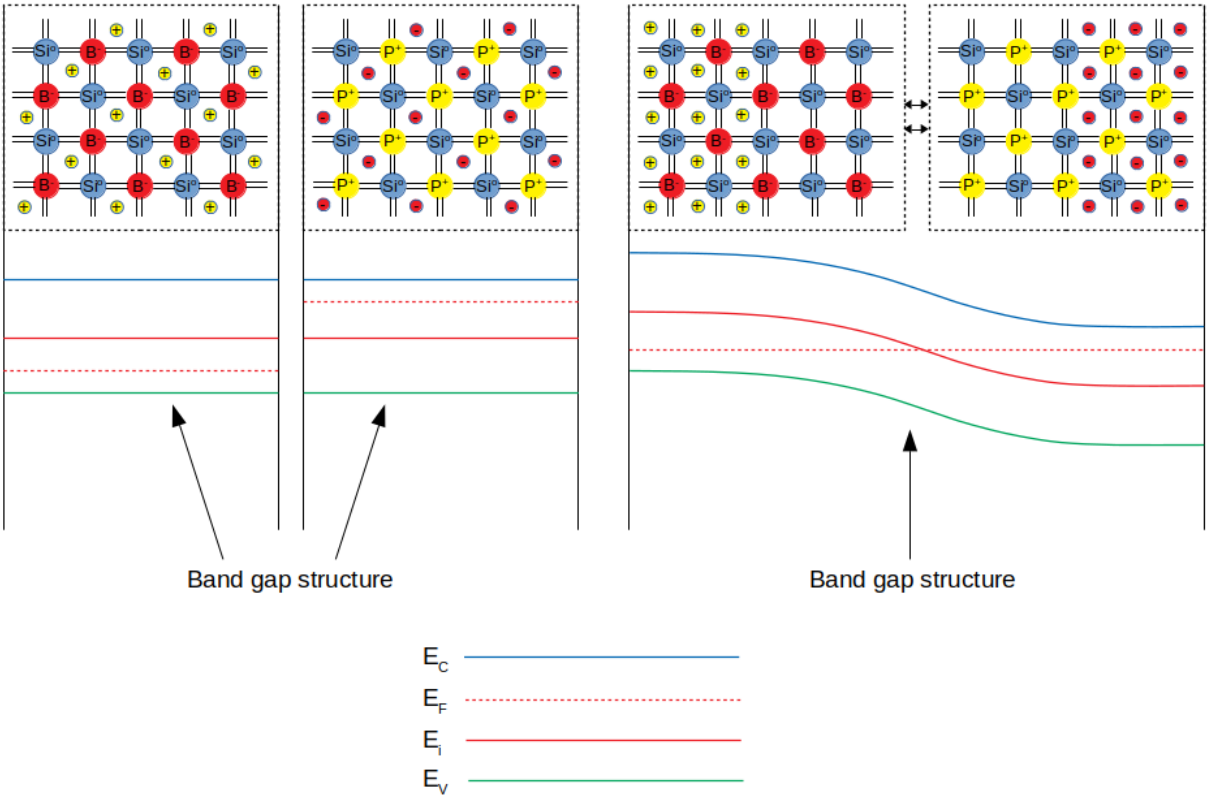

Figure 3.1: Schematic before and after p- and n-type contact.

It is worth noting that both metal-semiconductor and semiconductor-semiconductor contacts induce a depleted region in the silicon bulk. In the past, metal-silicon (Shockley diode) contacts have also been used for detector applications [11].

3.2 Electrical Properties of Silicon Detectors

3.2.1 Electric Field and Potential

As the applied reverse bias to a p-n junction increases, the built-in field is extended into the bulk, creating the depleted or active region. Once the entire bulk is depleted, it is considered fully depleted, and the corresponding bias voltage is known as the fully depleted voltage, V_{fd}. For p-type silicon, the distribution of the electric field and potential in this region can be calculated using the Poisson equation:

a) Parallel electrodes (See Fig. 3.2a):

$$-\frac{d^2V}{dx^2} = \frac{dF}{dx} = \frac{q_0}{\varepsilon\varepsilon_0}(-N_{\text{eff}}) \tag{3.1}$$

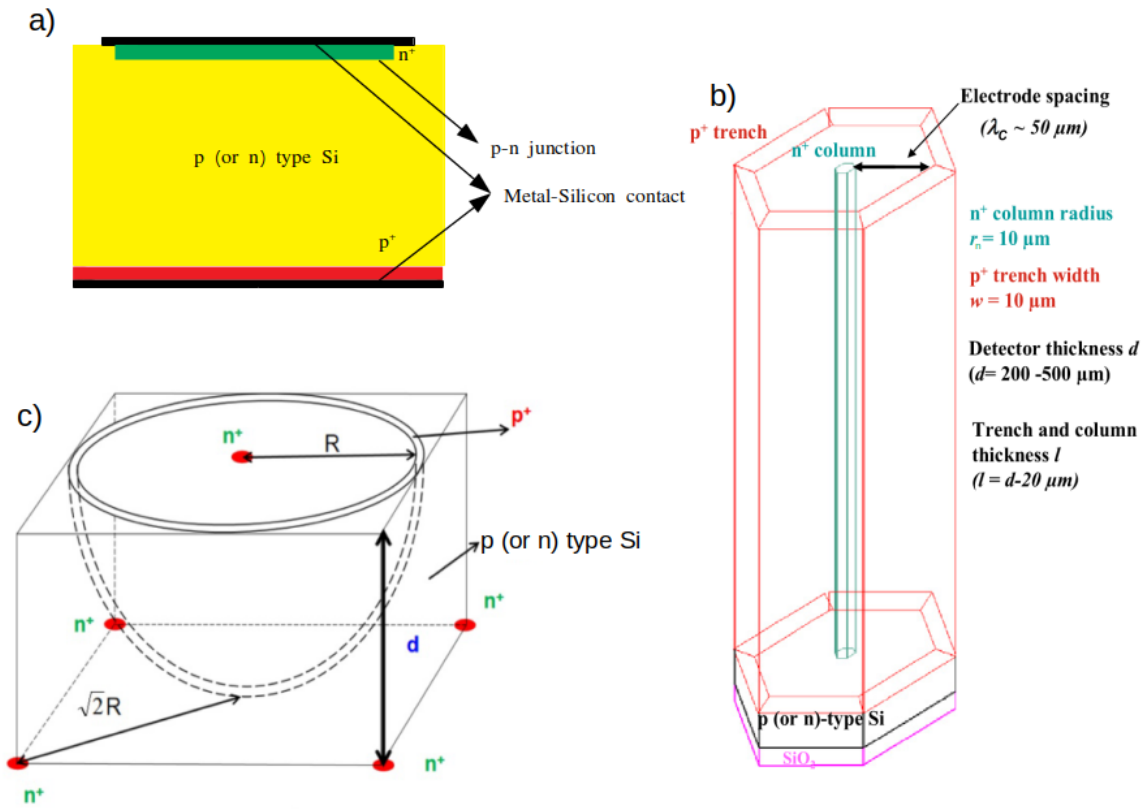

Figure 3.2: Examples for different designs of silicon detector structure. a) Detector with the parallel electrode, b) 3-D Trench silicon detector [62], c) Spherical silicon detector [63].

b) Cylindrical electrodes (3-D detector [62]. See Fig. 3.2b):

$$-\Delta^2 V = \frac{1}{r} \cdot \frac{d(rF(r))}{dr} = \frac{q_0}{\varepsilon\varepsilon_0}(-N_{\text{eff}}) \tag{3.2}$$

c) Spherical electrodes (Proposed by [63]. See Fig. 3.2c)

$$-\Delta^2 V = \frac{1}{r^2} \cdot \frac{d(r^2F(r))}{dr} = \frac{q_0}{\varepsilon\varepsilon_0}(-N_{\text{eff}}) \tag{3.3}$$

where, x represents the depth in the depleted region for parallel electrodes, while r stands for cylindrical or spherical electrodes. ε and ε_0 are the dielectric constants of silicon and vacuum permittivity, respectively. Assuming that the effective space charge density N_{eff} is homogeneously distributed in the bulk, the values of the electric field ($F(x)$ or $F(r)$) and potential ($V(x)$ or $V(r)$) for non-fully depleted diodes can be described as follows:

a) Parallel electrodes (Fig. 3.2a, $x < W(V)$. See Fig. 3.2a):

$$F(x) = \frac{q_0 N_{\text{eff}}}{\varepsilon\varepsilon_0}(W(V) - x), \quad V(x) = \frac{q_0 N_{\text{eff}}}{2\varepsilon\varepsilon_0}(W(V) - x)^2 \tag{3.4}$$

b) Cylindrical electrodes (3-D trench detector [64], $R = r_t - W(V)$, $R < r < r_t$. See Fig. 3.2b):

$$F(r) = \frac{q_0 N_{\text{eff}}}{2\varepsilon\varepsilon_0} r(\frac{R^2}{r^2} - 1), \quad V(r) = \frac{q_0 N_{\text{eff}}}{2\varepsilon\varepsilon_0}[R^2 \ln \frac{r}{R} - \frac{1}{2}(r^2 - R^2)] \tag{3.5}$$

c) Spherical electrodes (A is given by boundary condition [63]. $W(V) = r$ - r_{n+}. See Fig. 3.2c)

$$F(r) = \frac{q_0 N_{\text{eff}}}{3\varepsilon\varepsilon_0} r - \frac{A}{r^2}, \quad V(r) = \frac{q_0 N_{\text{eff}}}{6\varepsilon\varepsilon_0}(R^2 - r^2) - \frac{q_0 N_{\text{eff}}}{3\varepsilon\varepsilon_0} r^3 \left(\frac{1}{r} - \frac{1}{R}\right) \tag{3.6}$$

where, $W(V)$ denotes the depleted depth. Because of $V >> \phi_{bi}$, ϕ_{bi} is ignored in the above formulae. It should be noted that the distribution of the electric field strongly depends on the applied bias. Once the applied bias exceeds V_{fd}, an additional voltage-related term is needed to correct the results in the above equations [62].

3.2.2 Current

Leakage Current

The current of the diode (p-n junction, or detector) under reverse bias is called leakage current or reverse current, which consists of diffusion (non-depleted region) and generation current (depleted region). The diffusion current was caused by the carrier-concentration gradient, and it is given by Fick's law:

$$J_{D,n} = q_0 D_n \frac{dn}{dx} \text{ and } J_{D,p} = q_0 D_p \frac{dp}{dx} \tag{3.7}$$

where the $J_{D,n,p}$ is diffusion current density for electrons and holes. The diffusion coefficient for electrons and holes $D_{n,p}$ is given by thermal velocity ($v_{th,n,p}$) and scattering (τ_m) – $D_{n,p} = v_{th,n,p}\tau_m$. In general, the total diffusion current J_D is given by the sum of electrons (J_n) and holes (J_p) diffusion currents (detail see [35]):

$$J_n = \frac{q_0 D_n n_{p0}}{L_n}\left[\exp\left(\frac{q_0 V}{k_B T}\right) - 1\right] \tag{3.8}$$

$$J_p = \frac{q_0 D_p p_{n0}}{L_p}\left[\exp\left(\frac{q_0 V}{k_B T}\right) - 1\right] \tag{3.9}$$

$$J_D = J_0\left[\exp\left(\frac{q_0 V}{k_B T}\right) - 1\right] \tag{3.10}$$

where p_{n0} (n_{p0}) is the equilibrium hole (electron) density on the non-depleted n-side (p-side). The diffusion length for electrons and holes $L_{n,p}$ is given by $L_{n,p} = \sqrt{D_{n,p}\tau_{n,p}}$ with the carrier lifetime $\tau_{n,p}$. The generation current density was considered by the recombina-

tion processing in the bulk and determined by the lifetime of free carrier concentration:

$$J_g = \frac{q_0 n_i}{\tau_g} \tag{3.11}$$

where J_g is the generation current density. The τ_g is the generation carrier lifetime given by the carrier lifetime:

$$\tau_g = (1 + \frac{n}{n_i})\tau_p + (1 + \frac{p}{n_i})\tau_n \tag{3.12}$$

Therefore, the total leakage current (I_{LC}) under reverse bias is given by:

$$I_{LC} = q_0 \sqrt{\frac{D_n}{\tau_n}} \frac{n_i^2}{N_A} \left[\exp\left(\frac{q_0 V}{k_B T} \right) - 1 \right] + \frac{q_0 n_i \cdot AW(V)}{\tau_g} \tag{3.13}$$

where A is the active area of the p-n junction (or detector), and the $W(V)$ is the depleted depth of the p-n junction (or detector). Typically, the diffusion current is small and the leakage current is estimated by the generation current.

According to Eq. 3.13, the leakage current is heavily influenced by factors such as carrier lifetime, impurity concentrations, and temperature. Therefore, using high purity materials and operating at low temperatures can improve the discrimination between the pulse signal and noise.

Forward Current

Forward current is not typically used in the operation of silicon detectors. However, it is commonly employed to investigate defects in thermally stimulated techniques (Details see chapter 5). The forward current (I_F) consists primarily of leakage current, but since the depleted depth ($W(V)$) approximates to zero, the generation current can be ignored. As described by the total diffusion current in Eq.3.10, the forward current can easily reach high values under forward bias. Further details on the behaviour of forward current will be discussed in chapter 4.

3.2.3 Capacitance

The capacitance of a detector is an important factor in determining its characteristics and noise properties. Typically, the capacitance is determined by the structure of the detector. The capacitance ($C(V)$) of a p-n junction can be defined as the ratio of the change in charge (dQ) to the corresponding change in the voltage (dV):

$$C(V) = \frac{dQ}{dV} \tag{3.14}$$

where the dV is determined by Alternating Voltage - V_{AC}. According to the Poisson equation, the total potential difference in the depleted bulk V is given by:

$$V = -\int_0^{W(V)} F(x)dx = -xF(x)|_0^{W(V)} + \frac{q_0}{\epsilon\epsilon_0}\int_0^{W(V)} xdF(x) \tag{3.15}$$

the $dF(x)$ can be displaced by $N_{\text{eff}}(x)dx$. And the charge Q can be given by the space charge density N_{eff} in the bulk:

$$Q = q_0 \int_0^{W(V)} N_{\text{eff}}(x)dx \tag{3.16}$$

after differentiating V and Q with respect to $W(V)$, the depleted depth $W(V)$ can be extracted with active area A [35]:

$$W(V) = \frac{A\epsilon\epsilon_0}{C(V)} \tag{3.17}$$

And the $N_{eff}(W(V))$ can be extracted from $\frac{d(1/C^2)}{dV}$:

$$\frac{d(1/C^2)}{dV} = \frac{d(1/C^2)}{dW(V)} \cdot \frac{d(W(V))}{dV} = \frac{2}{A\epsilon\epsilon_0 N_{\text{eff}}(W(V))} \tag{3.18}$$

Thus, the doping profile can be extracted from the capacitance characterization, where the resulting curve shows the relationship between $N_{\text{eff}}(W(V))$ and $W(V)$. It should be mentioned here that the measured capacitance may include errors due to factors such as serial resistance [65], surface defects [66], and bulk defects [67].

3.3 Manufacture of Silicon Detectors

As mentioned in chapter 3, single-crystal silicon will be used to manufacture silicon detectors. Firstly, the growth pillar will be cut into pieces called wafers. Then, the cut wafer needs to be lapped and polished to obtain a uniformly thick wafer. After lapping and polishing, the wafer will be washed, and the dried wafer will be oxidized (usually with water vapour). The oxidized wafer will then undergo the following steps: opening windows → implantation → contact/metallization. These steps are the main processing; in fact, for each process, the wafer needs to be cleaned with a liquid that contains acids, solvents, surfactants, and deionized water. Then, lithography and etching are used to obtain the required structure. Finally, the wafer will be packaged with an electronic readout system. The detail about these procedures can be found in [68].

It should be mentioned that such processes may introduce several unexpected defects on the surface and in the bulk of the silicon detector, which may affect its performance. Thus, quality control is crucial at each step of the manufacturing process.

3.4 Operation of Silicon Detectors

3.4.1 Operation Principle

The processing of signal generation was first proposed by S. Ramo in 1938 [69] and was later developed by E. Gatti et al. for use in semiconductor detectors [70] [71]. In general, the signal induced by moving free-charge carriers is governed by the energy conservation equation:

$$dW_q + dW_V + dW_F = 0 \tag{3.19}$$

where the energy change by a charge moving a distance $d\vec{r}$ i.e. $dW_q = q_0\vec{F}_r d\vec{r}$, the energy change on power supply i.e. $dW_q = VdQ + QdV$ and the energy change on electric field i.e. $dW_F = d(\frac{1}{2}\epsilon\epsilon_0 \int_{V_{ol}} \vec{F}^2 dV_{ol})$, where the V_{ol} is the volume of studied region. In the case of constant V and the change in the electric field can be ignored, $dQ = -q_0\frac{\vec{F}_r}{V}d\vec{r}$. In the end, the signal introduced in the silicon detector is described by Ramo's theorem [69]:

$$i = Q(t) \cdot \vec{v} \cdot \vec{E_w} \tag{3.20}$$

This equation indicates that the induced current i is given by multiplying the total drifting charges $Q(t)$, the drifting velocity $\vec{v}$ of free charge carriers, and the weighting field $\vec{E_w} = \frac{\vec{F_r}}{V}$. The calculations of $\vec{E_w}$ can be found in [72].

After irradiation, the $Q(t)$ are reduced with the drifting time due to the decrease of the carrier's lifetime and can be described by:

$$Q(t) = Q_0 \cdot \exp\left(-\frac{t}{\tau}\right) \tag{3.21}$$

where Q_0 is the initial value of ionized charges, t is the drifting time and τ is the carrier's lifetime. Equation 3.21 indicates that the shorter t and longer τ can enhance the signal of the detector. The τ value, as mentioned in section 2.3.3, it strongly correlated to the defect concentration N_t (decreasing with N_t). This is the reason why charge collection efficiency (CCE) degrades after irradiation [73].

3.4.2 Operation in High Energy Physics

The operation environment of silicon detectors in high-energy physics is subjected to an intense radiation field, which results in significant radiation damage. This radiation damage can have detrimental effects on the performance of the silicon sensors. In this section, Compact Muon Solenoid (CMS) [74] is an example of the silicon detectors operation environment. CMS is one of the four experiments running in LHC, along with ATLAS, ALICE, and LHCb. The CMS detector is positioned at LHC Point 5, one of the inter-

action points designed to deliver high luminosity. As can be seen in Fig. 3.3, the silicon detector as tracker normally was set at the region nearest to the event. The fluence in this region is close to (1-10)$\times 10^{15}$ cm^{-2} (neutron equivalence value) per year [75], which will significantly degrade the performance of detectors.

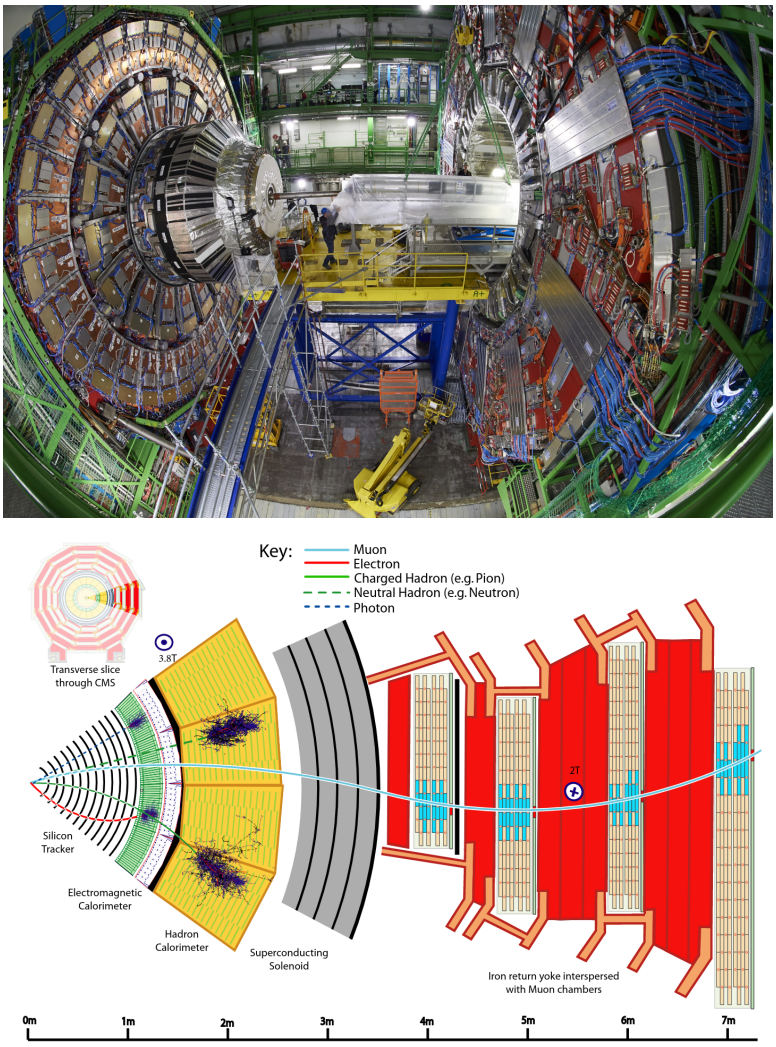

Figure 3.3: (up) Overview of CMS experiment. (down) Reconstruction scheme for different particle types in the CMS detector. Charged particles are identified as curved tracks in the silicon tracker and the muon system. Electrons and photons are stopped and deposit energy in the electromagnetic calorimeter, while hadrons interact predominantly in the hadronic calorimeter. Muons are typically reconstructed as long tracks in both the silicon tracker and the muon chambers. Taken from [75].

3.5 Types of Silicon Detectors

3.5.1 Planar Pixel and Strip Detectors

Pixel or strip refers to the shape of the implant in a planar segmented p-n junction. Such segmented sensors are the common tracking detectors for high-energy physics ex-

periment applications (see silicon tracker in Fig. 3.3). The sketch of common pixel and strip detectors can be found in Fig. 3.4. The operation principle can be found in [76].

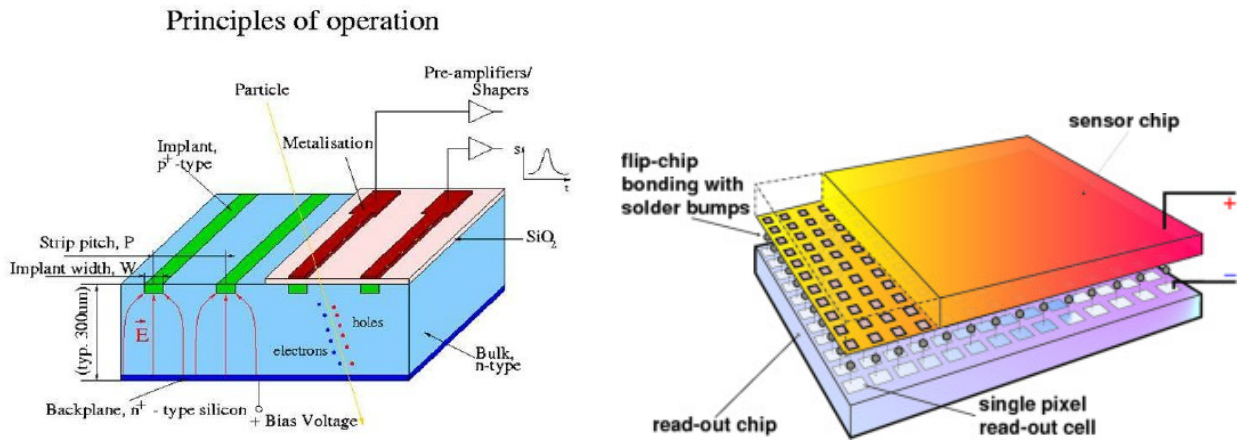

(a) (b)

Figure 3.4: (a) Principles of operation of a silicon strip detector [77]. (b) Silicon pixel detector [76].

3.5.2 3-D Detectors

In order to improve the radiation hardness of silicon detectors, the 3-D detector is proposed in 1999 [78, 79] to use as the silicon pixel detector as can be seen in the Fig. 3.5. In 2009, the 3D trench electrode Si detector structure had been proposed as can be seen in Fig. 3.2. The recently development of 3-D detector can be found in [80].

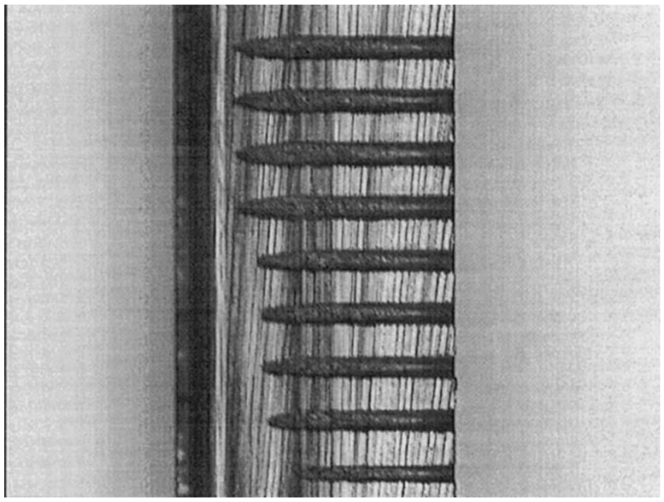

Figure 3.5: A view of part of a set of etched holes, showing the increased depth reached by holes of larger diameters. The wafer was 540 µm thick and the etch time was 5 h. The photo-mask hole diameters from top to bottom are four holes at 30 µm, four at 25 µm, and one at 20 µm. Taken from [79].

3.5.3 SiPM

A SiPM, or Silicon Photomultiplier, is a type of photodetector that is made up of an array of 10-100 µm avalanche photodiodes (APDs, see avalanche effect in [35]) that are operated in Geiger mode. SiPMs are commonly used in applications that require high sensitivity and fast response times, such as medical imaging [81], particle physics [82, 83], and LIDAR systems [84].

SiPMs work by detecting the light that is emitted or scattered by a target object. When a photon strikes one of the APDs in the array, it causes an electron to be released, which then triggers a self-sustaining avalanche effect, creating a measurable electrical pulse that is proportional to the amount of light that was detected.

One of the advantages of SiPMs is that they have a very high photon detection efficiency, which means that they are able to detect a high percentage of the photons that are emitted or scattered by a target object. They also have a very fast response time, which makes them useful in applications that require rapid data acquisition.

However, SiPMs also have some disadvantages, such as a relatively high dark current, which can lead to increased noise levels. Additionally, SiPMs are sensitive to temperature and can suffer from increased noise levels and reduced performance at higher temperatures.

The detail of radiation damage of SiPM can be found in [82].

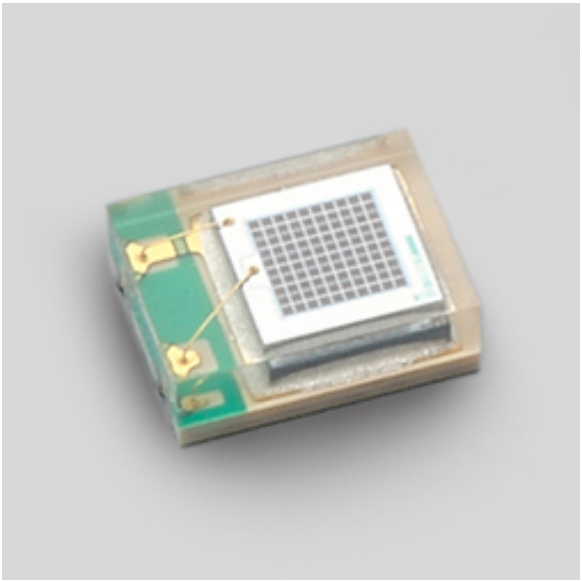

Figure 3.6: Overview of SiPM. Taken from [85].

3.5.4 LGADs

In order to cope with extraordinary high particle rate up to 200 p–p collisions per bunch crossing in High Luminosity Large Hadron Collider (HL-LHC) experiments, new types of silicon sensors were developed e.g. Low Gain Avalanche Detectors (LGADs) for high-precision timing ($\leq$ 50 ps) [2, 3]. As Fig. 3.7 shows, one highly doped p-type layer ($\approx$

1×10^{16} cm^{-3}) was introduced to generate a high electric field in this layer. Therefore, even the detector with a thinner thickness still can obtain a visible signal. In general, the time resolution of detectors is proportional to the ratio of the width S_w and high S_h of the signal peak: S_h/S_w. Thus, by this design, the time resolution of detectors can be improved. However, LGADs differ from SiPMs in that they have a lower gain, typically below 100, compared to SiPMs which have gains on the order of thousands.

However, the exposure of LGADs to radiation leads to a reduction of the sensor's internal gain with increasing particle fluence [2, 3, 86]. This will be discussed in the next chapter.

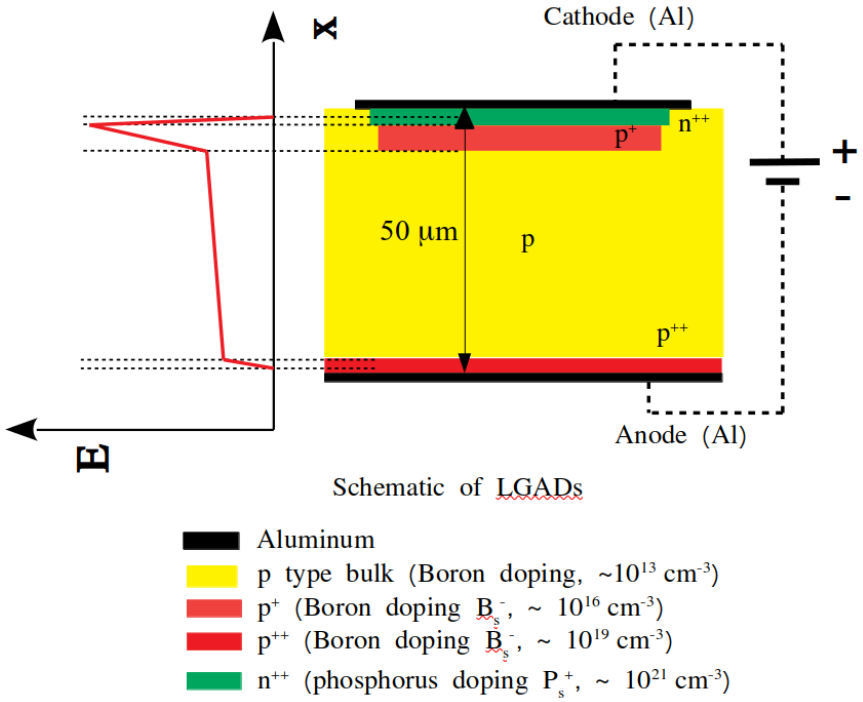

Figure 3.7: Schematic of LGADs with diagram of the distribution of the electric field.

4 Radiation Damage in p-type Silicon Detectors

Typically, radiation damage in silicon detectors occurs in both the surface and bulk regions. However, this work focuses on bulk damage, which results from elastic scattering between incident particles and atoms. Bulk damage in n-type silicon detectors has been well-studied over several decades, and the type conversion from n-type to p-type has been extensively researched by R. Wunstorf [10]. Subsequently, microscopic defect characterization methods, such as Thermally Stimulated Current (TSC) and Deep Level Transient Spectroscopy (DLTS), have been widely employed to investigate radiation-induced defects [11, 12, 13, 14, 87]. Based on these investigations, p-type silicon detectors have been utilized for high-energy physics experiments. However, boron, which is an important dopant in the p-type silicon crystal, can also be knocked out from its substitutional site by either incident particles or moving interstitial silicon atoms that obtain energy from incident particles. This procedure is known as the boron removal effect (the main reason for acceptor removal). This work aims to investigate the defects that are formed during this procedure. Although the main observed results in this work are related to bulk damage, unexpected surface damage was also observed in the case of ^{60}Co-γ irradiation.

This chapter will begin with a brief discussion of surface damage in section 4.1, followed by an explanation of the procedure of displacement damage. Subsequently, sections on Non-Ionization Energy Loss (NIEL), radiation-induced defects, annealing behaviour, and the effects on detectors will be presented.

4.1 Surface Damage

Similar to silicon, ionization can also occur in SiO_2 with a threshold value of 17 eV [88]. In the bulk of silicon sensors, free carriers will drift into the electrode and be collected by the read-out system. The ionizing radiation creates electron-hole pairs in the SiO_2. Immediately after the electron-hole pairs are created, most of the electrons will rapidly drift toward the gate and the hole will drift toward the Si-SiO_2 interface. However, even before the electrons can leave the oxide some of them will recombine with holes. Those holes which escape the initial recombination will be transported through the oxide toward the Si-SiO_2 interface by hopping through localized states in the oxide. As the holes approach the interface some will be trapped forming a positive oxide-trap charge.

It is believed that holes during hopping or as they are trapped can release hydrogen ions (protons) which will also drift to the Si-SiO_2 interface where they may react to form interface traps. Additionally, elastic scattering can occur in SiO_2 and result in disordered clusters that are similar to displacement damage. Since SiO_2 is typically used as protection and isolation and is grown on the surface by oxygenating the silicon surface, such damages are referred to as surface damage.

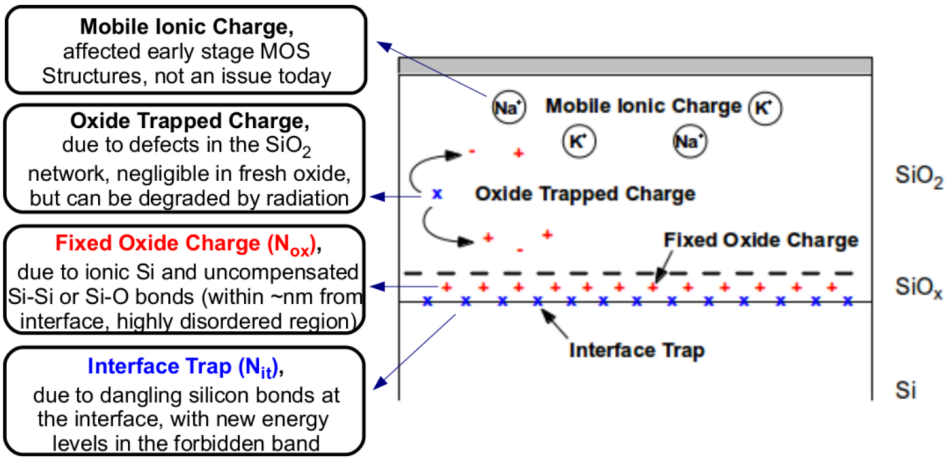

Figure 4.1: Schematic illustration of defects in the SiO_2 and at the Si-SiO_2 interface. Taken from [89].

As shown in Fig. 4.1, the damage on the surface of the silicon detector can be classified into four different types:

1. Mobile ionic charge: This is related to the impurities introduced into SiO_2, such as K^+, Na^+, Li^+, or H^+ during the manufacturing process. These ions can move under bias even at room temperature, resulting in changes in the electric properties of SiO_2, such as increased conductance. However, this issue has been resolved now.

2. Oxide-trapped charge: This is caused by ionization or radiation-induced free electron-hole pairs, which can be captured by the traps in SiO_2. This effect is normally negligible in well-produced detectors, but it can be degraded with radiation.

3. Fixed oxide charge: The interface layer between SiO_2 and silicon has a highly disordered region with deep-level defects. These defects can capture induced free charges and transform into a relatively stable state. The famous E′ centre [90] belongs to this effect, which is normally assumed to be caused by the weak bond between two silicon atoms. The density of the E′ centre increases with radiation, especially when irradiated by high-energy photons.

4. Interface trap: In addition to the E′ centre, two other defects, P_b and P_{b0} [90], are assumed to be caused by dangling silicon bonds.

All of the defects mentioned above increase with irradiation. However, due to the complicated crystal structure and microscope configurations of defects, the responsible defects for surface damage could not be identified in chapter 8 of this work, which focuses on γ-irradiated diodes (see details in chapter 8). Furthermore, surface damage is also induced by hadrons but the effects are obscured by the introduction of displacement damage in the bulk material.

4.2 Displacement Damage

Bulk damage in silicon sensors is related to the defects formed by hadrons (neutrons, protons, pions, and others) or lepton. The formation of defects is primarily caused by displacing a Primary Knock-on Atom (PKA) out of its lattice site with recoil energy. All atoms or particles that have passed through the lattice as a result of a collision may eventually disorder the initial crystal (the ideal crystal described in chapter 2), and the formed disordered region or lattice site is called the cluster-related or point-like (0.1 to 1 nm) defects, respectively.

In general, by assuming the interactions between the incident particles and atoms in the crystal are dominated by elastic scattering and non-relativistic momenta, the recoil energy of PKA $E_{R,max}$ can be obtained from the following Eq. 4.1 for an incident particle with energy E_P and m_P:

$$E_{R,max} = 4E_P \frac{m_P m_{Si}}{(m_P + m_{Si})^2} \tag{4.1}$$

The threshold kinetic energy of the silicon atom to leave the lattice site is 25 eV [91], which is normally assumed the threshold for forming a displacement atom. While the 5 keV is required for generating a disordered region (cluster defect) [91]. The corresponding kinetic energy of 185 eV and 35 keV for neutrons to reach the thresholds of point and cluster defect can be given by Eq. 4.1. The corresponding kinetic energy 255 keV and 5 MeV for an electron can also be obtained from the equation including the relativistic approach [92]. Typically, the defects generated by ^{60}Co γ-ray (1.33 MeV) were caused by a Compton electron that has the kinetic energy of roughly 1 MeV, in this case, therefore, only point defects will be generated in bulk.

It should be noted here that the temperature in the crystal will be increased by irradiation. Thus, the annealing behaviour mentioned in section 4.4.4 can also occur during irradiation. Meanwhile, the processes of defect formation do not end after irradiation. The Frenkel pairs (interstitial atom and vacancy pair) in silicon are very mobile at 150 K [11]. Therefore, some defects might be annihilated at room temperature, and others will transform to a comparatively stable state by reacting with impurities or disordered regions [93]. The formed final defect is called by bulk damage.

4.3 Non-Ionization Energy Loss (NIEL)

The introduced damage in a crystal due to irradiation depends on the properties of the incident particles, such as their mass, momentum, and charge state. For instance, when protons interact with silicon at lower energy levels, they primarily interact via coulombic interaction, which is mainly lost through ionization. On the other hand, neutrons only interact with nuclei and are mainly related to elastic collisions for kinetic energies $\geq$ 1.8 MeV [91]. These differences present a challenge in scaling radiation damage for different particles, which has led to the development of hypotheses, such as the Non-Ionization Energy Loss (NIEL) hypothesis.

4.3.1 Displacement Damage Cross Section

The definition of NIEL is the energy loss of particles caused by the displacing collision with atoms, in general, it was quantified by displacement damage cross-section ($D(E)$) [11, 94]:

$$D(E) = \sum_{v} \sigma_v(E) \cdot \int_0^{E_{R,max}} f_v(E,\ E_R) P(E_R) dE_R \tag{4.2}$$

with the recoil energy E_R of PKA and Lindhard partition function $P(E_R)$ [94]. The index v here indicates possible interaction between the incident particle with energy E and the silicon atom. $f_v(E,\ E_R)$ and σ_v are the probability and cross section for reaction v, respectively. The details for calculating the damage cross-section can be found in [95, 96].

The result for different particles (neutrons, protons, electrons and pions) are presented in Fig. 4.2 in the energy range from 10^{-10} up to 10^4 MeV. The detail about Fig. 4.2 can be found in [92]. Once all deposition of displacement energy was normalized at the same unit, the damage for different particles can be compared with each other.

4.3.2 Hardness Factor

A comparison of NIEL between different particles was achieved using the hardness factor κ, defined according to Equation 4.3:

$$\kappa = \frac{\int D(E)\Phi(E)dE}{D_{n,1\mathrm{MeV}} \int \Phi(E)dE} \tag{4.3}$$

In general, the NIEL value of different particles will be normalized to 1 MeV neutrons i.e. the displacement damage cross section $D_{n,1\mathrm{MeV}} = 95$ MeVmb. Thus, the fluence Φ of particles with energy E can be replaced by the equivalent 1 MeV neutron fluence Φ_{eq} by

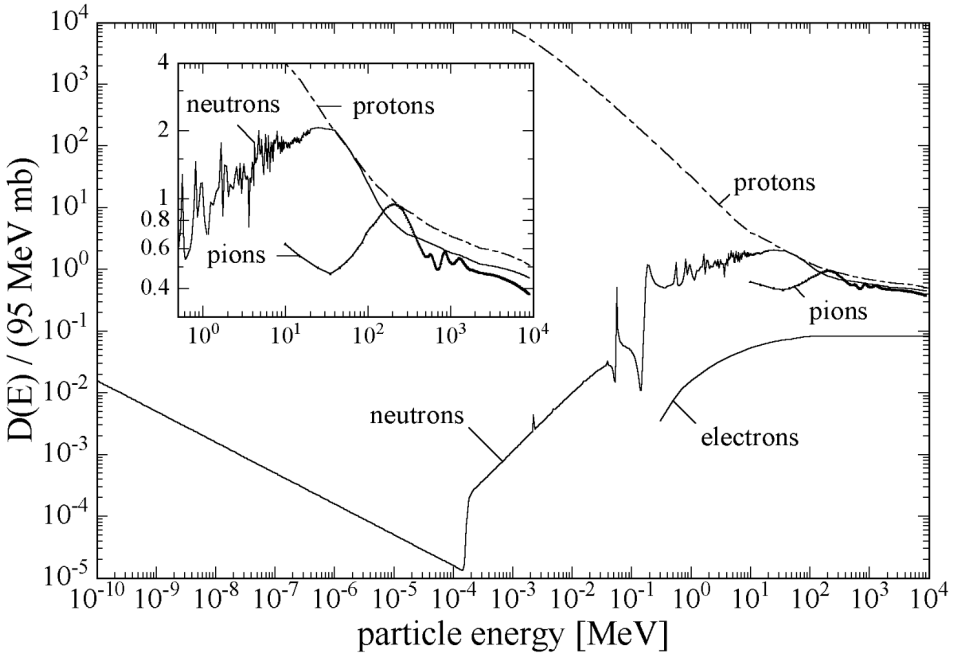

Figure 4.2: Displacement damage function $D(E)$ normalized to 95 MeVmb for neutrons (10^{-10} to 20 MeV [97], 20 to 400 MeV [98], 805 MeV to 9 GeV [95]), protons [95, 99], pions [95] and electrons [99]. Due to the normalization to 95 MeVmb the ordinate represents the damage equivalent to 1 MeV neutron. The insert displays a zoomed part of the figure. Taken from [11].

considering the damage function $D(E)$ or the corresponding NIEL values:

$$\Phi_{\text{eq}} = \kappa\Phi \tag{4.4}$$

4.4 Defect in p-type Silicon

Many of the defects in n- and p-type materials have already been reported in previous publications [11, 12, 13, 14, 87]. This section will discuss the properties of these defects, including their charge state, energy level, and impact on device performance.

4.4.1 Defect Classification

Electrically active defects can be classified based on a variety of factors, such as their energy level (deep or shallow), charge state (at room temperature), or size (cluster or point). Before discussing specific types of defects, it is essential to introduce the naming convention of the defects. The following rules are commonly used in previous publications to mark defects:

1. If the chemical composition and structure of the defect are already known, it is typically named after the elements that make up the defect. In this case, the index i or s represents the atom located at interstitial or substitutional sites e.g. B_iC_s

[15, 20] the defect consisted of an interstitial boron and substitutional carbon. V indicates a vacancy e.g. V_2 [19] consisted of two vacancies.

2. The defect had been investigated but still needs furthermore experiments to identify its chemical composition and structure, which sometimes are named by a special symbol e.g. I_P and Γ [100].

3. Similar to 2, the defect had been investigated but still needs furthermore experiments to identify its chemical composition and structure, which is normally named by the an E (electron traps) or H (hole traps) with the temperature at which it appears in TSC or DLTS spectra, e.g. E30K and H40K (see chapter 6) indicates the peak of an electron trap observe at T = 30 K and a hole trap appears at T = 40 K in TSC or DLTS spectra.

Point Defects

The point defect indicates the defect composed of few vacancies or interstitials e.g. B_iC_s and B_iO_i. The main technique to get information about the chemical composition and structure of defects is the EPR(Electron Paramagnetic Resonance) method. Also, the IR spectroscopy (InfraRed absorption spectroscopy) can partly deliver information about the elemental composition of defects. Local density functional theory is used for calculations of energy levels and thermal stability of defects, e.g. the boron related defects B_iO_i, B_iC_s and $B_iB_sH_i$ [101].

In the *n*-type materials, the doped phosphorus will be knocked out from the lattice site after irradiation and formed so-called the E-center e.g. phosphorous-vacancy (VP) defect. The VP normally is a point defect but can also be a cluster-related defect as fluence increases. The introduction of VP in *n*-type silicon is the so-called donor removal [44, 11, 102].

In *p*-type materials, an additional crucial defect is introduced. This defect is known as B_iO_i and is considered to be the main cause of degradation in *p*-type silicon detectors at low fluence values, depending on the doping concentration (details will be discussed in chapter 6-8). Besides that, the common point defects such as VO [24], C_iO_i [24], TDD (For Cz silicon, see section 2.2.2) and di-vacancies (V_2) [19] can be generated both in *n*- or *p*-type silicon.

The chemical composition and structure of most defects are known or exist in some reasonable hypothesis such as E30K(Si_II_i [103]) and E50K (double interstitial silicon with oxygen, $Si_{I,2}O$ [103, 104]). However, there are still some defects that are not clear e.g. H40K. This defect has been observed to behave similarly to point defects in Thermally Stimulated measurement (Poole Frenkle effect, see section 5.3).

Cluster Defect

The cluster model was first proposed by Gossick in 1959 [105] to explain the high minority carrier recombination rate observed after heavy particle irradiation compared to electron or γ-ray irradiation. The configuration of cluster defects is complicated and has slowly developed since it was first proposed. Recently, A. Scheinemann proposed a new model for special cluster defects in 2014 [106]. They used a loop as a simplified geometric structure for the cluster defect and discussed its corresponding behaviour in DLTS measurements. This model was later applied to TSC measurements by E.M. Donegani et al. in 2018 [107]. This method will also be used in this work and will be introduced later. In recent research, C. Besleaga et al. [22] reported results from diodes irradiated by neutrons, and High-Resolution Transmission Electron Microscopy (HRTEM) was employed to observe the damaged regions.

4.4.2 Electrical Properties of Defect

The band gap and recombination theory of silicon materials was introduced in Section 2.3. The electrical properties of the defect mainly depend on its energy level in the band gap.

Energy Levels

As mentioned in chapters 2 and 3, the electrical properties of defects can be illustrated by their energy level within the band gap. Figure 4.3 provides an example of the energy levels of some defects in p-type material with the band-gap structure of silicon. The activation energy used in this work denoted as E_a, is defined as the absolute value of the difference between the defect level (E_t) and E_C or E_V. For example, E_a is equal to 0.27 eV for B_iO_i. In general, if a defect level is closer to the conduction level, it is more likely to interact with the states in the conduction band, whereas if it is closer to the valence level, it is more likely to interact with the states in the valence band. However, some defects, such as I_P, has two energy levels [18], one near the conduction level ($E_a = E_C - E_t = 0.55$ eV) and the other near the valence level ($E_a = E_t - E_V = 0.23$ eV).

Based on the information presented in sections 2.3.3 and 3.2.2, the impact of induced defects on device performance can be estimated by considering their known properties, such as their energy level, capture cross-section, and defect concentration.

Diode Under Reverse Bias

Applying a reverse bias to the diodes leads to the formation of a space charge region or active region for detector operation. In general, the occupation of one type of defect can

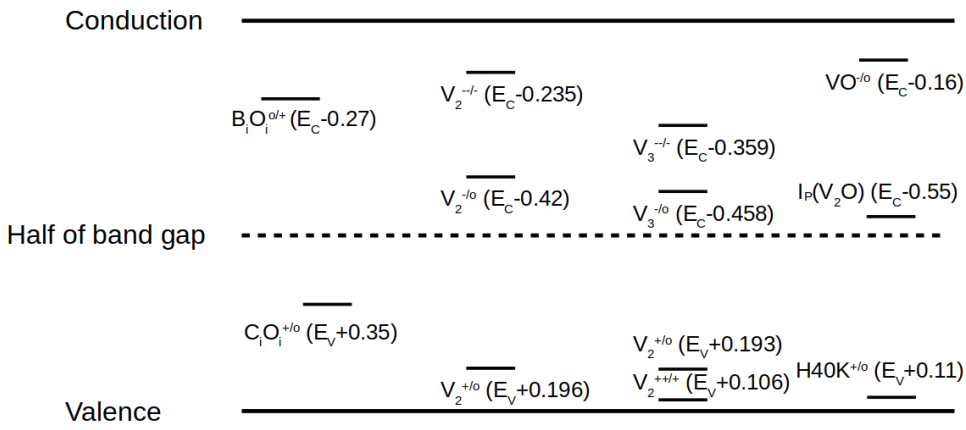

Figure 4.3: The corresponding energy level of defects in the band gap. o, -, + and = indicates the charged states neutral, negative, positive and double negative. / is used for isolating the left (after captured) and right (after emitted) the free charge carriers.

be described using SRH theory [61] with the following equations:

$$\frac{dn_t}{dt} = c_n n p_t - c_p p n_t + e_p p_t - e_n n_t, \quad \frac{dp_t}{dt} = -c_n n p_t + c_p p n_t - e_p p_t + e_n n_t \tag{4.5}$$

where the t is time. The other parameters in this equation are explained in section 2.3.3. In the case of diodes under revised bias, the free charge carrier concentrations n and p can be ignored, resulting in the simplified equations:

$$\frac{dn_t}{dt} = e_p p_t - e_n n_t, \quad \frac{dp_t}{dt} = -e_p p_t + e_n n_t \tag{4.6}$$

In a steady state, the occupation of traps is given by $\frac{dn_t}{dt} = \frac{dp_t}{dt} = 0$ resulting in:

$$n_t = N_t \frac{e_p}{e_n + e_p} \quad \text{and} \quad p_t = N_t \frac{e_n}{e_n + e_p} \tag{4.7}$$

Taking into account equation 2.20, the occupation of traps can be expressed as:

$$n_t,\ p_t = \frac{N_t}{1 + \left(\frac{c_n}{c_p}\right)^{\pm 1} \exp\left(\pm 2 \frac{E_t - E_i}{k_B T}\right)} \tag{4.8}$$

This equation can be used to estimate the effective doping concentration or space charge density N_{eff}, with known the properties of the defects (N_t, $c_{n,p}$ and E_t). More details can be found in [11].

The impact of defects on detector performance differs between during operation and TSC measurement. During operation, as discussed in section 3.2.2, the leakage current I_{LC} is mainly determined by the generation current, which is proportional to the carrier lifetime. For defects with energy levels near mid-gap, the carrier lifetime is proportional to $1/N_t$, as shown in Eq. 2.24. The detailed analysis of the effects of defects on carrier

lifetime and leakage current can be found in various textbooks and published articles, including the classic paper by Shockley and Read [61]. The impact of defects on TSC measurements will be discussed in detail in section 5.2.2.

Diodes Under Forward Bias

Forward bias is commonly used for filling defects with charge carriers in silicon diodes, specifically in TSC, TS-Cap, and DLTS techniques. During the filling procedure, charge carriers are injected through forward bias at low temperatures, typically $T_{\text{fill}} = 10$ K in this work. The capture rate exceeds the emission rate under these conditions, with $c_n n \gg e_n$ and $c_p p \gg e_p$ will be observed. Using Eq. 4.5, the steady-state occupation of electrons and holes for a specific defect can be readily calculated as:

$$n_t = N_t \frac{1}{1 + \frac{c_p p}{c_n n}} \quad \text{and} \quad p_t = N_t \frac{1}{1 + \frac{c_n n}{c_p p}} \tag{4.9}$$

We will discuss this equation and other filling methods in detail in chapter 5. However, for highly irradiated diodes, n_{p0} and p_{n0} in Eq. 3.8-3.10 tend to approach 0, making it difficult to inject a high current into the bulk under forward bias.

4.4.3 Kinetic of Defect Formation

In general, the defect formation depends on the type of impurities and their concentration, even exposed to the same irradiation. For the defects consisting of interstitial atoms that had been discussed in detail by L. C. Kimerling in 1989 [20]. This model was applied to specific cases, such as B_iO_i and C_iO_i, as discussed by L. F. Makarenko [21].

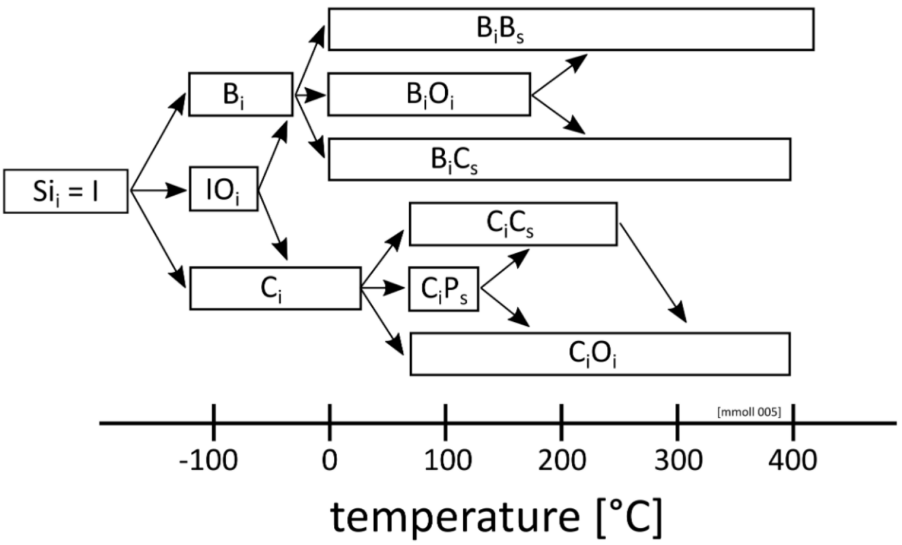

Figure 4.4: Silicon self-interstitial defect reactions with impurities. The temperature scale shows the stability of the defects under quiescent conditions (Proposed by L. C. Kimerling [20] and adapted by M. Moll [11]).

The defect formation process in p-type silicon detectors was presented in Fig. 4.4, along with its thermal stability. When incident particles hit the detector, they first knock out silicon atoms from the lattice, creating a primary knock-on atom (PKA) which results in the formation of an interstitial silicon atom (Si_I, sometimes I). Typically, Si_I either stops at a lattice site atom by replacing it (usually Si_s, sometimes B_s or C_s), or forms a cluster region. Occasionally, Si_I can be captured by oxygen and form Si_IO_i, but this can be annealed out at room temperature (the assumption of H40K configuration).

The defects formed in p-type silicon detectors are primarily B_iB_s, B_iO, B_iC_s, C_iC_s and C_iO_i. However, this conclusion is only valid when there is still a significant amount of B_s or C_s remaining and other impurities are negligible. Additionally, the formation of B_iB_s, B_iC_s and C_iC_s only occurs when the concentrations of B_s or C_s are high (normally, [O] >> [B_s] and [C_s]). Even in the highest-doped diodes studied in this work (chapter 6), which had [B_s] $\approx 1 \times 10^{15}$ cm^{-3} and [C_s] $\approx 3 \times 10^{16}$cm^{-3}, B_iB_s, B_iC_s and C_iC_s is not observed after irradiation with 5.5 MeV electrons at a fluence of 6×10^{15} cm^{-2}.

Therefore, in order to discuss the effect of boron removal, M. Moll and L. F. Makarenko proposed a simplified model that assumes the defects formed in the silicon bulk are dominated by B_iO_i and C_iO_i. According to this model, the reactions can be simplified into two outcomes, one of which is related to the formation of C_iO_i:

$$Si_I + C_s \xrightarrow{k_{IC}} C_i + Si_s \quad \text{with} \quad O_i + C_i \xrightarrow{k_{CO}} C_iO_i \tag{4.10}$$

And the other one related to the formation of B_iO_i:

$$Si_I + B_s \xrightarrow{k_{IB}} B_i + Si_s \quad \text{with} \quad O_i + B_i \xrightarrow{k_{BO}} B_iO_i \tag{4.11}$$

where the rates k_{IC}, k_{CO}, k_{IB}, and k_{BO} can be found in [20]. The introduction rate (g_A) describes the ability of particles to introduce specific defect (A) in silicon:

$$g_A = \frac{[A]}{\Phi} \tag{4.12}$$

where the A indicates one specific defect, Φ is the fluence of irradiation particles. Sometimes Φ_{eq} is used for comparing the g_A of different particles. Assuming all the C_i and B_i will be captured by O_i, the following ratio holds:

$$\frac{[C_i]}{[B_i]} = \frac{k_{IC}\,[C_s]}{k_{IB}\,[B_s]} = \frac{[C_iO_i]}{[B_iO_i]} \tag{4.13}$$

Assuming the Si_I only generate C_i and B_i: $[Si_I] = [C_i] + [B_i]$. Considering this equation with Eq. 4.12 and 4.13, the introduction rate of B_iO_i can be given by:

$$g_{B_iO_i} = g_{Si_I} \times \left(1 + \frac{k_{IC}\,[C_s]}{k_{IB}\,[B_s]}\right)^{-1} \tag{4.14}$$

where the introduction rate of Si_I, denoted as g_{Si_I}, has been discussed by G. Davies et al [108]. The ratio of $\frac{k_{IC}}{k_{IB}}$ can be found in [20]. Similar methods can be used to investigate the possible defects generated in the bulk by Si_I for other cases, such as C_iO_i and other defects. However, it should be noted that this method is only valid when considering all the main defects formed, and the formation of defects is more complex in practice than described here.

At lower fluences, where B_s and C_s are still present in the crystal, the observed traps are dominated by B_iO_i, C_iO_i, and cluster-related traps in 23 GeV proton-irradiated diodes. However, when the fluence is higher than the value at which most of the boron has been knocked out, Eq. 4.14 can not be valid.

4.4.4 Annealing Behaviors

In Fig. 4.4, thermal stability was discussed, which is commonly evaluated through annealing studies. This method is widely used to investigate defects, including their possible configurations and effects on electrical properties. Such investigations are typically conducted using macroscopic techniques (such as I–V and C–V measurements) and microscopic techniques (such as TSC, TS-Cap, or DLTS). Generally, annealing behaviour is studied using either ***isothermal*** or ***isochronal*** heat treatments. As the names suggest, isochronal annealing is performed at constant time intervals but with varying temperatures using constant temperature steps, while isothermal annealing is performed at a constant temperature for varying annealing times. Isochronal annealing provides an overview of the defect evolution at different temperatures, whereas isothermal annealing provides a more comprehensive understanding of the defect evolution at a particular temperature.

Annealing Mechanisms

The mechanisms leading to the annealing of defects can roughly be divided into migration, formation and dissociation processes.

Migration. Defects become mobile at different temperatures and migrate through the silicon lattice. There they can get trapped in so-called sinks (e.g. surface, dislocations) or impurities.

Formation. Migrating defects can react with other defects or impurities and build new defects or recombine (e.g. $B_i + C_s \rightarrow B_iC_s$).

Dissociation. A defect complex dissociates into its components due to a high-energy phonon. Parts of the complex migrate through the lattice until they are trapped by other defects or a sink (e.g. $B_iO_i \xrightarrow{T_{ann} \geq 150^oC} B_i + O_i$)

These processes had already been well described by a few references [11, 13]. Figure 4.5 is one of the widely used figures to describe those three processes. The processes were represented by three activation energy of annealing (E_m, E_f and E_d for migration, formation and dissociation respectively). In this work, the activation energy of annealing E_A

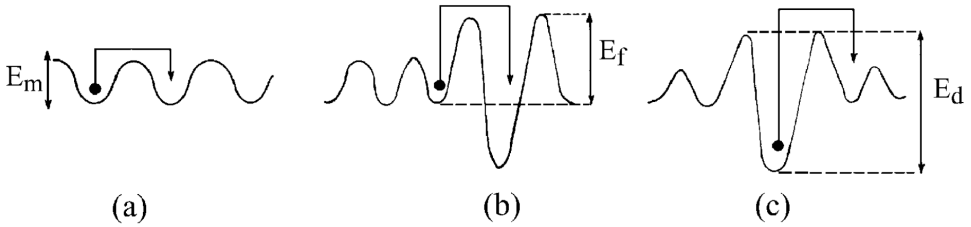

Figure 4.5: Schematic process of (a) defect migration, (b) complex formation and (c) complex dissociation. Energies are indicated as well. Taken from [11].

represents the energy of complex dissociation process E_f.

Annealing Kinetic

In the annealing process due to migration and dissociation, first-order processes can be used to describe them. This was initially explained by Waite in 1957 [109] and later elaborated on by Svensson and Lindström [110]. The same concepts introduced in [13] will be used here to explain the annealing kinetics. In a first-order process, each defect complex anneals out independently of the remaining defects. The dissociation or formation of defects can be expressed as:

$$\mathrm{A} + \mathrm{B} \rightleftharpoons \mathrm{AB} \tag{4.15}$$

where A and B is a defect or impurity which combines together into a more complex structure. When the concentration of B is more than one order of magnitude higher than defect A, B can be treated as constant for the reaction. The rate equation for a first-order process is then given by:

$$-\frac{d[\mathrm{A}]}{dt} = k_1[\mathrm{A}] \tag{4.16}$$

where [A] is the defect concentration and k_1 is the rate constant. The k_1 depends on the temperature and can be expressed by the Arrhenius relation:

$$k_1 = k_0 \cdot \exp\left(-\frac{E_A}{k_B T}\right) \tag{4.17}$$

where k_0 is the frequency factor and E_A is the activation energy for dissociation or migration. The rate constant for diffusion-limited reactions [109] between two different kinds of homogeneously distributed defects can be described by the rate equation:

$$-\frac{d[\mathrm{A}]}{dt} = 4\pi R D[\mathrm{B}]_{t=0}[\mathrm{A}] \tag{4.18}$$

with R being the capture radius [11] of the reaction, $[\mathrm{B}]_{t=0}$ is the concentration of the defect B at the beginning of the reaction and D is the sum of the diffusion coefficients

(sometimes called diffusivity). In many cases, the diffusion coefficient is dominated by the defect which diffuses the fastest. From Eq. 4.16 and Eq. 4.18 it can be seen, that the rate constant k_1 equals $4\pi RD[\mathrm{B}]_{t=0}$. It is well-established to describe the temperature dependence of the diffusivity by an Arrhenius relation:

$$D = D_0 \cdot \exp\left(-\frac{E_A}{k_B T}\right) \tag{4.19}$$

with the diffusion constant D_0, which can be approximated by $D_0 = \alpha a^2 v$. α describes the number of possible jump places, a the lattice constant and v the phonon frequency. This method will be used and discussed in detail in chapter 6.

4.5 Impact on p-type Silicon Detector

As the fluence increases and induces more defects, the performance of detectors degrades, which depends on the properties of the radiation-induced defects. As discussed in this chapter, the effects of defects on the electrical properties of p-type silicon can be illustrated through the bandgap structure. Fig. 4.6 summarises the impact of defects on p-type silicon detectors according to their energy level in the bandgap.

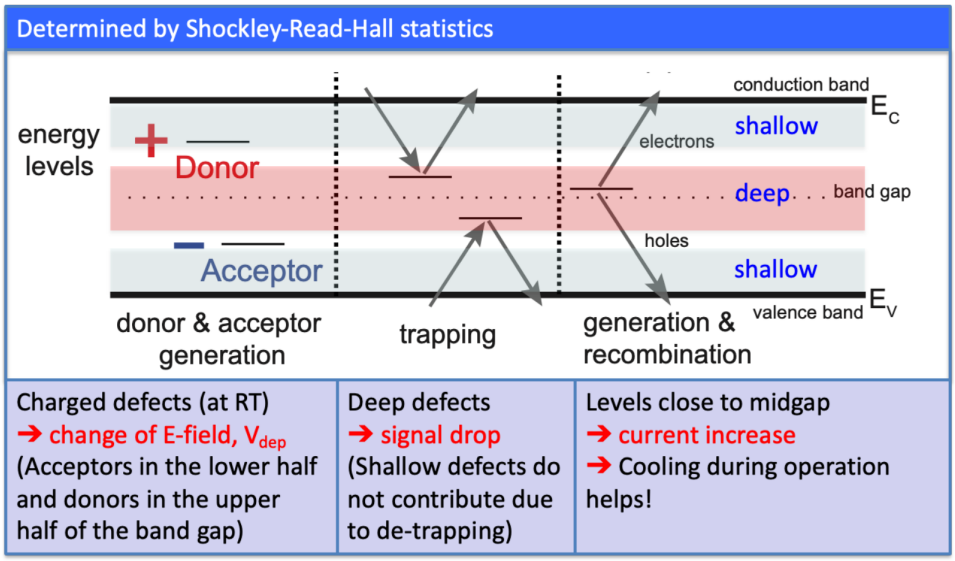

Figure 4.6: Schematic illustration of the effects of defects with different energy levels on the properties of p-type silicon detectors. Defects located near the valence band can act as acceptors and trap holes or located near the conduction band can act as donors and trap electrons, leading to changes in space charge density. Defects located in the middle of the bandgap can act as trapping centers for both electrons and holes, leading to a reduction in the carrier lifetime and it affecting the leakage current and charge collection efficiency. Taken from [111].

4.5.1 Space Charge Density

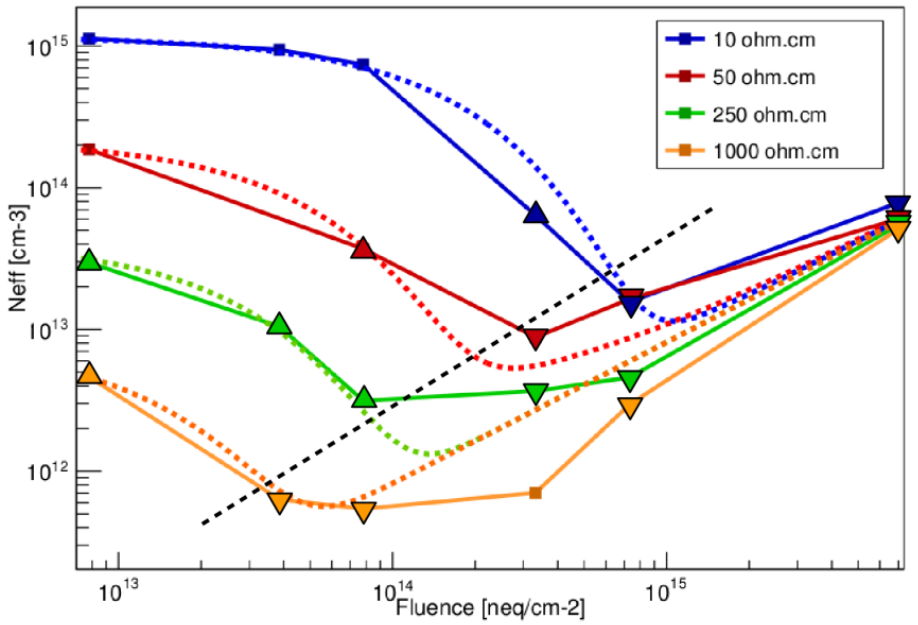

Figure 4.7: N_{eff} vs fluence for different initial doping concentrations [112].

The relationship between space charge density N_{eff} and fluence for different initial doping concentrations is shown in Fig. 4.7. The data points exhibit a trend where N_{eff} initially decreases and then increases as the fluence increases. However, it is important to note that the extracted N_{eff} values beyond the decreasing N_{eff} ranges are prone to significant errors. Further details can be found in section 5.2.

In general, the N_{eff} of p-type silicon is determined by all ionized complexes, such as defects and impurities. The charge state of defects in silicon can be found in [11]. The N_{eff} can be expressed as the sum for all space charges:

$$N_{\text{eff}} = \sum_x (Q_{P,x} - Q_{N,x}) - [\text{B}_\text{s}] \tag{4.20}$$

with the substitutional boron concentration $[\text{B}_\text{s}]$. The $Q_{P,x}$ and $Q_{N,x}$ indicate the positive and negative charges contributed by defect x and are determined by the occupation state of the defects, i.e. p_t and n_t as described in Eq. 4.8.

The $[\text{B}_\text{s}]$ decreases with fluence increase. This decrease in $[\text{B}_\text{s}]$ is responsible for the degradation of N_{eff}, as shown in Fig. 4.7. At low fluence ranges, the deactivation of boron and the formation of $\text{B}_\text{i}\text{O}_\text{i}$ occurs, which significantly affects the distribution of the electric field. When considering the generation of defects, the changes in the space charge density can be described by two components: acceptor removal and the introduction of other defects:

$$N_{\text{eff}}(\Phi_{\text{eq}}) = N_{\text{A},0} \exp(-c_A)\Phi_{\text{eq}} + g\Phi_{\text{eq}} \tag{4.21}$$

with acceptor removal coefficient c_A and introduction rate g found in [86]. $N_{A,0}$ represents the $[B_s]$ before irradiation and is referred to as the initial effective doping in the following chapters.

Taking the obtained value of N_{eff} into section 3.2, one can estimate the following changes in the electric field and potential. However, as defects accumulate in the bulk, trapping can occur even at room temperature. In such cases, the estimation of electrical properties is extremely complicated e.g. double junction effect [113, 114].

4.5.2 Leakage Current Increasing

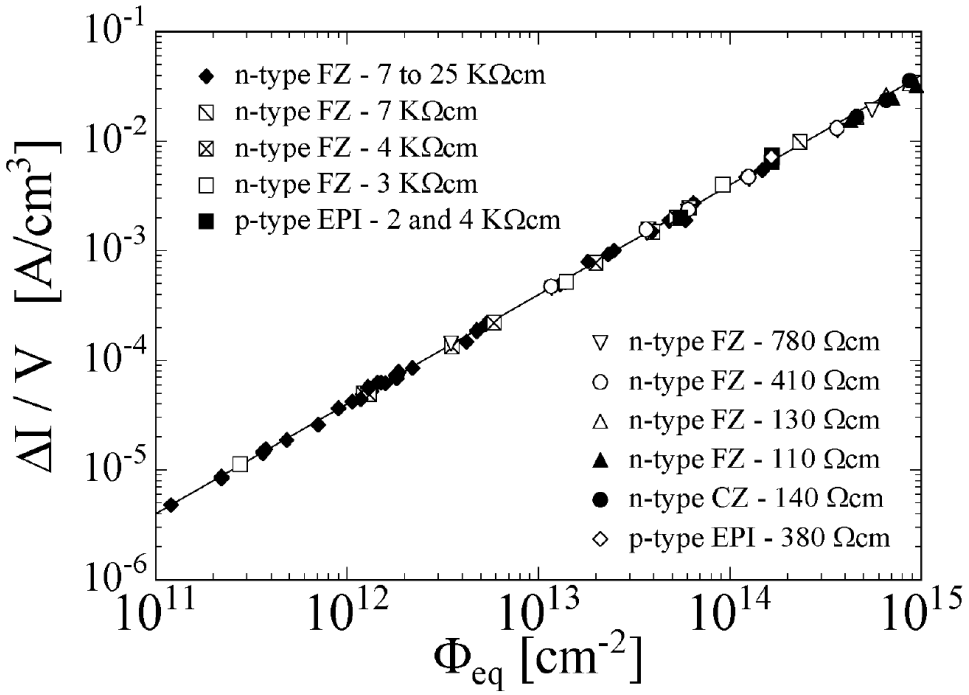

Figure 4.8: Fluence dependence of leakage current for silicon detectors produced by various process technologies from different silicon materials. Details can be found in [11].

Similar to n-type silicon, the leakage current in p-type silicon also increases with fluence. As mentioned in section 4.4.2, the leakage current is dominated by deep defects with energy levels close to the mid-gap. In general, the increase in leakage current is related to fluence by a factor α, which is the so-called current-related damage parameter:

$$\Delta I = \alpha \Phi_{eq} V_{ol} \tag{4.22}$$

where V_{ol} is the depleted volume. The value of α was obtained as $\alpha = 3.99 \pm 0.03 \times 10^{-17}$ A/cm from the presented Fig. 4.8 for neutron-irradiated n-type silicon [11].

4.5.3 Trapping

This section is taken from [115]. The Charge Collection Efficiency (CCE) of a sensor is a critical parameter for high-energy physics experiments. In general, the CCE can be considered to be produced by two terms [116]:

$$Q = Q_0 \cdot CCE_{GF} \cdot CCE_t \tag{4.23}$$

with the geometrical factor CCE_{GF}, the trapping factor CCE_t, and the induced total charge Q_0. The CCE_{GF} is related to the detector depletion thickness w, the waiting function (detector segmentation scheme) [71, 117] and the detector configuration (see Fig. 3.2) [118]. In general, the CCE_t is given by the Ramo theorem [69] (see section 3.4.1):

$$i(t) = Q_0'(t) \cdot \vec{E_w}(t) \cdot \vec{v}(t) \tag{4.24}$$

Assuming the E_w and distribution of N_{eff} are constant, the decrease in signal i is only caused by the $Q_0'(t)$:

$$Q_0'(t) = Q_0(t) \cdot e^{-t/\tau} \tag{4.25}$$

As the fluence increases, the τ is degraded and CCE decreases. Meanwhile, the increases on V_{fd} also significantly affect the CCE, as shown in Fig. 4.9.

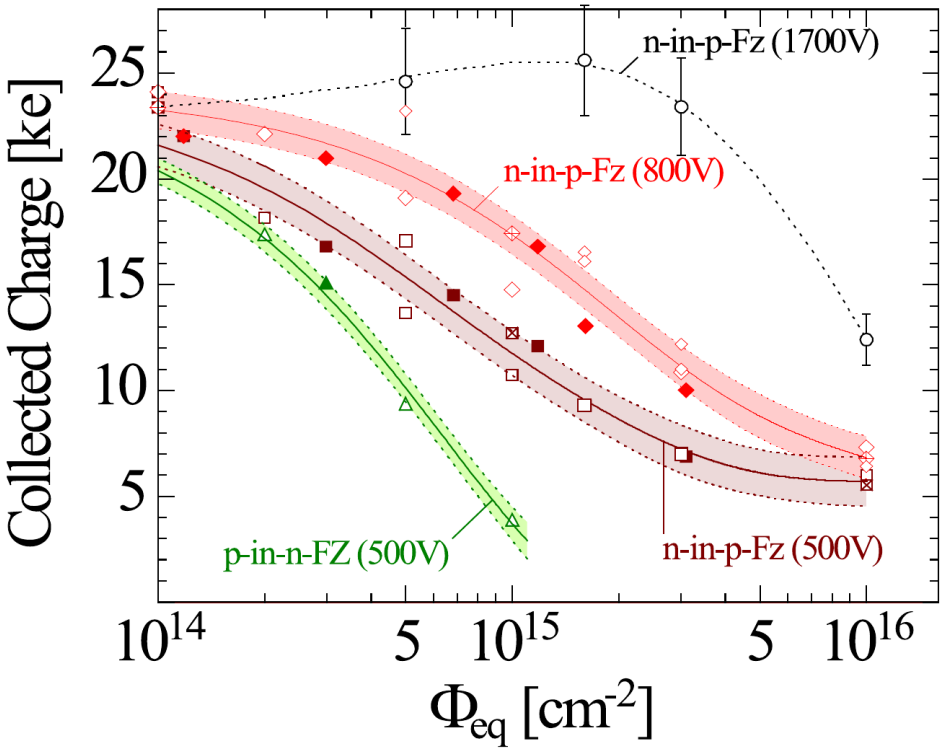

Figure 4.9: Collected charge as a function of n_{eq} fluence for 23 GeV proton, 26 MeV proton, and reactor neutron irradiated 300-µm-thick ministrip sensors [119].

4.5.4 The Degradation of LGADs

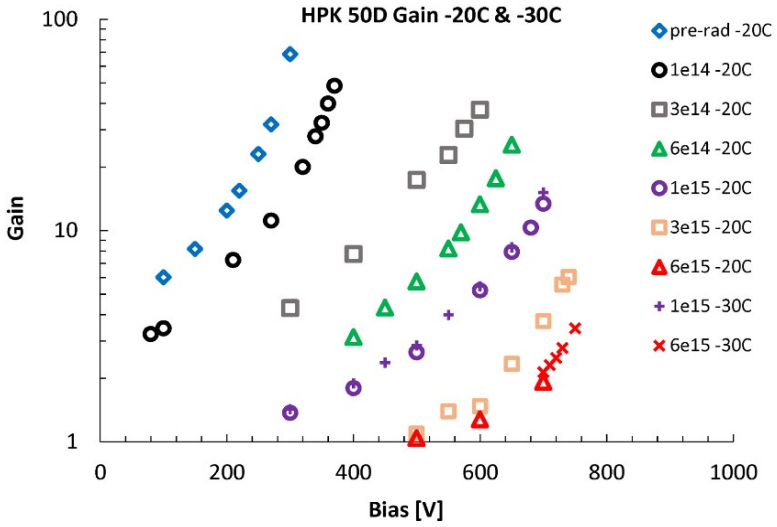

Figure 4.10: Gain as a function of bias of the HPK 50D LGAD irradiated to the indicated neutron fluences at −20 °C and −30 °C, showing the need for increasing the bias of irradiated sensors to reach adequate gain. The gain has a common systematic scale error of 20%. Taken from [120].

The LGADs detector mentioned in section 3.5.4 as well as the new pixel and strip devices will be manufactured on boron-doped (p-type) silicon. The degradation of the performance of these sensors is due to the expected high radiation field. As Fig. 4.10 shows, the exposure of LGADs to radiation leads to a reduction of the sensor's internal gain with increasing particle fluence [2, 3]. This degradation is caused by the deactivation of the active boron in the highly doped p-type layer, the gain layer, which leads to a reduction of the space charge and consequently a lowering of the electric field followed by a decrease in charge multiplication in this layer.

It is important to note that this degradation of performance is not limited to LGADs but is a general issue for all silicon-based detectors. Therefore, understanding the effects of radiation-induced defects on the electrical properties of p-type silicon is of utmost importance for the design and development of future radiation detectors. The research carried out in this thesis aims to contribute to this understanding and provide insights into the mechanisms behind the degradation of the performance of p-type silicon detectors under high radiation fields.

5 Experimental Setup

In this chapter, it will be briefly introduced that the main irradiation facilities used for reactor γ-ray, 5.5 MeV electron, and 23 GeV proton irradiation. The capacitance-voltage characteristics (C–V) and current-voltage characteristics (I–V) will then be discussed, which are used to characterize the electrical properties of the sensors. In the next section, the theory and setup of the Thermally Stimulated Current (TSC) and Capacitance (TSCap) will be presented. In the end, a few additional theories relevant to this work will be introduced.

5.1 Irradiation Facilities

Proton source [13]: Protons are extracted from the Proton Synchrotron PS at CERN with a momentum of 24 GeV/c. The PS delivers one to three spills per cycle depending on the beam sharing with other experiments. The facility IRRAD-1 is located at the PS-T7 beam line in an irradiation zone at the CERN PS East hall where samples can be exposed to a 24 GeV/c proton beam scanning over an area of about 2×2 cm^2 [121]. Depending on the beam focussing, a minimum fluence of 1.5×10^{11} protons per spill can be delivered by the PS, resulting in an average proton flux with one spill per cycle of 3 to 9×10^9 cm^{-2}s^{-1}. The beam profile alignment is monitored by Gofchromic Dosimetric Films XR [122] and by a recently installed online monitoring system, recording the X and Y profile perpendicular to the beam. The fluence is provided by measurement of the activity of ^{22}Na and ^{24}Na in 5×5 cm^2 aluminium (Al) foils. The isotopes are created by the nuclear reactions ^{27}Al(p,3pn)^{24}Na and ^{27}Al(p,3pn)^{22}Na. A germanium spectrometer allows the measurement of the ^{24}Na gamma emission at $E_\gamma = 1368.53$ keV with a half-life of $\tau_{1/2} = 14.96$ h and the ^{22}Na gamma emission at $E_\gamma = 1274.54$ keV with a half-life of $\tau_{1/2} = 2.6$ y. The accuracy for this method lies within 7% [123]. The detectors are packed into stacks of 5×5 cm^2 cardboards and then transported by a shuttle into the beam. The temperature at the point where the irradiation takes place is about 27 °C. As the flux is about 1 to 3×10^{13} pcm^{-2}h^{-1}, a fluence of $\Phi = 1 \times 10^{15}$ cm^{-2} is reached within 4 days, for $\Phi = 1 \times 10^{16}$ cm^{-2} more than 40 days are necessary if the beam is operated properly throughout the whole time. Hence annealing effects during irradiation are possible. Directly after irradiation, the activity of the sensor needs to decay for about 30 minutes to one hour, until it is decreased to a level where the material can be handled safely. Then the irradiated sensor is put into a freezer at the facility and kept at -20 °C

until the activity is below the limit allowed for packing and shipping.

Electron source: The electron irradiation was conducted at the Belarus National Academy of Science using their linear electron accelerator. The electrons used had a kinetic energy of 6 MeV, but lost 0.5 MeV during transfer through the air. For the purposes of this study, the irradiation is referred to as 5.5 MeV electron irradiation. More information about the laboratory and irradiation process can be found in [124].

γ-ray source [125]: The ^{60}Co facility in Zagreb hosts a panoramic γ ^{60}Co source. ^{60}Co is an isotope with a half-life of 5.27 years that emits mainly two photons with energies 1.17 MeV and 1.33 MeV. At these energies, Compton scattering is the prevalent mode of interaction with matter. The source consists of 24 hollow guiding rods arranged in a cylindrical geometry with a radius of 13 cm. Each rod contains four capsules with a cobalt pencil of 8 cm in length. The total activity of the source is around 2 PBq. The irradiation chamber is separated from the control room with a thick concrete wall. The chamber is accessed through a corridor separated by a 1.5 m thick concrete wall. Large samples are placed around the source where the dose rate ranges from 500 krad/h down to 1 krad/h of water equivalent dose. The small samples can be placed in the center of the cylinder where the dose rate is about 2.5 Mrad/h.

5.2 Instrumentation of Measurements

As mentioned in chapters 3 and 4, electrically active defects formed during radiation exposure can contribute to both leakage current and space charge density. To identify the properties of these defects, I–V and C–V measurements are essential, as shown in Fig. 5.1a. These measurements are typically performed at a temperature of 20 °C (or −20 °C) and can provide information on the effective doping concentration (N_{eff}) profile and leakage current. The results are influenced by specific defects and can impact the operation of the detector, depending on the radiation fluence. Therefore, these measurements are also referred to as **macroscopic measurements** in this work, as they provide a broad view on the electrical properties of the detectors.

To identify the defects responsible for changes in macroscopic measurements, the Thermally Stimulated Current (TSC) and Capacitance (TS-Cap) techniques were used. These methods involve measuring the properties of defects in the silicon crystal at various temperatures, starting from extremely low temperatures such as 10 K, up to temperatures above 250 K. By analyzing the TSC and TS-Cap data, information on the microscopic defects, such as activation energy (E_a) and trap density (N_t), can be obtained. For this reason, these techniques are referred to as **microscopic measurements** in this work, and an overview of the setup is presented in Fig. 5.1b.

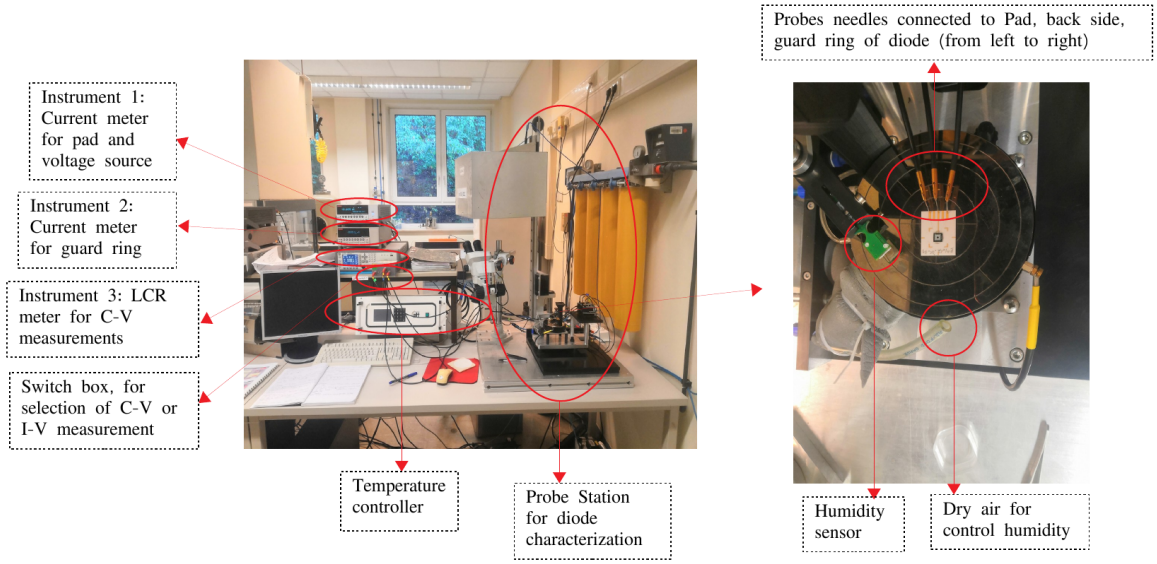

(a)

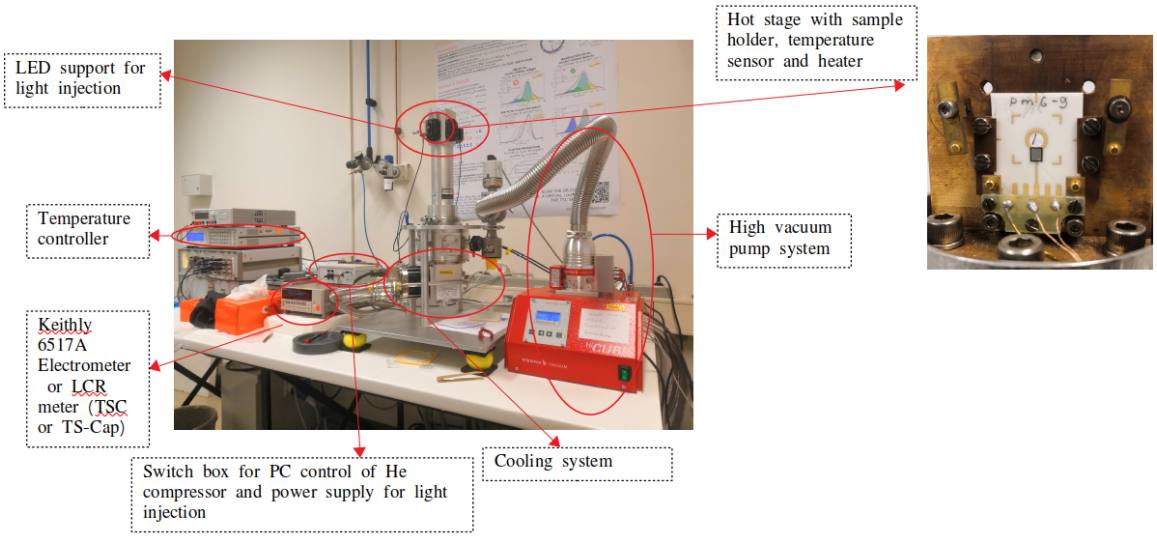

(b)

Figure 5.1: Overview of the experimental set-up. (a) I–V and C–V, (b) TSC and TS-Cap.

5.2.1 Current-Voltage (I–V) and Capacitance-Voltage (C–V)

As shown in Fig. 5.1a, the I–V and C–V setup includes a switch box that allows the user to select between the I–V and C–V measurement modes. Four plugs on the back of the switch box connect the Keithley 6517B electrometer with a voltage source (6517B), and two cables connect two needles shown on the right side of the Fig. 5.1a. On the front of the switch box, it connects the Agilent E4980A LCR meter.

During the measurement process, the needles connected to the switch box by cable are used to connect to the backside (p^+) and pad (n^+) of the measured diodes. The 6517B applies the reverse bias to the backside while grounding and recording the current of the pad. The guard ring is directly connected to the Keithley 6485 picoammeter (6485), which is used to ground it and measure its current.

The temperature in the probe station used for diode characterization (as shown in Fig. 5.1a) was controlled and monitored by the ATT Thermal Chuck Systems. The probe station includes three needles on the left side that make contact with the metal on the ceramic and connect to the pad (left), backside (middle), and guard ring (right) of the measured diodes. The humidity sensor and dry air system are used to control the humidity on the surface of the measured diodes, which is important for surface leakage current. All macroscopic measurements in this work were performed under humidity conditions below 10%.

Current-Voltage (I–V)

For I–V measurement, the switch box will turn to the up stage. The DC voltage is applied to the backside of the diode by the voltage source 6517B, while the 6517B also grounds and records the current of the pad. For the proton-irradiated diodes, the guard ring was connected as described above. The connection was changed for measuring surface current on γ-ray irradiated diodes, which will be discussed in chapter 8.

The C–V and I–V measurement procedures are controlled by the window shown in Fig. 5.2. The user fills in the table of **Physical Parameters** with information such as **Atmosphere** (Air condition), **Tester** (Name of the tester), **Environment** (Probe station), **Detector** (The label of detectors), **Annealing time [min]@T [°C]** (For example, 8@80 means anneal 8 min at 80 °C) and **Comments** (general comments of measurement).

The **Perform** indicates the measurements that will be performed e.g. the window in Fig. 5.2 indicates the I–V measurement will be performed. Then, the computer will communicate with the instruments indicated at **V source and I meter** and **Guard Current Mode** in Fig. 5.2 i.e. 6517B and 6485. The computer will record the data in the voltage range, which is indicated by the user in the table of **Voltage source parameters** e.g. start from 0 V and stop at -20 V in step of -1 V shown in Fig. 5.2. The **Mode** is to specify the increases in bias voltage e.g. the linear increase from 0 to -20 V. **V increment** is the ramping up of voltage. If the voltage step is larger than the value here and equal to $integer \cdot V_{increment}$, then the ramping up of the voltage will be set to $V_{increment}$. Otherwise, the ramping up of the voltage is the recorded voltage step e.g. 1 in Fig. 5.2. **V Inc. speed** is the time of voltage ramping up. The **Polarity** indicates the sign of voltage (positive, negative). **Compliance** is the expected error of measured data. The detail about how the instrument measures the data can be found in Model 6517B Electrometer User's Manual [126].

Capacitance-Voltage (C–V)

In general, the electrical properties of solids can be represented by the circuit of a resistor and a capacitance. With an LCR meter, the impedance Z or the admittance $Y = Z^{-1}$ of devices are measured under AC bias V_{AC}. As Fig. 5.3 shows, the directly recorded data

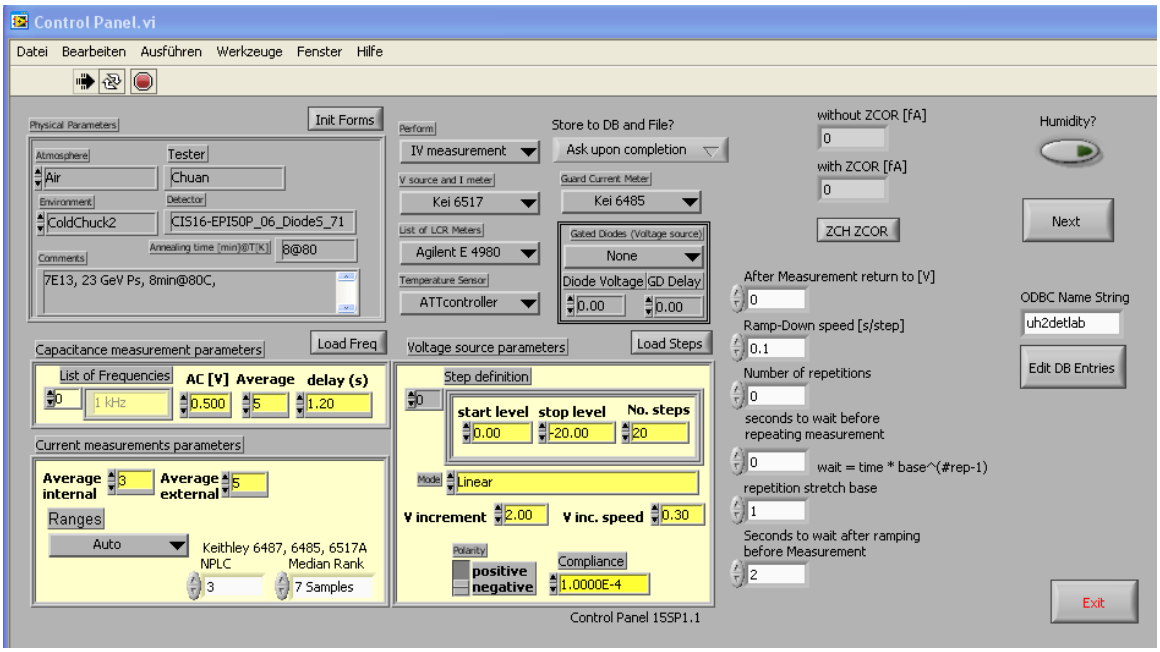

Figure 5.2: Overview of the window for controlling the I–V and C–V measurements.

in the instrument are the voltage (V_x) and current (I_x) on the samples. The Z or Y can be calculated as $\frac{V_x}{I_x}$ or $\frac{I_x}{V_x}$. Assuming the measured diodes can be regarded as a parallel circuit of resistor R_p and capacitance C_p, as shown in Fig. 5.4a, the admittance Y can be used to calculate the capacitance using the equation:

$$Y = \frac{1}{R_p} + j\omega C_p \tag{5.1}$$

where j represents the imaginary unit, and ω is the frequency. In general, the real part and imaginary part of a complex quantity can be determined from the magnitude ($|Y|$) and phase angle (θ). In C–V measurement, the phase difference between voltage and current shown in Fig. 5.4d is represented by θ. Consequently, the capacitance was calculated for the set frequency and averaging points (detail will be presented later). For equivalent serial circuits, impedance Z is used to calculate resistor R_s and capacitance C_s using the equation:

$$Z = R_s - \frac{j}{\omega C_s} \tag{5.2}$$

The remaining steps for obtaining C_s are similar to those for parallel circuits.

The input parameters can also be found in Fig. 5.2 – **Capacitance measurement parameters**. In general, the frequencies used in this work are 230 Hz, 455 Hz, 1 kHz and 10 kHz. The AC bias V_{AC} determined the thickness of the scanned layer (see section 3.2.3), which normally is set to 0.5 V. However, in some cases, the value of V_{AC} was adjusted depending on the space charge density (N_{eff}) of the measured diodes.

As mentioned in equations 5.1 and 5.2, the LCR meter typically uses two models. In

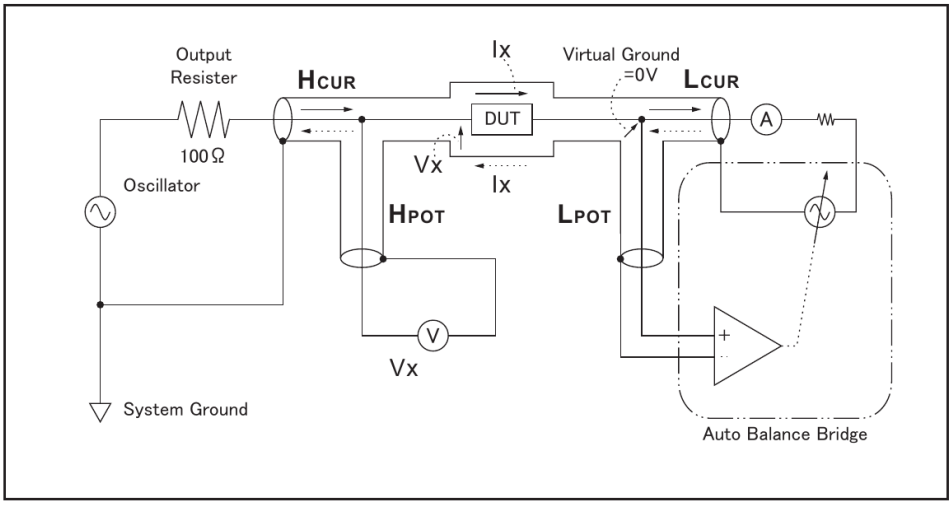

Figure 5.3: Schematic of measurement principle of C–V. Taken from Agilent E4980A LCR meter user manual (page 199, [127]).

this study, the admittance was used for C–V measurement, and the resulting capacitance (C_p) and conductance ($G = \frac{1}{R_p}$) were recorded. That means the ratio I_x/V_x was recorded as a capacitance value. First, the LCR meter measured C_p at the average points indicated at **Average Internal**. The mean value of these average points was then fed back to the computer. Next, the computer calculated the mean value of the average points indicated at **Average External** over a duration of 1 s. For example, as shown in Fig. 5.2, the LCR meter measured 3 points during a period of 0.2 seconds and sent the mean value of these 3 points to the computer. Then, the computer calculates the mean value for 5 points of external averaging.

It is important to note that, in this work, the parallel model is used to measure the capacitance of investigated diodes. In principle, this model is precise when the resistance of the non-depleted region can be ignored. However, in practice, it is known that the resistance of silicon increases with fluence [129], which introduces errors in the measured capacitance. This error can be estimated by using the equivalent circuit serially connected by two parallel circuits or one parallel circuit and one serial circuit. Details can be found in [65].

5.2.2 Thermally Stimulated Current and Capacitance (TSC and TS-Cap)

TSC and TS-Cap were introduced in detail in 1969 by C.T. Sah et al. [130]. Unlike the Deep Level Transient Spectroscopy (DLTS) method, TSC is applicable for highly irradiated sensors as it is not limited by the requirement of $N_t << N_{\text{eff},0}$. TS-Cap measurements can not only measure the depleted depth but also provide information about defects.

The setup and control window for both measurements are shown in Fig.5.1b and Fig.5.5, respectively. The setup consists of a closed cycle helium cryostat Model SRDK-205 (Sum-

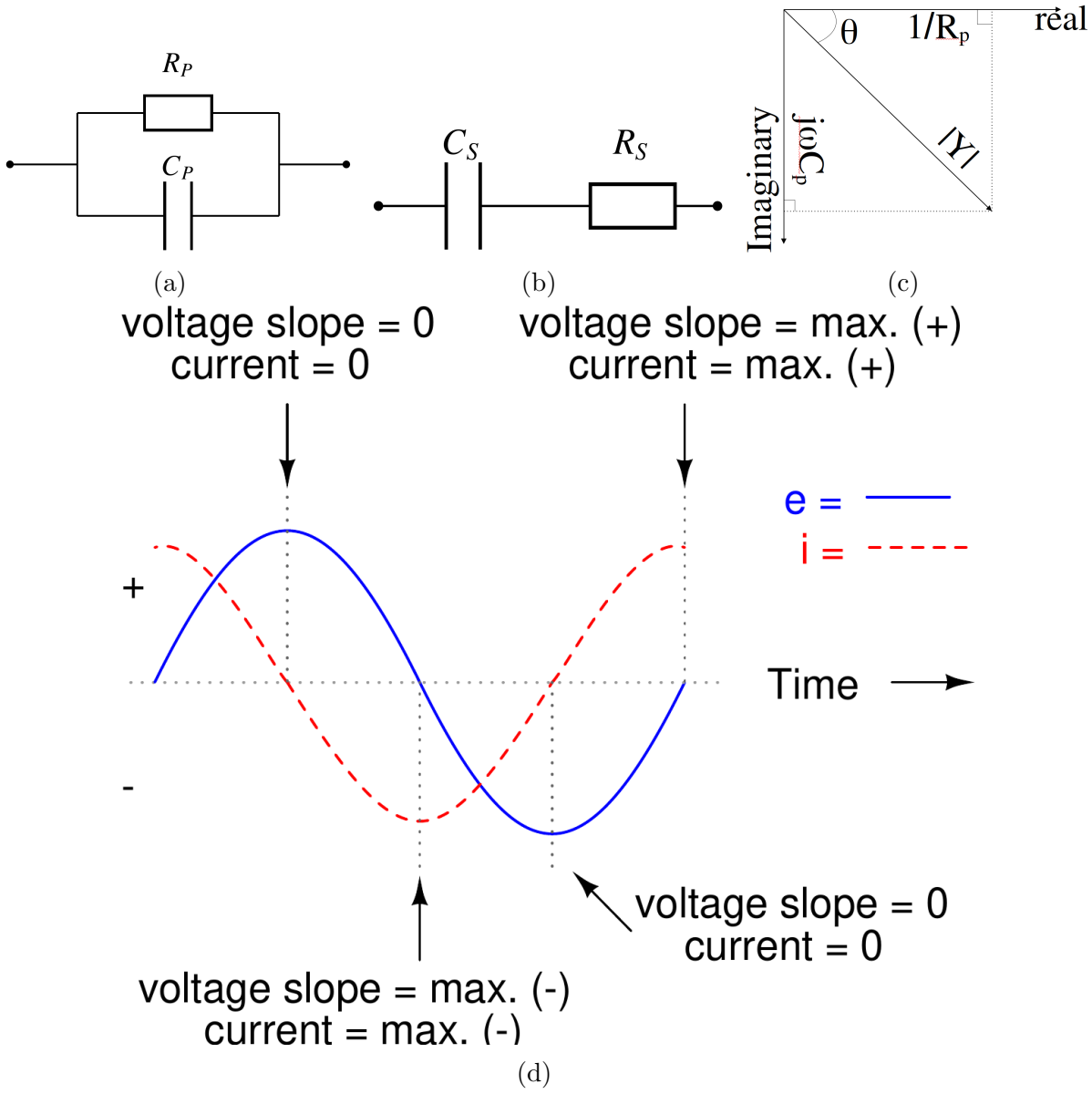

Figure 5.4: (a) parallel and (b) Serial are schematics of the equivalent circuits for measured samples. (c) Indication of how to calculate the C_p by using measured $|Y|$ and phase θ. (d) Example of phase difference in V_x (e in the figure) and I_x (i in the figure) [128].

itomo Heavy Industries, Ltd, Japan) equipped with a temperature controller Model 340 (Lake Shore, US) and a Keithly 6517A electrometer with a voltage source. For the TS-Cap an LCR meter 4263B from Hewlett Packard is used. The high vacuum pump system provided by Pfeiffer HiCube^{TM} ECO Dry Pumping Stations.

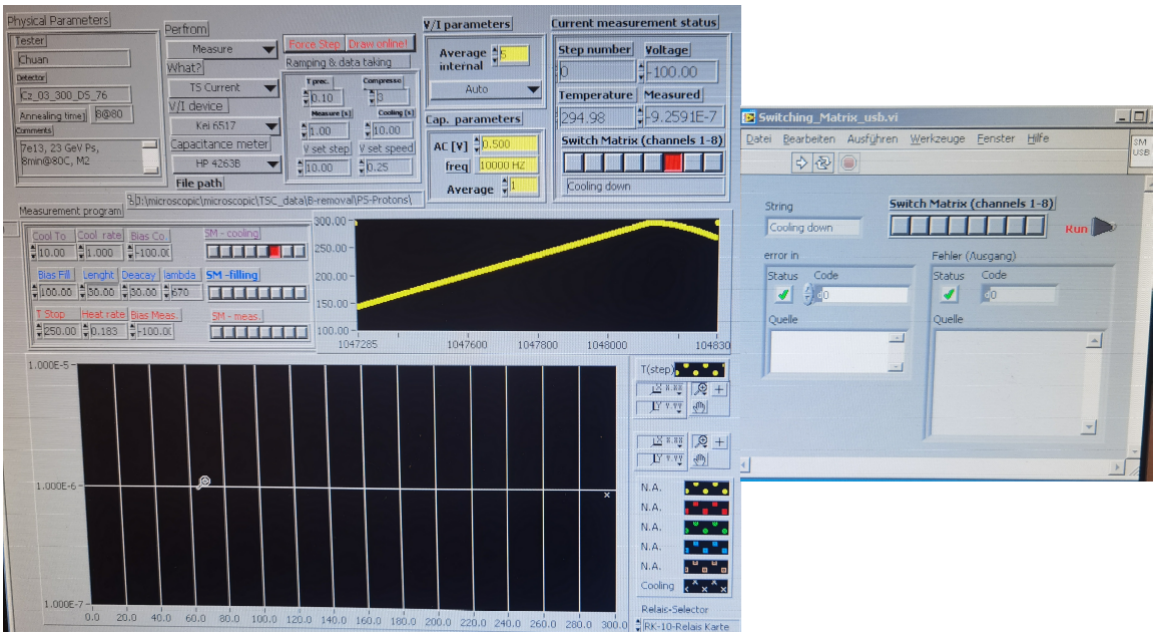

Figure 5.5: Overview of the window for controlling the TSC measurements.

Thermally Stimulated Current (TSC)

The TSC measurement contains three processes: cooling down, filling, and heating up, as shown in Fig. 5.6. First, the diode is fixed as shown in Fig. 5.1b, and its guard ring, backside, and pad are connected to three fixed needles. Then, the closed cryostat is cooled down under a vacuum below 1×10^{-5} mbar, and the bias voltage during cooling down (V_{down}) is set according to the filling procedure.

Cooling Down: For light injection, V_{down} is set to a reverse bias with a value $\geq |V_{\text{fd}}|$ to drive all the free carriers out of the bulk, allowing defects to emit their charge below 295 K. For majority filling, V_{down} is set to 0 V, causing the majority of carriers to be captured by the defects, and the filled state concentration depends on N_{eff}. For forward injection, V_{down} can be set to either a reverse bias or 0 V. It should be noted that V_{down} is discussed here for diodes that can be fully depleted. For diodes that cannot be fully depleted, in the light injection case, V_{down} should be chosen carefully to avoid the avalanche breakdown.

Filling: Once the device under test has cooled down to the filling temperature T_{fill}, the injection or filling process can begin. As mentioned in the previous paragraph, the injection can be performed using three methods: **Forward injection**, **Light Injection**, and **Majority Injection**. The details of forward injection have already been discussed in section 4.4.2. In this case, both electron and hole traps are filled under forward bias V_{fill} with current I_{fill}. Typically, light injection is used to distinguish between electron or hole

traps. In this method, the diodes are illuminated by a set light source under reverse bias $V_{\text{fill}} = V_{\text{down}}$. To generate electron-hole pairs, light with a high absorption coefficient is used, such as green light with a wavelength of 520 nm, which has an absorption coefficient of roughly 10^4 cm^{-1} (depending on the temperature) [131, 132]. This means that the light will deposit all its energy at roughly 1 µm, and only one type of charge can cross the bulk and fill the defects. The type of charge depends on the dopants and illuminating position. For example, in this work, p-type silicon diodes are illuminated at the n^+ side (pad) for hole injection and at the p^+ backside for electron injection. The majority carrier filling is similar to light injection and is used to identify the type of defect, whether electron or hole trap. In this case, $V_{\text{fill}} = V_{\text{down}} = 0$ V. The filling time t_{fill} in this work is 30s. After filling, the investigated diodes are biased (V_{decay} equal to heating up bias V_{bias}) at T_{fill} for a while to drive out the injected charge, which is called the decay time t_{decay} in this work. Generally, t_{decay} is 30 s. Sometimes, t_{decay} may be changed for using the decay method, which will be discussed later.

Heating Up: Following the decay process, the diodes will be heated up with the heating rate $\beta = 0.183$ K/s while under bias V_{bias}. The specific value of V_{bias} is dependent on V_{fd} and is typically set such that $V_{\text{bias}} \geq V_{\text{fd}}$. The resulting spectra, such as the one shown in Fig. 5.6d, provide information about the induced defects, with the peak in the spectrum corresponding to these defects.

All procedures related to the TSC and TS-Cap measurements are controlled by the window presented in Fig. 5.5. The table of the **Physical Parameters** is filled with the user's name, the label of the measured detector, annealing steps, and comments on measured diodes. The **Perform** button is used to select the processing of measurements, such as uploading documents of the measurement parameters or starting the measurement. The **What** field is used to choose the model of measurement, TSC or TS-Cap. The **T precise** field is filled with the expected error of temperature ramping up. Except for the **Measurement Program**, the rest of the window is similar to the I–V and C–V measurements. The **Measurement Program** is a table for filling the experiment parameters, including V_{down}, heating rate (β), and so on. The **Switching_Matrix_usb.vi** window is the controller for cooling down and light injection. It should be noted that the **Measurement Program** table is normally filled out in external documents and then uploaded to this window using the **Perform** button.

TSC method

In general, the TSC signal is the current measured during heat up under V_{bias}, which contains three different types of current: conduction current, displacement current and diffusion current.

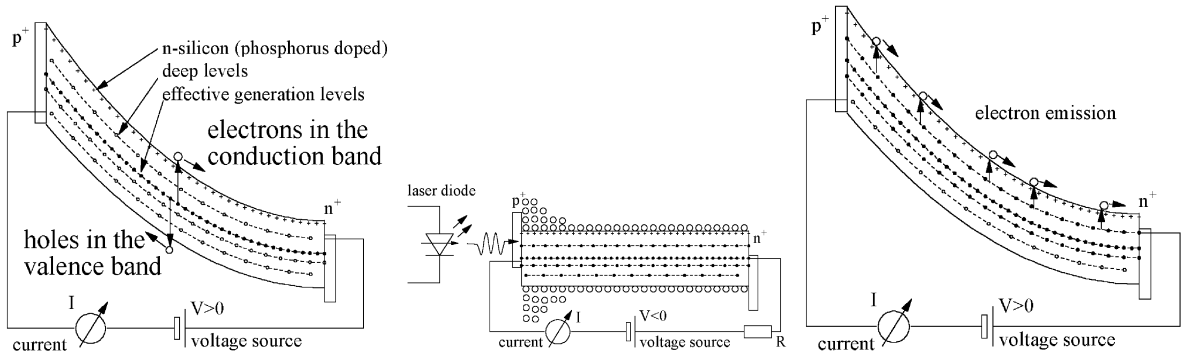

(a) (b) (c)

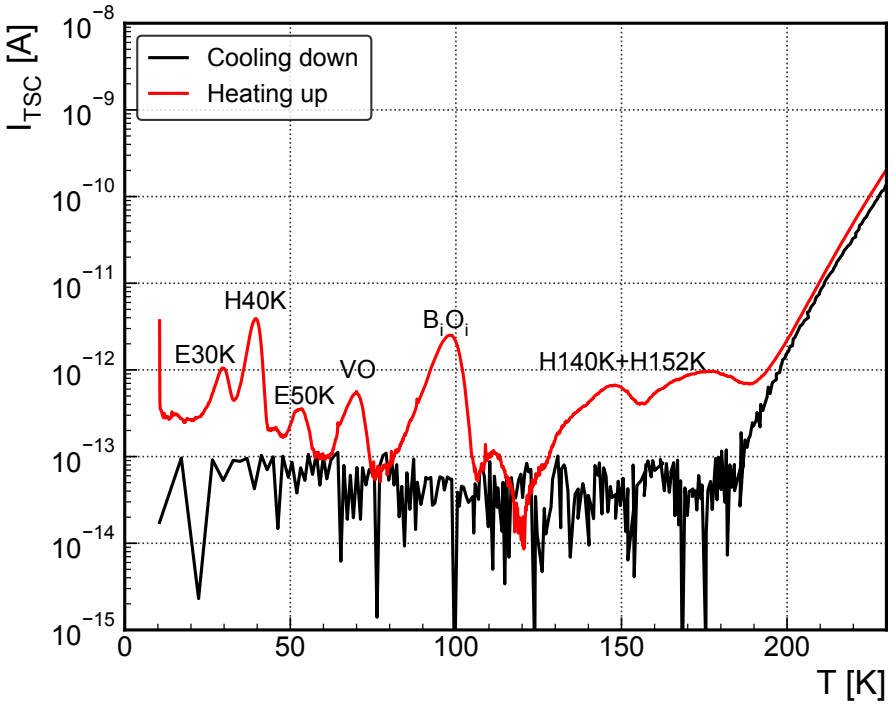

(d)

Figure 5.6: (a) Cooling down, (b) Filling and (c) Heating up is the schematic representation of the TSC measurement, taken from [11]. (d) Example of TSC measurement on the 23 GeV proton irradiated diodes EPI 12-74. Measured condition: $V_{\text{down}} = 0$ V, forward injection, $V_{\text{fill}} = 10$ V, $I_{\text{fill}} = 1$ mA, $T_{\text{fill}} = 10$ K, V_{bias}= -20 V ($V_{\text{fd}} <$ -10V).

1. Conduction current:

$$I_c = q_0 A \int \left(\frac{dn}{dt} + \frac{dp}{dt} \right) dx \tag{5.3}$$

2. Displacement current:

$$I_d = \frac{d(CV)}{dt} \tag{5.4}$$

The diffusion current can be found in chapter 3.

The widely used TSC method for extracting information is only valid for the fully depleted case, where the diffusion current is normally ignored. In this case, the sum of I_c and I_d can be simplified, and the corresponding current $I^{e,h}_{TSC}$ induced by electron or hole trap is given by [11, 130, 133, 134, 52]:

$$I^{e}_{TSC}(T) = \frac{q_0 A d}{2} e_n(T) f_n(T) N_t \tag{5.5}$$

or

$$I^{h}_{TSC}(T) = \frac{q_0 A d}{2} e_p(T) f_h(T) P_t \tag{5.6}$$

where, the $f_{n,h}(T) = \frac{n_t}{N_t}$ or $\frac{p_t}{P_t}$ are the occupation fraction for electrons or holes in electron traps with concentration N_t or hole traps with concentration P_t, and it can be given by the $e_{n,p} \rightarrow f_{n,h}(T) = \exp\left(-\int_T \frac{1}{\beta} e_{n,p}(T')dT'\right)$ (ignoring the e_p for electron traps or e_n for hole traps). The TSC spectra are given by the sum of $I^{e,h}_{TSC}$ for all electrically active defects. The concentration of defects filled by electrons ($n_t(T_{\text{fill}})$) or holes ($p_t(T_{\text{fill}})$) can be given by:

$$n_t(T_{\text{fill}}) \text{ or } p_t(T_{fill}) = \frac{2\int_{T_s}^{T_e} I^{e,h}_{TSC}(T')dT'}{q_0 A d} \tag{5.7}$$

according to:

$$\int_{T_s}^{T_e} e_{n,p}(T') f_{n,h}(T')dT' = \frac{n_t(T_{\text{fill}})}{N_t} \text{ or } \frac{p_t(T_{\text{fill}})}{P_t} \tag{5.8}$$

Equation 5.7 provides a general equation for extracting defect concentration with the temperature of the start of the emission T_s and end of the emission T_e. This equation indicates that the extracted concentration is proportional to the amplitudes of the TSC signal, and it corresponds to the occupied defect concentration $n_t(T_{\text{fill}})$ or $p_t(T_{\text{fill}})$. It should be noted that the obtained defect concentration is only the full defect concentration if the investigated defect was fully filled, i.e., $N_t = n_t(T_{\text{fill}})$ or $P_t = p_t(T_{\text{fill}})$.

Eq. 5.5 - 5.7 are only valid for fully depleted diodes. In the case of non-fully depleted

diodes, the TS-Cap method is important to get precise defect concentration. It will be discussed in chapter 7 for specific cases. For simplicity, in the following chapters, the $f_{n,h}(T)$ function is modified by multiplying it with $\frac{N_t}{n_t(T_{\text{fill}})}or\frac{P_t}{p_t(T_{\text{fill}})}$ for electron or hole traps, and in this case, equations 5.5 and 5.6 will be changed to:

$$I^e_{TSC}(T) = \frac{q_0 A d}{2} e_n(T) f_n(T) n_t(T_{\text{fill}}) \tag{5.9}$$

or

$$I^h_{TSC}(T) = \frac{q_0 A d}{2} e_p(T) f_h(T) p_t(T_{\text{fill}}). \tag{5.10}$$

Filling Procedures

It is important to note that changes in the amplitude of TSC spectra, measured on the same diode using different filling methods with varying V_{bias} and T_{fill}, were frequently observed in the following chapters. Therefore, it is essential to introduce the theory of filling procedures. If the depleted depth is constant, the amplitude is proportional to the final occupied defect concentration $n'_t(T_{\text{fill}})$ or $p'_t(T_{\text{fill}})$ (after the decay procedure). In general, the deviation in occupied concentration by electrons for electron traps ($n_t(T_{\text{fill}})$) or holes for hole traps ($p_t(T_{\text{fill}})$) at T_{fill} with time t can be described by:

$$\frac{dn_t(T_{\text{fill}})}{dt} = c_n n p_t(T_{\text{fill}}) - c_p p n_t(T_{\text{fill}}) + e_p p_t(T_{\text{fill}}) - e_n n_t(T_{\text{fill}}) \tag{5.11}$$

$$\frac{dp_t(T_{\text{fill}})}{dt} = -c_n n p_t(T_{\text{fill}}) + c_p p n_t(T_{\text{fill}}) - e_p p_t(T_{\text{fill}}) + e_n n_t(T_{\text{fill}}) \tag{5.12}$$

The solved $n_t(T_{\text{fill}})$ or $p_t(T_{\text{fill}})$ are:

$$n_t(T_{\text{fill}}) = N_t \frac{c_n n + e_p}{c_n n + c_p p + e_p + e_n} + \exp\left(-(c_n n + c_p p + e_p + e_n)t\right) \exp\left(C_1\right) \tag{5.13}$$

$$p_t(T_{\text{fill}}) = P_t \frac{c_p p + e_n}{c_n n + c_p p + e_p + e_n} + \exp\left(-(c_n n + c_p p + e_p + e_n)t\right) \exp\left(C_2\right) \tag{5.14}$$

where the $C_{1,2}$ are constant determined by the value of $n_t(T_{\text{fill}})$ or $p_t(T_{\text{fill}})$ at $t = 0$ s. Assuming the filling procedure is long enough to get:

$$\exp\left(-(c_n n + c_p p + e_p + e_n)t_{\text{fill}}\right) = 0 \tag{5.15}$$

Thus, after the filling procedure, the ($n_{t,\text{fill}}(T_{\text{fill}})$) or ($p_{t,\text{fill}}(T_{\text{fill}})$) can be evaluated:

$$n_{t,\text{fill}}(T_{\text{fill}}) = N_t \frac{c_n n_{\text{fill}}}{c_n n_{\text{fill}} + c_p p_{\text{fill}} + e_n} \tag{5.16}$$

$$p_{t,\text{fill}}(T_{\text{fill}}) = P_t \frac{c_p p_{\text{fill}}}{c_n n_{\text{fill}} + c_p p_{\text{fill}} + e_p} \tag{5.17}$$

with considering e_p for the electron traps ($n_t(T_{\text{fill}})$) and e_n for the hole traps ($p_t(T_{\text{fill}})$) are

equal to 0. The n_{fill} and p_{fill} are the free charge carriers concentration during filling.

Generally, the decay process under reverse bias occurs after filling, which means that the concentrations of free charge carriers n_{decay} and p_{decay} are equal to 0. Therefore, $\exp(C_{1,2})$ can be determined by using Eq. 5.13 and Eq. 5.14:

$$\exp(C_1) = N_t \frac{c_n n_{\text{fill}}}{c_n n_{\text{fill}} + c_p p_{\text{fill}} + e_n} \tag{5.18}$$

$$\exp(C_2) = P_t \frac{c_p p_{\text{fill}}}{c_n n_{\text{fill}} + c_p p_{\text{fill}} + e_p} \tag{5.19}$$

with t = 0 s, and $n_t(T_{\text{fill}})$ or $p_t(T_{\text{fill}})$ at $t = 0$ s given by $n_{t,\text{fill}}(T_{\text{fill}})$ or $p_{t,\text{fill}}(T_{\text{fill}})$. Thus, the final equations for evaluating the occupied defect concentration after filling and decay procedures are:

$$n'_t(t_{\text{decay}}, T_{\text{fill}}) = N_t \frac{c_n n_{\text{fill}}}{c_n n_{\text{fill}} + c_p p_{\text{fill}} + e_n(T_{\text{fill}})} \exp(-e_n(T_{\text{fill}}) t_{\text{decay}}) \tag{5.20}$$

$$p'_t(t_{\text{decay}}, T_{\text{fill}}) = P_t \frac{c_p p_{\text{fill}}}{c_n n_{\text{fill}} + c_p p_{\text{fill}} + e_p(T_{\text{fill}})} \exp(-e_p(T_{\text{fill}}) t_{\text{decay}}) \tag{5.21}$$

where the n_{fill}, p_{fill} depends on the filling method. For forward bias filling, $n_{\text{fill}} \approx p_{\text{fill}}$, and $c_n n_{\text{fill}}$ or $c_p p_{\text{fill}} >> e_n$ or e_p:

$$n'_t(T_{\text{fill}}) = \frac{N_t}{1 + \frac{c_p}{c_n}} \exp(-e_n(T_{\text{fill}}) t_{\text{decay}}) \tag{5.22}$$

$$p'_t(T_{\text{fill}}) = \frac{P_t}{\frac{c_n}{c_p} + 1} \exp(-e_p(T_{\text{fill}}) t_{\text{decay}}) \tag{5.23}$$

For the majority carriers filling in p-type silicon, $n_{\text{fill}} \approx 0$ and p_{fill} depends on effective doping:

$$n'_t(T_{\text{fill}}) \approx 0 \tag{5.24}$$

$$p'_t(T_{\text{fill}}) = P_t \frac{1}{1 + \frac{e_p(T_{\text{fill}})}{c_p p_{\text{fill}}}} \exp(-e_p(T_{\text{fill}}) t_{\text{decay}}) \tag{5.25}$$

The hole injection by light is similar to the majority of carriers filling, but p_{fill} depends on light. The electron injection by light is not used in this work. Besides that, the $e_{n,p}(T_{\text{fill}})$ is a strong temperature-dependent parameter (increase with T), and for charged defect (like B_iO_i) $e_{n,p}(T_{\text{fill}})$ is also V_{bias} dependent (increase with V_{bias}, see section 5.3). $c_{n,p}$ can also be temperature dependent e.g. C_iO_i and VO [24]. Thus, for obtain $n'_t(T_{\text{fill}}) = N_t$ or $p'_t(T_{\text{fill}}) = P_t$, the fill procedures need be adjusted. For example, the measured defects in this work:

1. **B_iO_i** is normally measured by the TSC method with forward bias filling at 10 K. It is an electron trap with roughly temperature-independent $c_{n,p}$, and c_n is much larger than c_p [22]. In this case, $n_t(T_{\text{fill}}) = N_t \exp(-e_n(T_{\text{fill}}) t_{\text{decay}})$, and for lower-

temperature filling, $n_t(T_{\text{fill}}) = N_t$.

2. $\mathbf{C_iO_i}$ is a hole trap and can be measured by the TSC method with forward bias filling. In this case, its amplitude increases with T_{fill} due to strongly decreased c_n with temperature (see chapter 8). Therefore, for forward bias filling, $p_t(T_{\text{fill}}) = P_t$ is only valid at high temperature (> 80 K, see the following chapter). Meanwhile, its P_t can also be measured by using majority carriers filling if p_{fill} or during cooling down the free hole p is large enough (see chapters 6 and 7).

3. **X-defect** is a hole trap. Its P_t is extracted by the TSC method with majority filling, which is due to the unknown changes of $c_{n,p}$ with temperature.

4. **Others:** The concentration of other defects is normally given by forward bias filling at T_{fill}, where $n_t(T_{\text{fill}})$ or $p_t(T_{\text{fill}})$ reach their maximum values.

In general, as the filling temperature (T_{fill}) increases up to the start emission temperature (T_s), the peak amplitude of this defect in the TSC spectrum strongly decreases with the decay time (t_{decay}) [11]. Therefore, to obtain precise values of N_t and P_t, the filling temperature should be below $T_s - 10$ K. However, this behaviour can be used to measure other properties of the defect, such as the activation energy (E_a) and the capture cross-sections ($\sigma_{n,p}$). This is the delayed heating method.

Delayed Heating Method

Considering the case for electron traps, and assuming all those traps were filled during filling, the occupation states can be given by:

$$n_t'(T_{\text{fill}}) = N_t \cdot \exp\left(-e_n t_{\text{decay}}\right) \tag{5.26}$$

after decay time t_{decay}. The t_{decay} as a function of n_t' can be observed by varying the t_{decay}. From the obtained curves of t_{decay} vs. $n_t'(T_{\text{fill}})$, the $e_n(T_{\text{fill}})$ can be extracted for specific T_{fill}. In the end, the curve of T_{fill} vs. $e_n(T_{\text{fill}})$ will be observed, which can be used to extract σ and E_a according to Eq. 2.20.

Thermally Stimulated Capacitance

In the TSC technique, the current induced by the movement of charge carriers emitted from defects is directly recorded, however, it is beforehand unknown whether for a given bias voltage the diode is fully depleted or the depleted depth is nearly constant during a full TSC temperature scan. There are situations when the bias needed for achieving the full depletion cannot be applied experimentally, e.g. requiring thousands of volts in highly doped diodes. In such cases, the bias that can be applied in a TSC experiment is only partly depleting the thickness of the devices. In addition, the depleted volume can vary

with temperature due to the change in the space charge caused by thermal emission from the different traps. Not knowing precisely the temperature dependence of the depleted volume can introduce large errors in the determination of defect concentrations. Such problems can partly be overcome with the help of the TS-Cap method which allows the evaluation of the depletion depth as a function of temperature.

Figure 5.7 shows an example of a TS-Cap measurement obtained from EPI-7 (Table 8.1) before annealing. During the measurement, the LCR meter is connected to the sample with the electrometer and switch box, similar to the C–V setup. The capacitance is recorded during heating up with V_{bias} applied by the electrometer. The cooling down and filling of the TS-Cap measurements are similar to TSC measurements performed with the same electrometer and cooling system.

In Fig. 5.7, the minimum value of capacitance initially decreases during heating up and then rapidly increases up to 30 K. This behavior is caused by the unfreezing of dopants and was observed in all TS-Cap measurements in this study. After 30 K, the changes in capacitance are caused by the emission of defects. For p-type silicon, the emission of electrons reduces the capacitance, while the emission of holes increases it.

In general, the TS-Cap measurement is used to extract the depleted depth e.g. Eq. 3.14:

$$W(V_{\mathrm{bias}}, T) = \frac{A\epsilon\epsilon_0}{C(T)} \tag{5.27}$$

where the W is not only voltage dependent but also T dependent. The obtained $W(V_{\mathrm{bias}}, T)$ can be used for analysing TSC spectra by taking $W(V_{\mathrm{bias}}, T)$ into Eq. 5.3 and 5.4.

Besides that, the TS-Cap can also be used to extract defect information directly. As discussed in section 3.2, the W is determined by V_{bias} and N_{eff}. Assuming the space charges are homogeneously distributed in the bulk, in the case of parallel electrodes $W(V_{\mathrm{bias}}, T)$ can be given by:

$$W(V_{\mathrm{bias}}, T) = \sqrt{\frac{2\epsilon\epsilon_0 V_{\mathrm{bias}}}{q_0 N_{\mathrm{eff}}(T)}} \tag{5.28}$$

The $N_{\mathrm{eff}}(T)$ is determined by the charge state of all defects and dopants, and for p-type silicon it can be written to:

$$N_{\mathrm{eff}}(T) = N_0 + \sum_t N_{\mathrm{t}} f_{\mathrm{n,\,t}}(T) - \sum_t P_{\mathrm{t}} f_{\mathrm{h,\,t}}(T) \tag{5.29}$$

where the t indicates a specific defect, N_0 is the space charge density before defect emission. The f was determined by the properties of the defect and T, which had been described in the previous section. In this way, the information about the defect can be extracted. The detail can be found in chapter 7.

Furthermore, it is important to note that the TS-Cap method discussed in this section is

only valid for the case of homogeneously distributed N_{eff} and non-fully depleted situations. However, the case of non-homogeneously distributed N_{eff} ($N_{\text{eff}}(x,T)$) will be discussed in more detail in chapter 7.

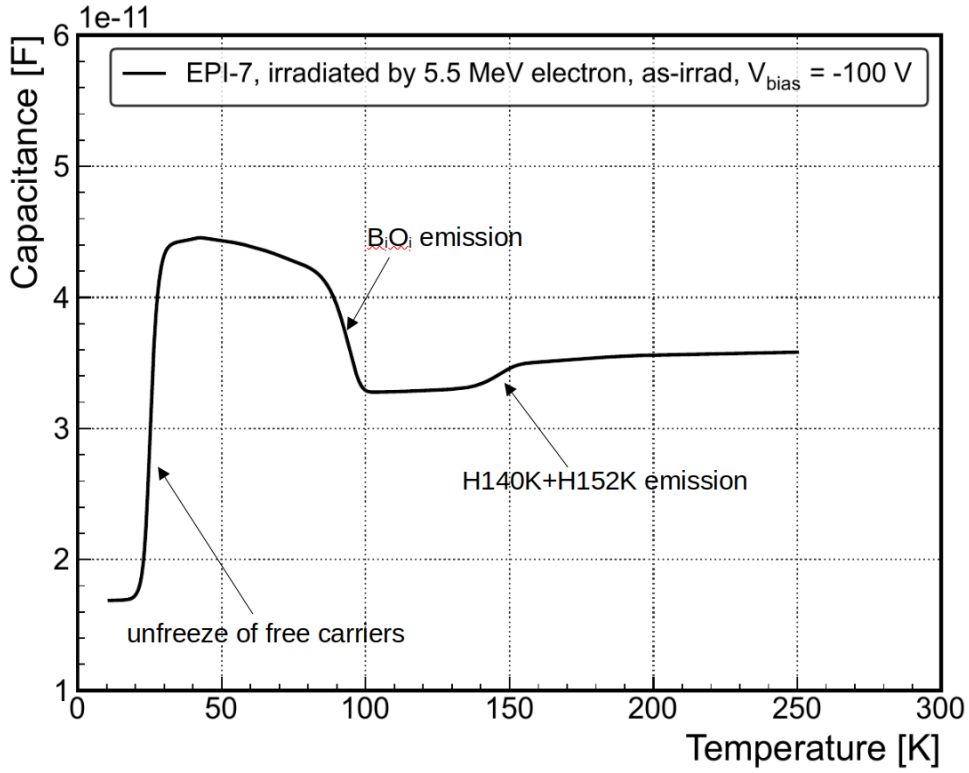

Figure 5.7: Example of TS-Cap measurement with forward bias filling on EPI-7. $V_{\text{fill}} =$ 10 V, $V_{\text{bias}} = -100$ V, $T_{\text{fill}} = 10$ K.

5.2.3 Error Discussion

At room temperature, the accuracy of measured admittance or impedance in the LCR meter is below 0.1%. Also, the accuracy of the measured current and applied bias is below 0.1% for the electrometer or picoammeter. However, the errors will increase for microscopic measurements due to the signal induced by the defect being comparable with noise.

As can be seen in Fig. 5.8, the TSC measurements are performed with ceramic without bonded diode. The maximum value of current is around 3×10^{-13} A, which is sometimes close to the current induced by the defect (e.g. E30K, E50K and VO in Fig. 5.6d). To subtract the noise shown in Fig. 5.8, the linear fitting was performed on the data obtained from V_{bias} = -300 V heating up:

$$I_{\text{TSC}} = a \cdot T + b \tag{5.30}$$

The parameters a = -$(9.36 \pm 0.05) \times 10^{-16}$ A/K and $b = (1.42 \pm 0.09) \times 10^{-14}$ A were extracted from the linear fits. The line given by these two parameters will be used to

partially subtract noise for all the spectra in this work.

Note that the errors mentioned here were mainly related to the measurement equipment and noise, and not necessarily to the physical properties of the defects themselves. Therefore, further analysis and interpretation of the data will also require consideration of other factors, such as the device structure and materials, as well as theoretical models and simulations. These aspects will also be discussed in the relevant chapters of this thesis.

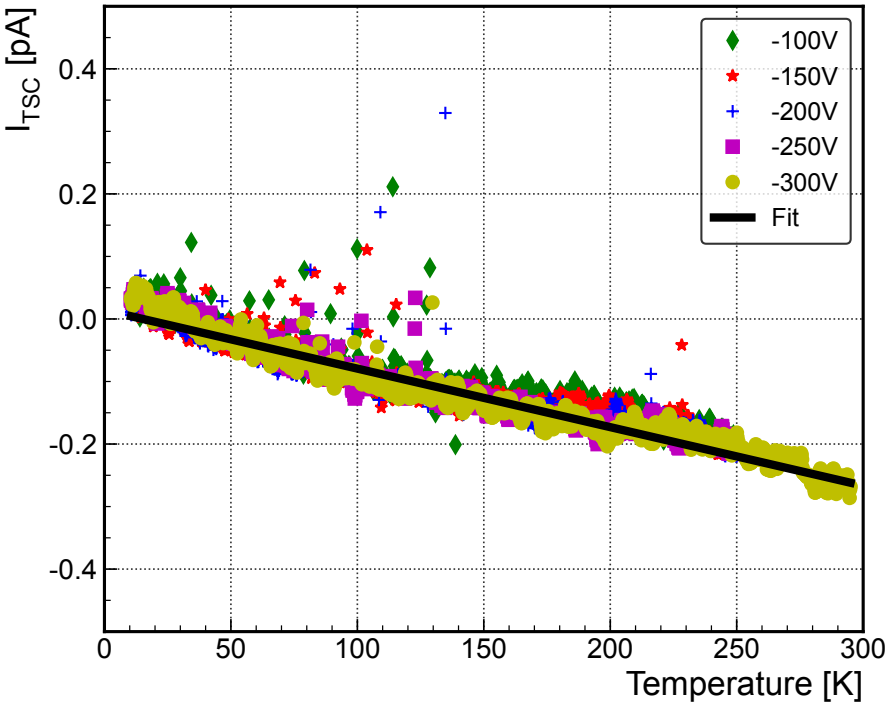

Figure 5.8: TSC measurements for different reverse biases (see legend) performed on ceramic without diode. The fit line was given by linear fits on data of V_{bias} = -300 V.

5.3 Additional Effects

The fundamental theory of macroscopic and microscopic measurements has been discussed in the above sections. To understand the data obtained, additional effects will also be presented in the following sections.

5.3.1 Poole Frenkel Effect

The Poole Frenkel Effect describes how an electric field assists in the thermal ionisation of trapped charge carriers in electronic semiconductors and insulators. It was first proposed by P. Frenkel in 1938 [135], with the assumption of a one-dimensional model, and later a three-dimensional model was developed by J. L. Hartke in 1968 [136].

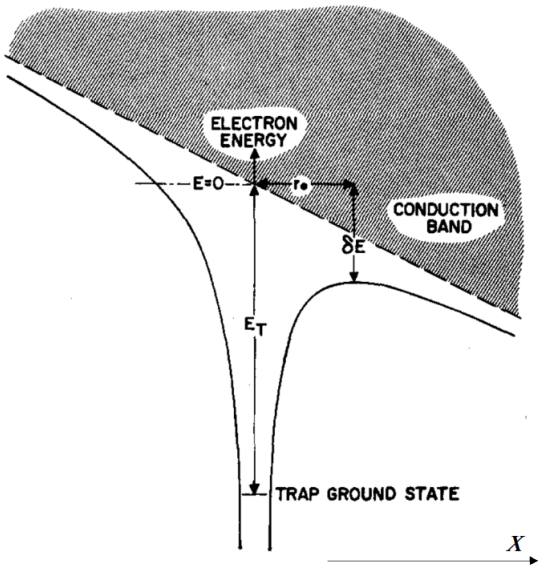

Figure 5.9: Energy of an electron bound to a positive point charge in the presence of a uniform applied field. Taken from [136].

Figure 5.9 depicts the schematic of the 3-D Poole Frenkel effect, which was first proposed by J. L. Hartke [136]. According to P. Frenkel's theory, the electrical potential of ionized atoms affects the distribution of potential around them, and this can be given as [135]:

$$\Delta U = q_0 r_0 E + \frac{q_0^2}{\epsilon \epsilon_0 r_0} \tag{5.31}$$

In this equation, ΔU is the change in potential in the nearby region, r_0 represents the distance between the emitted charge and the ionized atom, and E is the field value assumed to be constant in this region. In this case, the value of the activation energy E_a was obtained for a given electric field E:

$$E_a = E_{a0} - \sqrt{q_0 \frac{E}{\pi \epsilon \epsilon_0}} \tag{5.32}$$

with zero field activation energy E_{a0}. This equation is obtained under the assumption that the charge will be emitted at the position with minimum potential value.

However, as mentioned in [136], the reduction of E_a inside the region of $\sqrt{q_0 \frac{E}{\pi \epsilon \epsilon_0}}$ is smaller than expected from the Eq. 5.32. One explanation provided by J. L. Hartke is that the model used was derived from the one-dimensional assumption, which is not fully accurate. Therefore, he developed the Poole-Frenkel effect by considering three dimensions.

As can be seen in Fig. 5.9, Hartke achieved the 3-D PF effect by assuming the conduction and valence bands are the flat plane, with the constant E in the studied region. In this

case, the e_n was given by:

$$e_n = \sigma_n v_{th,n} N_C \cdot \exp\left(-\frac{E_{a0}}{k_B T}\right) \times \left[\left(\frac{1}{\gamma^2}\right)\left(e^{\gamma}(\gamma - 1) + 1\right) + \frac{1}{2}\right] \tag{5.33}$$

with the $\gamma = (q_0 E/\pi\epsilon\epsilon_0)^{1/2} \cdot q_0/(k_B T)$. Eq. 5.33 was used in this work to evaluate the E_{a0} of B_iO_i. A constant value of E_{a0} was obtained for different values of V_{bias} in chapter 6. However, this result is only valid for diodes with lower doping, as discussed in detail in chapter 6.

5.3.2 Tunnelling Effect

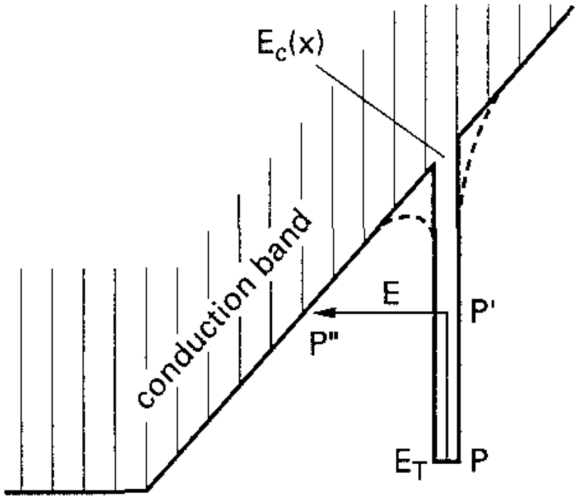

Figure 5.10: Energy-band diagram of a depletion layer around a reverse-biased junction. The tunneling-enhanced emission of an electron from a trap ($E_T = E_C$ - 0.4 eV) is indicated. The solid line denotes the potential well of the trap without Coulomb interaction and the dashed line with Coulomb interaction. Taken from [137].

The other effect that enhances the emission effect is the Tunnelling Effect, which was proposed by C. Zener in 1934 [138]. The mathematical model for calculating the tunnelling effect was developed by A. G. Chynoweth et al. in 1961 [139], and was later refined by Hurkx in 1992 [137], with the equations now widely used in TCAD simulations. In summary, the high electric field increases the slope of the conduction band, allowing charge carriers at the trap to transition from the energy position (E_T) as shown in Fig. 5.10. As a result, $e_{n,p}$ are enhanced by the electric field, and this effect becomes significant for electron when e.g. the field value is greater than or equal to 3.7×10^5 V/cm (F_{Γ_n}) at room temperature [137, 140]. However, the equation is given in [137, 140] for this effect ($e_{n,p} = e_{n0,p0}(\Gamma_{n,p}+1)$, with $\Gamma_{n,p} = 2\sqrt{3\pi}\frac{F}{F_{\Gamma_{n,p}}} \cdot \exp(F/F_{\Gamma_{n,p}})^2$ and $F_{\Gamma_{n,p}} = \frac{\sqrt{24 m^*_{de,dh}(k_B T)^3}}{q_0 \hbar}$), which is not valid at lower temperatures ($T \approx 0$, $e_{n,p} \approx \infty$ and this is apparently wrong).

5.3.3 Cluster Effect

The shape of TSC peaks after 23 GeV proton irradiation is remarkably different from those of point-like defects which were already extensively investigated with DLTS after ^{60}Co γ-ray or electron irradiation (with $E_{\text{kin}} \leq 6$ MeV). Such differences can be partially explained by the "**Cluster Effect**", which changes the emission of the defects in the cluster. One example of a cluster of defects in a dislocation loop is presented in Fig. 5.11 [106]. It was first proposed in 2014 [106] for DLTS measurements, and developed by E. M. Donegani et al [107] for TSC measurements.

In this effect, the activation (or ionisation) energy (E_a) was modified by the occupation fraction f_t with coulomb energy ΔE_a:

$$E_a = E_0 - \Delta E_a \cdot f_t \tag{5.34}$$

where the E_0 is the activation (or ionisation) energy of cluster defect after all the atoms are emitted, and $f_t = \frac{n_t}{N_t}$. Eq. 5.34 is for the case the traps emit electrons and become positive ions after emission. The other cases can be found in [107].

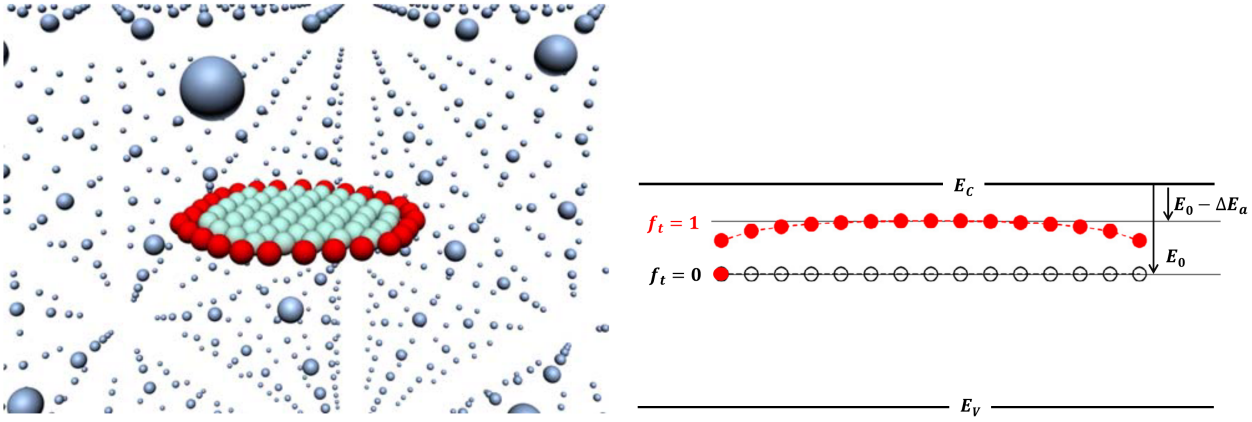

(a) (b)

Figure 5.11: (a) Schematic representation of a dislocation loop defect in the silicon lattice with the electrically active periphery. Taken from [106]. (b) Schematic presentation of the potential energy of the electrons in a cluster consisting of 15 point defects equally spaced on a straight line. E_V denotes the edge of the valence band and E_C of the conduction band. The filled dots show the ionisation energies for the individual defects when all traps are filled. The electron occupying the central defect has the lowest ionisation energy, E_0 - ΔE_a. It will discharge first when the sample is heated in the TSC measurement. The open circles correspond to the ionisation energy when only one state is filled with an electron. Its value is E_0, the ionisation energy of the point defects, which build the cluster. Taken from [107].

6 23 GeV Protons Irradiation

Note: This chapter is a copy of my published paper [23] with minor corrections. The additional materials can be found after the conclusion.

Abstract: In this work, the Thermally Stimulated Current technique has been used to investigate the properties of the radiation induced interstitial boron and interstitial oxygen defect complex (B_iO_i) by 23 GeV (E_{kin}) protons, including activation energy, defect concentration as well as the annealing behaviour. At first isothermal annealing (at 80 °C for 0 to 180 minutes) followed by isochronal annealing (for 15 minutes between 100 °C and 200 °C in steps of 10 °C) studies had been performed in order to get information about the thermal stability of the B_iO_i in the materials with different resistivities after irradiation with 23 GeV protons to a fluence of 6.91×10^{13} p/cm^2. The results are presented and discussed. Furthermore, the extracted data from Thermally Stimulated Current measurements are compared with the macroscopic properties derived from current-voltage and capacitance-voltage characteristics. In addition, the introduction rate of interstitial boron and interstitial oxygen defect as a function of the initial doping concentration was determined by exposing diodes with different resistivities (10 $\Omega \cdot$ cm, 50 $\Omega \cdot$ cm, 250 $\Omega \cdot$ cm, and 2 k$\Omega \cdot$ cm) to 23 GeV protons. These results are compared with data from Thermally Stimulated Current and Deep Level Transient Spectroscopy measurements achieved by the team of the CERN-RD50 "Acceptor removal project".

6.1 Motivation

In the frame of the CERN-RD50 collaboration new types of silicon sensors for the High Luminosity Large Hadron Collider (HL-LHC) experiments are under development and detailed investigation in order to cope with the extraordinary high particle rate – up to 200 p-p collisions per bunch crossing – and the related large radiation damage effects in the sensors. The new types of sensors which are recently developed are so-called Low Gain Avalanche Detectors (LGADs) for high precision timing ($\leq$ 50 ps) and position resolution (few hundred µm) [2, 3] and High Voltage CMOS devices (HV CMOS) for the inner tracking detectors [4, 5, 6, 7, 8, 9]. Both types of these sensors as well as the new pixel and strip devices will be manufactured on boron-doped (p-type) silicon. The degradation of the performance of these sensors due to the expected high radiation field (see section 4.5), and a search for a possible improvement of their radiation tolerance by defect engineering is of high relevance. For example, the exposure of LGADs to

radiation leads to a reduction of the sensor internal gain with increasing particle fluence [2, 3, 86]. This degradation is caused by the deactivation of the active boron in the highly doped p-type layer ($\approx 1 \times 10^{16}$ cm^{-3}), the gain layer, which leads to a reduction of the space charge and consequently a lowering of the electric field followed by a decrease of charge multiplication in this layer (see section 4.5). In general, the deactivation of the boron dopant is called acceptor removal. Such processes, adds to the degradation seen previously on n-type silicon caused by the formation of point and extended defects comprising vacancies, interstitials and carbon and oxygen intrinsic impurities in silicon with impact on a) Leakage current - V_3 and I_P defects with close to mid-gap energy levels [19, 141, 142]; b) effective space charge concentration - H(116 K), H(140 K), H(152 K) acceptors with levels in the lower half of the band gap and a shallow donor defect E(30 K) all with electric field enhanced emission [18], [16].

The reason for the deactivation of the boron dopant by radiation is its reaction with silicon interstitials created by irradiation. This way the boron atoms are moved from substitutional on interstitial sites and lose their acceptor character. These defect complexes can be detected by spectroscopic methods like Thermally Stimulated Current (TSC) and Deep Level Transient Spectroscopy (DLTS).

In this paper we will report at first in section 6.2 on the experimental details about the used p-type epitaxial diodes of different resistivities, the irradiation with 23 GeV protons and the methods for the investigation of the macroscopic and microscopic properties of the devices. In section 6.3 the results of the current-voltage and capacitance-voltage measurements are presented. The microscopic measurements using the TSC technique with the focus on the boron-oxygen (B_iO_i) defect complex, its correlation with the radiation induced change of the effective space charge density and annealing behaviour are described and discussed in section 6.4. Finally the generation rates as function of the initial boron content in the devices will be given.

6.2 Experimental Details

Table 6.1: Device information (* 1 MeV neutron equivalent fluence)

Label	EPI 01-73	EPI 06-71	EPI 09-73	EPI 12-74
$N_{\mathrm{eff},0}$ (cm^{-3})	1.37×10^{15}	1.97×10^{14}	4.53×10^{13}	6.24×10^{12}
Initial resistivity ($\Omega \cdot$ cm)	$\approx$10	$\approx$50	$\approx$250	$\approx 2 \times 10^3$
Proton fluence Φ_p (cm^{-2})	7×10^{13}	7×10^{13}	7×10^{13}	7×10^{13}
Fluence value Φ_{eq} (cm^{-2})*	4.3×10^{13}	4.3×10^{13}	4.3×10^{13}	4.3×10^{13}
Area A (cm^2)	0.06927	0.06927	0.06927	0.06927
Thickness d (µm)	50	50	50	50

A set of 50 µm thick p-type epitaxial layers with different resistivity between 10 $\Omega \cdot$ cm and 2 k$\Omega \cdot$ cm (see Table 6.1) were grown on highly boron-doped Cz substrates ($\rho \approx 0.003\ \Omega \cdot$ cm)

by ITME [143] and pad-sensors with a sensitive area of 2.632×2.632 mm^2 have been processed by CiS [144]. The pad is surrounded by a current collection ring and several guard rings. For a possible light injection also into the rear side of the diode a 3×3 mm^2 cavity was etched into the Cz substrate down to the EPI layer and a circular opening was processed with a diameter of 1.2 mm in the metallization.

The irradiation with 23 GeV protons was performed at the CERN-PS IRRAD facility (irradiated at room temperature). According to the literature [145] we used a hardness factor of 0.62 when determining Φ_{eq} after irradiation with 23 GeV protons. The devices were unbiased during irradiation. Significant charging or ESD effects have not been observed. The investigated diodes exhibit a quite large n^+ implanted area and only a small region of the outer rim with several guard rings have oxide layers in between.

The macroscopic device performance of the investigated diodes was measured by means of current-voltage (I–V) and capacitance-voltage (C–V) characteristics. The radiation induced changes in the effective doping concentration (N_{eff}) and the full depletion voltage V_{fd} were determined from C–V measurements using different frequencies (230 Hz, 445 Hz, 1 kHz and 10 kHz) and guard ring grounded.

For the characterization of the radiation induced electrically active defects the TSC method was used [11, 52, 130, 133, 134]. The TSC experimental procedure consists of cooling down (0 V) the sample to low temperatures (typically 10 K) where filling of the defects is performed by forward biasing of the diode. A TSC spectrum is then recorded by measuring the diode current during heating up the device with a constant rate of 0.183 K/s under reverse bias applied to the diode [11]. The guard ring was always grounded and the time step for the read-out of the current and temperature was set by the software to 1 s.

Isothermal annealing experiments were performed at a temperature of 80 °C for all irradiated diodes and the macroscopic as well as the microscopic properties evaluated. For one 50 Ω · cm diode isochronal annealing in the temperature range from 100 °C to 200 °C in steps of 10 °C for 15 min at each step was studied in order to get information on the thermal stability of the specific B_iO_i defect which is mainly responsible for the acceptor removal effect in this material.

6.3 I–V, C–V Measurements

In this section, the properties and parameters of the measured I–V and C–V characteristics of the irradiated sensors are presented and discussed.

As an example in Fig. 6.1a I–V curves of the diode 06-71 (50 Ω · cm material) for different annealing steps are shown. The measurement temperature was always 20 °C and the guard ring connected to ground. After full depletion the current is still increasing, which might be due to the high electric field at the n^+ - p junction which is in order of 10^5 V/cm for a bias voltage of 300 V, leading to a possible trap assisted tunneling

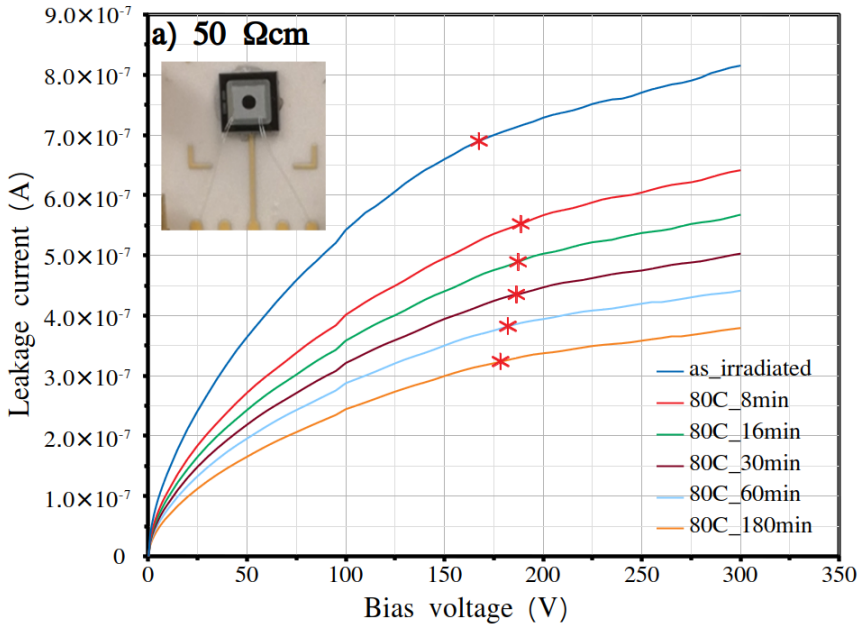

(a)

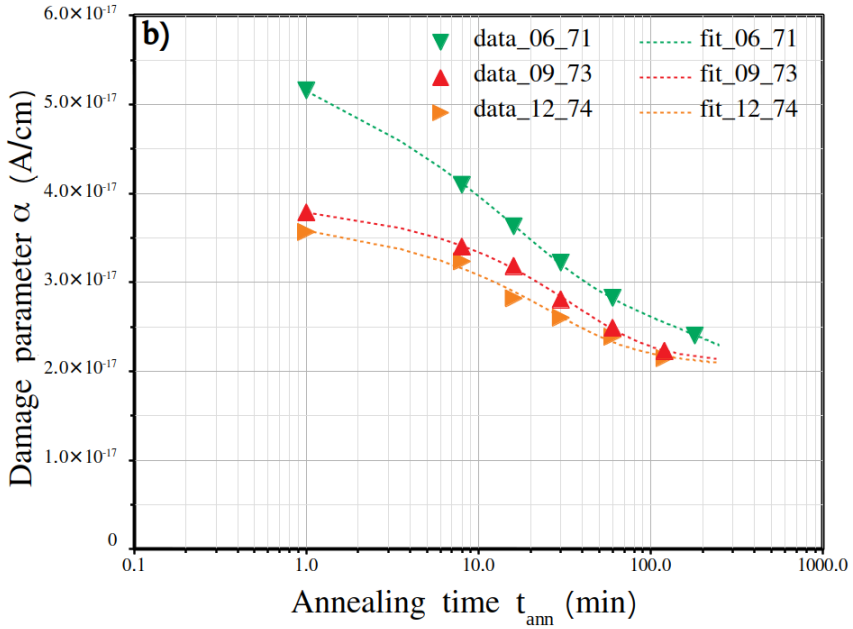

(b)

Figure 6.1: (a) Current-voltage characteristics of 50 $\Omega \cdot$ cm diode (06-71), irradiated with $\Phi_{eq} = 4.28 \times 10^{13}$ cm^{-2} after different annealing steps at 80 °C. The red asterisks indicate the full depletion voltages at which the current related damage parameter α is determined. Measurement condition: T = 20 °C, humidity $\leq$ 10%; (b) Current related damage parameter $\alpha(T_{ann}, t_{ann})$ versus t_{ann} annealing time at 80 °C for 3 diodes with different initial resistivity (06-71 - 50 $\Omega \cdot$ cm, 09-73 - 250 $\Omega \cdot$ cm, 12-74 - 2 k$\Omega \cdot$ cm) irradiated with the same Φ_{eq} of 4.28×10^{13} cm^{-2}. The dashed lines represent the fits to the data according to Eq. 6.2.

effect [137]. But a contribution of surface current from interface traps of the oxide layer surrounding the pad cannot be excluded [89]. The full depletion voltage V_{fd} for the annealing steps between 0 min and 180 min at 80 °C are indicated as red stars in Fig. 6.1a. The values slightly changed around (170 ± 10) V for annealing at 80 °C. For the annealing steps between as irradiated and 180 min at 80 °C a strong decrease of the current is measured, which is a well-known observation for hadron irradiated silicon sensors and mainly due to the annealing property of the radiation induced three-vacancy (V_3) defect [13]. A characteristic parameter for the radiation induced generation current ΔI is the so-called current related damage parameter α defined by:

$$\alpha(T_{\text{ann}}, t_{\text{ann}}) \quad = \quad \frac{\Delta I}{V_{ol} \times \Phi_{\text{eq}}} \tag{6.1}$$

where V_{ol} is the depleted volume of the device, Φ_{eq} the 1 MeV neutron equivalent fluence, T_{ann} the annealing temperature and t_{ann} the annealing time. A parameterization of the time dependence is given by [11]:

$$\alpha(t_{\text{ann}}) \quad = \quad \alpha_I \exp\left(-\frac{t_{\text{ann}}}{\tau_I}\right) + \alpha_0 - \beta \ln\left(\frac{t_{\text{ann}}}{t_0}\right) \tag{6.2}$$

with amplitude α_I and the time constant τ_I of the short term component, the constant term α_0, the parameter β of the logarithmic term with $t_0 = 1$ min. The dependence of the parameter on the annealing temperature can be found in [11]. Fig. 6.1b shows the α values extracted from the I–V curves (at $V \approx V_{\text{fd}}$) as function of annealing time and the corresponding fits according to Eq. 6.2. The parameters of the fitted curves are presented in Table 6.2. The estimated errors of the parameters in Eq. 6.2 are caused by systematic uncertainties in the voltage at which the current data were taken due to the large increase of the I–V curves near and above the full depletion voltage.

Table 6.2: Current related damage parameter

label	EPI 12-74	EPI 09-73	EPI 06-71	Ref [11]
Nominal resistivity ($\Omega \cdot$ cm)	2000	250	50	100 - 7000
α_I (1×10^{-17} A/cm)	1.00 ± 0.1	1.29 ± 0.1	1.00 ± 0.1	1.13
τ_I (min)	17.22 ± 2	35.11 ± 3	26.17 ± 2	9
α_0 (1×10^{-17} A/cm)	4.21 ± 0.2	2.53 ± 0.2	2.62 ± 0.2	4.23
β (1×10^{-18} A/cm)	3.47 ± 0.3	0.71 ± 0.02	0.95 ± 0.1	2.83

The other macroscopic property which is affected by radiation is the effective space charge density N_{eff} or full depletion voltage V_{fd} of the device. Both quantities have been extracted from C–V characteristics measured at frequency of 10 kHz, an AC signal amplitude of 0.5 V and in parallel mode operation of the LCR-meter. For the evaluation of the full depletion voltage V_{fd} it is a common procedure to perform linear fits to the rising part of the $1/C^{-2}$ - V curve in a proper voltage range and the saturation part above full

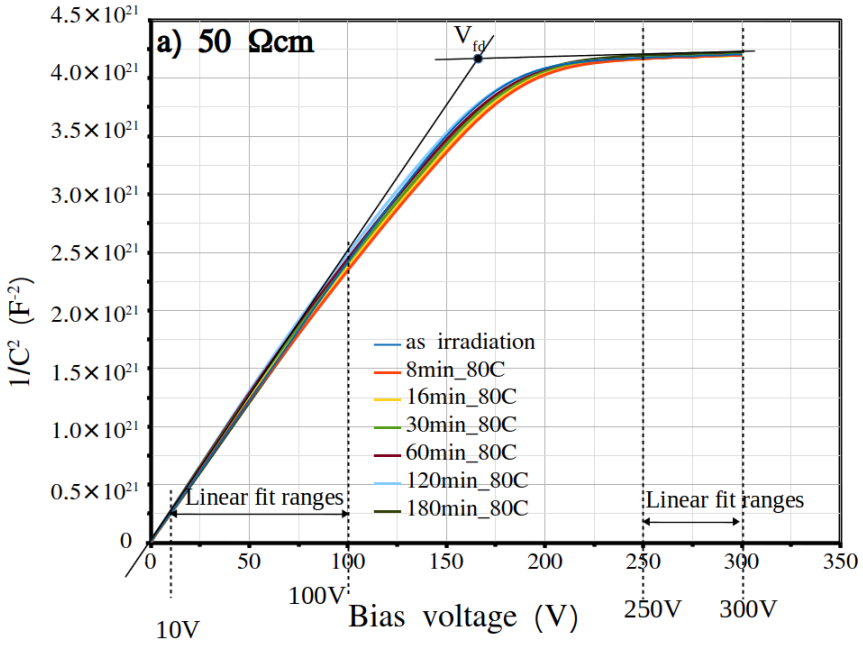

(a)

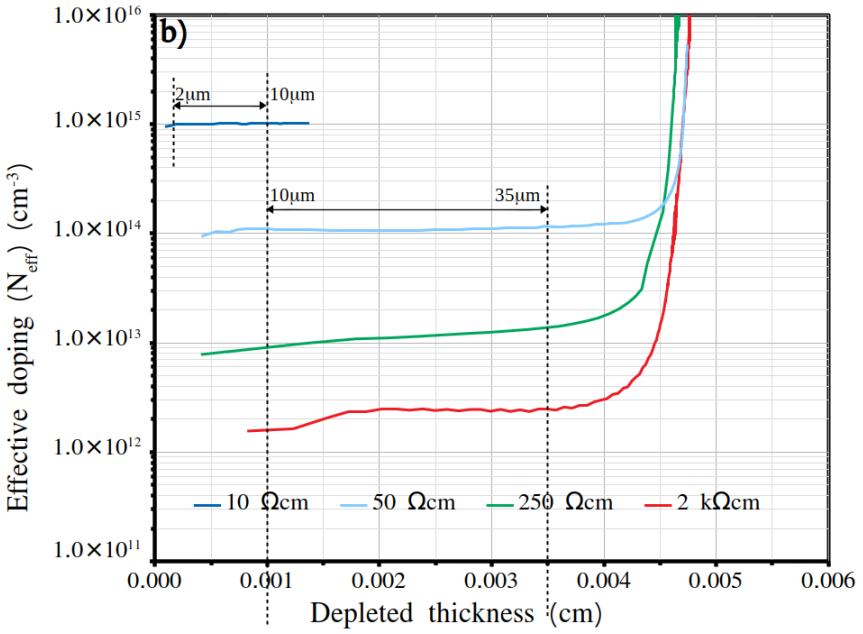

(b)

Figure 6.2: (a) $1/C^{-2}$ - V curves for 50 Ω · cm diode (06-71) for all annealing steps at 80 °C. Measurement parameter: measurement temperature T = 20 °C, frequency freq = 10 kHz, humidity ≤ 10%, V_{AC} = 0.5 V. The voltage ranges of the linear fits in the rising and saturation part of the curve for 0 min at 80 °C and the crossing point of the straight lines at V_{fd} are indicated. (b) Doping profiles of the diodes with different resistivity are shown for an annealing of 30 min at 80 °C. The profiles were evaluated from C–V measurements by using Eq. 6.4 and Eq. 6.5. The mean values of N_{eff} are derived from the indicated depth ranges and are presented in Fig. 6.3.

depletion (see Fig. 6.2a). The voltage of the crossing point is then taken as V_{fd}. But such procedure is only valid if N_{eff} is constant throughout the entire sensor volume and requires the conductivity of the un-depleted bulk to be large. The $1/C^{-2}$ - V curves measured for the 50 $\Omega \cdot$ cm diode after different annealing steps are demonstrated in Fig. 6.2a. The effective space charge concentration N_{eff} can then be calculated in two ways:

$$N_{\text{eff}} = \frac{2\varepsilon_0 \varepsilon_r V_{fd}}{q_0 d^2} \tag{6.3}$$

$$N_{\text{eff}}(V) = \frac{2}{\varepsilon_0 \varepsilon_r A^2 q_0 \frac{d(1/C^2)}{dV}} \tag{6.4}$$

where ε_0 is the permittivity of vacuum, ε_r the relative permittivity of silicon (11.9), q_0 the elementary charge, A the active pad area and d the full depletion depth, which is derived from:

$$w(V) = \frac{\varepsilon_0 \varepsilon_r A}{C(V)}, \quad V < V_{fd} \tag{6.5}$$

where for $V = V_{\text{fd}}$ the depletion depth is given by $w(V_{\text{fd}}) = d$ and the capacitance $C_{\text{fd}} = \varepsilon_0 \varepsilon_r A/d$. The full depletion voltages extracted from $1/C^{-2}$ - V curves for the high resistivity diode (2 k$\Omega \cdot$ cm, 12-74) are very small in the range from about 4 V to 5 V for the annealing steps between 0 min to 120 min and for the 250 $\Omega \cdot$ cm diode (09-73) V_{fd} varies between 15 V to 20 V.

For C–V measurements the guard ring was grounded and the measurements were performed at 20 °C.

According to Eq. 6.4 and Eq. 6.5, the doping profiles are extracted for diodes with different resistivities (10 $\Omega \cdot$ cm, 50 $\Omega \cdot$ cm, 250 $\Omega \cdot$ cm and 2 k$\Omega \cdot$ cm) and annealing time of 30 min at 80 °C, as shown in Fig. 6.2b. In this figure the range of the depletion depth (2 µm to 10 µm for 10 $\Omega \cdot$ cm and 10 µm to 35 µm for the other diodes) for evaluating the mean values of N_{eff} is also indicated. Finally, the extracted values N_{eff} as function of annealing time for most devices are plotted in Fig. 6.3. The Eq. 6.3 is approximately valid for non-irradiated diodes under the assumption of an abrupt n^+ - p junction and a homogeneously distributed space charge density. But it has to mentioned that there are several shortcomings for irradiated devices. For example in radiation damaged diodes the effective space charge might be non-homogeneous leading to complex electric field distributions, the influence of strong changes in free charge carrier concentrations on the evaluation of the depletion depth [146], or frequency dependence of C–V measurements for highly irradiated sensors especially observed in high resistivity material [65]. While for the irradiated diodes ($\Phi_{\text{eq}} = 4.28 \times 10^{13}$ cm^{-2}) with a resistivity of 10 $\Omega \cdot$ cm and 50 $\Omega \cdot$ cm a frequency dependence in C–V measurements is not observed, vice versa in the higher resistivity material (250 $\Omega \cdot$ cm and 2 k$\Omega \cdot$ cm) a frequency dependence is seen. Considering these effects the differences in the evaluated N_{eff} values for the 50 $\Omega \cdot$ cm

diode by using Eq. 6.3 and Eq. 6.4 are estimated to below 3% for the different annealing steps. Using only Eq. 6.4 the deviations are below 1% if the voltage ranges are chosen properly (10 V to 100 V for 50 Ω · cm, 4 V to 10 V for 250 Ω · cm and about 1 V to 3 V for 2 kΩ · cm depending on the annealing step). Much larger differences in N_{eff} up to 17% are found for the 2 kΩ · cm material taking the data measured at frequencies of 230 Hz and 10 kHz and using Eq. 6.3. On the other hand the evaluation according to Eq. 6.4 results for both frequencies in a much smaller differences of the 3% order.

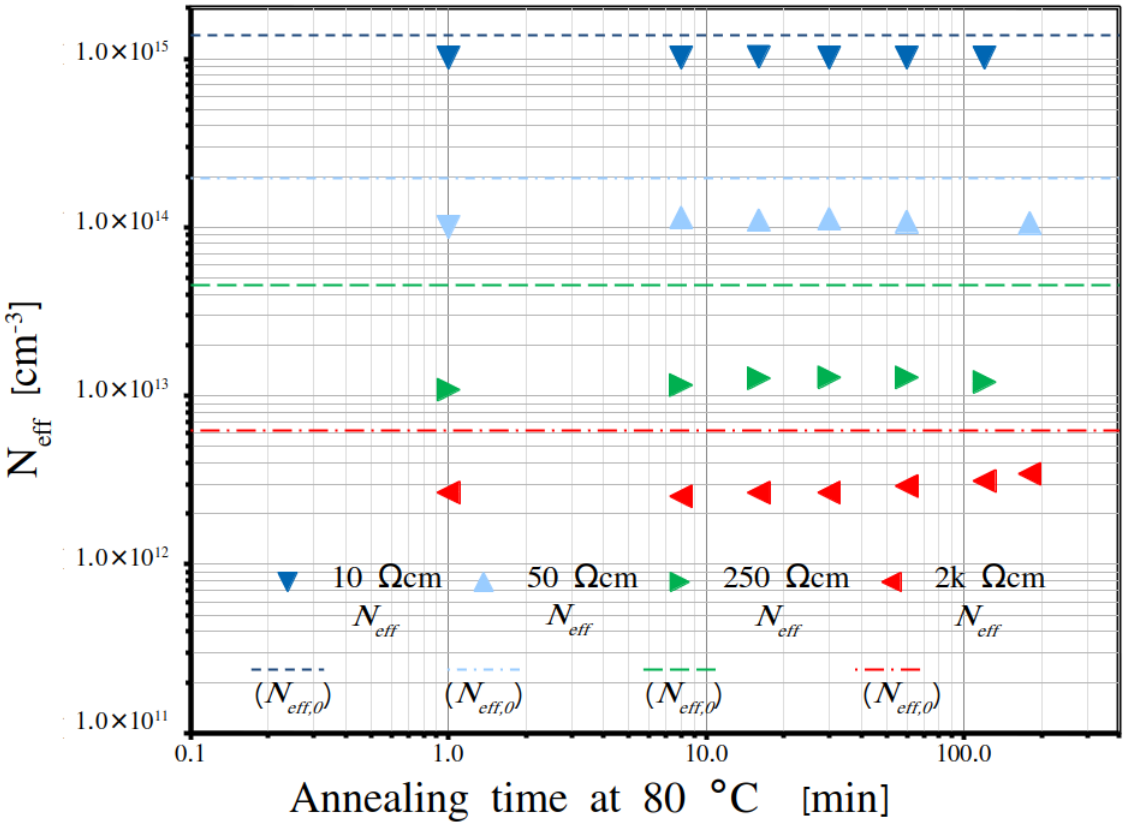

Figure 6.3: Development of the effective doping concentration $N_{\text{eff}} \pm 3\% N_{\text{eff}}$ with annealing time for 50 µm thick epitaxial diodes of different resistivities (see legend) after irradiation with 23 GeV protons to $\Phi_{\text{eq}} = 4.3 \times 10^{13}$ cm^{-2}. The dashed lines indicate the initial doping concentration $N_{\text{eff,0}}$ of the different diodes.

As can be seen in Fig. 6.3, the changes of N_{eff} versus annealing time at 80 °C are quite small. Only for the high resistivity diode (2 kΩ · cm) an increase of N_{eff} is observed. These results can be explained by the thermal stability of the radiation induced boron related defect B_iO_i and are discussed in the next section.

6.4 TSC Measurements for B_iO_i Defect

The TSC technique has been used to investigate the properties of the radiation induced B_iO_i defect complex by 23 GeV protons, including activation energy, defect concentration as well as the annealing behaviour.

As an example, Fig. 6.4a shows TSC spectra of the irradiated diodes with different resistivities (10 $\Omega \cdot$ cm, 50 $\Omega \cdot$ cm, 250 $\Omega \cdot$ cm, 2 k$\Omega \cdot$ cm). The spectrum of the 10 $\Omega \cdot$ cm diode was recorded at 100 V and normalized to the fully depleted depth by a factor $d/w(V)$. All other spectra were taken at voltages above fully depletion (see caption Fig. 6.4a). Fig. 6.4b shows TSC spectra of the irradiated diode 06-71 (initial resistivity of 50 $\Omega \cdot$ cm, see Table 6.1) for different applied bias voltages in the range between 100 V and 300 V during heating up. The observed dominant peaks in the temperature range of 90 K to 100 K and their shifts to lower temperature with increasing bias voltage are attributed to the B_iO_i defect. Such assignment was presented by different authors who investigated radiation induced defects in boron doped material [20, 15, 101]. The main arguments are that the introduction of this defect depends on the boron, carbon and oxygen content in the material and that the defect kinetics rate depends on the ratio of the oxygen concentration to the boron concentration [20, 15]. Also theoretical calculations support these properties [101]. This voltage dependence of the shift of the peak maximum is a typical property of so-called coulombic centers which are governed by the Poole Frenkel effect [16], [135], [136] that means an electrical field dependence of the emission rate or the activation energy of the defect center, respectively. This will be described in more detail in the next paragraph. Another observation is the increasing peak amplitude of the B_iO_i complex with bias which is due to firstly an increase of the depletion depth before fully depletion and thereafter for higher voltages an extension of the depleted region into the p^+ backside of the highly doped substrate.

It is worth mentioning here that the annealing experiments in this work have been performed with samples in open circuit. This way, the migration of the possible existing hydrogen atoms from the passivated surface to the bulk is prevented [147], [148]. In addition, there are known two phenomena which can be used to indicate possible hydrogen effect on radiation damage in the diodes under study: (i) the reactivation of boron impurity during thermal annealing in the temperature range of 100-160 °C [149]; (ii) the appearance of hydrogen-related complexes with radiation-induced defects. As it was observed in Ref. [150], the vacancy-oxygen-hydrogen complex is formed under thermal annealing of irradiated hydrogen containing structures. This complex has two energy levels in the higher and lower parts of Si energy gap [151] and can be easily observed with defect spectroscopy techniques when they exist. According to the spectra in Fig. 6.4 we could not identify any of these two markers, indicating that hydrogen effects in the investigated structures are negligible.

6.4.1 Some Theoretical Background of TSC

The general formalism of the TSC technique is in detail described in the literature [11, 52, 130, 133, 134]. The general formula for a single electron trap existing in N_t concentration

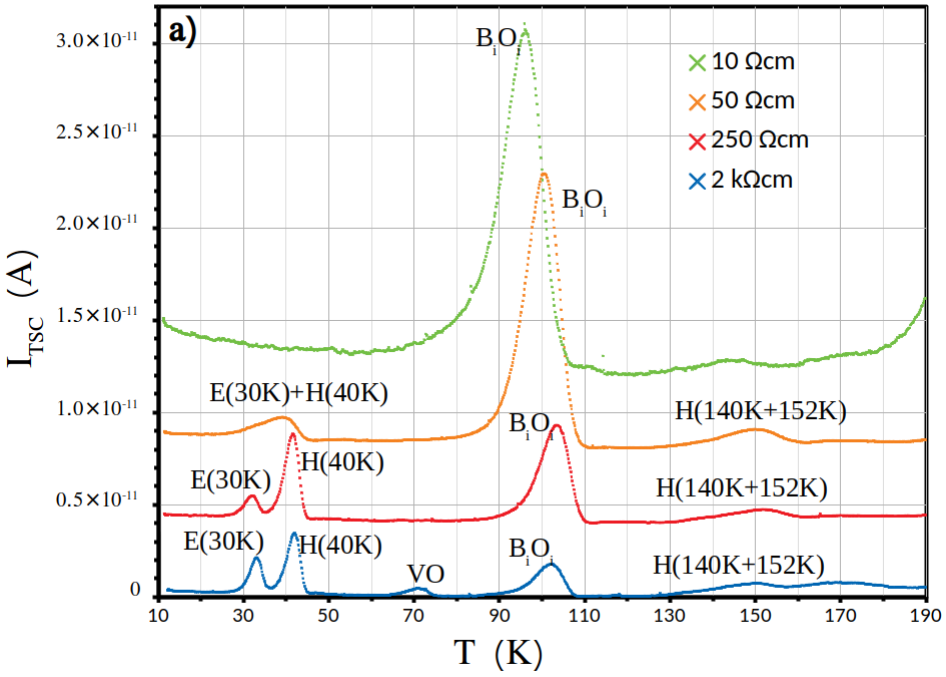

(a)

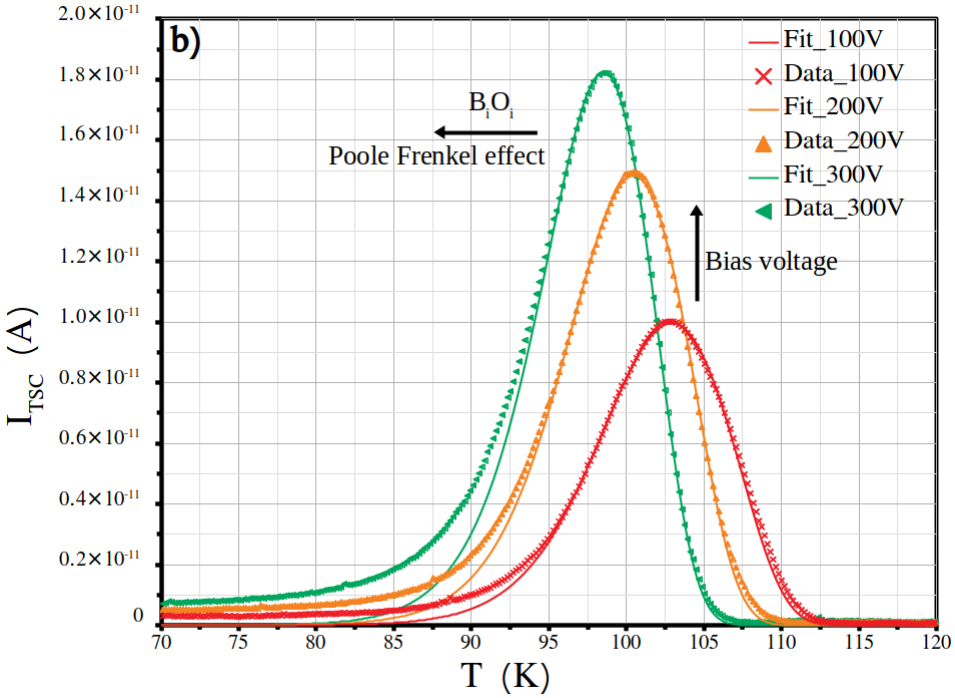

(b)

Figure 6.4: (a) TSC spectra of diodes with different resistivity after 23 GeV proton irradiation to $\Phi_{eq} = 4.3 \times 10^{13}$ cm^{-2} for reverse bias 20 V (2 k$\Omega \cdot$ cm), 40 V (250 $\Omega \cdot$ cm), 200 V (50 $\Omega \cdot$ cm) and 100 V (10 $\Omega \cdot$ cm, spectrum normalized to d/w(100 V)). TSC parameters: $T_0 = 10$ K, $V_{fill} = 5$ V, heating rate $\beta = 0.183$ K/s. For clarity, the individual curves are shifted vertically by 4 pA. (b) TSC spectra of 50 $\Omega \cdot$ cm diode (06-71) for different bias voltages (V) during heating up and after annealing for 16 min at 80 °C. TSC parameters are the same as presented in (a).

in a fully depleted diode is given by:

$$I^e_{TSC}(T) = \frac{1}{2} \cdot q_0 \cdot A \cdot d \cdot e_n(T) \cdot n_t(T_0) \cdot f\,(T) \tag{6.6}$$

$$e_n = \sigma_n \cdot v_{th,n} \cdot N_C \cdot \exp\left(-\frac{E_a}{k_B T}\right) \tag{6.7}$$

$$e_p = \sigma_p \cdot v_{th,p} \cdot N_V \cdot \exp\left(-\frac{E_a}{k_B T}\right) \tag{6.8}$$

$$f(T) = \exp\left(-\frac{1}{\beta}\int_{T_0}^{T} (e_n(T') + e_p(T'))\, dT'\right) \tag{6.9}$$

where q_0 is the elementary charge, T the temperature, A the active area, d the fully depleted depth, e_n and e_p are the emission rate for electrons and holes. N_C and N_V are the density of states in the conduction band and valence band, respectively and are taken from [59]. The activation energy for electrons is $E_a = E_C$ - E_t and for holes $E_a = E_t$ - E_V, where E_t is energy level of the electrons or holes trap and $E_{C,V}$ the conduction and valence band edge, respectively. $\sigma_{n,p}$ are capture cross section for electrons and holes, $v_{th,n,p}$ are the thermal velocities for electrons and holes taken from [59]. k_B is the Boltzmann constant, $f(T)$ describes the fraction of defects occupied by electrons at temperature T, β is the heating rate and $n_t(T_0)$ is the density of defects that are filled with electrons at T_0.

In the investigated p-type diodes, the B_iO_i defect on which this study is focusing is detected in a TSC experiment only if electrons can be injected at low temperature. This is done by forward biasing the diodes at 10 K, by injecting both electrons and holes. In the hypothesis that equal amounts of electrons and holes are injected during the forward biasing the density of defects filled with electrons is given by [52]:

$$n_t(T_0) = N_t \frac{c_n}{c_n + c_p} \tag{6.10}$$

where c_n and c_p are capture coefficients for electrons and holes, respectively ($c_{n,p} = \sigma_{n,p}$ $v_{th,n,p}$). N_t is the total defect concentration in the bulk. For the B_iO_i defect the capture cross sections σ_n and σ_p had been measured [15], [22] and values of 1×10^{-14} cm^2 and 1×10^{-20} cm^2 were derived. Therefore σ_p and c_p can be neglected in Eq. 6.8, Eq. 6.9 and Eq. 6.10. Thus, the B_iO_i TSC signal can be approximated by:

$$I^e_{TSC}(T) = \frac{1}{2} \cdot q_0 \cdot A \cdot d \cdot e_n \cdot N_t \cdot f\,(T) \tag{6.11}$$

$$f(T) = \exp\left(-\frac{1}{\beta}\int_{T_0}^{T} e_n(T')\, dT'\right) \tag{6.12}$$

For coulombic trap centers like the B_iO_i the emission rate e_n is not anymore a constant quantity with respect to the applied bias voltage but becomes field dependent. The 3D

Poole-Frenkel effect in the emission rate e_n is given by [135, 136, 16]:

$$e_n^{pf} = e_{n,0}(T) \cdot \left[\left(\frac{1}{\gamma^2} \right) (e^{\gamma}(\gamma - 1) + 1) + \frac{1}{2} \right] \tag{6.13}$$

$e_{n,0}(T)$ denotes the field independent emission rate with the so-called zero field activation energy $E_a = E_{a,0}$ and $\gamma = (q_0|\vec{E}|/(\pi\varepsilon_0\varepsilon_r))^{\frac{1}{2}} q_0/(k_B T)$. $|\vec{E}|$ is the electric field in the sensor bulk and is position dependent. In this case the TSC current is given by:

$$I_{TSC} = \frac{1}{2} q_0 A w(V,T) N_t e_n^{pf} \exp\left(-\frac{1}{\beta} \int_{T_0}^{T} e_n^{pf}(T')\, dT' \right) \tag{6.14}$$

In this equation the position dependent electric field is not taken into account. As a first approximation the average value $\langle|\vec{E}|\rangle = V/w$ is applied.

If the diode is not fully depleted the value d has to be exchanged by the depleted width $w(V,T)$ which depends on the applied bias voltage V and temperature T. The temperature dependence of w is mainly neglected if the concentration of the trap is small compared to the overall space charge concentration in the T range of interest. Another effect influencing the peak shape is a possible cluster effect [106], [107] which leads to a dependence of the activation energy $E_a(T)$ on the trap occupation $f(T)$. For an attractive Coulomb interaction this results in:

$$E_a(T) = E_{a0} + (1 - f(T))\Delta E_a \tag{6.15}$$

The value of the energy shift ΔE_a depends on the density of charged traps inside the cluster. However the results of ΔE_a extracted from B_iO_i peak (see Table 6.3) indicate that the B_iO_i is a point defect.

6.4.2 Extracted Parameters for BiOi from TSC Measurements

In order to reproduce the TSC peak of the B_iO_i defect in all measured spectra of the irradiated diodes with different resistivities the data were fitted according to Eq. 6.14, taking the cluster effect (Eq. 6.15) into account. For the fitting procedures the temperature ranges of the B_iO_i TSC peak are chosen to T_{max} - 2 K and T_{max} + 4 K where T_{max} corresponds to the temperature at the maximum value of the TSC peak. There are 3 free parameters - zero field activation energy E_{a0}, cluster related energy shift ΔE_a and the defect concentration N_t - which are extracted from the fits. The $\sigma_n = 1 \times 10^{-14}$ cm^2, determined from the variation of DLTS capacitive transients with the filling pulse width, at constant temperature [22], was fixed in the fitting routine. The resulting parameters are summarized in Table 6.3 for three diodes with different resistivities and different annealing steps. It should be mentioned here that the low temperature tail of the B_iO_i peak could not be reproduced by the fitting routine, especially at higher bias voltages

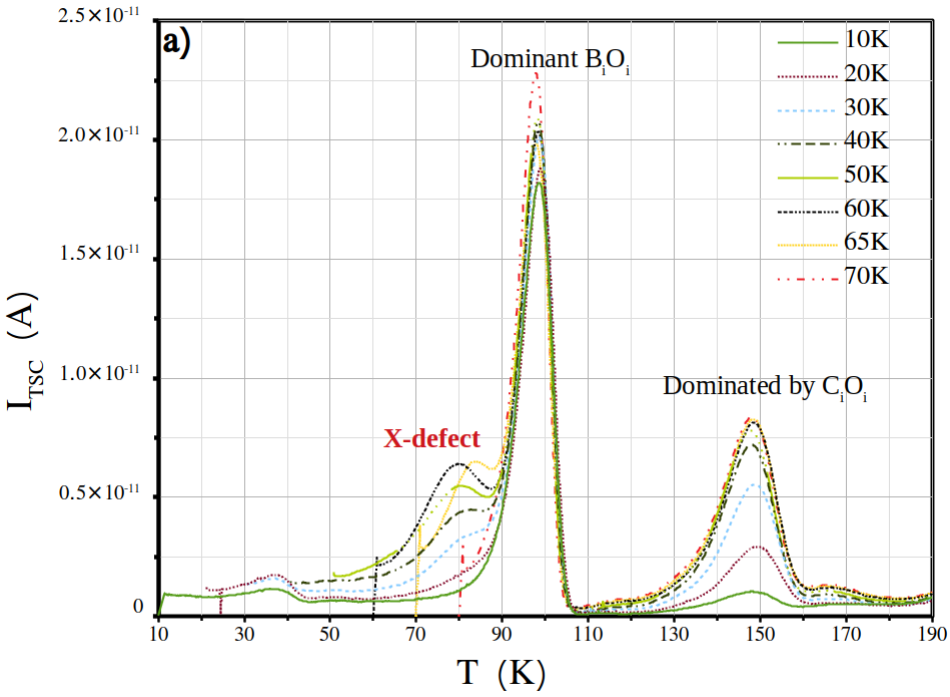

(a)

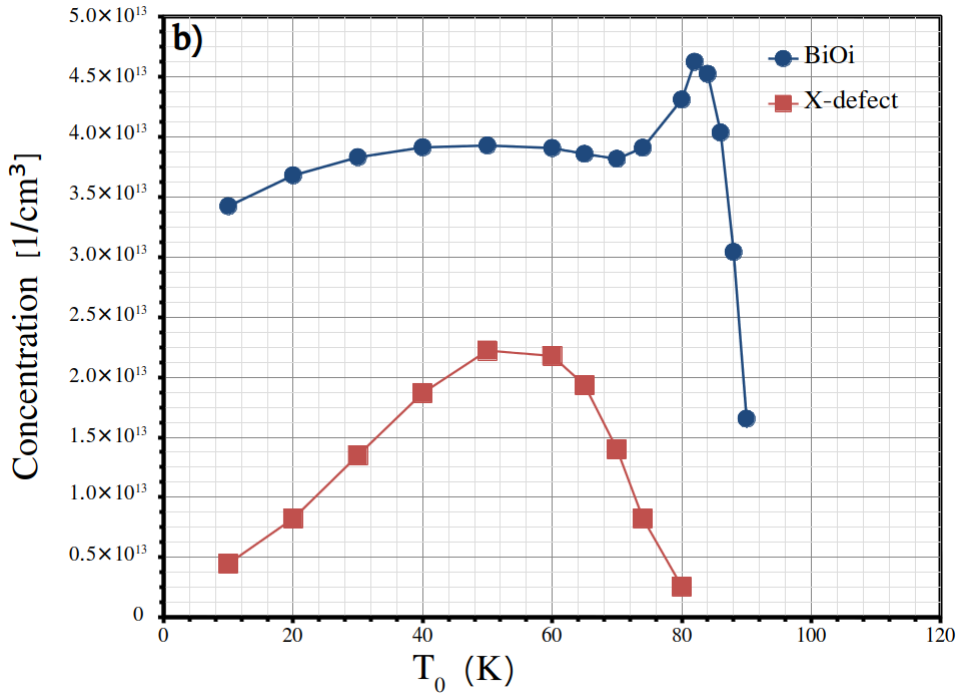

(b)

Figure 6.5: (a) TSC spectra for different T_0 of 50 $\Omega \cdot$ cm diode after 23 GeV proton irradiation. Annealing step t_{ann} = 30 min, T_{ann} = 80 °C. Experimental parameter of TSC: V_{fill} = 5 V, $V_{reverse}$ = 250 V. (b) Concentration of B_iO_i and X-defect versus filling temperature T_0 extracted from the TSC spectra shown above. The estimated errors in the determined concentration of B_iO_i defect are below 1%, and result from statistical errors of the data (noise, RMS: ± 0.02 pA), including the specified accuracy of the used current meter (1% of the reading) and of the temperature measurement (± 0.5 K).

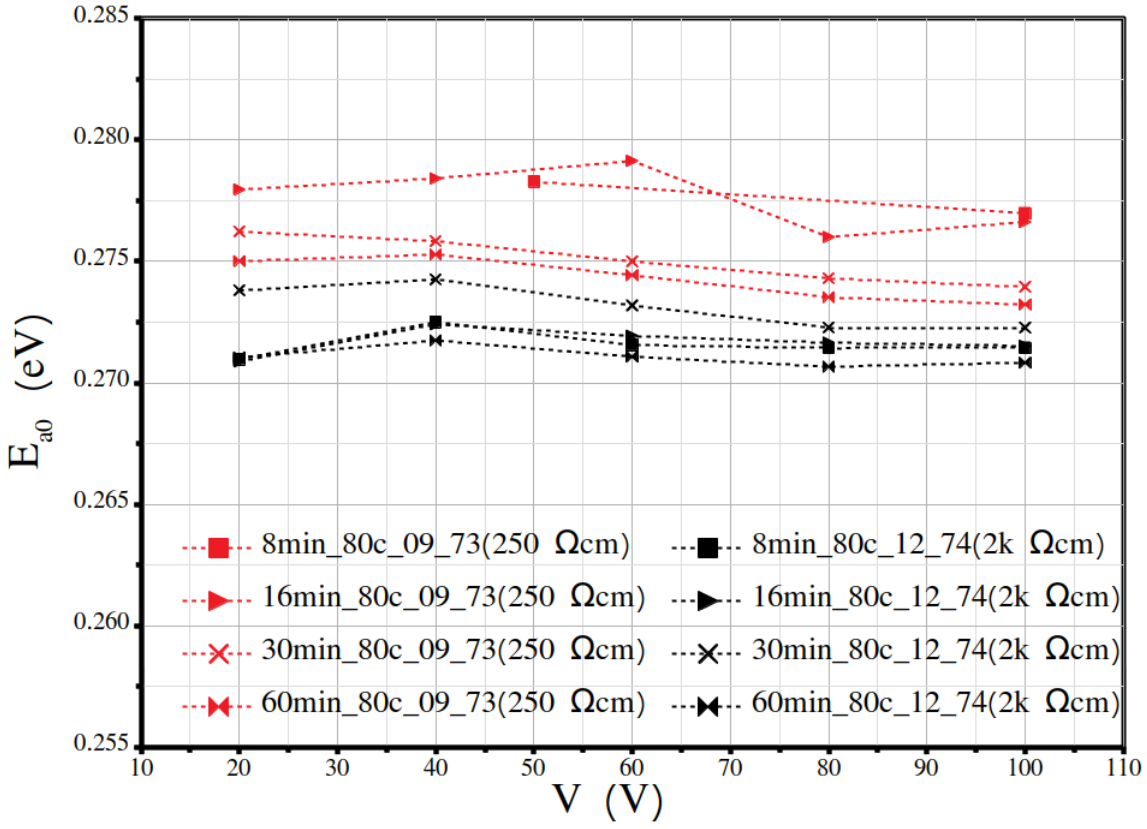

Figure 6.6: Zero field activation energy E_{a0} versus bias voltage of B_iO_i defect extracted from TSC spectra of the 250 $\Omega \cdot$ cm diodes (09-73) and 2 k$\Omega \cdot$ cm diodes (12-74) and all annealing steps at 80 °C.

(Fig. 6.4b). Therefore, it was supposed that in this temperature range a further unknown defect might be hidden. In order to clarify this problem TSC studies were performed by changing the filling temperature T_0 in the range 10 K - 70 K. From Fig. 6.5a it is obvious that indeed a defect (labeled as X-defect) is showing up in that region with increasing peak height for larger T_0. Specific studies on this defect resulted in the fact that it is a hole trap showing a strong Poole-Frenkel effect with a zero field energy level of $E_{a0} = E_t$ - $E_V \approx 0.21$ eV. Fig. 6.5b shows the concentration of the B_iO_i and the X-defect as function of T_0. While the B_iO_i concentration exhibits only a small increase with T_0 the change of the X-defect concentration is much stronger. More information about the X-defect can be found in additional material or [152].

The extracted zero field activation energies E_{a0} as function of the applied bias voltage are presented for the 250 $\Omega \cdot$ cm and 2 k$\Omega \cdot$ cm diode (09-73, 12-74) in Fig. 6.6 for the different isothermal annealing steps, respectively. The E_{a0} values presented in Table 6.3 show a dependent on the material resistivity and annealing step. This might be due to the different applied bias voltages for the different diodes leading to different electric field strength values which are highest in the 50 $\Omega \cdot$ cm one. Another effect could be caused by the X-defect which contributes partly to the B_iO_i signal, especially for the 50 $\Omega \cdot$ cm diode. A slight voltage dependence is observed as well as some changes with the annealing

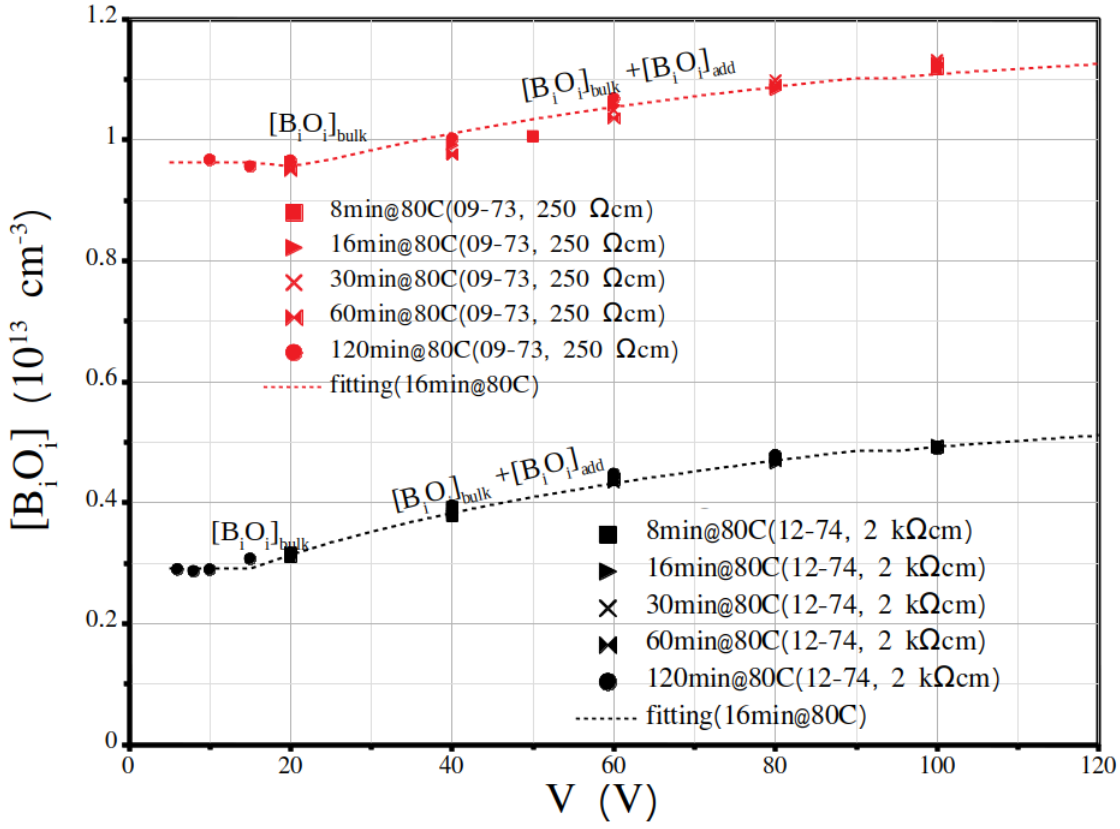

Figure 6.7: B_iO_i concentration as function of bias voltage (V) for the 250 $\Omega \cdot$ cm diode (09-73) and 2 k$\Omega \cdot$ cm diode (12-74) extracted from TSC spectra measured after annealing steps between 8 min and 120 min at 80 °C. The curves are the result of fits of Eq. 6.19 to the data. The parameters are presented in the text.

time. Further, it should be mentioned that the values given in Table 6.3 are mean values with respect to all results gained from the analysis of different bias voltages. The errors depend on fitting ranges. Both errors are based on the assumption that the temperature dependence of σ and w can be neglected.

Further, the unexpected increases of the B_iO_i concentration ($[B_iO_i]$) for bias voltages higher than the voltage for full depletion as shown in Fig. 6.7 for the 250 $\Omega \cdot$ cm and the 2 k$\Omega \cdot$ cm diode will be discussed. Here it is essential that the boron concentration near to the highly doped p^+ Cz substrate increase to very large values. But this transition from the epitaxial bulk material to the p^+ substrate is smooth due to the out-diffusion of boron from the Cz substrate into the epitaxial layer during the high temperature steps in the fabrication process. This leads to a small increase of the depletion depth for bias voltages larger than the voltage for full depletion as extracted from C–V measurements together with an increase of the substitutional boron concentration $[B_s]$. Assuming now a similar creation rate of the B_iO_i defect as described in section D which depends on the local boron concentration $[B_s]$ the increase of the B_iO_i concentration above full depletion can be qualitatively explained.

Considering a one-dimensional model for a diode, the B_iO_i concentration can be described by:

$$[B_iO_i](w(V)) = \frac{\int_0^{w(V)} [B_iO_i](x)dx}{w(V)} \tag{6.16}$$

where $w(V)$ is the voltage dependent depletion depth. Assuming that the B_iO_i defect is homogeneously distributed in the bulk of diode, the evaluated concentration of the corresponding TSC peak $[B_iO_i]_{TSC}$ can be separated into two terms, the concentration of the bulk ($[B_iO_i]_{bulk}$) and an additional component ($[B_iO_i]_{add}$) from the region above full depletion (the value extracted from C–V measurement), i.e. $(w(V > V_{fd}) > d)$:

$$[B_iO_i]_{TSC}(w(V)) = [B_iO_i]_{bulk} + [B_iO_i]_{add}(w(V)) \tag{6.17}$$

with

$$[B_iO_i]_{add}(w(V)) = \frac{\int_d^{w(V)} ([B_iO_i]'(x) - [B_iO_i]_{bulk})dx}{w(V)} \tag{6.18}$$

where $[B_iO_i]'$ is the concentration in the region above fully depletion. Here the effective doping concentration N_{eff}, assumed to be given by the local boron concentration $[B_s]$ is strongly increasing with bias (see Fig. 6.2b).

Taking both equations into account the increase of $[B_iO_i]_{add}$ can be estimated by:

$$\frac{\sum_{V_0=20V}^{V_{max}} ([\Phi_{eq} \cdot g_{B_iO_i}(N_{eff}(V)) - [B_iO_i]_{bulk}]\Delta w(V))}{w(V)} \tag{6.19}$$

where the $N_{eff}(V)$ are given by Eq. 6.4 and $w(V)$ by Eq. 6.5 the sums runs from $V_0 = 20$ V (near to full depletion voltage V_{fd}) up to $V_{max} = 100$ V in steps of 5 V. The $g_{B_iO_i}$ term represents the introduction rate of B_iO_i defect, defined by:

$$g(B_iO_i) = \frac{[B_iO_i]}{\Phi_{eq}} \tag{6.20}$$

where $[B_iO_i]$ is B_iO_i concentration after irradiation to Φ_{eq}. The mechanism of B_iO_i defect generation is described by the kinetic model of boron removal [86] which assume that the silicon interstitials (I) which escape from the primary displacement damage can react with substitutional boron (B_s) or carbon (C_s). In a so called Watkins replacement mechanism both atoms become themselves interstitials ($I + B_s \xrightarrow{k_{IB}} B_i$, $I + C_s \xrightarrow{k_{IC}} C_i$), migrate through the lattice and can further react with other impurities like oxygen O_i creating thus e.g. B_iO_i or C_iO_i. If all silicon interstitials (I) end up only in these two defects their concentration ratio $[C_iO_i]/[B_iO_i]$ should reflect the ratio $(k_{IC}/k_{IB}) \times [C_s]/[B_s]$, where the ratio of the capture coefficient of carbon k_{IC} and boron k_{IB} has been evaluated to be

$(k_{IC}/k_{IB}) \approx 1/7$ [21, 20]. Thus, the introduction rate of B_iO_i can be described by [86]:

$$g_{B_iO_i} \approx g_I \times \left(1 + \frac{k_{IC}[C_s]}{k_{IB}[B_s]}\right)^{-1} \tag{6.21}$$

In Fig. 6.7 the B_iO_i as function of bias voltage V near to and above full depletion is plotted for the 250 $\Omega \cdot$ cm and 2 k$\Omega \cdot$ cm diode (09-73, 12-74) including the different annealing steps. The presented curves are the result of fits of Eq. 6.19 to the measured data taken at the annealing step of 16 min at 80 °C.

The generation rate of interstitial silicon g_I, the substitutional carbon concentration $[C_s]$ and $[B_iO_i]_{bulk}$ are considered as free parameters in the fit of Eq. 6.19 to the data of both sensors (250 $\Omega \cdot$ cm and 2 k$\Omega \cdot$ cm). The resulting parameters of the fits are: $g_I = 6.28 \pm 0.5$ cm^{-1}, $[C_s] = (7.20 \pm 1) \times 10^{15}$ cm^{-3}, $[B_iO_i]_{bulk} = (2.91 \pm 0.1) \times 10^{12}$ cm^{-3} for 2 k$\Omega \cdot$ cm, and $g_I = 6.00 \pm 0.5$ cm^{-1}, $[C_s] = (1.21 \pm 0.1) \times 10^{16}$ cm^{-3}, $[B_iO_i]_{bulk} = (9.64 \pm 0.1) \times 10^{12}$ cm^{-3} for 250 $\Omega \cdot$ cm. These values are different. A possible reason might be that the studied transition region between the EPI and the highly doped Cz-material with the position dependent boron concentration $[B_s]$ behaves quite different compared to the EPI bulk material.

The $[B_iO_i]_{bulk}$ values extracted from TSC measurements at $V_{reverse} = 20$ V are included in Table 6.3 for both sensors.

Table 6.3: Properties of B_iO_i defect for isothermal annealing steps. ($E_{a0} \pm 1\% E_{a0}$ (eV), $N_t \pm 1\% N_t$ (10^{13} cm^{-3}). The errors were observed from different fitting ranges)

EPI 12-74	8min@80 °C	16min@80 °C	30min@80 °C	60min@80 °C
E_{a0} (eV)	0.272	0.272	0.273	0.271
ΔE_a (eV)	≈ 0	≈ 0	≈ 0	≈ 0
N_t (10^{13} cm^{-3})	0.31	0.31	0.32	0.32
EPI 09-73	8min@80 °C	16min@80 °C	30min@80 °C	60min@80 °C
E_{a0} (eV)	0.278	0.278	0.275	0.274
ΔE_a (eV)	≈ 0	≈ 0	≈ 0	≈ 0
N_t (10^{13} cm^{-3})	0.95	0.95	0.95	0.95
EPI 06-71	8min@80 °C	16min@80 °C	30min@80 °C	60min@80 °C
E_{a0} (eV)	0.288	0.289	0.283	0.282
ΔE_a (eV)	≤ 0	≤ 0	≤ 0	≤ 0
N_t (10^{13} cm^{-3})	3.2	3.2	3.2	3.2

6.4.3 Isochronal Annealing Behavior of B_iO_i

After the isothermal annealing at 80 °C for 180 min of the 50 $\Omega \cdot$ cm diode 06-71 an isochronal annealing study was performed. The procedure started at 100 °C with an annealing time of 15 min and continued in 10 °C steps up to 200 °C. *I–V* and *C–V*

measurements were recorded before the TSC measurements. While from the C–V characteristics the effective doping concentration N_{eff} was determined, the B_iO_i concentrations were evaluated from the TSC spectra for each annealing step. The resulting values are plotted in Fig. 6.8 versus the annealing temperature. The concentration of the B_iO_i is nearly constant with a value of about 3.3×10^{13} cm^{-3} up to 150 °C and start to anneal out at 160 °C decreasing to a value of 1.5×10^{12} cm^{-3} at 200 °C. On the other hand the effective space charge density N_{eff} stays nearly constant between 100 °C and 150 °C (1.01×10^{14} cm^{-3} to 1.1×10^{14} cm^{-3}) and increases for higher temperatures. Comparing the increase of N_{eff} with the decrease of the B_iO_i concentration ($[B_iO_i]$) one finds that a change of N_{eff} (ΔN_{eff}) is about two times the change of $[B_iO_i]$. This result indicates that the B_iO_i defect dissociates for T > 150 °C and all the resulted B_i goes back on substitutional sites, regaining the acceptor character of the boron dopant. More information can be gained from the isochronal annealing behaviour of defects. If a first order process is assumed for the annealing-out of a defect it can be described by:

$$N_{t,i} = N_{t,i-1}(T_{ann,i-1}) \times \exp\left(-k_i \Delta t\right) \tag{6.22}$$

where $N_{t,i}$ is the concentration of B_iO_i for the annealing step i, $N_{t,i-1}(T_{\text{ann},i-1})$ the concentration at step i-1 for the annealing temperature at this step and Δt the constant annealing time of 15 min. The frequency factors k_i are given by the Arrhenius relation:

$$k_i = k_0 \exp\left(-\frac{E_A}{k_B T_{\text{ann},i-1}}\right) \tag{6.23}$$

E_A is the activation energy for the annealing-out of B_iO_i and k_B the Boltzmann constant. Taking the B_iO_i concentrations for the different annealing temperatures larger than 150 °C, which are plotted in Fig. 6.8, the frequency factors k_i were evaluated according to Eq. 6.22. The Arrhenius plot k_i versus $1/(k_B T_{\text{ann},i-1})$ is shown in Fig. 6.9. From a linear fit to the data the activation energy E_A [eV] and the frequency factor k_0 [s^{-1}] were extracted resulting in:

$$E_A = 1.35 \pm 0.01 \text{ [eV]} ,$$
$$k_0 = (2.58 \pm 0.5) \times 10^{11} \text{ [s}^{-1}\text{]} .$$

The high value of k_0 factor indicates a dissociation process of the B_iO_i defect with an activation energy close to values from 1.35 eV to 1.40 eV presented in [15], [153, 154, 155]. The error of E_a and k_0 are the results of the estimated error of the k_i values ($\pm 1\% \cdot k_i$) in Eq. 6.23. The frequency factor k_0 depends on the content of boron, carbon and oxygen in the material. When the carbon concentration is relatively small then according to [154] the value of k_0 is determined by the ratio of the oxygen concentration to that one of boron ($[O]/[B]$). The larger this ratio is the less is the B_iO_i annealing rate due to re-trapping of

interstitial boron by oxygen. As seen from Fig. 6.9 this ratio is in the 50 $\Omega \cdot$ cm epitaxial material smaller compared to $[O]/[B] \approx 200$ observed in the material used by Makarenko [153] or Feklisova [155].

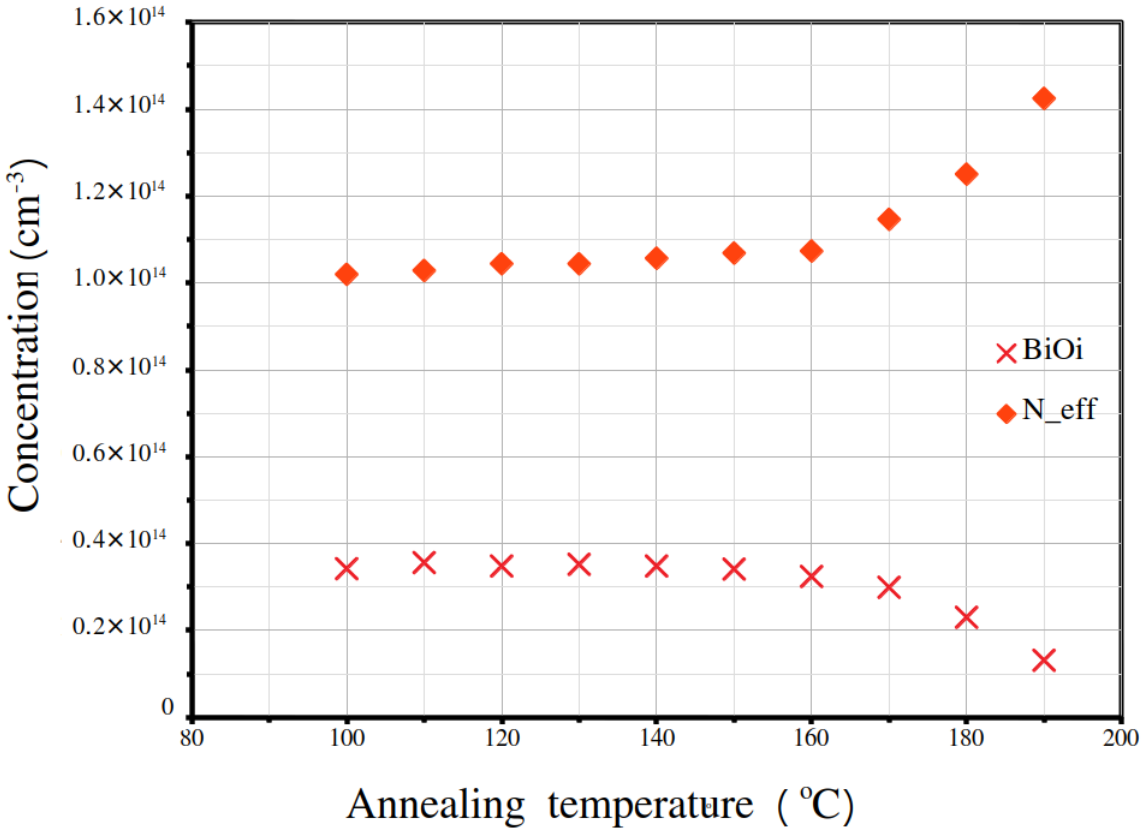

Figure 6.8: Dependence of the effective doping density N_{eff} and the B_iO_i defect concentration on the isochronal annealing temperature for the 50 $\Omega \cdot$ cm diode (06-71) after exposure to 4.3×10^{13} cm^{-2} 23 GeV protons. The errors are given in Table 6.3 and are given by the statistical errors of the data (noise, RMS: $\pm$ 0.02 pA) and the accuracy of the temperature measurement ($\pm$ 0.5 K).

6.4.4 Introduction Rate of BiOi

In Ref. [86] the acceptor removal effect in LGAD and HV-CMOS sensors as well as p-type diodes is parameterized with an exponential function including an acceptor removal coefficient c_A. For small fluence values and high initial boron doping diodes, the acceptor removal component can be approximated by:

$$N_{eff}(\Phi_{eq}) = N_{eff,0} \exp\left(-c_A \Phi_{eq}\right) \approx N_{eff,0} - g_B \Phi_{eq} \tag{6.24}$$

where $N_{\text{eff, 0}}$ is the initial doping concentration and $g_B = c_A \times N_{\text{eff,0}}$ the initial acceptor removal rate. In our case the acceptor removal rate has to be identified with the removal rate of electrically active boron and should be strongly correlated with the introduction rate of boron related defects, which can be extracted from TSC measurement by Eq. 6.20.

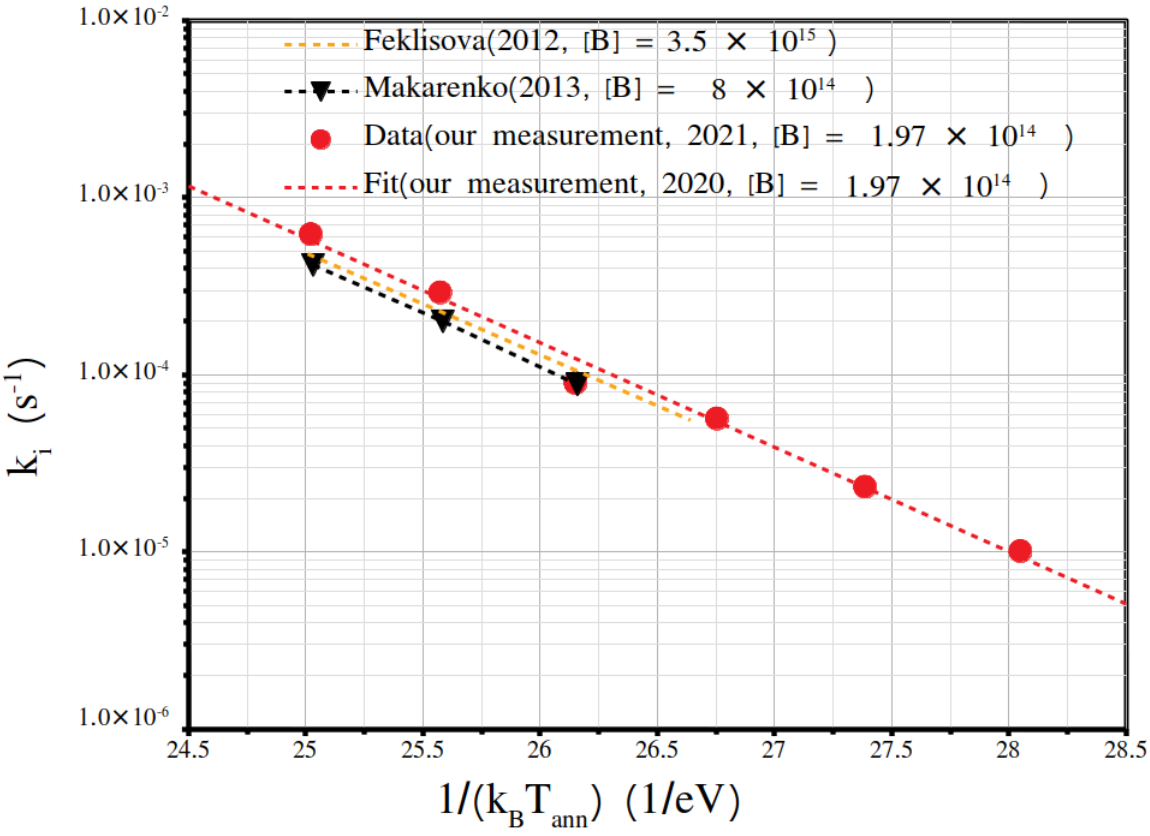

Figure 6.9: Arrhenius plot k_i versus $1/(k_B T)$. The k_i values were evaluated according to Eq. 6.22 for the temperature interval from 130 °C to 190 °C. For comparison the data of L. F. Makarenko et al. [153] derived from diodes with an initial doping of $[B] \approx 8 \times 10^{14}$ cm^{-3} and O. V. Feklisova et al. [155] evaluated from diodes with a doping of $[B] \approx 3.5 \times 10^{15}$ cm^{-3} are also presented in the figure.

The most likely created defect is the B_iO_i defect complex [86], [20] taking into account that in our silicon material the oxygen concentration is much larger compared to the carbon and boron content ($[O_i] \gg [C_s]$, $[B_s]$). The introduction rate of the B_iO_i defect is plotted in Fig. 6.10 as function of the initial doping concentration $N_{A,\,0}$. Included in the figure are the introduction rates reported previously on EPI silicon by employing TSC measurements [156] and DLTS experiments [22], [157], [158], all calculated by accounting Φ_{eq} (hardness factor of 0.62 for 23 GeV protons and of 0.0398 for 6 MeV electrons). It can be observed that all TSC results, although are in very good agreement with each other, give systematically lower values for the introduction rate of B_iO_i defect than the DLTS results. This is an expected result considering that previous experiments have shown that the introduction rates start to decrease with increasing Φ_{eq} above 10^{12} cm^{-2} [22] which is the case for the presented TSC results. The depicted experimental data show also that, among the different irradiating particles, the 6 MeV electrons lead to the highest introduction rate of B_iO_i defect, a result in agreement with the already known behaviour that low energy charged particles induce the formation of more point defects than the hadrons [18]. The observed increase with $N_{eff,\,0}$ is expected according to the

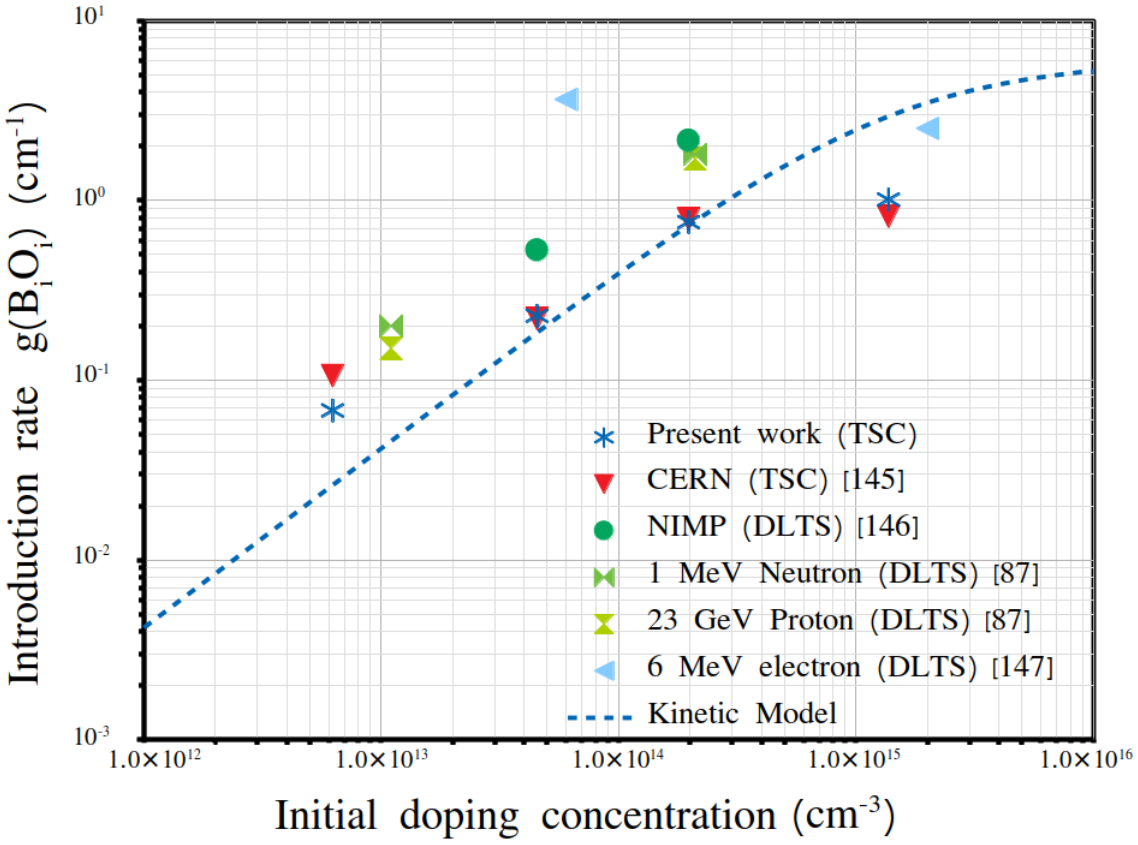

Figure 6.10: Development of the B_iO_i introduction rate $g_{B_iO_i}$ as function of the initial doping density $N_{\text{eff},0}$. Our introduction rates in the plot are mean values taken from all isothermal annealing steps and the fluence value of 4.3×10^{13} cm^{-2} 23 GeV protons. Included are data of the other team members and from the literature, accounting for the hardness factors of the irradiation particle (see text). The dashed line represents the defect kinetic model calculation according to Eq. 6.21 with parameters given in the text. The uncertainty in the introduction rates resulted from this study is dominated by the uncertainty of the fluence, which is of 7% for the irradiation facility at CERN.

initial acceptor removal rate g_B (see above) but at higher $N_{\text{eff},0}$ a saturation occurs. Such a behaviour can be explained with the help of a simplified defect kinetics model [86], [21].

The dashed line in Fig. 6.10 represents the prediction of the kinetic model based on Eq. 6.21 and accounting for the average values of the g_I and C_s determined in section B for our EPI diodes of 250 $\Omega \cdot$ cm and 2 k$\Omega \cdot$ cm resistivity, of $g_I = 6.14$ cm^{-1} and $[C_s] = 0.95 \times 10^{16}$ cm^{-3}. Compared with the kinetic model presented in [86] which accounts for $g_I = 1 - 3$ cm^{-1} obtained for high resistivity Cz material [108], our g_I value, determined for EPI material, is 2-3 times larger. As can be seen from Fig. 6.10 the predicted introduction rate increases with the initial doping concentration nearly linear up to about 3×10^{14} cm^{-3} and tends to saturation above some 1×10^{16} cm^{-3}. Why the generation rate for LGAD sensors which are much larger than expected by this model cannot be explained so far [2], [3].

6.5 Conclusion

The boron-oxygen defect B_iO_i has been investigated in p-type epitaxial silicon diodes with different resistivities and exposed to 23 GeV protons. For all diodes isothermal annealing studies at 80 °C had been performed up to 120 min and for a 50 $\Omega \cdot$ cm diode an isochronal annealing followed in order to get information on the annealing-out of the B_iO_i. The macroscopic properties (current related damage parameter $\alpha(T_{\text{ann}}, t_{\text{ann}})$ and N_{eff}) were obtained from I–V and C–V measurements. The α-values decrease with the annealing time as expected and the change of N_{eff} is quite small which correlates with the nearly constant concentration of the B_iO_i defect. The properties of the B_iO_i defect were studied by TSC measurements for different trap filling procedures (different T_0) and bias voltages during the heating up period. The observed temperature shift of the B_iO_i peak for different bias voltages is a clear indication for the so-called Poole-Frenkel effect. From a detailed analysis of the B_iO_i TSC signal the defect parameter for the zero field activation energy E_{a0}, defect concentration N_t and energy shift ΔE_a due to clustering were extracted which are summarized in Table 6.3. These results for the different isothermal annealing steps show that the activation energy slightly depends on the initial doping and ΔE_a is very small between 0-3 meV. But the concentration extracted from diodes irradiated to the same fluence depends strongly on the initial doping. Isochronal annealing studies were performed for one 50 $\Omega \cdot$ cm diode irradiated to a fluence of $\Phi_{\text{eq}} = 4.3 \times 10^{13}$ cm^{-2}. The concentration of B_iO_i (N_t) versus annealing temperature from TSC was used to determine the activation energy for annealing-out of the B_iO_i being $E_A = 1.35$ eV and a frequency factor of $k_0 = 2.58 \times 10^{11}$ s^{-1} was derived. On the other hand the increase of N_{eff} at temperatures above 150 °C correlates with the annealing-out of B_iO_i where the change of N_{eff} is about two times the change of B_iO_i, indicating that all the B_i resulted from the dissociation of the B_iO_i donor defect goes back on substitutional sites, regaining the acceptor character of the boron dopant. Finally, the generation rate of B_iO_i ($g_{B_iO_i}(N_{\text{eff, 0}})$) is presented together with data of other groups and compared with a defect kinetics model [86], [21]. It is shown that $g_{B_iO_i}$ increases with the initial doping up to some 1×10^{14} cm^{-3} and tends to saturation for higher values.

It should be mentioned that the acceptor removal coefficient c_A (see Eq. 6.24) evaluated from our B_iO_i introduction rates are comparable with data derived from irradiated p-type sensors including HV-CMOS devices in a wide range of initial doping densities (see for example reference [86] and cited literature therein). But the scattering of the data is quite large despite the known difference between proton and neutron irradiated devices. On the other hand macroscopic and first microscopic studies on radiation damaged LGADs had resulted in much larger generation rates for boron related defects compared to our results obtained for epitaxial material [2], [3], [86]. This problem has to be investigated in further experiments.

6.6 Additional Materials

6.6.1 *I–V*, *C–V*

The *I-V* and *C-V* characteristics for the diodes presented in Table 6.1 after isothermal annealing are shown in Fig. 6.11 and Fig. 6.12, respectively. The current before irradiation was approximately 1×10^{-11} A, and all curves are plotted using log-log scales.

In Fig. 6.11, the slight changes in V_{fd} and the decrease in leakage current with t_{ann} at 80 °C can be observed. In Fig. 6.12, the *C–V* curves for all diodes, except for EPI 12-74, are identical. This is because N_{eff} was dominated by $[\mathrm{B_s}]$ and $[\mathrm{B_iO_i}]$, which are stable at 80 °C.

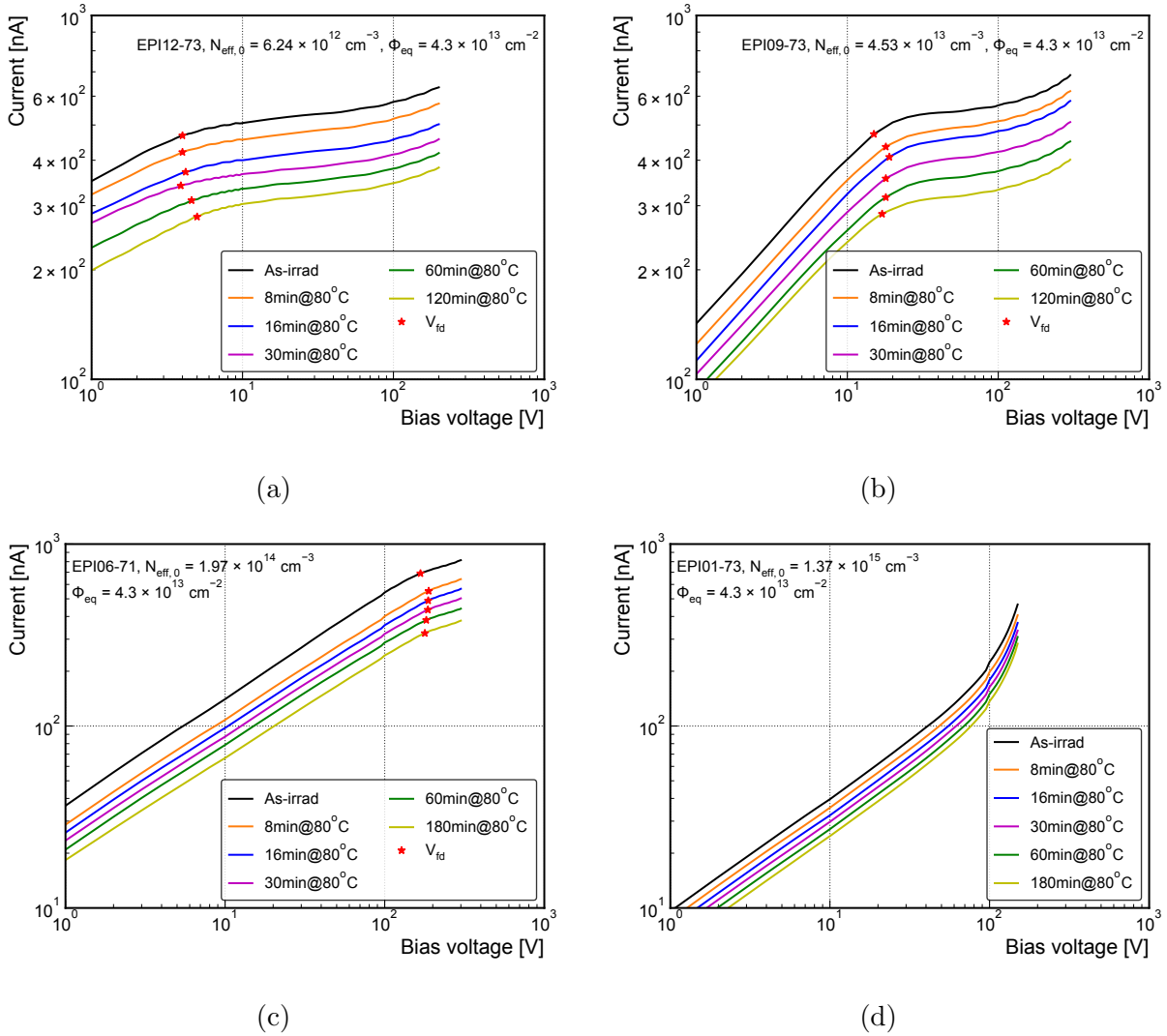

Figure 6.11: Current-voltage characteristics for 4 diodes with different initial resistivity irradiated with the same Φ_{eq} of 4.3×10^{13} cm^{-2}, and after different annealing steps at 80 °C. (a) 12-74 - 2 k$\Omega \cdot$cm, (b) 09-73 - 250 $\Omega \cdot$cm, (c) 06-71 - 50 $\Omega \cdot$cm and (d) 01-73 - 10 $\Omega \cdot$cm. The red asterisks indicate the full depletion voltages at which the current related damage parameter α is determined. Measurement condition: $T = 20$ °C, humidity $\leq 10\%$.

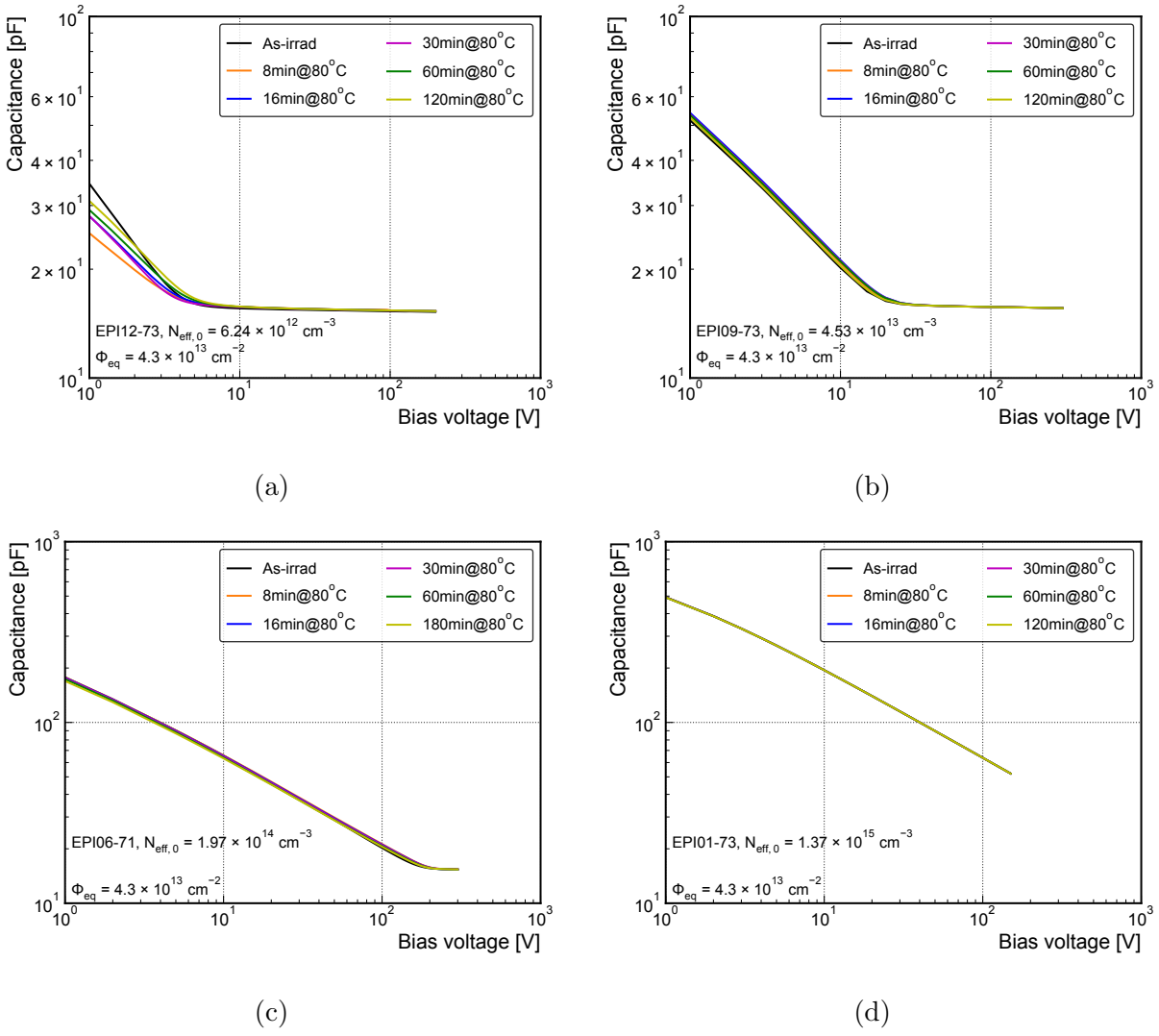

Figure 6.12: C-V characteristics for 4 diodes with different initial resistivity irradiated with the same Φ_{eq} of 4.3×10^{13} cm^{-2}, and after different annealing steps at 80 °C. (a) 12-74 - 2 k$\Omega \cdot$ cm, (b) 09-73 - 250 $\Omega \cdot$ cm, (c) 06-71 - 50 $\Omega \cdot$ cm and (d) 01-73 - 10 $\Omega \cdot$ cm. Measurement condition: $T = 20\,°\text{C}$, freq = 10 kHz, humidity $\leq 10\%$, $V_{AC} = 0.5$ V.

Figures 6.13 and 6.14 show the I-V and C-V characteristics for other diodes after isochronal annealing (steps see section 6.2). In Fig. 6.13, it can be observed that the current decreases as T_{ann} increases. Fig. 6.13a and Fig. 6.13b show that V_{fd} continuously increases with increasing T_{ann} and similar behaviour can be found in Fig. 6.14a and Fig. 6.14. This behaviour indicates that the space charge density (N_{eff}) of EPI 12-74 and 09-73 after irradiated with 23 GeV protons with a fluence Φ_{eq} of $4.3 \times 10^{13}\text{cm}^{-2}$, of these diodes are not only dominated by [B_s] and [B_iO_i] but also affected by other defects, such as E30K, H40K, and H140K+H152K. Changes in N_{eff} for EPI 06-71 are described in section 6.4.3. The breakdown voltage shows a decrease with increasing T_{ann} in Fig. 6.13d, which is due to the increase in N_{eff}, leading to the enhancement of the electric field at the same bias voltage.

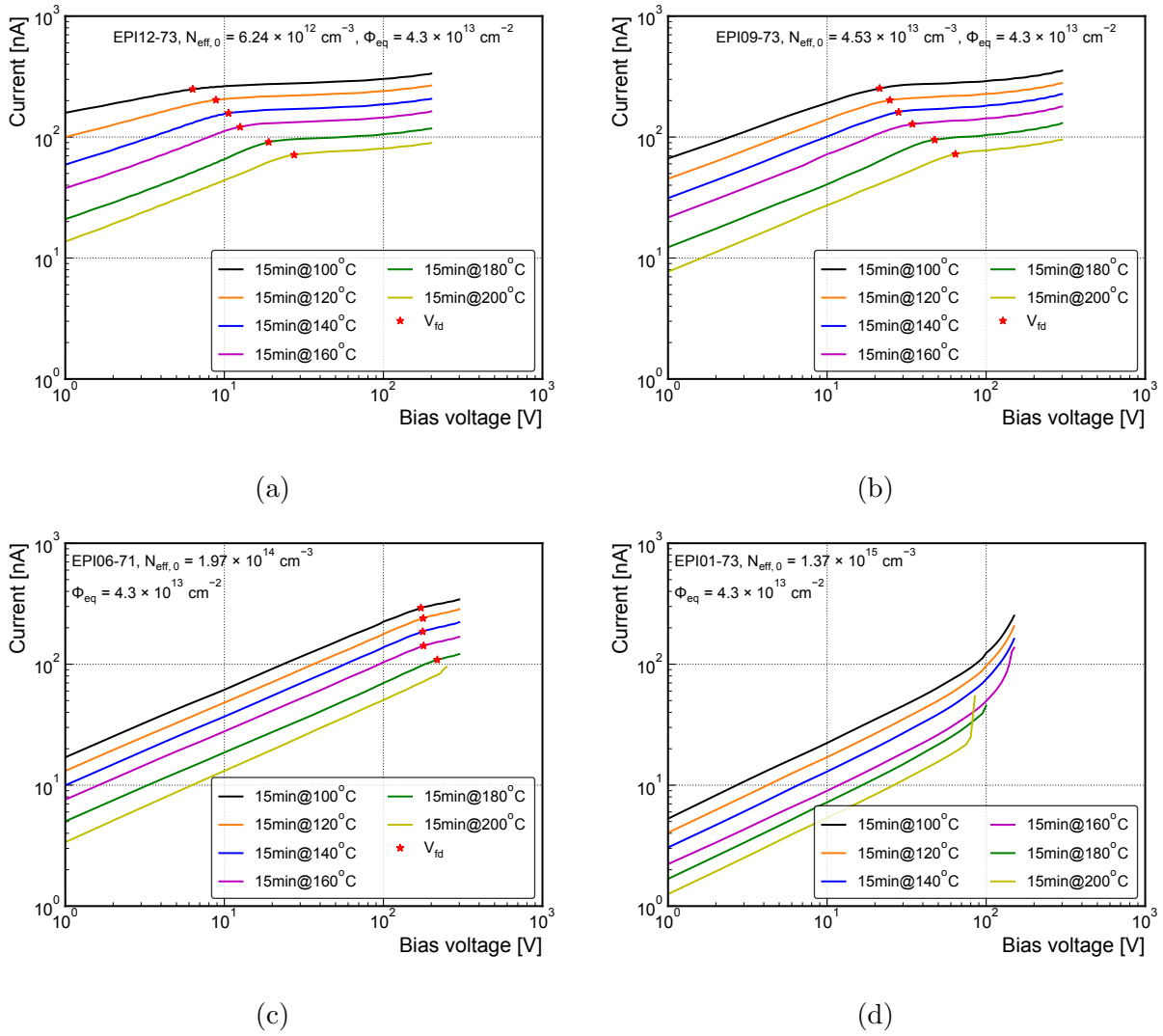

Figure 6.13: Current-voltage characteristics for 4 diodes with different initial resistivity irradiated with the same Φ_{eq} of 4.3×10^{13} cm^{-2}, and after different steps of isochronal annealing from 100 °C to 200 °C. (a) 12-74 - 2 k$\Omega \cdot$ cm, (b) 09-73 - 250 $\Omega \cdot$ cm, (c) 06-71 - 50 $\Omega \cdot$ cm and (d) 01-73 - 10 $\Omega \cdot$ cm. The red asterisks indicate the full depletion voltages extracted from Fig. 6.14. Measurement condition: $T = 20\,^{\circ}\text{C}$, humidity $\leq 10\%$.

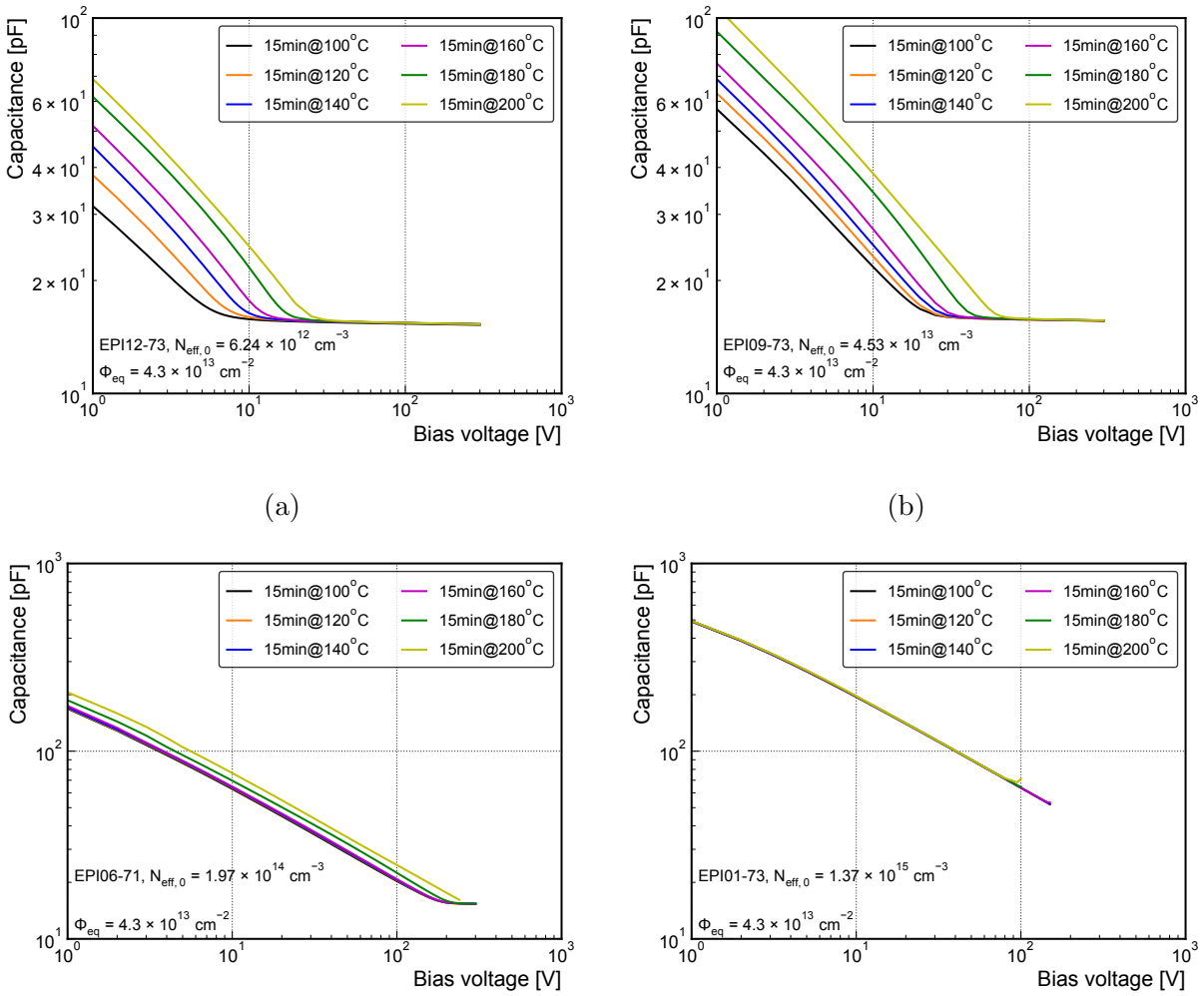

Figure 6.14: C-V characteristics for 4 diodes with different initial resistivity irradiated with the same Φ_{eq} of 4.3×10^{13} cm^{-2}, and after different steps of isochronal annealing from 100 °C to 200 °C. (a) 12-74 - 2 k$\Omega \cdot$ cm, (b) 09-73 - 250 $\Omega \cdot$ cm, (c) 06-71 - 50 $\Omega \cdot$ cm and (d) 01-73 - 10 $\Omega \cdot$ cm. Measurement condition: $T = 20\,°\text{C}$, freq = 10 kHz, humidity $\leq 10\%$, $V_{AC} = 0.5$ V.

6.6.2 Frequency Dependent C–V for EPI 12-74

The capacitance-voltage (C-V) measurements of EPI 12-74 diodes exhibited a frequency dependence (see section 6.3). To investigate this effect, C-V curves were measured at different frequencies after various annealing steps, and the results are shown in Fig. 6.15. It can be observed from Fig. 6.15 that the capacitance-frequency dependence decreases with increasing annealing temperature, indicating that the capacitance becomes less sensitive to the measurement frequency after annealing. Possible reasons for this effect include:

1. The decrease in resistivity due to increasing N_{eff} [65].
2. The effect of surface states, which is discussed in section 8.

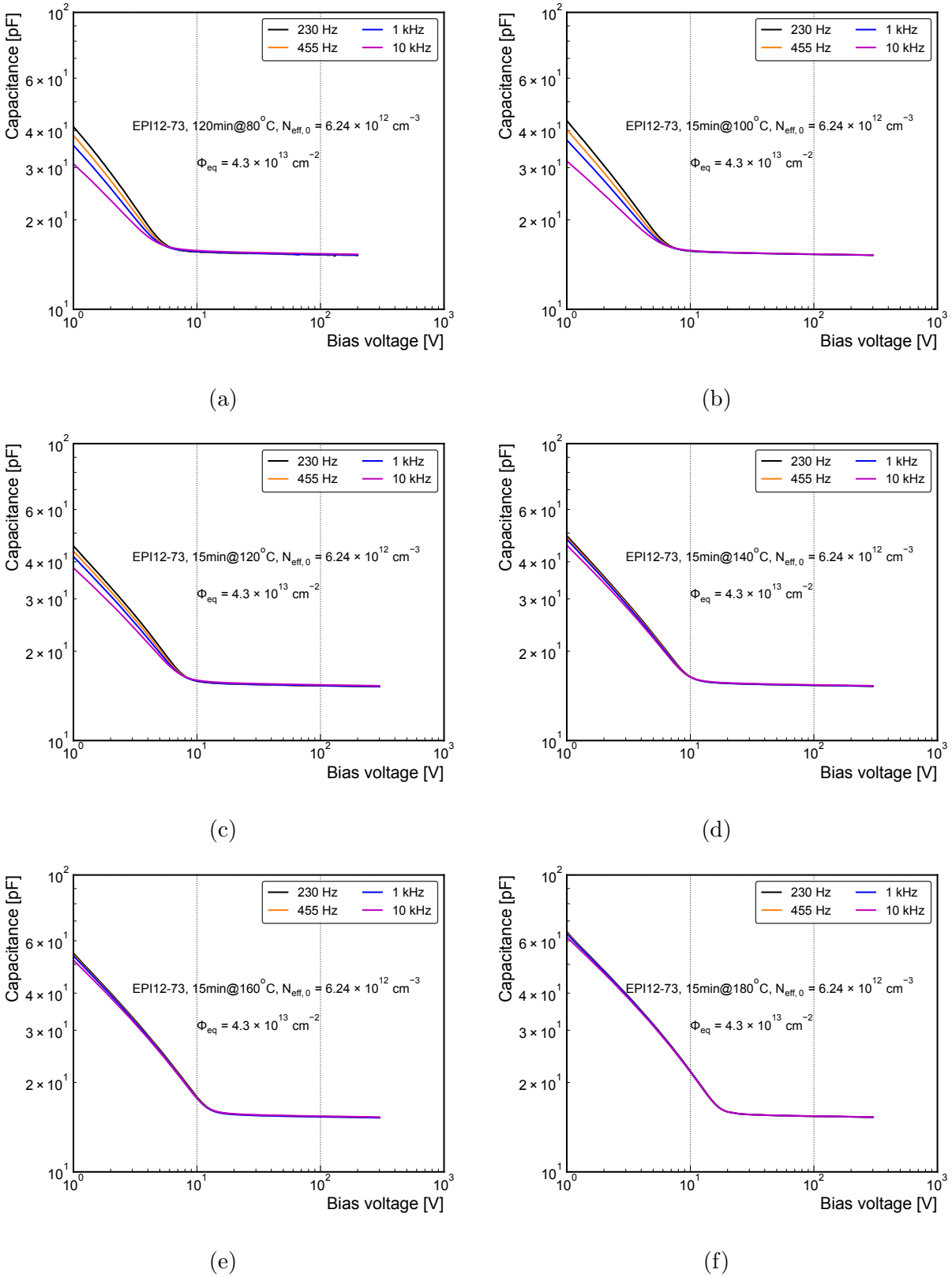

Figure 6.15: *C-V* characteristics with different frequencies (230 Hz, 455 Hz, 1 kHz and 10 kHz) measured on EPI 12-74 irradiated with $\Phi_{eq} = 4.3 \times 10^{13}$ cm^{-2}, and after different annealing steps: (a) After 120 min at 80 °C. (b) After 15 min at 100 °C. (c) After 15 min at 120 °C. (d) After 15 min at 140 °C. (e) After 15 min at 160 °C. (f) After 15 min at 180 °C. Measurement conditions can be found in Fig. 6.11 and Fig. 6.13.

6.6.3 TSC Measurements

TSC Measurements with Different V_{bias} and T_{fill}

Figure 6.16 shows the TSC spectra for diodes with varying resistivities and T_{fill}. It's interesting to note that, apart from the B_iO_i peak, all other peaks increase with an increase in T_{fill}. For a more detailed analysis of the changes in peak amplitude with T_{fill}, please refer to section 5.2.2. Moreover, the $[B_iO_i]$ increases while the others decrease with an increase in $[B_s]$ (approximately $N_{\text{eff},0}$).

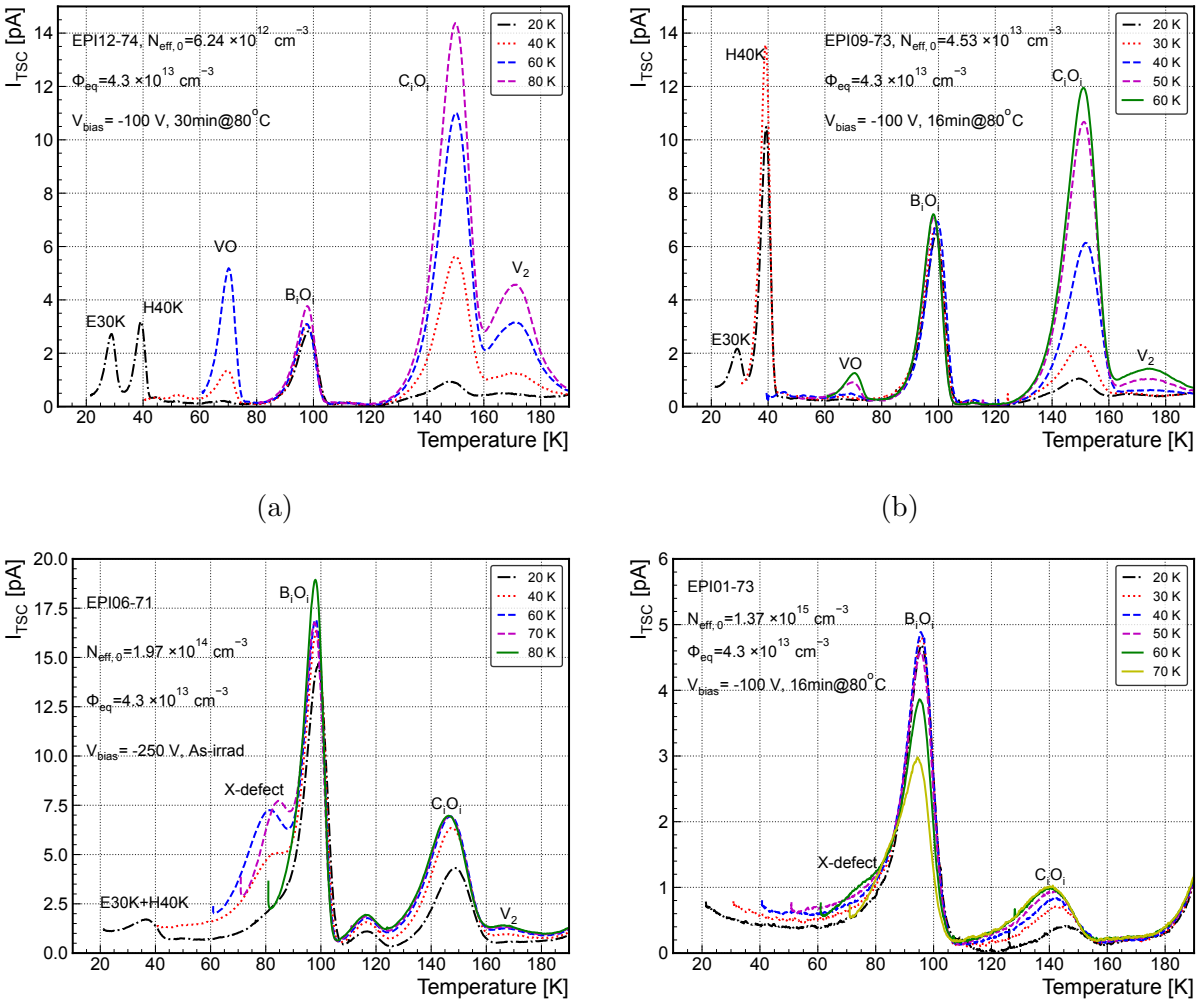

Figure 6.16: TSC spectra for different T_{fill} of (a) 2 k$\Omega \cdot$cm, (b) 250 $\Omega \cdot$cm, (c) 50 $\Omega \cdot$cm and (d) 10 $\Omega \cdot$cm diodes after 23 GeV proton irradiation with fluence value $\Phi_{\text{eq}} = 4.3 \times 10^{13}$ cm^{-2}. Annealing steps can be found in the figures. Experimental parameter of TSC: forward bias filling with $I_{\text{fill}} = 1$ mA. V_{bias} and T_{fill} are indicated in the figures.

Figure 6.17 shows TSC spectra for diodes with varying resistivities and V_{bias}. Figure 6.17a-6.17d were measured with forward bias injection $I_{\text{fill}} = 1$ mA and different V_{bias} values as indicated in the legend. Figure 6.17e and Fig. 6.17f were measured with majority

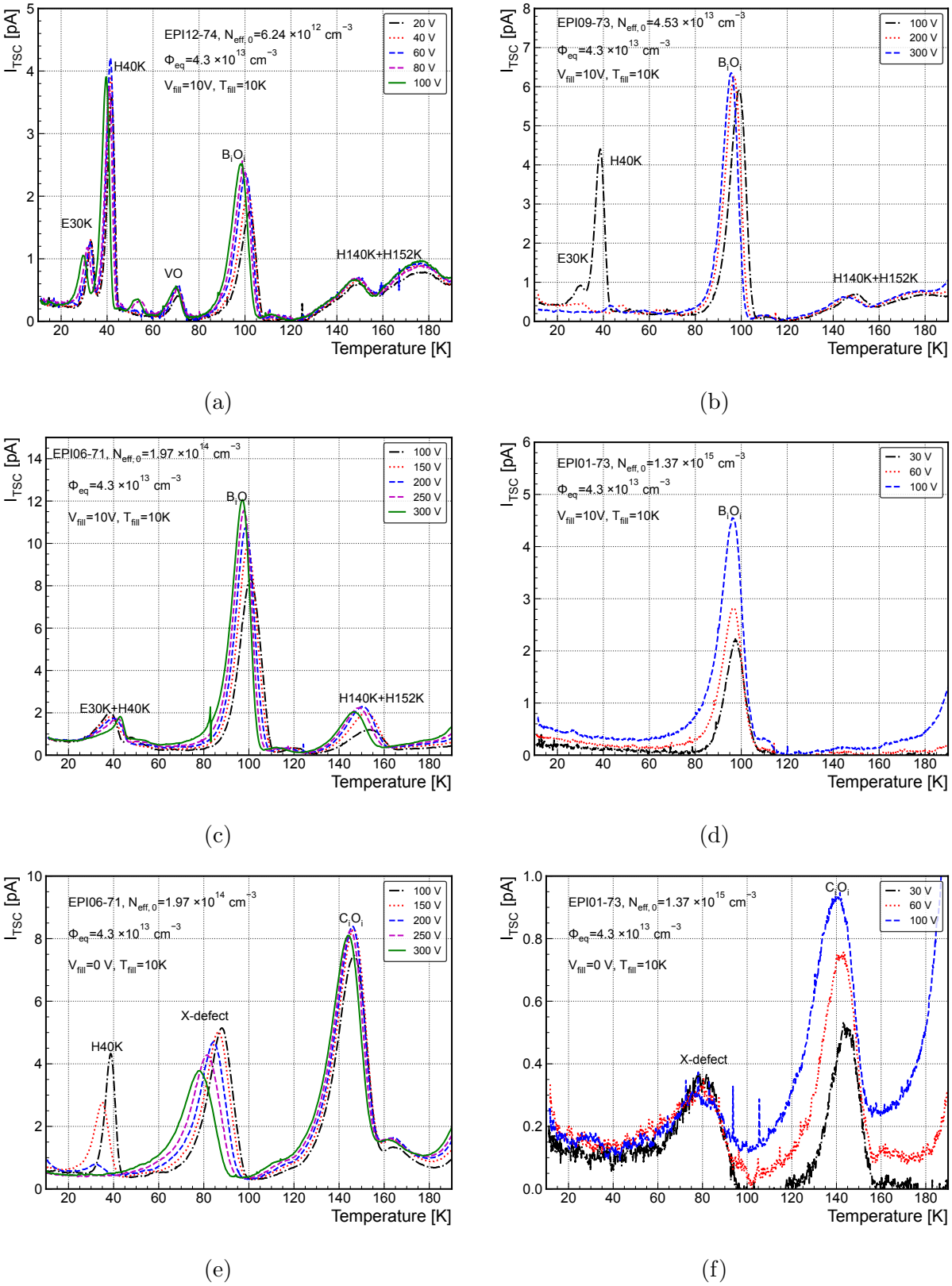

Figure 6.17: (a) (b), (c) and (d) are the TSC spectra with forward bias filling ($I_{\text{fill}} = 1$ mA) different V_{bias} indicated in the legend (Absolute value) for diodes EPI 12-74, EPI 09-73, EPI 06-71 and EPI 01-73. EPI 06-74, respectively. (e) and (f) are TSC spectra with majority carriers filling ($V_{\text{fill}} = 0$ V) and different V_{bias} indicated in the legend (Absolute value) for diodes EPI 06-71, EPI 01-73. TSC parameters: T_{fill}=10 K, others can be found in the figures.

carrier injection, with $V_{\text{fill}} = 0$ V and different V_{bias} values as indicated in the legend.

TSC Spectra for Isothermal Annealing

In Fig. 6.18, the TSC spectra with $T_{\text{fill}} = 10$ K measured on the diodes after isothermal steps are presented. As can be seen, only the TSC spectra of E30K and H40K show changes with t_{ann}. Compared to the results presented in Fig. 6.11, the changes in N_{eff} (or V_{fd}) of high resistivity materials (i.e., EPI 12-74 and EPI 09-73) are most likely caused by the E30K and H40K defects.

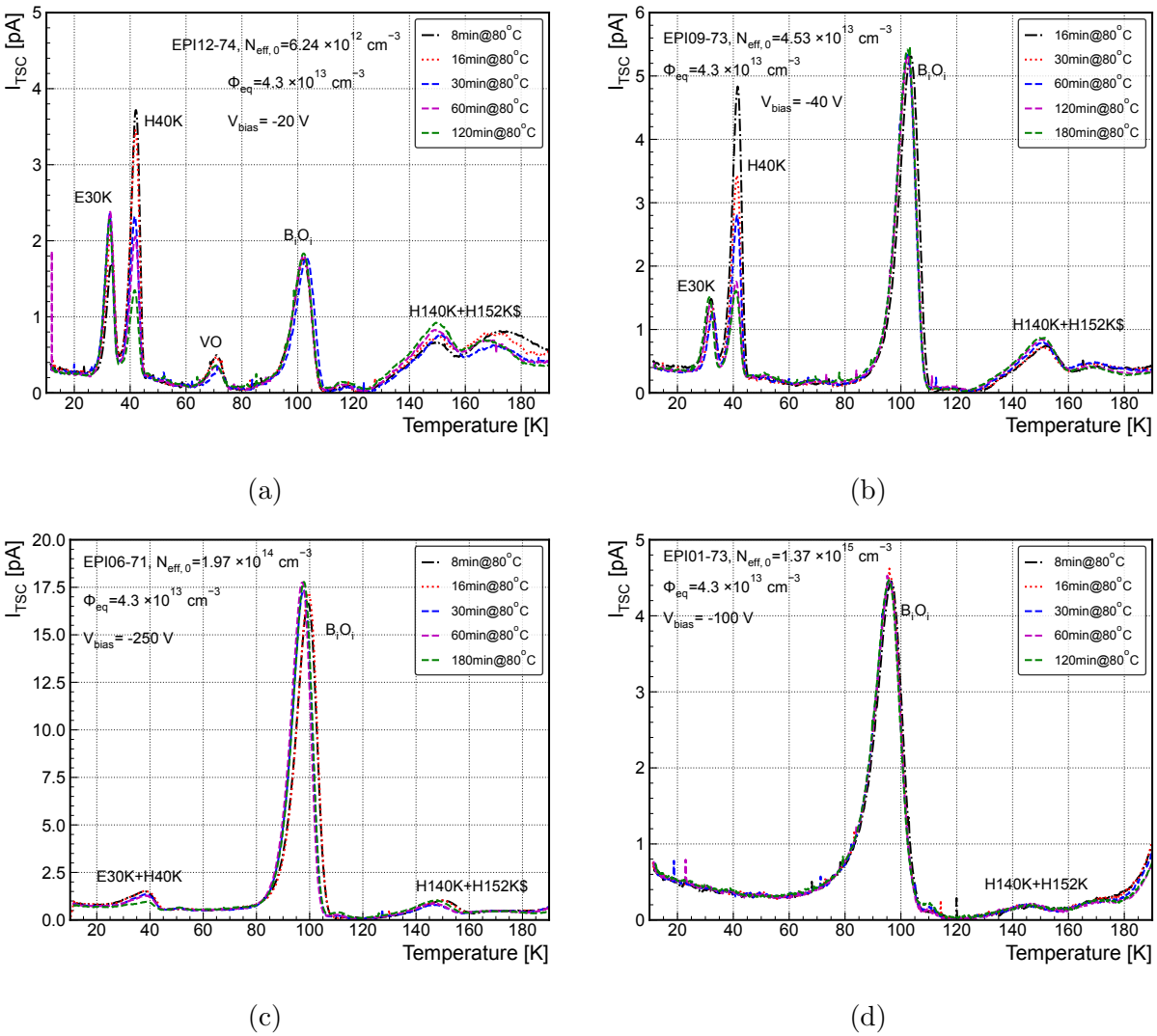

Figure 6.18: TSC spectra for (a) 2 kΩ · cm, (b) 250 Ω · cm, (c) 50 Ω · cm and (d) 10 Ω · cm diodes after 23 GeV proton irradiation with the same fluence value indicated in the figure, and after different isothermal annealing steps. Annealing steps can be found in the legend. Experimental parameter of TSC: forward bias filling with $I_{\text{fill}} = 1$ mA, $T_{\text{fill}} = 10$ K and V_{bias} indicated in the figure.

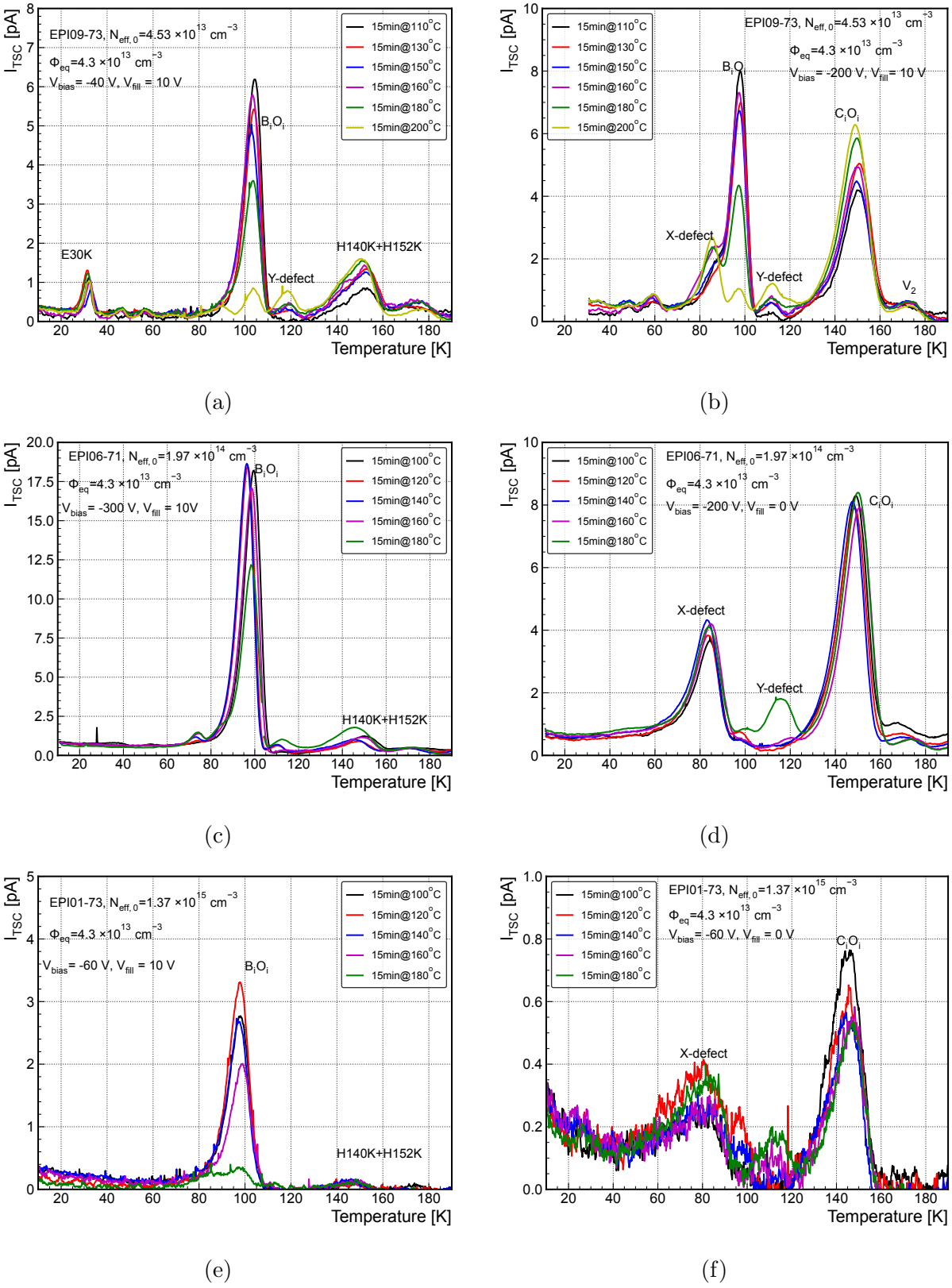

Figure 6.19: TSC spectra for the diodes after different isochronal annealing steps indicated in the figure. (a) and (b) are TSC with forward bias filling at $T_{\text{fill}} = 10$ K and 30 K, respectively. Both are measured on EPI 09-73. (c) and (d) are TSC with $V_{\text{fill}} = 10$ V and 0 V at $T_{\text{fill}} = 10$ K. Both are measured on EPI 06-71. (c) and (d) are TSC with $V_{\text{fill}} = 10$ V and 0 V at $T_{\text{fill}} = 10$ K. Both are measured on EPI 01-73.

TSC Spectra for Isochronal Annealing

The TSC spectra measured after isochronal annealing are presented in Fig. 6.19. As can be seen here, the B_iO_i peak decreases when $T_{ann} > 160\,°C$ for the measured diodes. The C_iO_i peak in the TSC spectra with $T_{fill} = 100\,°C$ shows stability for different T_{ann}. The X-defect is stable with T_{ann} up to 180 °C. In Fig. 6.19a and Fig. 6.19b, the E30K peak remains stable with isochronal annealing up to 200 °C.

Concentration of Different Defects in Different Diodes

The defect concentration as a function of T_{ann} is summarized in Fig. 6.20. The $[B_iO_i]$ and N_{eff} for EPI 06-71 can be found in Fig. 6.8.

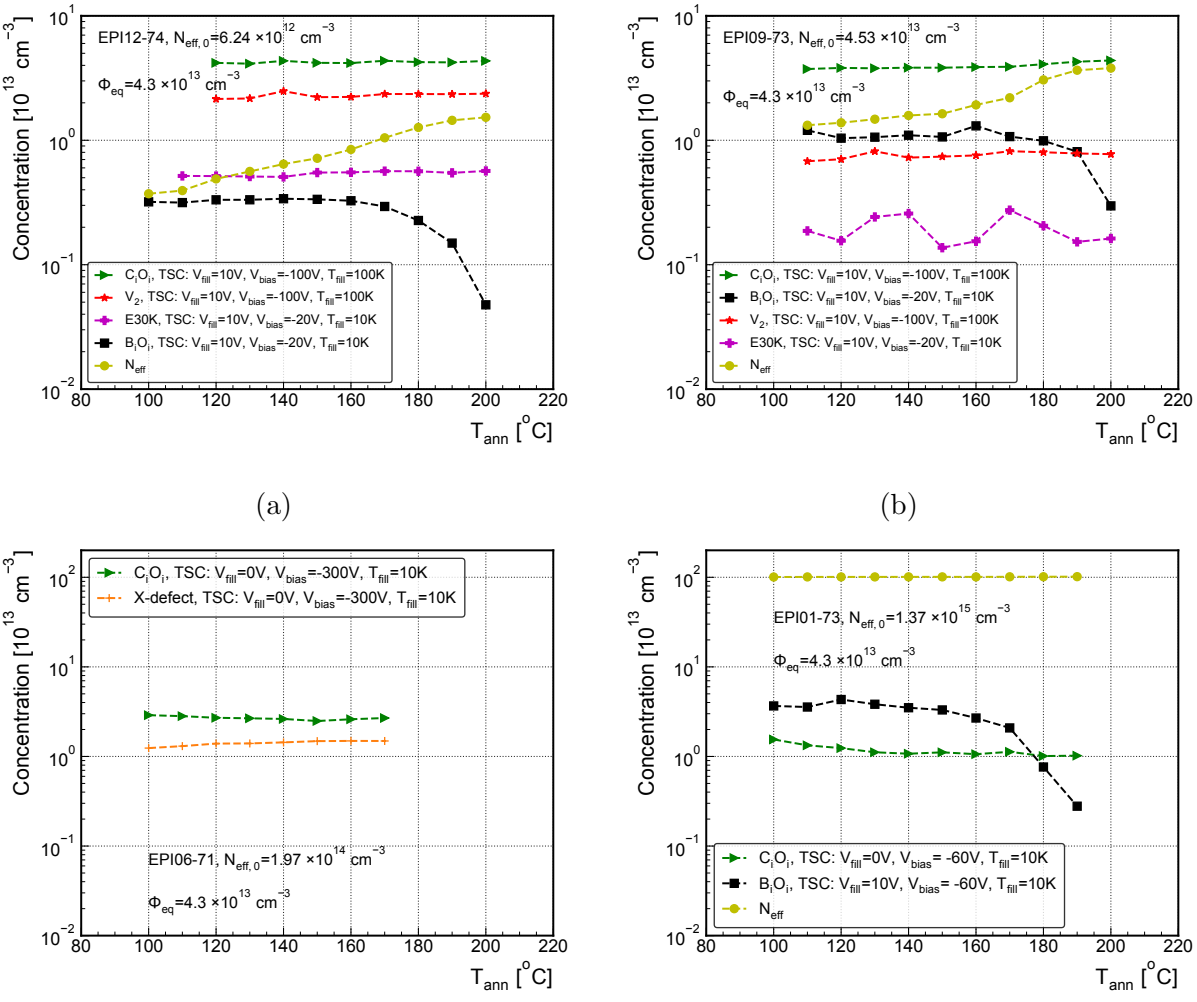

Figure 6.20: Defect concentration extracted from TSC spectra measured on the (a) EPI 12-74, (b) EPI 09-73, (c) EPI 06-71 and (d) EPI 01-73 after different isochronal annealing steps are presented. The parameters of TSC measurement are shown in the legend.

6.6.4 TS-Cap Measurements

The TS-Cap measurements were conducted on two low-resistivity diodes, namely EPI 06-72 (see Table 1) and EPI 01-73. The measurements were performed at different bias voltages (V_{bias}), and the results are presented in Fig. 6.21a for EPI 06-72 and Fig. 6.21b for EPI 01-73.

In Fig. 6.21a, it can be observed that the emission of B_iO_i has a significant impact on the capacitance (C) when V_{bias} is lower than the forward bias voltage (V_{fd}). This indicates substantial changes in the depleted depth (W). Therefore, it is important to note that the assumption of a constant W is not valid when $V_{\mathrm{bias}} < V_{\mathrm{fd}}$. The extracted defect concentration in this study may introduce errors in this bias range.

For EPI 01-73, the changes in capacitance during the heating process are less than 2%. Hence, the extracted defect concentration only introduces an error of approximately 2% from the estimated W.

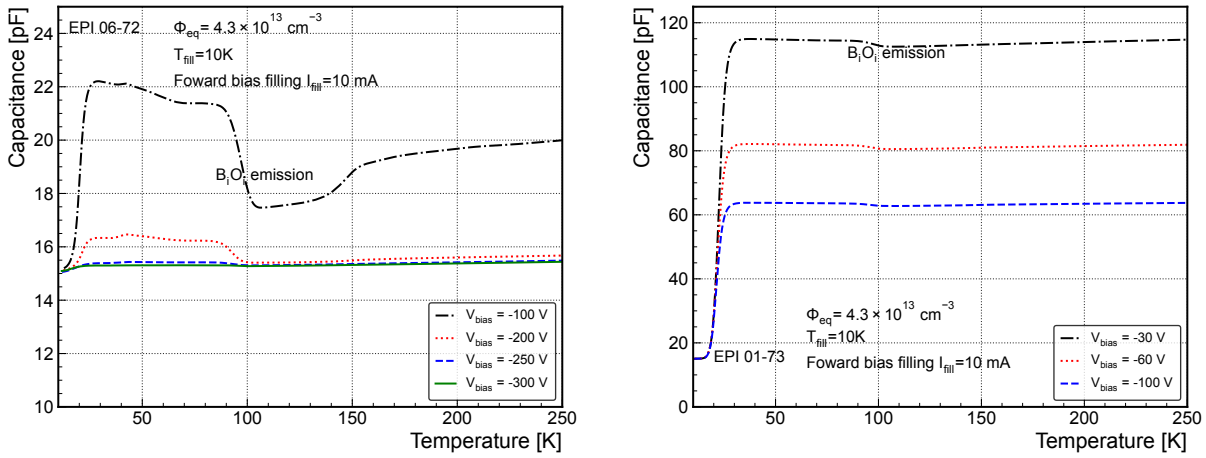

(a) (b)

Figure 6.21: (a) TS-Cap measurement on EPI 06-72 after isothermal annealing at 80 °C during $t_{\mathrm{ann}} = 120$ min, the V_{bias} during heating up indicated in the legend. (b) TS-Cap measurement on EPI 01-73 after isochronal annealing at 100 °C during $t_{\mathrm{ann}} = 15$ min, the V_{bias} during heating up indicated in the legend.

7 5.5 MeV Electron Irradiation

Note: This chapter is a copy of the published paper [159] with minor corrections. The additional materials can be found after the conclusion.

Abstract: This study focuses on the properties of the B_iO_i (interstitial boron - interstitial oxygen) and C_iO_i (interstitial Carbon - interstitial Oxygen) defect complexes by 5.5 MeV electrons in low resistivity silicon. Two different types of diodes manufactured on *p*-type epitaxial and Czochralski silicon with a resistivity of about 10 Ω·cm were irradiated with fluence values between $1 \times 10^{15}\,\mathrm{cm}^{-2}$ and $6 \times 10^{15}\,\mathrm{cm}^{-2}$. Such diodes cannot be fully depleted and thus the accurate evaluation of defect concentrations and properties (activation energy, capture cross-section, concentration) from Thermally Stimulated Currents (TSC) experiments alone is not possible. In this study, we demonstrate that by performing Thermally Stimulated Capacitance (TS-Cap) experiments in similar conditions to TSC measurements and developing theoretical models for simulating both types of B_iO_i signals generated in TSC and TS-Cap measurements, accurate evaluations can be performed. The changes of the position-dependent electric field, the effective space charge density N_{eff} profile as well as the occupation of the B_iO_i defect during the electric field dependent electron emission, are simulated as a function of temperature. The macroscopic properties (leakage current and N_{eff}) extracted from current-voltage and capacitance-voltage measurements at 20 °C are also presented and discussed.

7.1 Motivation

In order to cope with extraordinary high particle rates up to 200 p–p collisions per bunch crossing in High Luminosity Large Hadron Collider (HL-LHC) experiments, new types of silicon sensors were developed e.g. Low Gain Avalanche Detectors (LGADs) [2, 3, 160], and High Voltage CMOS devices (HV-CMOS) for inner tracking detectors [4, 5, 6, 7, 8]. Both types of sensors as well as the new pixel and strip devices will be manufactured on boron doped (*p*-type) silicon. The degradation of the performance of these sensors is due to the expected high radiation field. For instance, exposing the LGADs to a particle radiation field leads to the reduction of the internal gain value with increasing fluence. This degradation is caused by a deactivation of the active boron in the highly doped *p*-type gain layer (about $5 \times 10^{16}\,\mathrm{cm}^{-3}$), which leads to a reduction of the space charge and consequently, a lowering of the electric field followed by a decrease in charge multiplication in this layer.

In general, the deactivation of the boron dopant is a process called boron removal. A possible way to reduce boron removal is a co-implantation of carbon into the gain layer [3]. The assumed mechanism behind this effect is the competition between the displacement of substitutional boron (B_s) and substitutional carbon (C_s) by primary silicon interstitials (Si_I) into interstitial positions (B_i) and (C_i), respectively. Both interstitial atoms are mobile at room temperature and can react with different impurities, ending up e.g. in the formation of B_iO_i or C_iO_i defects [15, 20, 21, 22, 23, 24]. Although both defects have donor states in the bandgap of silicon, the B_iO_i act as a trap for electrons and the C_iO_i as hole trap. At room temperature (RT) the B_iO_i is positively charged and its concentration affects the effective space charge density (N_{eff}) while C_iO_i is in a neutral charge state with no influence on N_{eff}. The C_iO_i defect has an energy level in the lower half of the bandgap of silicon, with an activation energy of 0.36 eV and temperature dependent capture cross sections for holes and electrons [24]. On the other hand, the B_iO_i defect is a coulombic center having an energy level in the upper half of the silicon bandgap with activation energy depending on the electric field, experimentally determined to be between 0.24 and 0.26 eV [23], and independent on temperature capture cross sections of 1×10^{-14} cm^2 for electrons and 1×10^{-20} cm^2 for holes [15, 22].

The reactions with these defects are still under investigation and are of high relevance for improving the radiation hardness of LGADs. In order to get more information about the introduction of both defects and their interplay as well as a quantitative determination of the boron removal rate, the main goal of this work is to accurately characterize the radiation-induced defect complexes B_iO_i and C_iO_i, and evaluate the boron removal rate in highly boron-doped silicon diodes with different carbon concentrations.

The investigated n^+-p diodes were manufactured on 10 Ω·cm p-type epitaxial silicon (EPI) and Czochralski material (Cz), and exposed to high fluences of 5.5 MeV electrons in the range of (1-6) $\times 10^{15}$ cm^{-2}. The radiation-induced defect complexes B_iO_i and C_iO_i were investigated by means of the Thermally Stimulated Current technique (TSC). One problem in the evaluation of the defect concentrations from the measured TSC spectra arises from the fact that the irradiated low resistivity diodes can only be partially depleted during the temperature scan, due to the limit of the maximal reverse voltage which can be applied. That means, that the depleted volume is beforehand not known for the temperature range of the charge emission of the defects. We show that this problem can be overcome if in addition to TSC experiments Thermally Stimulated Capacitance (TSCap) method is employed. This method allows the determination of the depleted volume at any temperature.

The paper is structured as follows. In section 7.2 the experimental details about the used diodes manufactured on p-type epitaxial (EPI)- and Czochralski (Cz)-silicon, the irradiation with 5.5 MeV electrons and the methods for the investigation of the macroscopic and microscopic properties of the devices are presented. In section 7.3 we provide the results of the current-voltage and capacitance-voltage measurements. Next, section 7.4 is

dedicated to TSC and TS-Cap experiments, data simulation and analyses, with a focus on the boron-oxygen (B_iO_i) defect complex and its correlation with the boron removal process.

7.2 Experimental Details

Table 7.1: Device information (* 1 MeV neutron equivalent fluence)

Label	EPI-3	EPI-7	EPI-9	Cz-3	Cz-7
$N_{eff,0}$ (cm^{-3})	1.1×10^{15}	1.1×10^{15}	1.1×10^{15}	1.05×10^{15}	1.05×10^{15}
Initial resistivity ($\Omega \cdot cm$)	≈10	≈10	≈10	≈10	≈10
Electron fluence Φ_e (cm^{-2})	1×10^{15}	4×10^{15}	6×10^{15}	1×10^{15}	4×10^{15}
Fluence value Φ_{eq} (cm^{-2})*	3.98×10^{13}	1.59×10^{14}	2.39×10^{14}	3.98×10^{13}	1.59×10^{14}
Area A (cm^2)	0.0621	0.0621	0.0621	0.029	0.029
Thickness d (μm)	50	50	50	400	400
Carbon [C_s] (cm^{-3})	2×10^{15}	2×10^{15}	2×10^{15}	3×10^{16}	3×10^{16}
Oxygen [O_I] (cm^{-3})	1.5×10^{17}	1.5×10^{17}	1.5×10^{17}	1.5×10^{17}	1.5×10^{17}

(a) (b)

Figure 7.1: Overview of the diodes irradiated by 5.5 MeV electron. (a) Epitaxial, (b) Czochralski.

All the investigated diodes are produced by the company – "Transistors" that belongs to Integral (https://en.integral.by/). Five sets of n^+-p silicon diodes with a deep diffusion junction of 7.2 μm depth were investigated [161]. Three of them (EPI-3, EPI-7, EPI-9) are 50 μm thick epitaxial layers grown on a highly boron-doped Cz substrate of 525 μm thickness and resistivity of 0.006 Ω·cm. Those three sets have the same boron content of 1.1×10^{15} cm^{-3} in the epitaxial layer, corresponding to a resistivity of about 10 Ω·cm. The other two diodes (Cz-3, Cz-7. see Fig. 7.1b) were processed on p-type Cz silicon with about the same resistivity of 10 Ω·cm and a thickness of about 400 μm. Except for boron the main impurities are oxygen and carbon. According to [21] the Cz and EPI diodes have similar oxygen content, of $\sim 1.5 \times 10^{17}$ cm^{-3}, while the carbon content differs, being in the

range of 2-3 $\times$ 10^{16} cm^{-3} and 1.5-2 $\times$ 10^{15} cm^{-3} in Cz and EPI, respectively. All diodes have been manufactured without a guard ring structure [161]. The distance between the pad boundary and the chip edge is roughly 100 µm for all diodes.

The irradiation with 5.5 MeV electrons was performed at room temperature using the accelerator facility at Minsk. Since the range of 5.5 MeV electrons is much larger than the thickness of the EPI- and the Cz-silicon the distribution of the radiation induced defects is uniform throughout the whole bulk of the material. More detailed information can be found in [124]. The achieved fluence values were in the range of (1-6) $\times$ 10^{15} cm^{-2}. For the calculation of the corresponding 1 MeV neutron equivalent values, a hardness factor of 0.0398 was used according to the Non-Ionizing Energy Loss (NIEL) data of I. Jun et al. [162]. More detailed information of the investigated diodes is summarized in Table 7.1.

The macroscopic device performance of the investigated diodes was measured by means of current-voltage (I–V) and capacitance-voltage (C–V) characteristics. The radiation induced changes in the effective space charge density N_{eff} and the full depletion voltage V_{fd} were determined from C–V measurements at 10 kHz. The capacitances were measured with a LCR meter in parallel mode.

For the characterization of the radiation induced electrically active defects, the TSC and TS-Cap methods were used [11, 52, 130, 133, 134]. The experimental setup consists of a closed cycle helium cryostat Model SRDK-205 (Sumitomo Heavy Industries, Ltd, Japan) equipped with a temperature controller Model 340 (Lake Shore, US) and a Keithly 6517A electrometer with a voltage source. For the TS-Cap a LCR meter 4263B from Hewlett Packard is used. The experimental procedure consists of cooling down the sample under zero bias to low temperatures (typically 10 K) where filling of the defects is performed for 30 s either by forward biasing of the diode (electron and hole injection by injecting 1 mA forward current) or 0 V filling (only majority carrier (hole) injection). Then, the diode is reverse biased and a temperature scan is then recorded by measuring the diode current (TSC) or capacitance (TS-Cap) during heating up the device with a constant rate of β = 0.183 K s^{-1} [11]. It should be mentioned here that the range of the reverse bias was chosen that way that the current density was below the soft breakdown. For example for EPI-3 and Cz-3 V_{bias} < 100 V. Isothermal annealing experiments were performed up to 120 min at a temperature of 80 °C for all irradiated diodes, with the subsequent evaluation of the macroscopic and microscopic properties.

7.3 I–V and C–V Measurements

In this section, the measured I–V and C–V characteristics of the irradiated sensors are presented and discussed. As an example, in Fig. 7.2a the I–V curves of all EPI- and Cz-diodes irradiated with different fluences are shown. As it can be seen, for all diodes, except EPI-9 irradiated to 6 $\times$ 10^{15} cm^{-2}, a so-called soft breakdown occurs at a certain bias voltage. Such behaviour may have different reasons, e.g. the diodes have no guard

ring limiting the current to the active pad size and excluding contributions from the outer surface region or edge and/or the high electric field near to the n^+-p junction triggers trap assisted Poole Frenkel [16] or tunnelling effects [137]. Nevertheless, determining the depleted depth $w(V)$ from C–V characteristics (Fig. 7.2b and 7.2c) and assuming that the active area A is given by the n^+-pad size, the depleted volume $V_{\mathrm{vol}} = A \cdot w(V)$ has been calculated and used for estimating the leakage current density $j_d = I/V_{\mathrm{vol}}$ as a function of the applied bias voltage shown in Fig. 7.2d. One would expect flat curves if edge effects and soft breakdown could be neglected. However, a soft breakdown behaviour is observed in all diodes, except EPI-9. According to Fig. 7.2c, w is plotted as a function of $\sqrt{V}$, in the $\sqrt{V}$ range of (6-10) $\mathrm{V}^{0.5}$ (V between 36 V and 100 V), where the edge effects do not contribute to the rise of the current, w is proportional to $\sqrt{V}$ (except for the diode Cz-7), a typical for the bulk generation current. An average current density J_d was taken in the voltage range from 50 V to 100 V, where, a small linear increase of the current is recorded, due to the extension of the electric field in the lateral area of the electrodes in the absence of grounded guard rings.

The average values J_d of the current densities are plotted as function of the electron fluence Φ_{e} in Fig. 7.3, showing an approximately linear increase. The current related damage parameter α, given by:

$$\alpha = \frac{\Delta J_d}{\Delta \Phi_{\mathrm{e}}} \tag{7.1}$$

had been evaluated to $\alpha = (3.2 \pm 0.2) \times 10^{-19}\,\mathrm{A\,cm^{-1}}$. Such a small α value was also observed in previous experiments on 5.5 MeV electron damage induced in n-type silicon [14, 163]. Accounting for the hardness factor of 0.0398 the current related damage parameter becomes $\alpha = 0.8 \times 10^{-17}\,\mathrm{A\,cm^{-1}}$, being much smaller compared to the value of $\alpha = 4 \times 10^{-17}\,\mathrm{A\,cm^{-1}}$ determined for hadron irradiation and an annealing of 80 min at 60 °C (see e.g. [11, 164, 165]).

The C–V characteristics were measured for 4 different frequencies (230 Hz, 445 Hz, 1 kHz and 10 kHz). A slight frequency dependence is observed and the related explanation can be found in reference [65, 67]. The relative deviations measured at 200 V between the values measured at frequencies of 230 Hz and 10 kHz are below 4% for all the samples.

The effective space charge density profile $N_{\mathrm{eff}}(w(V))$ and the depletion depth $w(V)$ were extracted from the 10 kHz C–V curves (see Fig. 7.2b) according to Eq. 7.2 and Eq. 7.3:

$$N_{\mathrm{eff}}(V) = \frac{2}{\epsilon_0 \epsilon_r A^2 q_0\, d(1/C^2)/dV} \tag{7.2}$$

$$w(V) = \frac{\epsilon_0 \epsilon_r A}{C(V)} \tag{7.3}$$

Where C is the measured capacitance, ϵ_0 is the permittivity of vacuum, ϵ_r the relative permittivity of silicon (11.9), q_0 is the elementary charge, A is the active pad area. Fig-

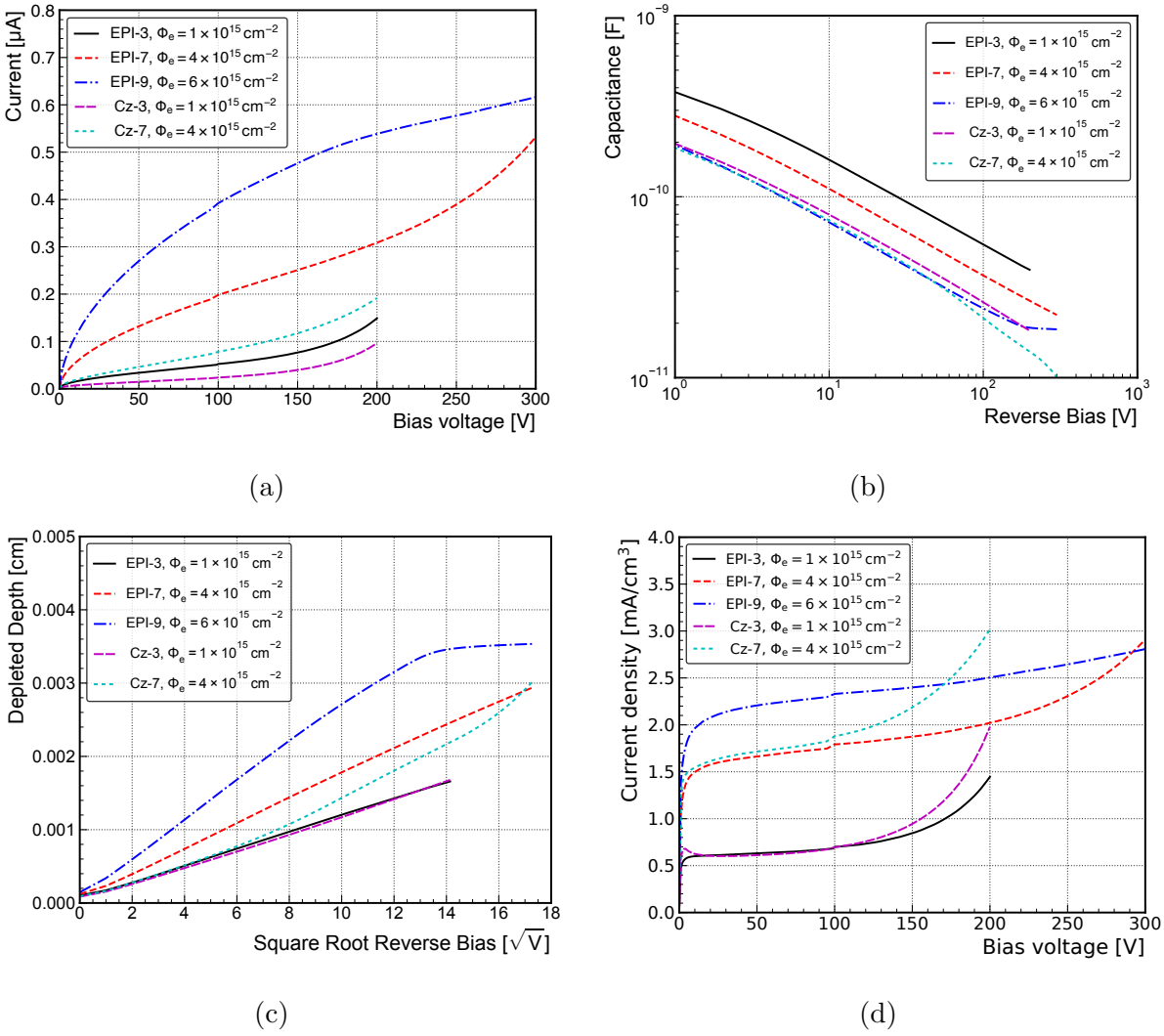

Figure 7.2: (a) Current-voltage characteristics of the 10 Ω·cm diodes, irradiated with 5.5 MeV electrons $\Phi_e = 1,\ 4,\ 6\ \times\ 10^{15}$ cm^{-2}. Measurements conditions: $T = 20\,^{\circ}$C, humidity $\leq 10\%$. (b) C–V characteristics and (c) Depleted Depth vs $\sqrt{V}$ of the same 10 Ω·cm diodes presented (a). Measurements conditions: $V_{AC} = 0.5$ V. Frequency = 10 kHz. (d) Density of leakage current (j_d) versus bias voltage V.

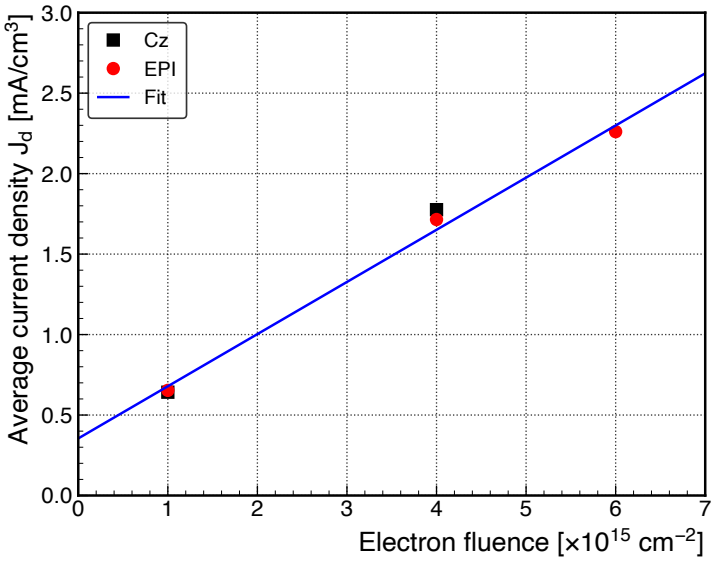

Figure 7.3: Average current density J_d vs. electron fluence (details see text).

ure 7.4 presents the calculated $N_{\text{eff}}(w(V))$ profiles for the EPI- and Cz-diodes, irradiated with different fluences.

With increasing fluence, the profiles of N_{eff} are shifting to lower values, a fact that is expected mainly due to the deactivation of the initial boron concentration caused by irradiation, the so-called boron removal effect. Of course, some hole traps e.g. H140K and H152K will also affect the space charge density N_{eff} but their concentrations are much smaller compared to the concentration of the B_iO_i defect ([H140K + H152K] $\approx 2.5 \times 10^{13}$ cm^{-3} and [B_iO_i] $\approx 4.5 \times 10^{14}$ cm^{-3} in EPI-9).

The isothermal annealing behaviour of the generation current density J_d at 80 °C is depicted in Fig. 7.5. The observed changes with annealing time are much smaller compared to the ones observed for a 23 GeV proton irradiated 10 Ω·cm EPI-diode, which are also included in Fig. 7.5 [23].

Due to the significant affection by lateral effect especially in Cz diodes, it is deserved to mention the error in the extracted N_{eff} and j_d. In this work, the lateral effect was estimated by the difference on j_d as shown in Fig. 7.2d, under the assumption that the lateral effect in EPI diodes can be neglected. Thus, for applied bias voltages of 100 V and 200 V, the error will rise from 0.7% up to 36% for Cz-3 and from 5% to 49% for Cz-7, respectively. The $V_{\text{bias}} = 100$ V corresponds to depleted depths of about 11 µm and 14 µm for the diode Cz-3 and Cz-7, respectively. Only the J_d values from EPI-diodes were used to extract α. Thus the error for the J_d was estimated from the bias interval for averaging and resulted in a value of 3%. This introduces an uncertainty of 5% in the obtained α value.

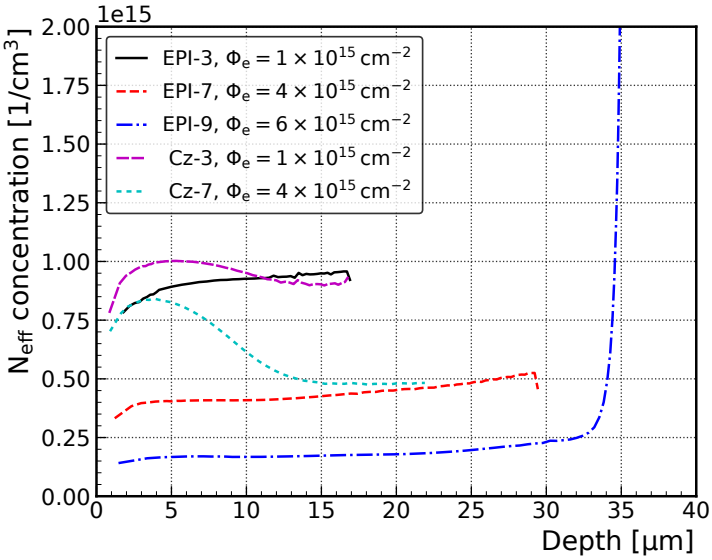

Figure 7.4: N_{eff} profile of the diodes irradiated with different fluences. The data were evaluated from C–V measurements (Fig. 7.2b) at room temperature by using Eq. 7.2 and Eq. 7.3.

7.4 Results from TSC and TS-Cap Measurements

The Thermally Stimulated measurement techniques were used to investigate the defect complexes induced by irradiation with 5.5 MeV electrons, especially the boron-oxygen (B_iO_i) and the carbon-oxygen (C_iO_i) defects in the EPI- and Cz-materials. Figure 7.6a shows the TSC spectra measured on all diodes (EPI- and Cz-samples) irradiated with different fluences after injecting both electrons and holes (1 mA forward injection) at 10 K. Figure 7.6b presents the spectra of the same diodes after filling the traps only with holes by cooling the sample to 10 K under 0 V. As can be seen here, the dominant TSC signal occurs at about 150 K and is attributed to the carbon-oxygen (C_iO_i) defect complex. The C_iO_i signal height in Cz-diodes is much larger compared to the EPI-diodes at the same fluence, due to the higher concentration of carbon in Cz silicon (see Table 7.1). While Fig. 7.6b shows only the TSC peaks corresponding to hole traps, Fig. 7.6a reveals also the ones corresponding to electron traps which can be filled by a forward current injection. As it can be seen in Fig. 7.6a, there is a dominant peak in the temperature range between 90 K and 100 K that is not even traced in the spectra depicted in Fig. 7.6b corresponding to hole traps only. This dominant peak corresponds to an electron trap, increases with increasing fluence, shows a dependence on the electric field in the sensor, the so-called Poole-Frenkel effect [135, 136, 16] as well as a dependence on the impurity content (boron, oxygen, carbon) in the material [15, 21, 20, 101] and thus, it is attributed to the B_iO_i defect complex. Also, theoretical calculations support this identification [101]. Because the diodes cannot always be fully depleted during the temperature scan and for a better comparison of the different spectra, the measured currents shown in Fig. 7.6a

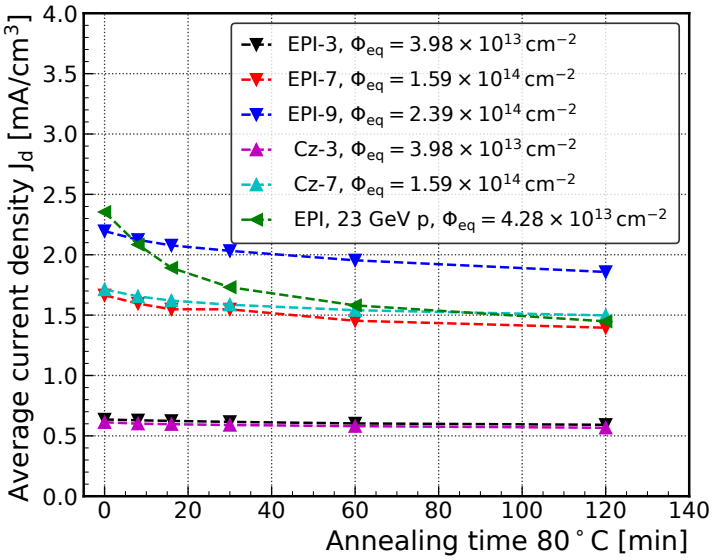

Figure 7.5: J_d versus. annealing times at 80 ^{o}C. The data for 23 GeV proton irradiation correspond to a 10 Ω·cm resistivity EPI-diodes with A = 0.06927 cm^2, and have similar N_{eff} and d to electron irradiated EPI-diodes.

and 7.6b had been normalized to the active depleted volume ($V_{\text{vol}}(V,T) = A \cdot w(V,T)$). The $w(V,T)$ values were extracted from the corresponding TS-Cap measurements.

The TS-Cap data are presented in Fig. 7.6c and Fig. 7.6d corresponding to the TSC spectra shown in Fig. 7.6a and Fig. 7.6b, respectively. For the case of forward current injection the TS-Cap measurements show a drop of the capacitance values in the temperature range of the B_iO_i emission. This correlates with the change of the B_iO_i defect charge state, being neutral when occupied with an electron at temperatures before the emission starts and positively charged after the electron is thermally emitted. This leads to a change of the space charge density to a less negative value, corresponding to an increase in the space charge width and consequently to the drop of the capacitance mentioned above. On the other hand, the increase of the capacitance in the range of the C_iO_i emission (Fig. 7.6d) is due to the change of the charge state of the C_iO_i from positive (occupied by holes) to the neutral state after the holes emission. Thus, the space charge density changes from less negative to more negative leading to a decrease in the space charge width $w(V,T)$ and an increase of the capacitance at the given bias voltage. In both cases, the defect concentration can be determined despite the fact that the detector is not fully depleted, as the TS-Cap data can be used to determine the depletion depth at any temperature (see section 4.1.). Further, it is known that the B_iO_i is a coulombic center [15, 101] and thus the electron emission from this defect is governed by the Poole-Frenkel effect, manifesting in a shift of the TSC peak position to lower temperatures with increasing bias voltage. A related shift is then also observed in the TS-Cap curves (see e.g. Fig. 7.7).

A quantitative evaluation of defect concentrations from TSC spectra of not fully de-

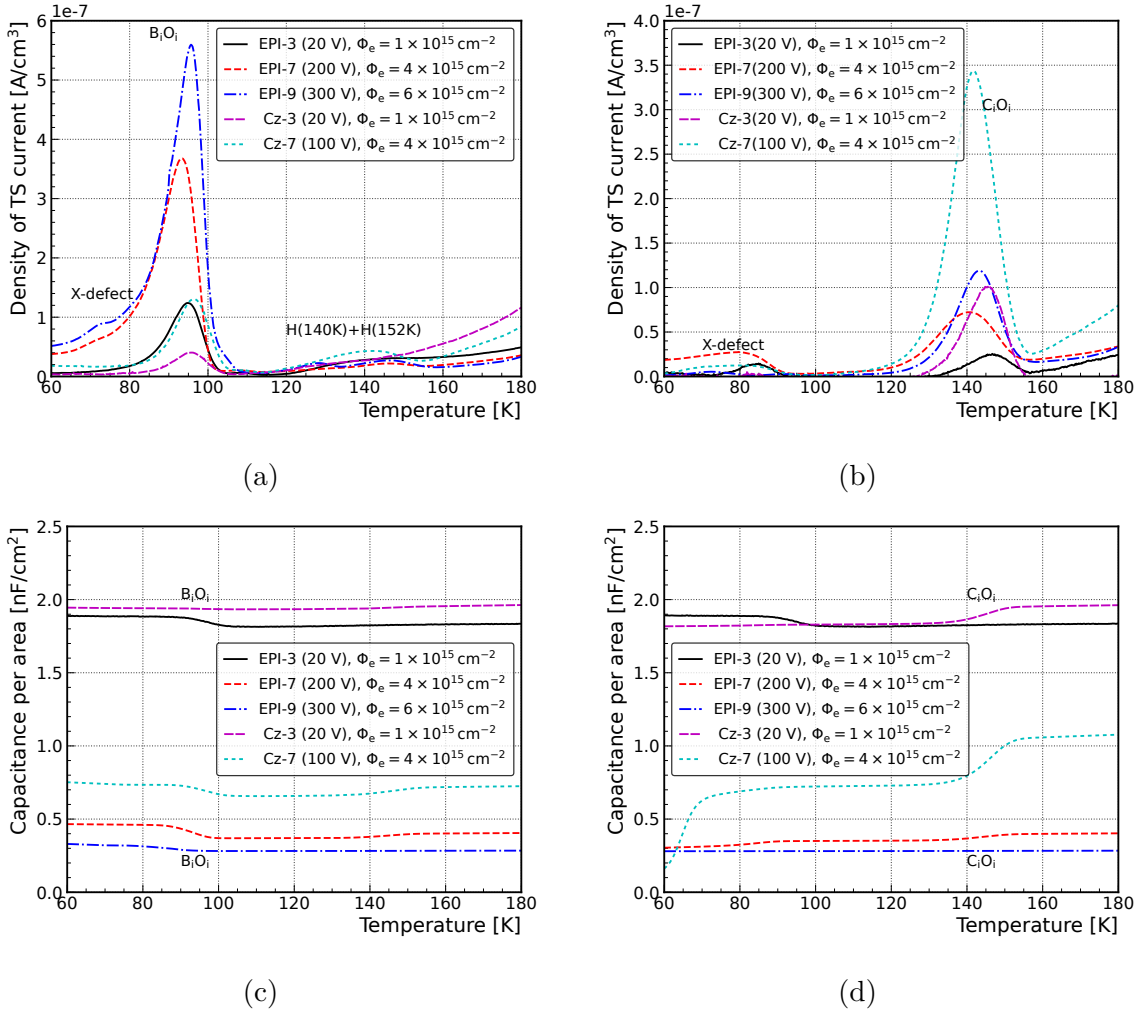

Figure 7.6: (a) TSC Spectra after trap filling by forward current injection and (b) after filling with majority carriers (holes). Both types of spectra are measured on EPI-(EPI-3, 7, 9) and Cz-diodes (Cz-3, 7) after irradiation with 5.5 MeV electrons, fluences of $\Phi_e = 1,\ 4,\ 6\ \times\ 10^{15}$ cm^{-2}. The applied bias voltages are indicated in the legends and each diode current is normalized to their individual depleted volume (normalization factor $1/(A \cdot w)$), A = active pad area, $w(V,T)$ = depleted depth. (c) and (d) are the TS-Cap measurements corresponding to figures (a) and (b), respectively. The capacitance values are normalized to the pad area of each diode.

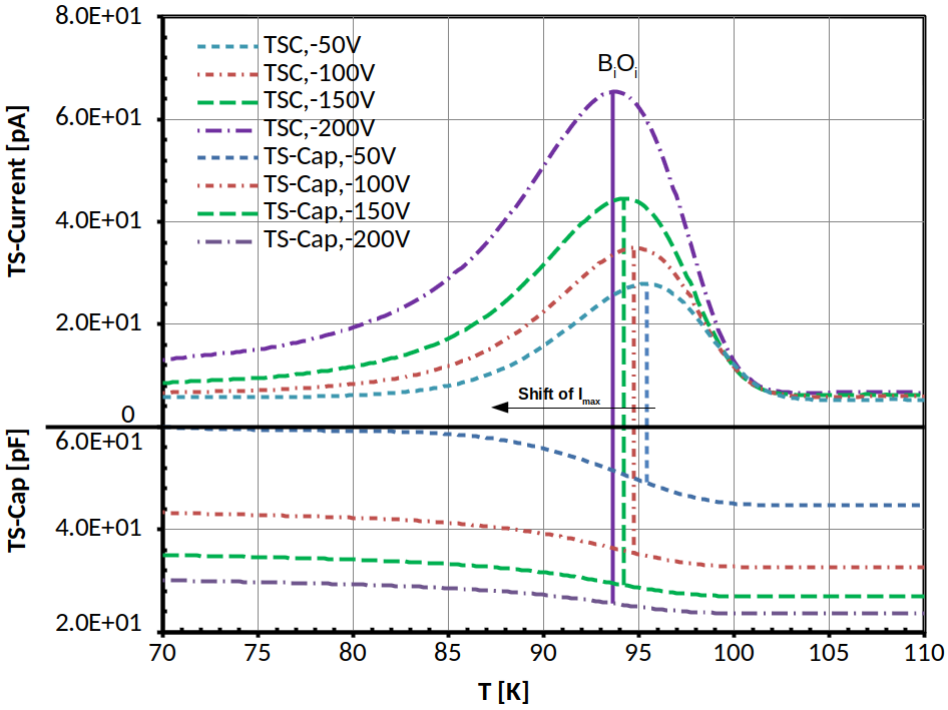

Figure 7.7: Temperature shift of the B_iO_i TSC peak in the case of EPI-7 diode ($\Phi_e = 4 \times 10^{15}$ cm^{-2}) for different bias voltages (top) and the corresponding shifts of the TS-Cap curves (bottom). The shifts are indicated by vertical lines between the TSC peak maxima and the turning point of the TS-Cap curves.

pleted diodes is only possible if the changes of the depleted depth in the corresponding temperature ranges are known. This issue will be discussed in the following section.

7.4.1 Evaluation of Concentrations in Case of Partially Depleted Sensors

The TSC method and evaluation of defect properties are described in detail in numerous publications [11, 52, 130, 133, 134]. In our case of not fully depleted devices and the traps homogeneously distributed in the bulk, the current for emission from an isolated electron trap $I^e_{TSC}(T)$ with the concentration $n_t(T_0)$, is:

$$I^e_{TSC}(T) = q_0 A n_t(T_0) \int_0^{w(T)} \frac{x}{w(T)} e_n(T,x) f\,(T,x) dx \tag{7.4}$$

$$e_n = \sigma_n \cdot v_{th,n} \cdot N_C \cdot \exp\left(-\frac{E_a}{k_B T}\right) \tag{7.5}$$

$$e_p = \sigma_p \cdot v_{th,p} \cdot N_V \cdot \exp\left(-\frac{E'_a}{k_B T}\right) \tag{7.6}$$

$$f(T) = \exp\left(-\frac{1}{\beta} \int_{T_0}^{T} \left(e_n(T') + e_p(T')\right) dT'\right) \tag{7.7}$$

where T is the measured temperature, $w(T)$ the depleted depth at temperature T, x is the coordinate of the depth in the depleted region, e_n and e_p are the emission rates for electrons and holes, respectively, N_C and N_V are the density of states in the conduction band and valence band, respectively. The activation energy for electrons is $E_a = E_C - E_t$ and for holes $E'_a = E_t - E_V$, where E_t is the energy level of the electron traps and $E_{C,V}$ the conduction and valence band edge, respectively. $\sigma_{n,p}$ is the cross section for electrons and holes, $v_{th,n,p}$ is the thermal velocity for electrons and holes. k_B is the Boltzmann constant, $f(T)$ describes the fraction of the defects occupied by electrons at temperature T, β is the heating rate and $n_t(T_0)$ is the density of defects that are filled with electrons at T_0. The N_C, N_V, $v_{th,n,p}$ values were taken from [101] ($N_{C,V} = 2.540\,933 \times 10^{19} \times \left(\frac{m^*_{dC,V}}{m_0}\right)^{3/2} \left(\frac{T}{300}\right)^{3/2}$). Eq. 7.4 defines the total current which accounts for the conduction and the displacement currents [130]. When $f(T)$ and $e_n(T)$ are not position dependent the Eq. 7.4 can be simplified to:

$$I^e_{TSC}(T) \;=\; \frac{1}{2} \cdot q_0 \cdot A \cdot w(T) \cdot e_n(T) \cdot n_t(T_0) \cdot f\,(T) \tag{7.8}$$

In the investigated p-type diodes, the B_iO_i defect, on which this study is focusing, is detected in a TSC experiment only if electrons can be injected at low temperature. This is done by forward biasing the diodes at 10 K injecting both electrons and holes. According to [22] the capture cross section for holes of the B_iO_i defect is neglectable compared with the capture cross section of electrons and thus, $n_{t,0}$ is equal to the defect concentration N_t, and e_p can be neglected. Thus, the B_iO_i defect concentration can be determined by integrating the TSC corresponding signal after filling with forward bias given by Eq. 7.8 and considering the depleted volume:

$$N_t = \frac{2}{\beta q_0} \cdot \int_{T_s}^{T_e} \frac{I^e_{TSC}(T)}{A \cdot w(T)}\, dT = \frac{2}{\beta q_0} \cdot \int_{T_s}^{T_e} j_{tsc}(T)\, dT \tag{7.9}$$

where j_{tsc} is the thermally stimulated current density, T_s and T_e are the temperature of the start and the end of the electron emission of the defect, respectively. It should be mentioned here that Eq. 7.9 is only valid if the defect concentration and the emission rate are position independent. For the investigated irradiated diodes, three different situations have to be considered when evaluating the B_iO_i concentration:

(i) At the lowest fluence of 1×10^{15} cm^{-2} the diodes EPI-3 and Cz-3 are partially depleted before and after emission of the defect for all the applied bias voltages. As it can be observed in Fig. 7.6c the capacitance stays nearly constant, i.e. also the depletion depth $w(T)$ is constant in the temperature range of interest. Therefore, Eq. 7.9 can be simplified to:

$$N_t = \frac{2}{\beta q_0} \cdot \int_{T_s}^{T_e} \frac{I^e_{TSC}(T)}{A \cdot w}\, dT = \frac{2 \cdot Q}{q_0 A w} \tag{7.10}$$

Where w can be extracted from TS-Cap data as an average value in the range T_s to T_e.

(ii) The sensor is partially depleted before emission and fully depleted after emission. This holds for the device EPI-9, which was irradiated to $\Phi_e = 6 \times 10^{15}$ cm^{-2}. In this case, the concentration can be evaluated from the TSC spectrum only if $w(T)$ is extracted from TS-Cap measurements.

(iii) Similar to case (i), the sensors are partially depleted before and after emission, but $C(T)$ or $w(T)$ shows visible changes in the temperature range where the electron emission from the defect takes place(see Fig. 7.6c and 7.6d for the diodes EPI-7 and Cz-7). In this case, the corresponding defect concentration can be directly extracted from the TS-Cap measurement as described in the following.

For high defect concentration where the change in the occupancy of the defects due to the thermal emission of captured electrons or holes leads to measurable variations of the capacitance with increasing temperature, the TS-Cap method can be used to extract the defect concentration. For the B_iO_i defect the TS-Cap can be described, in the 1-D approach, by the following equations:

$$C(T) = \frac{\epsilon_0 \epsilon_r A}{w(T)} \tag{7.11}$$

with

$$w^2(T) = \frac{2\epsilon_0 \epsilon_r (V + V_{bi})}{q_0 \cdot |N'_{\text{eff}}(T)|} \tag{7.12}$$

where

$$N'_{\text{eff}}(T) = N_0 - N_t \cdot (1 - f(T)) \tag{7.13}$$

Here $C(T)$ is the capacitance of the device at temperature T and for a given bias voltage V, V_{bi} is the build-in voltage, which is negligible compared to the applied bias voltage V. The term N_0 in Eq. 7.13 denotes the absolute N_{eff} value before the start of the electron emission of B_iO_i, i.e when all defect centers are neutral and their contribution to the effective space charge concentration is 0. The second term in Eq. 7.13 accounts for the donor character of the B_iO_i defect, becoming positively charged after thermal emission of captured electrons and thus leading to a progressive reduction of N_0 with increasing the temperature until the electron emission from the defect ends. Assuming no other defects with similar emission rates are present, $[B_iO_i]$ is given by:

$$[B_iO_i] = \frac{2\epsilon_0 \epsilon_r V}{q_0} \left(\frac{1}{w^2(T_s)} - \frac{1}{w^2(T_e)} \right) \tag{7.14}$$

Here $w(T)$ is extracted from Eq. 7.11 and T_s and T_e are the temperatures before and after the electron emission from B_iO_i, respectively.

In Fig. 7.8a the B_iO_i and the C_iO_i concentrations extracted from the TSC and TS-

Cap measurements as a function of the 5.5 MeV electron fluence Φ_e are plotted for EPI- and Cz-materials. They were extracted by Eq. 7.9 in the temperature range 80-105 K for [B_iO_i] and 120-155 K for [C_iO_i]. Included are also the N_{eff} values for both materials as extracted from C–V measurements performed at room temperature. Assuming the boron removal rate $R = |(\Delta N_{eff})/(\Delta\Phi_{eq})|$, values of 2.18 cm^{-1} and 3.7 cm^{-1} can be extracted by linear fitting of the curves in Fig. 7.8a for Cz and EPI, respectively. The difference of 41% between the Cz and the EPI rates is attributed to the different amounts of carbon content in both materials as given in Table 7.1. For the EPI-diodes the change of N_{eff} with fluence is roughly a factor 2 larger compared with the increase of the B_iO_i concentration. This can be explained by the boron removal process, i.e. the negatively charged substitutional boron B_s^- is transformed into a positively charged $B_iO_i^+$ defect ($B_s^- \rightarrow B_iO_i^+$). For the Cz-material this cannot be stated due to the strong non-uniform profile of the space charge density (see Fig. 8.4). The introduction rates $g_{B_iO_i} = [B_iO_i]/\Phi_{eq}$ and $g_{C_iO_i}$ =[C_iO_i]/Φ_{eq} were extracted from the linear increase with fluence, and are plotted in Fig. 7.8b as a function of the carbon content in the EPI- and Cz-diodes. It is obvious that the generation rate of the B_iO_i is much lower for the material with the higher carbon content. On the other hand, the increase of the C_iO_i generation rate with increasing carbon content is an indication for the beneficial effect the carbon impurity in reducing the creation of B_iO_i. This dependence on the carbon concentration has led to the approach of carbon co-implantation into the gain layer of LGADs in order to improve their radiation hardness [3].

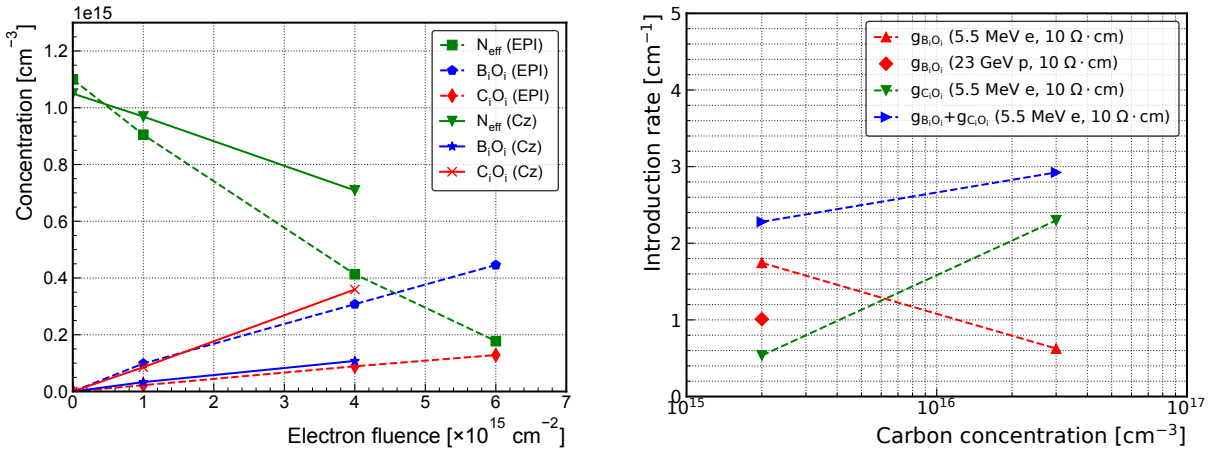

(a) (b)

Figure 7.8: (a) Dependence of the effective doping density N_{eff}, B_iO_i and C_iO_i defect concentration on the 5.5 MeV electrons fluence for EPI- and Cz- diodes. The N_{eff} values were extracted from Fig. 7.5 in the bias range of 1-100 V and 1-20 V for EPI and Cz diodes, respectively. (b) Variation of $g_{B_iO_i}$ and $g_{C_iO_i}$ as a function of the Carbon content for EPI- and Cz- diodes. Included is the $g_{B_iO_i}$ value after irradiating a 10 Ω·cm EPI diode with 23 GeV protons at $\Phi_{eq} = 4.3 \times 10^{13}$ cm^{-3}.

Included in Fig. 7.8b is also the introduction rate of B_iO_i for an EPI-diode with the same $N_{eff,\,0}$ and irradiated with the same Φ_{eq} of 23 GeV protons as the irradiation with 5.5 MeV electrons. As it can be seen, the generation rate of B_iO_i defect after 5.5 MeV electron irradiation is about a factor 1.6 larger than the value determined after irradiation with 23 GeV protons.

In principle, both TSC and TS-Cap are performed with V_{bias} where the lateral effect is not significant. However, the obtained concentrations strongly depend on the integration ranges of the TSC spectra or the selection of T_s and T_e. Thus, in this work, the error of the extracted B_iO_i concentrations is given by varying T_s from 75 K to 80 K. The obtained errors for EPI-3, 7, 9 are 5%, 8% and 9%, for Cz-3 and 7 are 5% and 6%, respectively. The slightly increasing errors are caused by the overlapping peak at the low temperature tail possibly related to the X-defect. The estimated error of the N_{eff} value shown in Fig. 7.8a are due to the selected interval of averaging the data (see Fig. 7.5). They are about 3% for all EPI diodes and 5% for Cz-3. For Cz-7 the estimated error is 20% due to the non-uniform profile.

7.4.2 Simulation of TSC and TS-Cap Data for the B_iO_i Defect

Compared to the TSC and DLTS methods the TS-Cap technique is rarely used to get information about radiation induced defects. However, when high concentrations of defects are involved, the method delivers important information on the changes in the depletion depth during a temperature scan from 10 K up to room temperature, which can be used, via developing simulation models, to determine the defect type (capturing electrons or holes) and trapping parameters (activation energy, capture cross section of the emitted charge) as well as its concentration. In our simulations the following assumptions are made:

- Lateral effects are neglected.
- The device is partially depleted in the temperature range of interest.
- The series resistance of the non-depleted part of the device can be neglected.

Because the B_iO_i is a coulombic trap center, the emission rate e_n is not anymore a constant quantity with respect to the applied bias voltage, but field dependent. By accounting for the 3-D Poole-Frenkel effect, the emission rate can be expressed by [135, 136, 16]:

$$e_n^{pf}(T) = e_{n,0}(T) \cdot \left[\left(\frac{1}{\gamma^2} \right) \left(e^{\gamma} \left(\gamma - 1 \right) + 1 \right) + \frac{1}{2} \right] \tag{7.15}$$

where

$$\gamma = \sqrt{\frac{q_0|\vec{E}|}{\pi\varepsilon_0\varepsilon_r}} \cdot \frac{q_0}{k_B T} \tag{7.16}$$

and $e_{n,0}$ denotes the field independent emission rate with the so-called zero field activation energy $E_a = E_{a,0}$. $|\vec{E}|$ is the electric field in the sensor bulk and depends on the position x in the depleted zone. According to the reference [136], the Poole-Frenkel effect is given by the electrostatic energy of an electron which is attracted to a single charged positive ion under the influence of a uniform applied electric field (see Fig. 5.9). In the diodes, especially highly doped ones, such an assumption might not be fully valid, since the electric field distribution is not uniform. Thus, in this paper, we introduce a parameter ξ to modify the force between the positively charged ion and the electron. Therefore, the γ value is modified to:

$$\gamma = \xi\sqrt{\frac{q_0|\vec{E}|}{\pi\varepsilon_0\varepsilon_r}} \cdot \frac{q_0}{k_B T} \tag{7.17}$$

In this case the Eq. 7.13 has to be revised to:

$$N'_{\text{eff}}(T,x) = N_0 - [\text{B}_\text{i}\text{O}_\text{i}] \cdot (1 - f(T,x)) \tag{7.18}$$

Furthermore, the electric field distribution $E(T,x)$ in the depleted bulk of the diodes is calculated from the corresponding Poisson equation:

$$\frac{dE(T,x)}{dx} = \frac{q_0 \cdot N'_{\text{eff}}(T,x)}{\varepsilon_0\varepsilon_r} \tag{7.19}$$

The electric field E, the occupation fraction f and the N'_{eff} are temperature and position dependent. For coulombic centers, the emission rate e_n^{pf} has to be used for calculating the occupation fraction defined in Eq. 7.7.

Considering the involved set of equations, an analytical solution for simulating the TSC and TS-Cap measurements will be extremely complicated. Therefore, the finite element method is used for simulating the experimental data. The details are presented in the section 7.4.3.

In the following part, the simulation results and comparison with the corresponding TS-Cap and TSC measurements will be presented for two devices, both annealed for 2 h at 80 ^{o}C after irradiation: the electron irradiated sample EPI-7 (see Table 7.1) and a 50 Ω·cm p-type diode irradiated with $\Phi_{\text{eq}} = 4.3 \times 10^{13}$ cm^{-2} 23 GeV protons for which more detailed information can be found in reference [23]. The measurement parameter for both diodes is the same, i.e. V_{bias} = -100 V, heating rate $\beta = 0.183$ K/s and the frequency for the capacitance measurement $f = 10$ kHz.

All parameters, the fixed and the adjusted ones, used for the simulations of both diodes are summarized in Table 7.2. For the presented data, the details about N_0 can be found

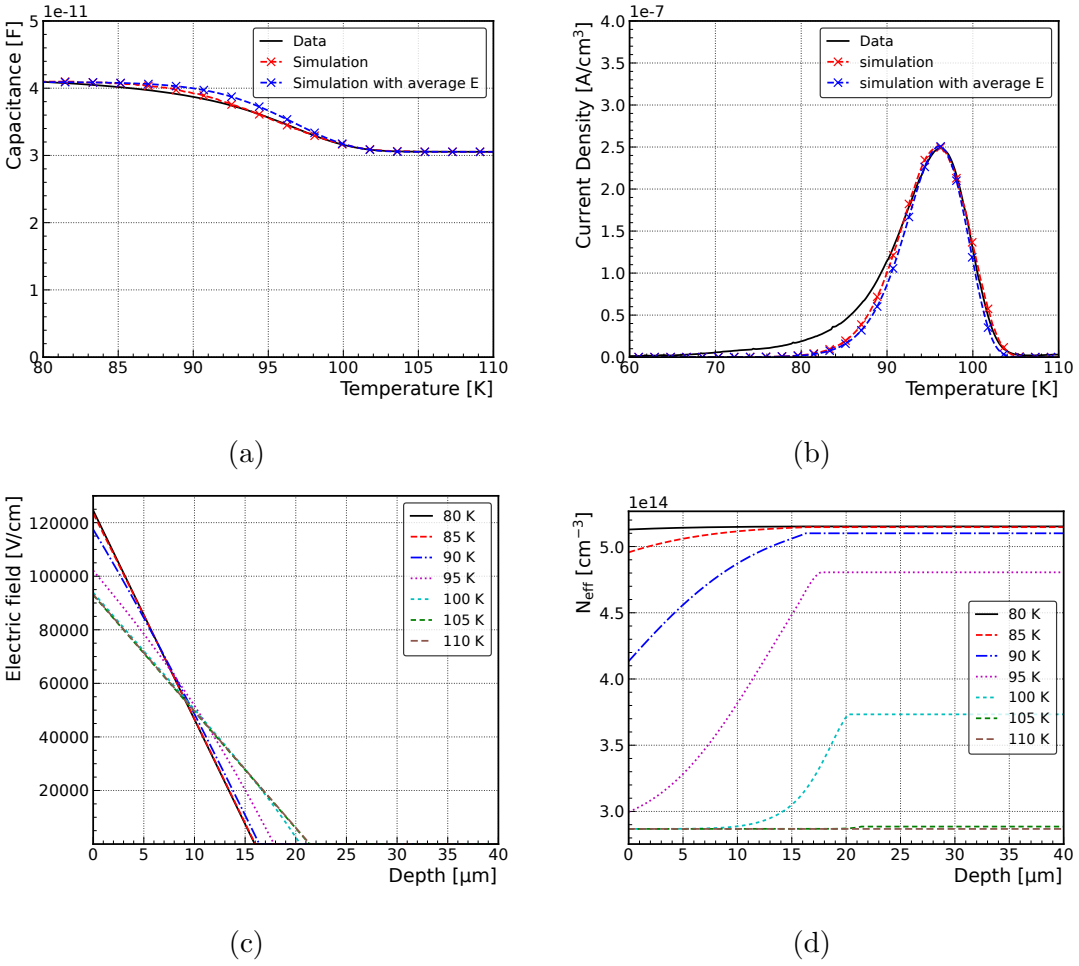

Figure 7.9: Simulation results of the B_iO_i generating signals in EPI-7 diode: (a) TS-Cap, comparison with experiment; (b) density of TSC signal, comparison with the measured spectra; (c) and (d) the electric field distribution and the N_{eff} profile, respectively, for different temperatures, from 80 K to 110 K, in steps of 5 K. All simulations and given experimental data correspond to a reverse bias of 100 V applied during TS-Cap and TSC temperature scans.

Table 7.2: Parameters of simulation. Adjusted parameters are indicated by *. The $E(T,x)$ represents the position and temperature dependent electric field and $< E(T) >$ is the average electric field in the diodes

Methods Irradiation Assumption	TS-Cap Proton $E(T,x)$	TSC Proton $E(T,x)$	TS-Cap Electron $E(T,x)$	TSC Electron $E(T,x)$	TS-Cap Electron $< E(T) >$	TSC Electron $< E(T) >$
$N_{\text{eff},0}$ (10^{14} cm^{-3})	1.1	1.1	5.1	5.1	5.1	5.1
$[B_iO_i]$ (10^{13} cm^{-3})*	3.5	3.3	23	16	23	16
E_{a0} (eV)*	0.265	0.273	0.258	0.258	0.284	0.284
σ_n (10^{-14} cm^2)	1.05	1.05	1.05	1.05	1.05	1.05
Area A (cm^2)	0.06927	0.06927	0.0621	0.0.0621	0.0.0621	0.0.0621
ξ*	0.85	0.85	0.5	0.5	1	1

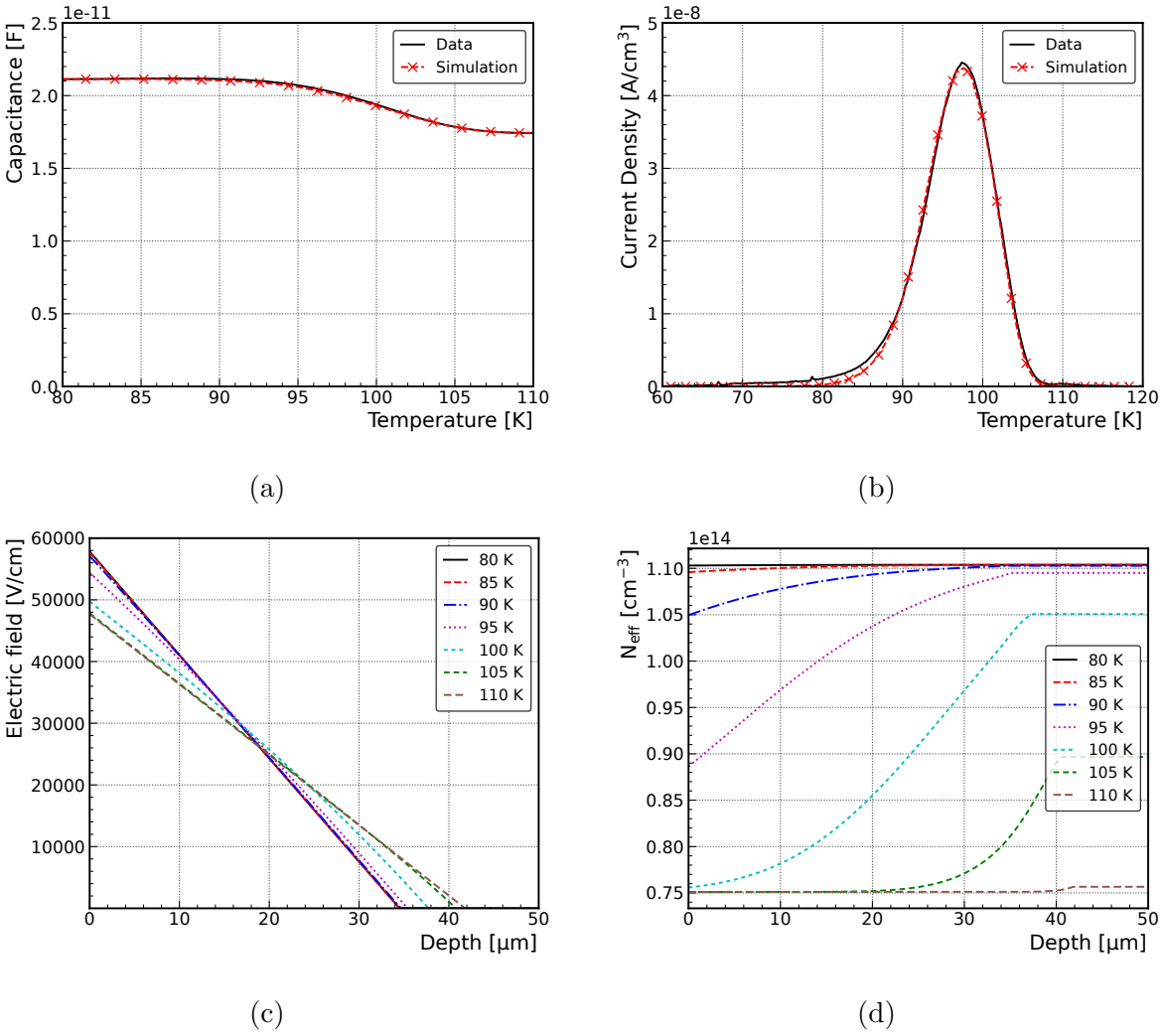

Figure 7.10: Simulation results of the B_iO_i generating signals in a 50 Ω·cm EPI diode irradiated with 23 GeV protons up to $\Phi_{eq} = 4.3 \times 10^{13}$ cm^{-2}: (a) TS-Cap, comparison with experiment; (b) density of TSC signal, comparison with the measured spectra; (c) and (d) the electric field distribution and the doping profile, respectively, for different temperatures, from 80 K to 110 K, in steps of 5 K. All simulations and given experimental data correspond to a reverse bias of 100 V applied during TS-Cap and TSC temperature scans.

in the Appendix. In order to reproduce the TS-Cap measurement (see Fig. 7.9a and Fig. 7.10a), the $[B_iO_i]$ was extracted via Eq. 7.14. For getting a better fit to the data, the $[B_iO_i]$ for the simulation of the TSC spectrum (see Fig. 7.9b and Fig. 7.10b) is adjusted. The $[B_iO_i]$ extracted from the TSC spectrum by integration from 80 K to 105 K is about 13 % larger compared to the value used for the simulation. This difference is due to the low temperature tail in the spectrum which was not reproduced in the simulation. The significant difference of $[B_iO_i]$ between TS-Cap and TSC is caused by some unknown effect.

In principle, the E_{a0} is known with value in between 0.27-0.28 eV [23] with fixed $\sigma_n = 1.05 \times 10^{-14}$ cm^2. However, in this work, for matching the data the essential adjustment was applied for different measurements. The difference of E_{a0} between TSC and TS-Cap measurements for proton irradiated diode is due to the difference in the temperature of the peak maximum $T_{\max}$ in the TSC spectrum and the temperature of the turning point in the TS-Cap curve. The related effect is still unknown. The difference of E_{a0} between the proton and electron irradiated devices might be caused by the different production technology of both devices, the diode with a guard ring (p irradiated) and the other one without. The explanation can be proved by comparing the results from the EPI-diode irradiated with protons ([23]). This diode has roughly the same E_{a0} as the one presented in Table 7.2 for proton irradiation. Another possible effect, which might be responsible for the difference of the E_{a0} values, could be that the proton irradiation introduces a clustering of the B_iO_i defects, leading to a change of the TSC peak shape [107].

The difference in E_{a0} between the two different electric field distributions (linear electric field $E(x)$ and homogeneous electric field distribution $< E(T) >$) is 26 meV ($\sim$10%). The reason for this difference can be understood by the fact that the emission rate $e_n^{pf}(T, E(x), E_{a0})$ depends exponentially on the electric field distribution. At a specific temperature T, the emission rate is enhancing with $E(x)$ and is decreasing when increasing the E_{a0} values. Thus, for the same bias voltage, the values of $E(T, x)$ in the case of linear field distribution and of the average electric field $< E(T) >$ coincide only in the middle of the depleted width, in the front region of the junction $E(T, x)$ being larger than $< E(T) >$ and in the back side smaller. Consequently, the same measured TSC signal can be reproduced in both cases if in the calculation of the emission rates the values of E_{a0} and ξ are smaller for a linear distribution of the electric field than for the constant, average one. This has with respect to the emission rate to be compensated by a lower E_{a0} or a lower ξ value compared to the constant field case in order to reproduce the same measured TSC signal.

The other adjusted parameter is the defined ξ. Due to the fact that by using Eq. 7.16 the experimental data could not be reproduced this constant ξ was introduced for modifying the field dependence in the Poole-Frenkel effect.

The simulation results for the EPI-7 diode are displayed in Fig. 7.9 (a-d). In order to reproduce the TS-Cap measurement (Fig. 7.9a) the B_iO_i concentration was extracted via

the Eq. 7.14, the ξ value for the Poole-Frenkel effect was set to $\xi = 0.5$ and the zero-field activation energy $E_{a0} = 0.258$ eV. With the same values for ξ and E_{a0} parameters but a lower B_iO_i concentration, the TSC signal could be reproduced in the temperature range between 90 K and 105 K. The low temperature tail, which cannot be described by the simulation, is most probably due to the so-called X-defect (see Fig. 7.6a and 7.6b). Contrary to the TSC case, where the charge emission from the X defect can be separated from that of the B_iO_i defect, in TS-Cap measurements the contributions of both defects cannot be separated. Therefore, the concentration extracted from the TS-Cap curve is larger compared to the value derived from the TSC spectrum.

Included in Fig. 7.9a and 7.9b are also the results from simulations which use the position independent average electric field $< E(T) > = V_{bias}/w(T)$ where $w(T)$ is given by:

$$w(T) = \sqrt{\frac{2\varepsilon_0\varepsilon_r V_{bias}}{q_0 N'_{\text{eff}}(T)}} \tag{7.20}$$

Here $N'_{\text{eff}}(T)$ is constant over the depth of the diode and given by Eq. 7.13 where $f(T)$ is calculated with the average electric field $< E(T) >$ of the previous temperature step. For this case, the value $\xi = 1$ and a higher zero-field activation energy of $E_{a0} = 0.284$ eV is needed in the simulation, in order to get the best fit to the experimental data.

In Fig. 7.9c and 7.9d the electric field distribution and the N_{eff} profiles as a function of the depleted depth are plotted for temperatures between 80 K and 110 K in steps of 5 K. As it can be seen in Fig. 7.9c, with increasing the temperature, the maximal value of $E(T_k, x = 0)$ decreases and the depleted depth increases. This corresponds to the development of the effective space charge density $N'_{\text{eff}}(T_k, x)$ for the different temperature steps as shown in Fig. 7.9d. Further, the distribution of the electric field shows a constant gradient before and after the B_iO_i emission (below 85 K and above 100 K) and position dependent gradients during emission of the B_iO_i in the range between 85 K and 100 K. This is due to the non-uniform distributed space charge density resulting from the field dependent emission from the defect energy level.

Similar simulations have been performed for the 23 GeV proton irradiated diode and the results are presented in Fig. 7.10. As it can be seen, the simulation of the TS-Cap signal, shown in Fig. 7.10a, is in excellent agreement with the measured data. In this case, the parameters from the measured $C(T)$ curve, by using the same procedure as for the electron irradiated diode, are $\xi = 0.85$, $E_{a,0} = 0.265$ eV and $[B_iO_i] = 3.5 \times 10^{13}$ cm^{-3}. In Fig. 7.10b the corresponding TSC data and simulated spectra are given. Also in this case the simulation reproduces the data very well, but compared with the TS-Cap simulations, the best agreement is found for slightly different $E_{a,0}$ and $[B_iO_i]$ values, of $E_{a,0} = 0.273$ eV and $[B_iO_i] = 3.3 \times 10^{13}$ cm^{-3}. The ξ value is the same for both simulations. The distributions of the electric field and the N_{eff} profiles are plotted in

Fig. 7.10c and 7.10d for temperatures between 80 K and 110 K in steps of 5 K. In this case, the maximal electric field $E(T_k, x = 0)$ also decreases with increasing the temperature while the depleted region depth increases. The main difference to the electron irradiated device is the lower field strength in the bulk.

7.4.3 Finite Element Method

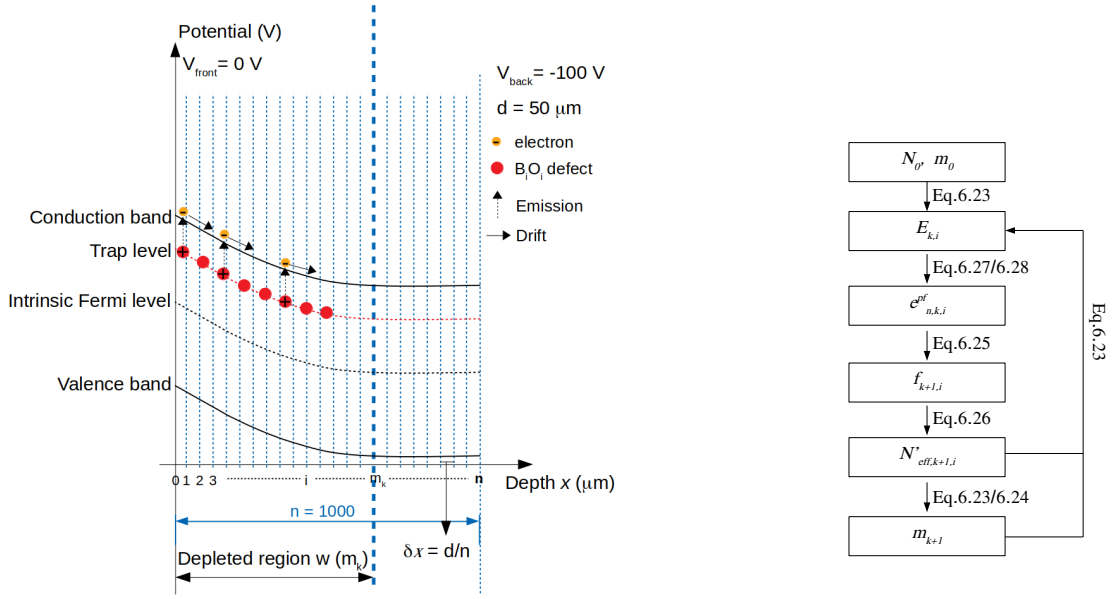

(a) (b)

Figure 7.11: (a) Schematic of finite elements approach applied for describing the field dependent B_iO_i emission in TS measurements. The band gap structure has been divided into n layers by blue lines. (b) simulation procedure.

In this section, the simulation procedure for the TS-Cap and the TSC spectra of the B_iO_i defect will be described. The simulations are performed by using Python software. The bulk of the sensor is divided into n sufficient thin layers of a thickness $\delta x = d/n$, where d is the thickness of the EPI- or Cz-silicon (see Fig. 7.11a)). The index i in Fig. 7.11a runs from 0 to n and the boundary between the depleted and the non-depleted region is labelled m_k. The index k indicates the temperature step T_k and varies between 0 (the start temperature T_0) and f (the final temperature T_f).

As the emission rate of the B_iO_i defect is governed by the 3-D Poole-Frenkel effect (Eq. 7.15, Eq. 7.16 and Eq. 7.17) the applied electric field distribution $E(T, x)$ has to be calculated via the Poisson equation (Eq. 7.19) for a known effective space charge density $N'_{\text{eff}}(T, x)$ (Eq. 7.18). Considering the finite element method mentioned above, the Poisson equation can be written as:

$$E_{k,i+1} - E_{k,i} = \frac{q_0 N'_{\text{eff},k,i}}{\varepsilon_0 \varepsilon_r} \cdot \frac{d}{n} \tag{7.21}$$

Considering the boundary condition between the depleted and the non-depleted region

$$E_{k,i} = 0 \quad \text{for} \quad i \geq m_k \tag{7.22}$$

the $E_{k,i}$ is given by (according to Eq. 7.21):

$$E_{k,i} = \sum_{j=0}^{m_k} \frac{q_0 N'_{\text{eff},k,j}}{\varepsilon_0 \varepsilon_r} \cdot \frac{d}{n} - \sum_{j=0}^{i} \frac{q_0 N'_{\text{eff},k,j}}{\varepsilon_0 \varepsilon_r} \cdot \frac{d}{n} \tag{7.23}$$

where the index j is used to sum $N'_{\text{eff},k,i}$ for layer i from 0 to the boundary or the indicated layer i. Further, the applied bias voltage V_{bias} is given by the sum of all electric field steps $E_{k,i}$ up to the temperature dependent m_k value, as given by:

$$V_{bias} = \sum_{i=0}^{m_k} E_{k,i} \cdot \frac{d}{n} \tag{7.24}$$

This equation (Eq. 7.24) is then used to calculate m_k by rising m_k from 0 up to the value that fulfils Eq. 7.24. Thus for the description of Eq. 7.21-7.24, the only unknown parameter for obtain the $E_{k,i}$ is $N'_{\text{eff},k,i}$. In Eq. 7.18, $N'_{\text{eff},k,i}$ can be obtained by $f_{k,i}$, which in finite elements method can be written to:

$$f_{k+1,i} = \exp\left(-\sum_{j=0}^{k} \frac{\Delta T_j}{\beta} e_{n,j,i}\right) \tag{7.25}$$

where the index j was used to sum the emission rate from temperature T_0 to the T_k. And the Eq. 7.18 can be changed to:

$$N'_{\text{eff},k,i} = N_0 - [\mathrm{B_iO_i}] \cdot (1 - f_{k,i}) \tag{7.26}$$

Considering the 3-D Poole Frenkel effect, the emission rate can be written to:

$$e^{pf}_{n,k,i} = \sigma_n v_{th,n} N_c \exp\left(-\frac{E_{a0}}{k_B T_k}\right) \left[\left(\frac{1}{\gamma^2_{k,i}}\right)\left(e^{\gamma_{k,i}}\left(\gamma_{k,i}+1\right)\right) + \frac{1}{2}\right] \tag{7.27}$$

with

$$\gamma_{k,i} = \xi \cdot \sqrt{\frac{q_0 |E_{k,i}|}{\pi \varepsilon_0 \varepsilon_r}} \cdot \frac{q_0}{k_B T_k} \tag{7.28}$$

For the electron capture cross section we used the value of $\sigma_n = 1.05 \times 10^{-14}$ cm^2 determined experimentally in [22]. The zero field activation energy of the $\mathrm{B_iO_i}$ defect, E_{a0}, was previously determined to be between 0.271 eV and 0.288 eV for silicon diodes with

resistivities varying from 50 Ω·cm to 2 kΩ·cm and irradiated with 23 GeV protons [23]. E_{a0} values were tuned for getting the best fit between simulated and measured data, and all parameters used in the simulation are given in Table 7.1. The concentration [B_iO_i] used for TS-Cap simulation was extracted from the TS-Cap measurement according to Eq. 7.14.

The initial conditions for T_k, $N'_{\mathrm{eff},k,i}$, $e^{pf}_{n,k,i}$, $f_{k,i}$, n and the applied bias voltage V_{bias} are: T_0 = 40 K, $N'_{\mathrm{eff},0,i}$ (N_0) as extracted from TS-Cap at 80 K, $e^{pf}_{n,0,i} = 0$, $f_{0,i} = 1$, n = 1000 and V_{bias} = -100 V. Then, it is obtained that for initial (T_0 = 40 K) electric field distribution $E_{0,i}$ linear decreases from 1.2×10^5 and 5.8×10^4 to 0 V/cm for 5.5 MeV electrons with $\Phi_e = 4 \times 10^{15}$ cm^{-2} and 23 GeV protons $\Phi_p = 6.91 \times 10^{13}$ cm^{-2} irradiation, respectively. And it was also given that the m_0 is equal to 320 and 690 for electrons and protons irradiation, respectively. Such values were extracted from Eq. 7.23 and Eq. 7.24. Next, these values were used to calculate the emission rate $e^{pf}_{n,1,i}$, $f_{1,i}$ and $N'_{\mathrm{eff},1,i}$ (Eq. 7.25-7.28), with which the distribution of the electric field $E_{1,i}$ and m_1 are calculated. This step by step calculation continues until the final temperature T_f is reached. Also, the temperature dependent depletion depth is calculated according to $w(T_k) = m_k \cdot d/n$. The selected T_e must be higher than the temperature of the end of emission, which in this work T_e = 120 K was chosen for simulation. The TSC values at T_k can also be calculated according to:

$$I^e_{TSC,k} = q_0 A[B_iO_i] \sum_{j=0}^{m_k} \frac{j \cdot \frac{d}{n}}{w(T_k)} \cdot e^{pf}_{n,k,j} \cdot f_{k,j} \cdot \frac{d}{n} \tag{7.29}$$

Considering the depleted depth extracted from the TS-Cap measurements, the TSC spectrum was also simulated and compared with the measured data.

7.5 Conclusion

In this work investigations of radiation damage of silicon diodes manufactured on p-type EPI- and Cz-material with a resistivity of about 10 Ω·cm and exposed to 5.5 MeV electrons of different fluence values (1×10^{15}, 4×10^{15}, 6×10^{15} cm^{-2}) have been performed. The macroscopic properties of the devices, the leakage current density J_d and N_{eff}, were obtained from I–V and C–V measurements. The microscopic properties of the B_iO_i and C_iO_i defects were studied using the TSC and TS-Cap methods and the results are discussed in connection with boron removal process observed in macroscopic measurements.

The main results obtained in this study are:

a) The density of leakage current J_d increases linearly with the achieved fluence and the corresponding current related damage parameter is determined to be $\alpha = 3.2 \times 10^{-19}$ A/cm. Such a small value was also reported for n-type silicon diodes after irradiation with 5.5 MeV electrons [163]. Compared with hadron irradiation, the

obtained α parameter is much smaller, indicating that the increase of the leakage current caused by low energy electrons is substantially less than that caused by hadrons. Also, the change of J_d with annealing time at 80 ^{o}C is strongly suppressed compared with hadron irradiated devices indicating that the irradiation with low energy electrons creates less current generation centers and more stable defects.

b) The N_{eff} decreases nearly linear with increasing fluence and remains stable during the isothermal annealing at 80 ^{o}C, in agreement with the thermal stability of the B_iO_i defect [165].

c) The development of B_iO_i and C_iO_i defects with fluence is linear, however, with different introduction rates for EPI and Cz materials, due to the different carbon content in the two materials (more in Cz than in EPI) and the competing reactions between boron and carbon interstitials with abundant oxygen interstitials in silicon. Thus, while the introduction rate of B_iO_i is much smaller in Cz than in EPI material, of 0.63 cm^{-1} compared with 1.75 cm^{-1}, the opposite is happening for C_iO_i. Similar behaviour was also reported in the RD50 collaboration program [21, 86].

d) The formation of B_iO_i defect is the main cause for the change seen in N_{eff} after irradiation with 5.5 MeV electrons. This was nicely evidenced in EPI diodes where the homogeneous boron doping profile allowed accurate evaluations. Thus, by comparing the boron removal rate of 3.7 cm^{-1} resulted from C–V measurements with that of 3.5 cm^{-1} resulted by accounting twice the value of B_iO_i introduction rate due to the donor character of the defect, a good agreement is obtained.

e) The TS-Cap technique proved to be a valuable complementary to the TSC tool in order to accurately characterize the radiation induced defects in highly irradiated and partially depleted silicon sensors. This is especially important in the case of low resistivity diodes when the total depletion of the device in TSC measurements cannot be achieved or the depletion depth cannot be kept constant during the temperature scan. However, TS-Cap allows the evaluation of defect concentrations only if the defects are well isolated in the silicon bandgap, not overlap with other defects.

f) The temperature dependence of the thermally stimulated capacitance at constant bias voltage and of the corresponding TSC spectra, for a 5.5 MeV electron and a 23 GeV proton irradiated devices were simulated in the temperature range of the B_iO_i defect emission. For reproducing the TS-Cap and TSC data the Poole-Frenkel effect was accounted and modified by a subunitar factor ξ and small variations in the defect's zero-field activation energy. Different ξ and E_{a0} values resulted from simulating the experimental data measured on differently damaged silicon diodes, an aspect that has to be further studied in more detail. Presently, we justify these adjustments by the fact that the Poole-Frenkel theory was not developed for position

dependent electric fields as existing in diodes and more pronounced in low resistivity ones, but for constant field around the defect. In the absence of a proper Poole-Frenkel theory for accounting the position dependent electric field in diodes, the adjustments were made for describing as good as possible both B_iO_i current and capacitance signals. In addition, when accounting for the electric field dependent electron emission from B_iO_i defect, the simulated electric field distributions $E(T, x)$ for the temperature range where the B_iO_i defect discharges, between 80 K and 110 K, show position dependent gradients, corresponding to the position dependent effective space charge densities $N'_{\text{eff}}(T, x)$.

7.6 Additional Materials

7.6.1 Forward Bias Filling vs Vbias

In general, the extracted $[B_iO_i]$ from TSC and TS-Cap measurements with forward bias filling should be consistent, regardless of the applied V_{bias}. However, it is important to consider the influence of lateral effects and the non-uniform distribution of $[B_iO_i]$ in Cz diodes. As shown in Fig. 7.12, which displays the TSC and TS-Cap measurements with different V_{bias} values conducted on EPI-7 and Cz-7, an evident increase in the B_iO_i peak amplitude and a change in the depleted depth caused by B_iO_i emission can be observed as the V_{bias} increases.

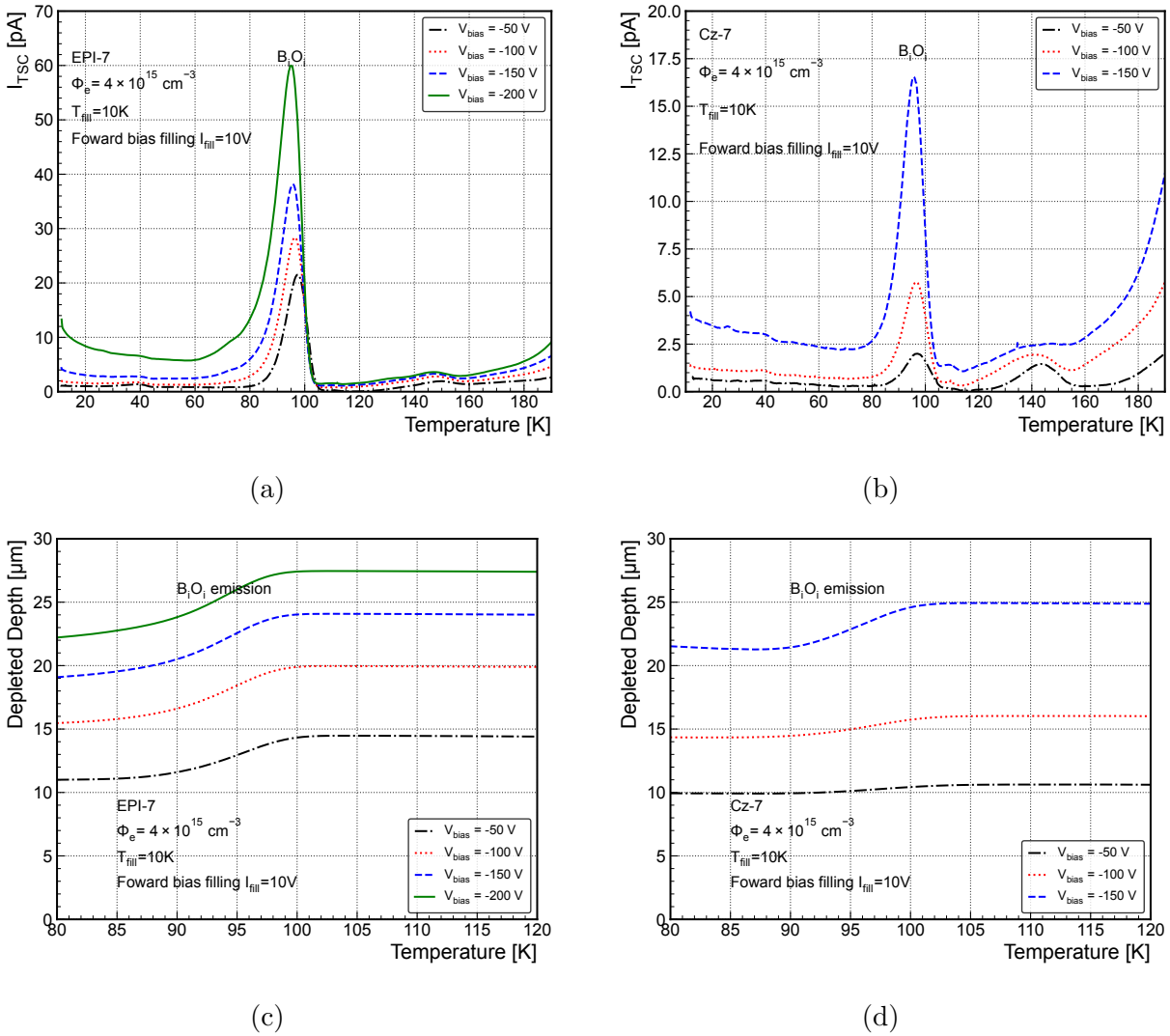

Figure 7.12: (a) and (b) are the TSC spectra with forward bias filling (I_{fill} = 1 mA) different V_{bias} indicated in the legend for diodes EPI-7 and Cz-7, respectively. (c) and (d) are the corresponding TS-Cap measurements for (a) and (b) respectively.

The extracted $[B_iO_i]$ values obtained from the measurements shown in Fig. 7.12, using Eq. 7.9, are presented in Fig. 7.13. These measurements were performed prior to anneal-

ing, and it was observed that [BiOi] remained stable after isothermal annealing at 80 °C. In the case of Cz-7, it was found that the lateral effect significantly influenced the current when V_{bias} exceeded 100V, as shown in Fig. 7.2. Therefore, the [B_iO_i] values extracted from measurements with V_{bias} of 100 V were used in this study.

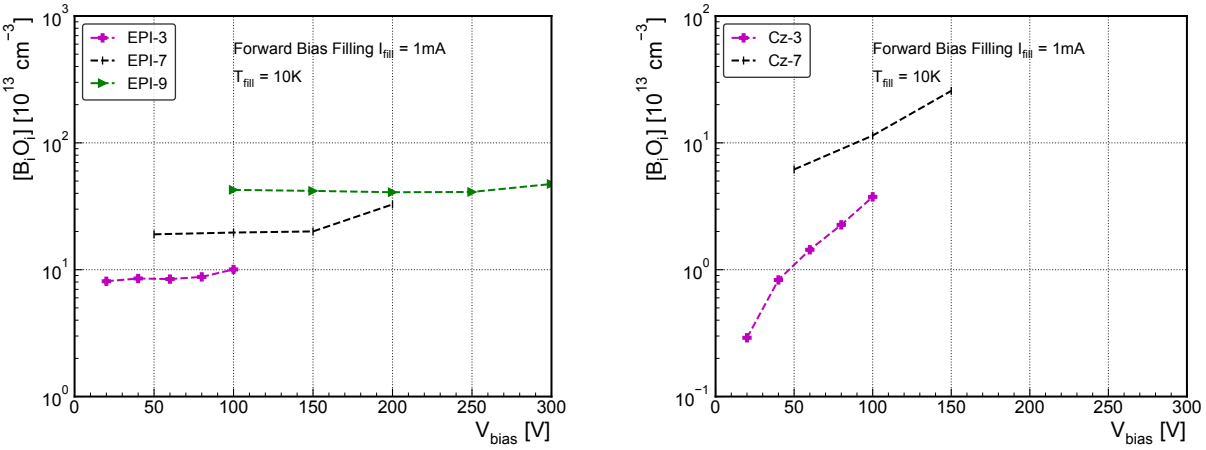

(a) (b)

Figure 7.13: [B_iO_i] extracted from (a) EPI and (b) Cz diodes before annealing, the radiation detail can be found in Table 7.1.

7.6.2 TS-Cap with Different Frequency

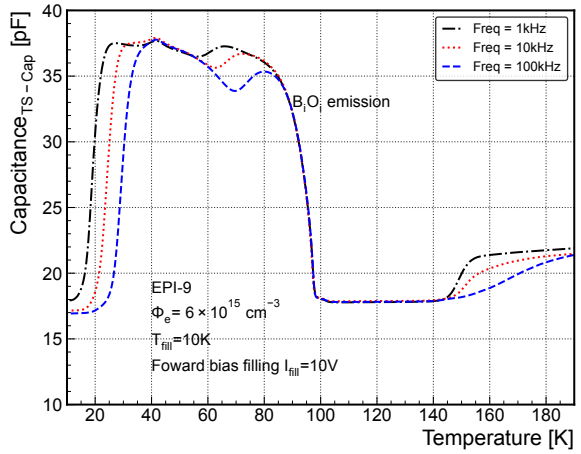

Figure 7.14: TS-Cap measurement with different frequencies indicated in the legend. TS-Cap parameters: Forward bias filling with I_{fill}=1 mA, T_{fill}=10 K.

In order to understand the frequency-dependency of TS-Cap measurements, the TS-Cap with different frequencies (1 kHz, 10 kHz, and 100 kHz) were presented for the diode irradiation with the highest fluence, i.e. EPI-9, in Fig. 7.14. As can be seen here, frequency-dependency is not observed. In this work, all the TS-Cap measurements are performed with frequencies of 100 kHz.

7.6.3 Majority Carrier Filling vs Vbias

In this study, TSC and TS-Cap techniques with majority carrier filling were employed to investigate the radiation-induced C_iO_i defect. However, it was observed that the N_{eff} decreases as the fluence increases in the investigated diodes. This behaviour poses challenges when performing majority carrier filling in diodes irradiated at different fluence levels. The main challenge arises from the increase in leakage current with the V_{bias}, which impacts the accuracy of the extracted defect concentration, particularly for defects appearing in the high-temperature range such as C_iO_i.

EPI-3, Cz-3

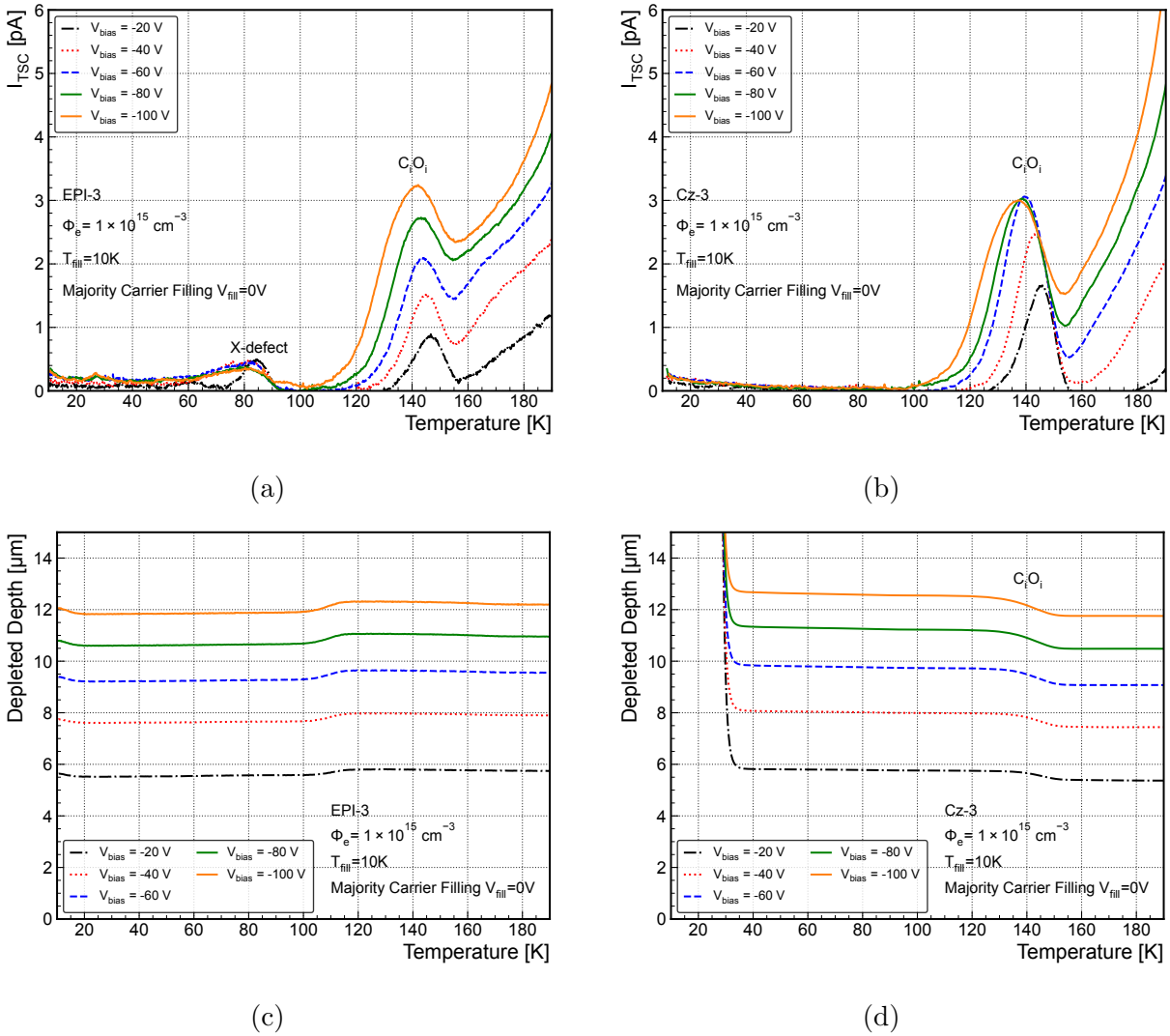

Figure 7.15: (a) and (b) are the TSC spectra with majority carrier filling (V_{fill} = 0 V) different V_{bias} indicated in the legend for diodes EPI-3 and Cz-3, respectively. (c) and (d) are the corresponding TS-Cap measurements for (a) and (b) respectively.

Figure 7.15 depicts the majority carrier filling TSC and TS-Cap measurements with

varying V_{bias}. It is evident from the figure that the leakage current or noise substantially increases in the C_iO_i peak as the applied bias voltage (V_{bias}) increases. Consequently, to extract the concentration of C_iO_i in this study, a fixed bias voltage of $V_{\text{bias}} = 20$ V was employed.

EPI-7, Cz-7

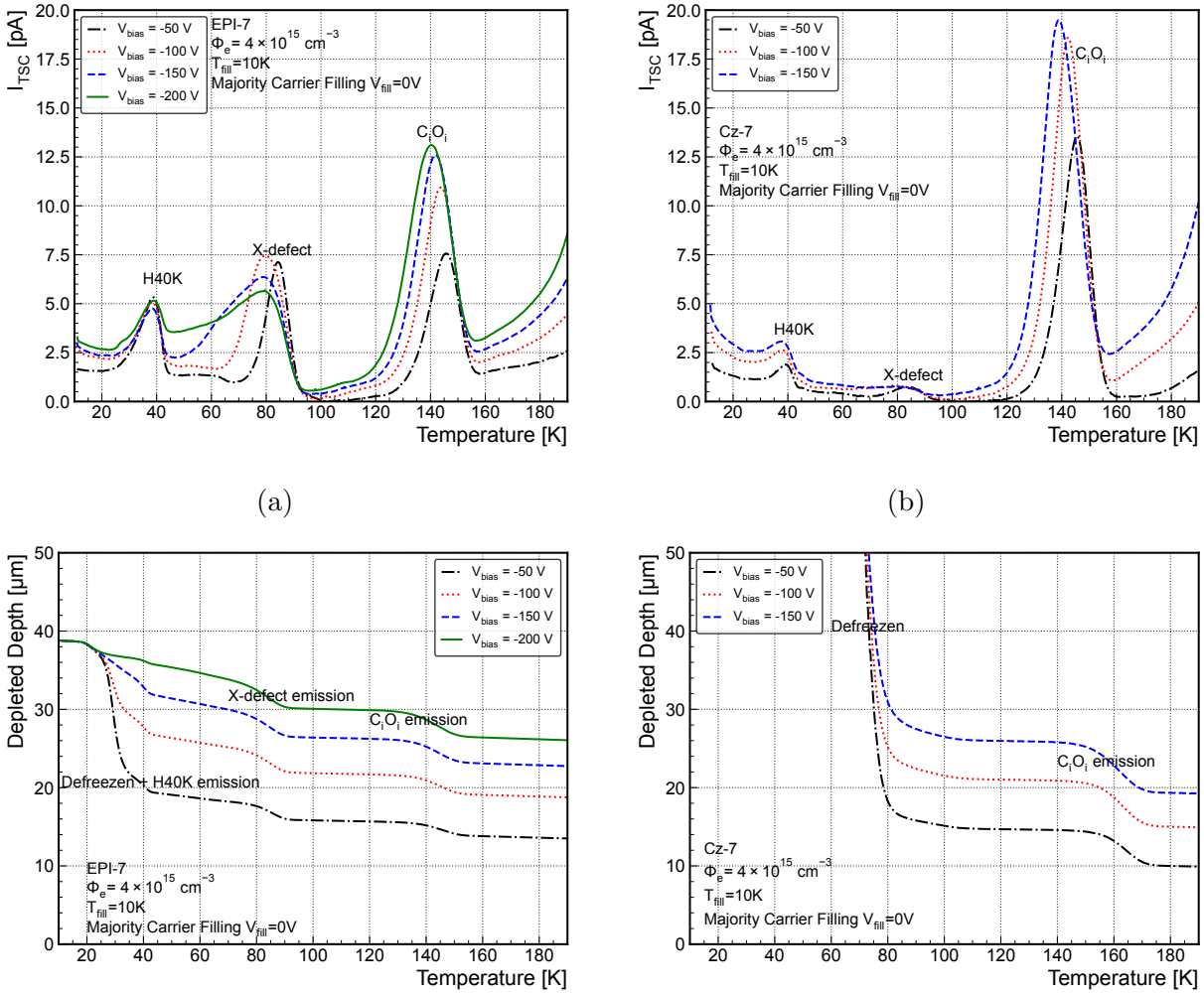

Figure 7.16: (a) and (b) are the TSC spectra with majority carrier filling ($V_{\text{fill}} = 0$ V) different V_{bias} indicated in the legend for diodes EPI-7 and Cz-7, respectively. (c) and (d) are the corresponding TS-Cap measurements for (a) and (b) respectively.

The increase in leakage current with V_{bias} is also observed in EPI-7 and Cz-7 diodes, as shown in Fig. 7.16. However, its impact on the maximum of the C_iO_i peak is relatively small, less than 10%. In addition to the effect of leakage current, the presence of H40K and X-defects discussed in chapter 6, is also observed in this group of diodes. The results for the X-defect in EPI-3 can be found in Fig. 7.15a. It can be concluded that these

two defects decrease with increasing [C_s] by comparing the results between EPI- and Cz-diodes.

8 ^{60}Co γ-ray Irradiation

Note: This chapter is a copy of the published paper [166] with minor corrections. The additional materials can be found after the conclusion.

Abstract: In this work, the effects of ^{60}Co γ-ray irradiation on high resistivity p-type diodes have been investigated. The diodes were exposed to dose values of 0.1, 0.2, 1, and 2 MGy. Both macroscopic (I–V, C–V) and microscopic (Thermally Stimulated Current (TSC)) measurements were conducted to characterize the radiation-induced changes. The investigated diodes were manufactured on high resistivity p-type Float Zone (FZ) silicon and were further classified into two types based on the isolation technique between the pad and guard ring: p-stop and p-spray. After irradiation, the macroscopic results of current-voltage and capacitance-voltage measurements were obtained and compared with existing literature data. Additionally, the microscopic measurements focused on the development of the concentration of different radiation-induced defects, including the boron interstitial and oxygen interstitial (B_iO_i) complex, the carbon interstitial and oxygen interstitial C_iO_i defect, the H40K, and the so-called I_P^*.

To investigate the thermal stability of induced defects in the bulk, isochronal annealing studies were performed in the temperature range of 80 °C to 300 °C. These annealing processes were carried out on diodes irradiated with doses of 1 and 2 MGy and the corresponding TSC spectra were analysed. Furthermore, in order to investigate the unexpected results observed in the C–V measurements after irradiation with high dose values, the surface conductance between the pad and guard ring was measured as a function of both dose and annealing temperature.

8.1 Motivation

In High Luminosity Large Hadron Collider (HL-LHC) experiments, strip and pixel silicon sensors in the inner tracking detectors have to cope with extraordinarily high particle rates of up to 200 p–p collisions per bunch crossing. New types of sensors to be used for this purpose, started to be developed. They are manufactured on boron doped (p-type) silicon and have different structures, from the simplest p-i-n diode to devices which amplifies the signals and have better time resolution, as e.g. the Low Gain Avalanche Detectors (LGADs) [2, 3]. The degradation in the performance of these sensors is caused by the generation of electrically active radiation-induced defects. For instance, the charged defects at room temperature (e.g. E30K, B_iO_i, H140K, H152K and I_P) [15, 16, 17, 18]

cause changes of the space charge density (N_{eff}). Vacancy related traps such as V_2 and V_3 [19] lead to the degradation of charge collection efficiency (CCE) and an increase of dark current. In general, the radiation-induced defects can be classified according to their size: point defects, up to 2-3 atoms size, or more extended ones, also known as cluster-related defects. All the radiation-induced defects contribute to the degradation of silicon sensors and can be characterized using spectroscopic techniques such as Deep Level Transient Spectroscopy (DLTS), for low defect concentration, and Thermally Stimulated Current (TSC) after high levels of irradiation when DLTS does not work anymore. During a temperature scan, both, point and cluster-related defects are contributing to the signals observed in TSC and DLTS measurements. Detecting and analyzing the combined effects of these defects pose a challenge for these techniques.

The main radiation damage effect seen in p-type silicon sensors is the deactivation of the boron dopant. Thus, the atoms of substitutional Boron (B_s) may switch the sites with interstitial silicon (Si_i) created during radiation via a Watkins replacement mechanism [20] and transform in boron interstitial (B_i), losing its acceptor character. The B_i atoms migrate in the crystal and react with interstitial oxygen, found in abundance in silicon, leading to the formation of B_iO_i complex. Another possible acceptor removal mechanism in p-type silicon considers the interaction between the negatively charged acceptor dopant (B_s for boron-doped silicon) and the positively charged Si_i atoms forming the B_s-Si_i complex [167, 168]. The boron removal effect induced by 23 GeV protons, 5.5 MeV electrons and 1 MeV neutrons was investigated in the framework of the CERN-RD50 "Acceptor removal project" [22, 23, 160, 169, 170]. This effect can also be introduced by high-energy photons i.e. ^{60}Co γ–rays. While hadrons can produce both point and cluster-related defects, γ–rays introduce only point defects [11, 171]. In this work, n^+-p diodes irradiated with ^{60}Co γ–rays are investigated. This means that the changes in the macroscopic properties of silicon sensors, as determined from Current-Voltage (I–V)/Capacitance-Voltage (C–V) characteristics are attributed to point defects only.

The paper is structured as follows. Section 8.2 includes information on the fabrication of the investigated diodes, irradiation details and measurement procedures. In section 8.3 the results of the macroscopic (I–V/C–V) and microscopic (TSC) investigations, on as-irradiated and annealed samples, are presented and discussed. The conclusions of this work are presented in section 8.4.

8.2 Experimental Details

The study was performed on 12 p-type silicon diodes which were designed for upgrading the planar pixel sensors in the Compact Muon Solenoid (CMS) inner tracker for HL-LHC at CERN. These diodes were manufactured by Hamamatsu Photonics K. K. (HPK), and were processed on, so-called, FDB150 (float zone Si-Si direct bonded) wafers, obtained by bonding together two wafers: a high resistivity float zone (FZ) wafer and a low resistivity

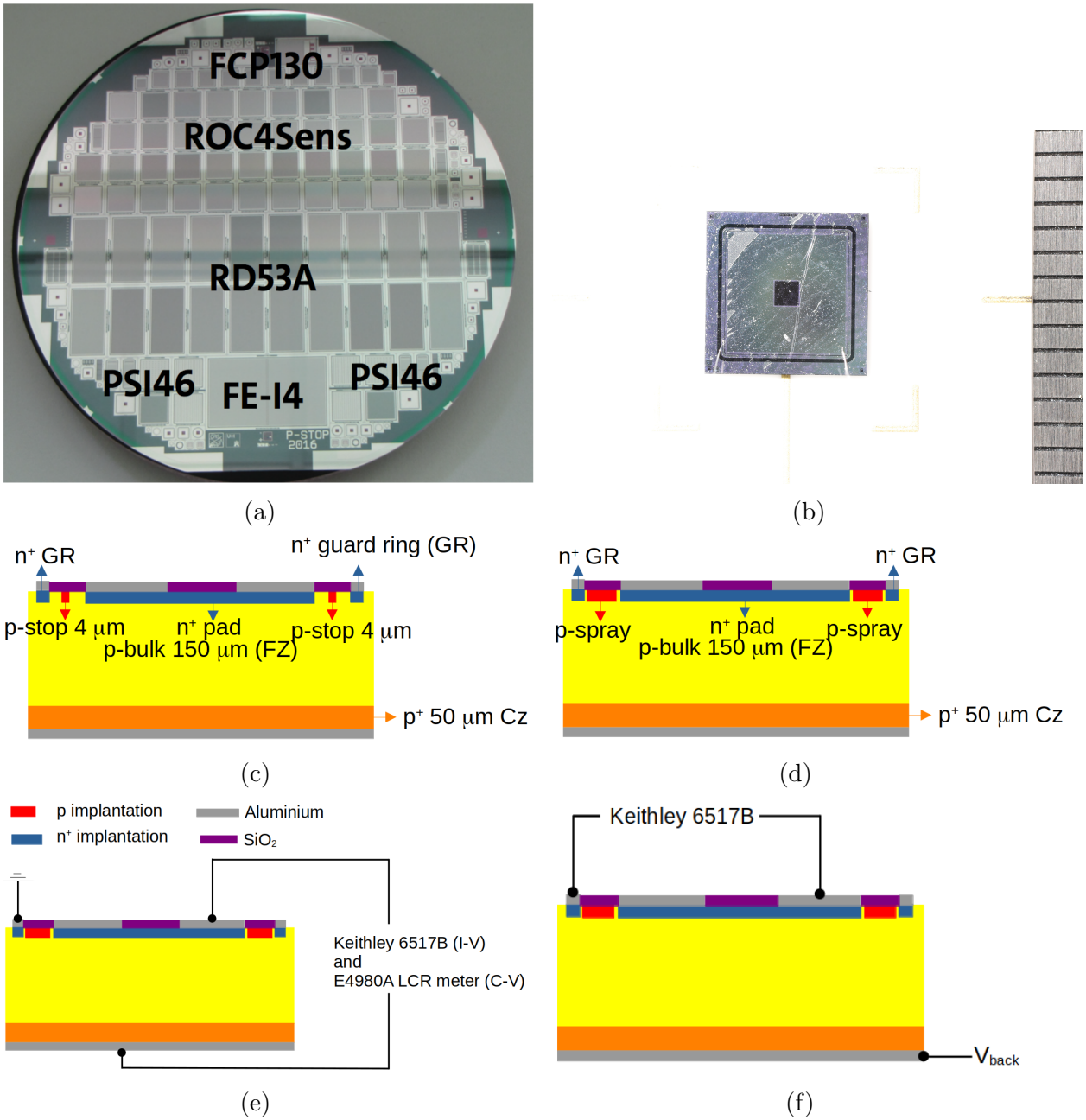

Figure 8.1: (a) Wafer layout of a 6-inch HPK wafer with *p*-stop isolation. The figure is taken from [172]. (b) Overview of F150P-1, the value of 1 mm between two lines on the right side. (c) Side view of p-stop diodes. (d) Side view of p-spray diodes. (e) Schematic representation of the electrical setup used for I–V/C–V measurements. (f) Schematic representation of the electrical circuit used for measuring the surface current.

handle one, produced with the Czochralski (Cz) method. The FZ wafer is thinned down to an active thickness of 150 µm and after processing the pixel sensors, diodes and other test structures, the handle wafer is thinned down to 50 µm, resulting in a total thickness of 200 µm-see Fig. 8.1c and Fig. 8.1d.

The initial boron doping of the FZ bulk is $N_{\text{eff},0} = 3.5 \times 10^{12}$ cm^{-3}, corresponding to a resistivity of about 4 k$\Omega \cdot$ cm. Besides boron, the main impurity in the bulk is oxygen,

having a concentration of about 1×10^{17} cm^{-3} [173]. The backside Cz material has a boron content of 1×10^{19} cm^{-3}. According to the design of the isolation between the pad and guard ring structure, there are two types of diodes: with *p*-stop (FDB150P, simplified to F150P in this work)and *p*-spray (FDB150Y, simplified to F150Y in this work). The pad and guard ring are isolated by a thin (4 µm) boron-implanted region on the surface in the case of *p*-stop, while *p*-spray is a boron implant across the full wafer surface before the processing of the sensors-see Fig. 8.1c and Fig. 8.1d. The active area of the diodes is 0.25 cm^2. More details can be found in [173, 172].

The 12 diodes were divided into four groups, each containing two *p*-stop type and one *p*-spray type diode. The proposed dose values for ^{60}Co γ irradiation of each of the groups were 0.1, 0.2, 1 and 2 MGy. The irradiation was performed using the ^{60}Co Panoramic Irradiation facility at Rudjer Boskovic Institute [125]. Considering the radiation flux and exposure time, the following dose values were achieved: 94±0.96, 189±3.9, 924±27 and 1861±56 kGy. The investigated diodes and the achieved irradiation doses are given in Table 8.1.

The electrical performance of the diodes was measured by means of *I*–*V* and *C*–*V* characteristics at 20 ± 0.01 °C. For all the diodes, the space charge density (N_{eff}) and the depleted depth $w(V)$ were determined from *C*–*V* measurements corresponding to a frequency of 500 kHz, and an AC voltage of 500 mV. The electrical circuit for measuring *I*–*V*/*C*–*V* characteristics is depicted in Fig. 8.1e. The current flow between the pad and the guarding was measured using the circuit given in Fig. 8.1f. The radiation-induced electrically active defects were investigated by means of the TSC technique. Details of the experimental setup can be found in [23, 11, 133, 52]. In this work, the trap filling was performed at different filling temperatures (T_{fill} = 10-100 K, in steps of 10 K) by injection of a forward current (I_{fill}) produced by a forward bias of V_{fill} = 10 V for 30 s. For T_{fill} = 10 K, the $I_{\text{fill}} < 1$ mA and shows negligible dependence on the dose and the type of isolation. For $T_{\text{fill}} \geq 20$ K, all the I_{fill} roughly equal to 1 mA. The TSC spectra were then recorded for different reverse biases V_{bias} applied to the sample (-100 to -300 V in steps of 50 V) during heating up the samples with a constant heating rate of $\beta = 0.183$ Ks^{-1}. Isochronal annealing experiments were conducted using a Thermo SCIENTIFIC oven with air as the annealing atmosphere.

8.3 Results and Discussion

8.3.1 As-irradiated devices

In Fig. 8.2 are given the *I*–*V* and the $1/C^2$–*V* curves of all *p*-spray diodes irradiated to different dose values. Included are also the data for the F150Y-8 diode before being irradiated. The N_{eff} depth profile was determined from *C*–*V* measurements,considering the following relations for $N_{\text{eff}}(w(V))$ and the depletion depth $w(V)$:

Table 8.1: Device information

p-stop(label)	F150P-1	F150P-3	F150P-5	F150P-8
p-stop(label)	F150P-2	F150P-4	F150P-7	F150P-9
p-spray(label)	F150Y-1	F150Y-2	F150Y-5	F150Y-8
Initial resistivity $N_{\text{eff},0}$ (cm^{-3})	3.5×10^{12}	3.5×10^{12}	3.5×10^{12}	3.5×10^{12}
Initial resistivity ($\text{k}\Omega \cdot \text{cm}$)	$\approx$4	$\approx$4	$\approx$4	$\approx$4
Dose value (kGy)	94$\pm$0.96	189$\pm$3.9	924$\pm$27	1861$\pm$56
Area A (cm^2)	0.25	0.25	0.25	0.25
Geometric thickness D (μm)	200	200	200	200
Active thickness d (μm)	150	150	150	150
Oxygen concentration [O] (cm^{-3})	$\sim 1 \times 10^{17}$	$\sim 1 \times 10^{17}$	$\sim 1 \times 10^{17}$	$\sim 1 \times 10^{17}$

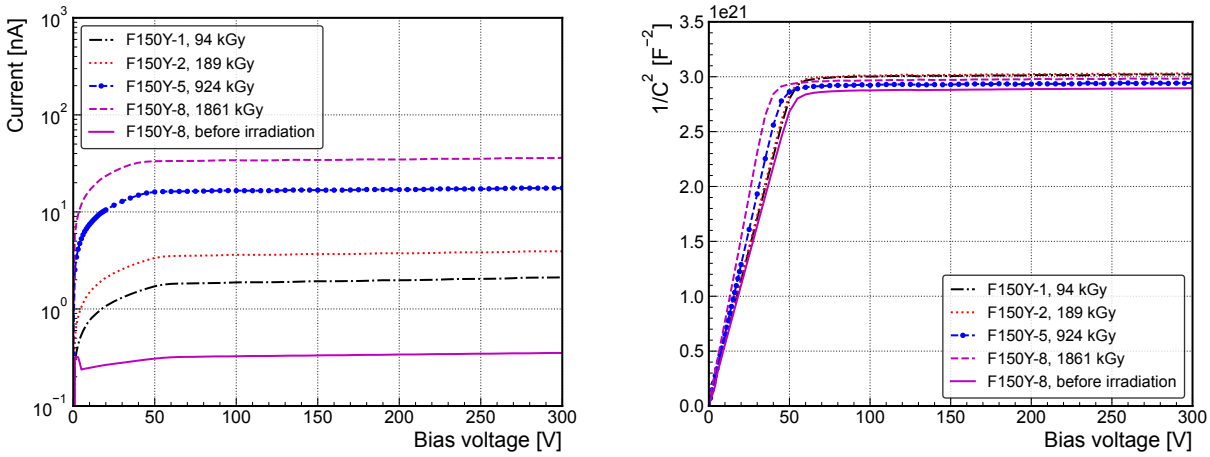

(a) (b)

Figure 8.2: (a) Current-voltage (I–V) characteristics of p-spray diodes irradiated to different dose values (see legend). (b) Capacitance-voltage ($1/C^2$-V) characteristics for the same diodes as in (a) for a frequency f = 500 kHz and $V_{\text{AC}} = 500$ mV. Included in (a) and (b) are data for one diode before irradiation. Measurement condition: $T = 20\,^{\circ}\text{C}$, humidity $\leq 10\,\%$.

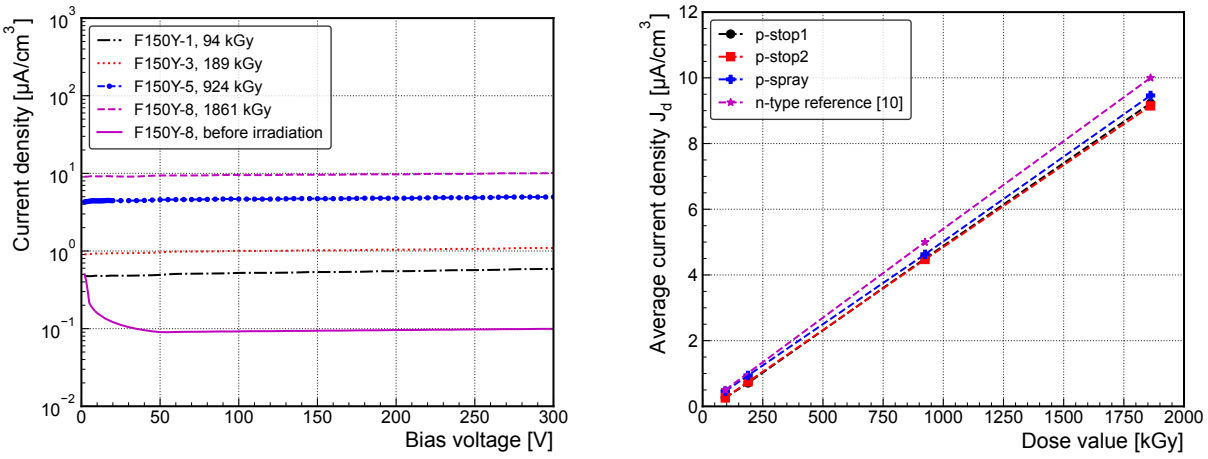

(a) (b)

Figure 8.3: (a) Density of leakage current (j_d) versus bias voltage V, which developed from Fig. 8.2a and 8.2b. (b) Average current density J_d vs. Dose value (details see text).

$$N_{\text{eff}}(V) = \frac{2}{\epsilon_0 \epsilon_r A^2 q_0 \, d(1/C^2)/dV} \tag{8.1}$$

$$w(V) = \frac{\epsilon_0 \epsilon_r A}{C(V)} \tag{8.2}$$

where C is the measured capacitance, ϵ_0 is the permittivity of vacuum, ϵ_r the relative permittivity of silicon (11.9), q_0 is the elementary charge, A is the active pad area. Considering the voltage dependence of the depletion depth (Eq. 8.2) the current density $j_d(V)$ can be calculated from the measured I-V curves according to $j_d(V) = I(V)/(\text{A}\cdot w(V))$. The results are shown in Fig. 8.3a, for the different dose values applied to the corresponding p-spray diodes. Average current densities J_d as taken from $j_d(V)$ data, in the 100 V and 150 V voltage range for V_{bias}, are plotted in Fig. 8.3b as a function of the dose, for both, p-stop and p-spray diodes. The data achieved for n-type oxygen-enriched DOFZ diodes, taken from reference [174], are also included. As can be observed in Fig. 8.3b, all the presented results are nearly identical.

For the current density J_d of the p-spray type diodes, an error of 1% was estimated. This includes the uncertainty of the measured current and the depleted volume extracted from the C–V data. The corresponding value for the p-stop diodes was estimated to be 2%. The definition of current-related damage parameters α can also be applied to γ-ray damage with dose value (D):

$$\alpha_\gamma = \frac{\Delta J_d}{\Delta D} \tag{8.3}$$

According to Eq. 8.3 the α_γ value for the p-spray diodes is estimated to be $\alpha_\gamma =$

5.09×10^{-12} A/(Gy · cm^3) with an error of 4.4%. The value for the *p*-stop diodes is 5.07×10^{-12} A/(Gy · cm^3) with an error of 5.4%. The errors are dominated by the uncertainties of the dose values (see Table 8.1). Figure 8.4 presents the extracted N_{eff} profiles for *p*-spray diodes, different irradiation dose values. With increasing the dose, the profiles are shifted to lower N_{eff} values. Such behaviour is expected due to the deactivation of the initial boron concentration caused by irradiation, the so-called acceptor removal effect [22, 23, 160, 169, 170].

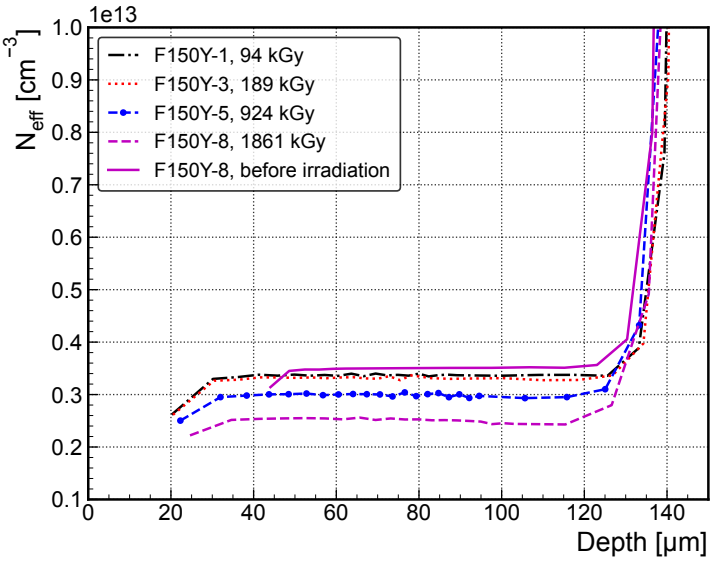

Figure 8.4: N_{eff} profile of the diodes for different dose values. The data were evaluated from *C*–*V* measurements by using Eq. 8.1 and Eq. 8.2.

It should be mentioned here that the *C*–*V* measurements were also performed for different frequencies (230 Hz, 455 Hz, 1 kHz, 10 kHz, 100 kHz, 200 kHz, 400 kHz, 500 kHz) and a frequency dependence was observed only for *p*-stop diodes. This aspect will be discussed later in the section 8.3.3 "Surface effects".

In order to investigate the radiation-induced defect complexes by ^{60}Co γ-rays in the high resistivity FZ diodes, the TSC method is used. Figure 8.5a and 8.5b show TSC spectra of *p*-stop and *p*-spray diodes irradiated to different dose values, respectively. All spectra in Fig. 8.5 were measured on fully depleted sensors ($V_{\text{bias}} = -200$ V, $V_{\text{dep}} = -50$ V) over the entire TSC temperature range. As can be seen in Fig. 8.5, several peaks are induced after irradiation and increase with dose. Some of these traps corresponded to the previously detected radiation induced defect complexes H40K [17, 175], VO [24], B_iO_i [15], C_iO_i [11, 24] and V_2 [19]. A TSC peak, similar to the one labelled as I_P^* in Fig. 8.5, has been reported as I_P defect in previous studies and associated with V_2O complex, a defect predominantly generated via a second order process in oxygen-lean material, thermally stable up to 350 °C and with a strong impact on both, the leakage current and N_{eff} [18, 163, 100, 176]. However, the trapping parameters determined for the I_P^* defect are different compared with of I_P defect - see Table 8.2. Accordingly, also

the impact of the I_P^* defect on both leakage current and N_{eff} are negligible. By comparing Fig. 8.5a and Fig. 8.5b, it can be observed that some of the peaks observed in the *p*-spray diodes are smaller compared to those recorded in the *p*-stop ones (H40K, E50K, VO and C_iO_i). This might be due to the different filling of the defects at 10 K. As demonstrated in Fig. 8.5c most peaks show a strong dependence on the filling temperature, except the B_iO_i and I_P^* traps. Previous studies have shown that for the C_iO_i defect an extremely strong dependence on the filling temperature (T_{fill}) exists and thus, suggesting a multi-phonon capture process [11, 12]. To get the full defect concentration TSC measurements with different T_{fill} (from 20-100 K in steps of 10 K) were performed.

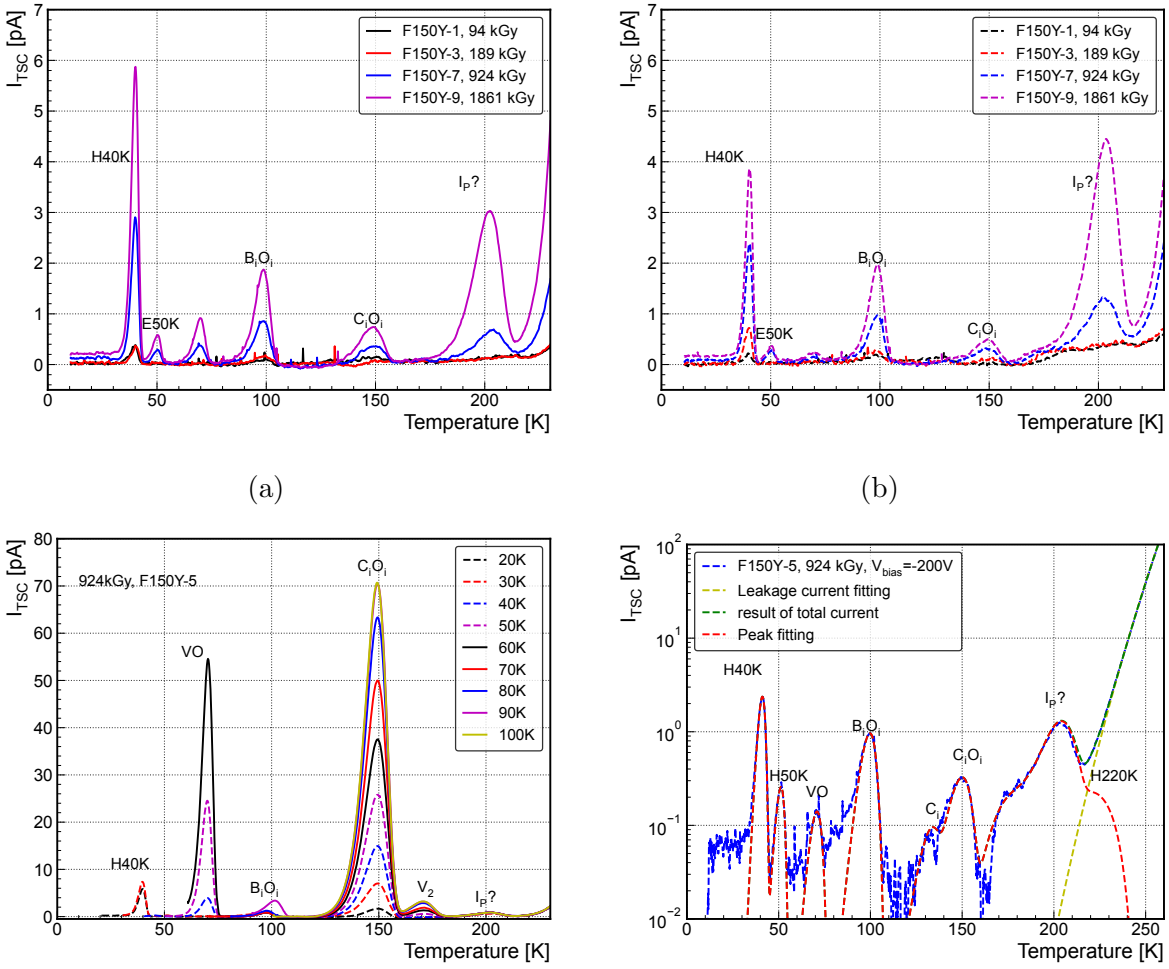

Figure 8.5: (a) TSC Spectra for *p*-stop diodes after trap filling by forward current (V_{fill} = 10 V) injection at 10 K and (b) for *p*-spray diodes. Both spectra are measured on the diodes after irradiation with ^{60}Co-γ to dose values given in the legend. The heating up bias voltages V_{bias} = -200 V. (c) TSC Spectra after same filling processing but with different T_{fill} for diode F150Y-5. (d) Example of reproducing a TSC spectrum by fitting the different peaks.

As can be seen in Fig. 8.5c, an increase of the peak height with increasing T_{fill} is not only observed for the C_iO_i defect but also for the H40K, VO and the V_2 defect complexes.

Only the B_iO_i and I_P^* have the same peak maximum for different T_{fill}. The abrupt increase in the B_iO_i peak after filling at 90 K is attributed to the higher and not constant heating rate at the initial stage of the temperature ramp. In the fully depleted diodes, the general formula of thermally stimulated current $I^e_{TSC}(T)$ or $I^h_{TSC}(T)$ for a single electron or hole trap is given by [11, 52, 130, 133, 134]:

$$I^e_{TSC}(T) = \frac{1}{2} \cdot q_0 \cdot A \cdot d \cdot e_n(T) \cdot n_t(T_{fill}) \cdot f\,(T) \tag{8.4}$$

$$I^h_{TSC}(T) = \frac{1}{2} \cdot q_0 \cdot A \cdot d \cdot e_h(T) \cdot p_t(T_{fill}) \cdot f\,(T) \tag{8.5}$$

$$e_{n,p} = \sigma_{n,p} \cdot v_{th,n,p} \cdot N_{C,V} \cdot \exp\left(-\frac{E_a}{k_B T}\right) \tag{8.6}$$

$$f(T) = \exp\left(-\frac{1}{\beta}\int_{T_0}^{T} \left(e_n(T') + e_p(T')\right) dT'\right) \tag{8.7}$$

where T is the measured temperature, d is the fully depleted depth. e_n and e_p are the emission rates for electrons and holes. $v_{th,n,p}$ and $N_{C,V}$are the thermal velocity of electrons/holes and the density of states in the conduction/valence band, respectively, both taken from [59]. The activation energy is defined as $E_a = E_C - E_t$ or $E_a = E_t - E_V$ according to the type of emitted charge, electrons or holes, respectively, with E_t being the energy level of the trap and $E_{C,V}$ the conduction/valence band edges. The $\sigma_{n,p}$ terms stand for the capture cross-section of electrons/holes, k_B is the Boltzmann constant and the $f(T)$ function is the defect occupancy at temperature T. The $n_t(T_{fill})$ and $p_t(T_{fill})$ terms represent the density of defects that are filled with electrons or holes after injection at temperature T_{fill}. The considered trapping parameters are given in Table 8.2 and kept fixed in the peak fitting procedure.

Table 8.2: The trapping parameters of the detected defects. An example of how much these defects contribute to the change in N_{eff} and J_d at RT is given for F150Y-5.

label	H40K [175]	E50K [11]	VO [24]	B_iO_i [22]	C_iO_i [24]	V_2 [11]	I_P^* This work
σ_p (10^{-15} cm^2)	4.3	-	-	1×10^{-5}	0.94	-	0.02
σ_n (10^{-15} cm^2)	-	5.4	6.1	10.5	-	1.5	7.1
	E_t-E_V	E_C-E_t	E_C-E_t	E_C-E_t	E_t-E_V	E_C-E_t	E_C-E_t
E_a (eV)	0.108	0.11	0.16	0.26	0.37	0.43	0.52

For describing the leakage current, I_{LC} measured at temperatures $T \geq 230\,\text{K}$, the following equation is used [177]:

$$I_{LC} = \chi \cdot T^2 \cdot \exp\left(-\frac{\delta E}{k_B T}\right) \tag{8.8}$$

where the χ and δE are free parameters in the fitting procedure. The extracted values are achieved from fits to the data in the temperature ranges from 230 K to 250 K at V_{bias} = -200 V, which are included in Table 8.3. For both parameters, the errors were estimated to be below 1%.

Table 8.3: Extracted fit parameters for the leakage current LC (V_{bias} = -200 V) by using Eq. 8.8.

	F150P-1	F150P-3	F150P-7	F150P-8
p-stop χ (A/K)	0.0021	0.0204	0.1273	0.4415
p-stop δE (eV)	0.6594	0.7103	0.7103	0.7196
	F150Y-1	F150Y-2	F150Y-5	F150Y-8
p-spray χ (A/K)	0.0005	0.0037	0.1260	0.2002
p-spray δE (eV)	0.6410	0.6744	0.7103	0.7103

The concentrations of defects were determined by fitting the measured TSC peaks using the equations Eq. 8.4-8.7. An example of fitting a TSC spectrum is presented in Fig. 8.5d for a p-spray diode irradiated with a dose of 94 kGy. The dependence of the C_iO_i concentration ($[C_iO_i]$) on the filling temperature T_{fill} is shown in Fig. 8.6a. As it can be observed, $[C_iO_i]$ initially increases with T_{fill} and saturates at $T_{\text{fill}} \geq 60$ K. To describe the T_{fill} dependence of $[C_iO_i]$ the following equation is used [11, 12, 178]:

$$n_t(T_{fill}) = N_{offset} + N_t \times \frac{1}{1 + a \cdot \exp\left(\frac{E_s}{k_B T_{fill}}\right)} \tag{8.9}$$

The offset value is caused by the background current. N_t is the total C_iO_i concentration $[C_iO_i]$, and a is a constant. E_s is the activation energy for non-radiative multi-phonon capture of a charge carrier, accounting for the temperature dependence of the capture cross sections [178]. The term $a \cdot \exp\left(\frac{E_s}{k_B T_{fill}}\right)$ is given by the ratio $\frac{n \cdot c_n}{p \cdot c_p}$, where n and p are the concentrations of free electrons and holes under forward bias injection and $c_{n,p}$ are the capture coefficients of the corresponding charge carriers.

The parameters obtained for fitting the C_iO_i data in Fig. 8.6a are: a = (1.18 ± 0.03) ×10^{-2}, E_s = (13.2 ± 0.2) meV, N_{offset} = (6.1 ± 0.5) ×10^{10} cm^{-3}, and N_t = (2.5 ± 0.1) ×10^{12} cm^{-3}. The fitted result is plotted in Fig. 8.6a together with the experimental data. We also included a calculated curve using the values of $a = 10^{-4}$ and E_s = 37.3 meV given in a previous study on neutron irradiated diodes [11], considering the same values of N_{offset} and N_t as in our data fit. The different a and E_s values in our fit compared with those from Moll [11] might be explained by the potential barriers surrounding the clustered regions induced by neutron irradiation, which can slow down the carriers capturing process [179, 180].

The increase with dose in the concentration of the TSC detected defects on the p-spray

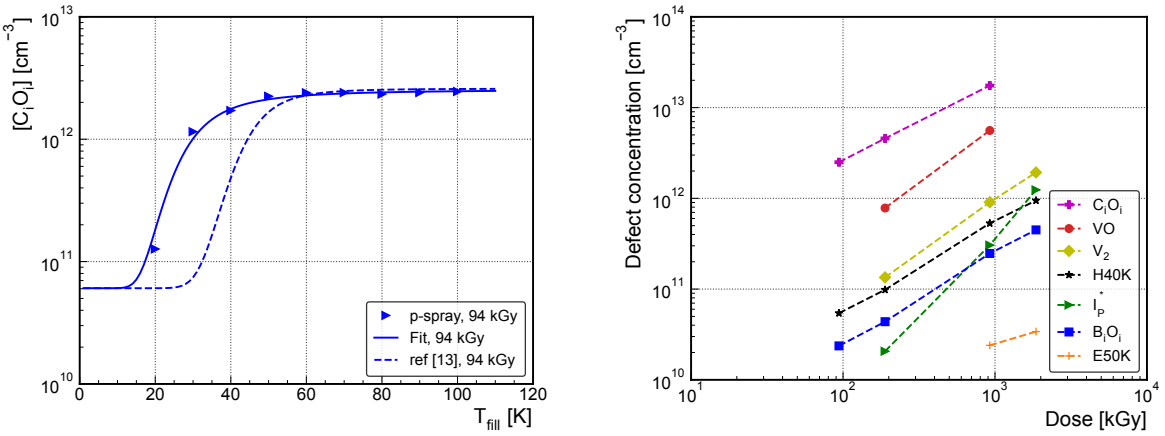

(a) (b)

Figure 8.6: (a) $[C_iO_i]$ vs T_{fill}, which included the data, our fits and literature value. The data of $[C_iO_i]$ are extracted from TSC spectra e.g. Fig. 8.5c. The fit results are given by fitting using Eq. 8.8. (b) Defect concentration vs Dose value included all observed defects.

diode is shown in Fig. 8.6b. Worth noting is that among all the defects, only the I_P* defect does not have a linear dependence on Dose, but a quadratic one (slope $\sim$ 2 in Fig. 8.6b) as previously reported for the I_P defect, a radiation-induced defect formed via a second order process. Considering the definition of the introduction rate $g = \frac{\Delta N_t}{\Delta D}$, the rates for γ-ray irradiation were extracted from the linear fits to the data (see Fig. 8.6b) and are summarized in Table 8.4.

Table 8.4: Introduction rates g_D

Defect	H40K	E50K	VO	B_iO_i	C_iO_i	V_2
g_D (cm^{-3}·Gy^{-1})	5.2×10^5	1.1×10^4	6.5×10^6	2.5×10^5	1.9×10^7	1.0×10^6

It should be mentioned here that the errors in the extracted defect concentrations are caused by different reasons:

a) The fitting procedure of the peak maxima leads to about 2% error in the determined defect concentration.

b) Errors of about 3% are estimated for calculating the $n_t(T_{fill})/N_t$ fraction of filled defects at low temperature by forward current injection, due to the filling temperature dependence of in the case of H40K, C_iO_i and V_2.

c) The noise of the TSC signal contributes to an error in the determined defect concentration of about 2%.

Assuming all errors to be uncorrelated, the total error on the defect concentration is below 5%.

8.3.2 Annealing studies

Two p-stop diodes, F150P-7 and F150P-8, and one p-spray diode F150Y-8 have been subjected to annealing experiments and the changes in the macroscopic and microscopic properties of these diodes have been studied. Isochronal annealing experiments have been performed for 15 min at different temperatures, between 100 °C and 300 °C. The temperature was increased in steps of 10 °C for annealing up to 200 °C and in steps of 20 °C in the higher temperature range. The annealing behaviour of the reverse current at -300 V is plotted in Fig. 8.7a for the three annealed irradiated diodes. As can be seen, while the change of the leakage current for $T_{\text{ann}} \leq 200$ °C is very small, it becomes significant for higher temperatures for all the diodes. A sudden increase of the leakage current takes place in the 200 °C-260 °C temperature range, being followed by a sharp decrease for higher temperatures. The reason for this sudden change is not clear yet.

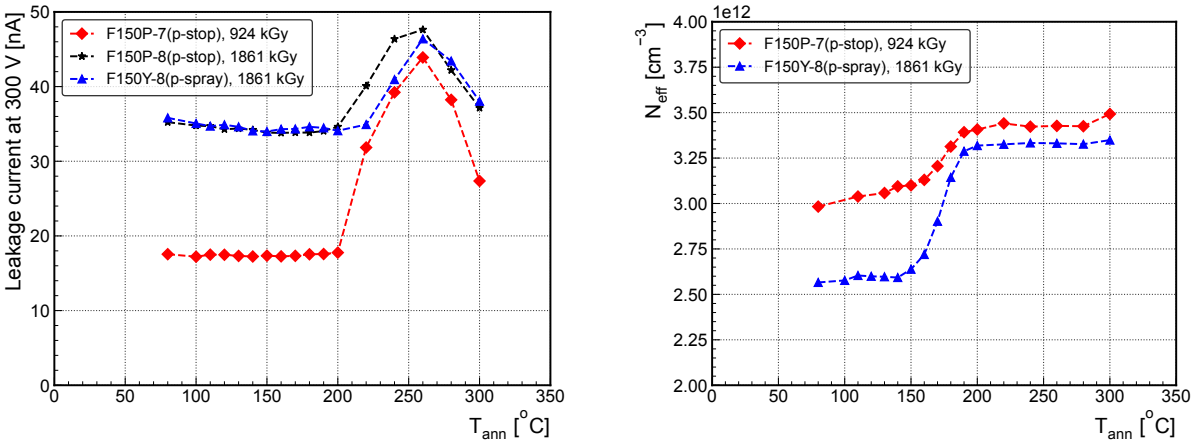

(a) (b)

Figure 8.7: (a) The development of leakage current measured at room temperature and V = -300 V with annealing temperature. (d) Extracted N_{eff} from C–V measurement at room temperature as a function of annealing temperature.

The development of N_{eff} with annealing temperature is presented in Fig. 8.7b. The given N_{eff} data represents the average values determined from the $N_{\text{eff}}(w)$ profiles in the 60 μm and 100 μm depth range. Between 150 °C and 200 °C the N_{eff} increases, recovering most of the initial doping value of not-irradiated devices 3.5×10^{12} cm^{-3}, e.g. 98% for F150P-7 and 95% for F150Y-8. This recovery of the acceptor doping is related to the dissociation of the B_iO_i defect which anneals out in the 150 °C-200 °C temperature range [15, 20, 181, 155].

The TSC spectra recorded on the diode F150P-8 after annealing at different temperatures are given in Fig. 8.8a and Fig. 8.8b. As it can be seen while H40K anneals out at 120 °C, B_iO_i and I_p* defects starts to anneal at 160 °C and are disappearing after the treatment at 200 °C. Worth noting is the significantly lower thermal stability of the I_p* defect compared with the previously reported one for the I_p defect in [176]. Thus, although both defects show a quadratic dose dependence, there are significant differences

between them concerning trapping parameters (see Table 8.2) and thermal stability, indicating that they are different structural point defects. The dominant C_iO_i defect is stable in all the studied temperature ranges.

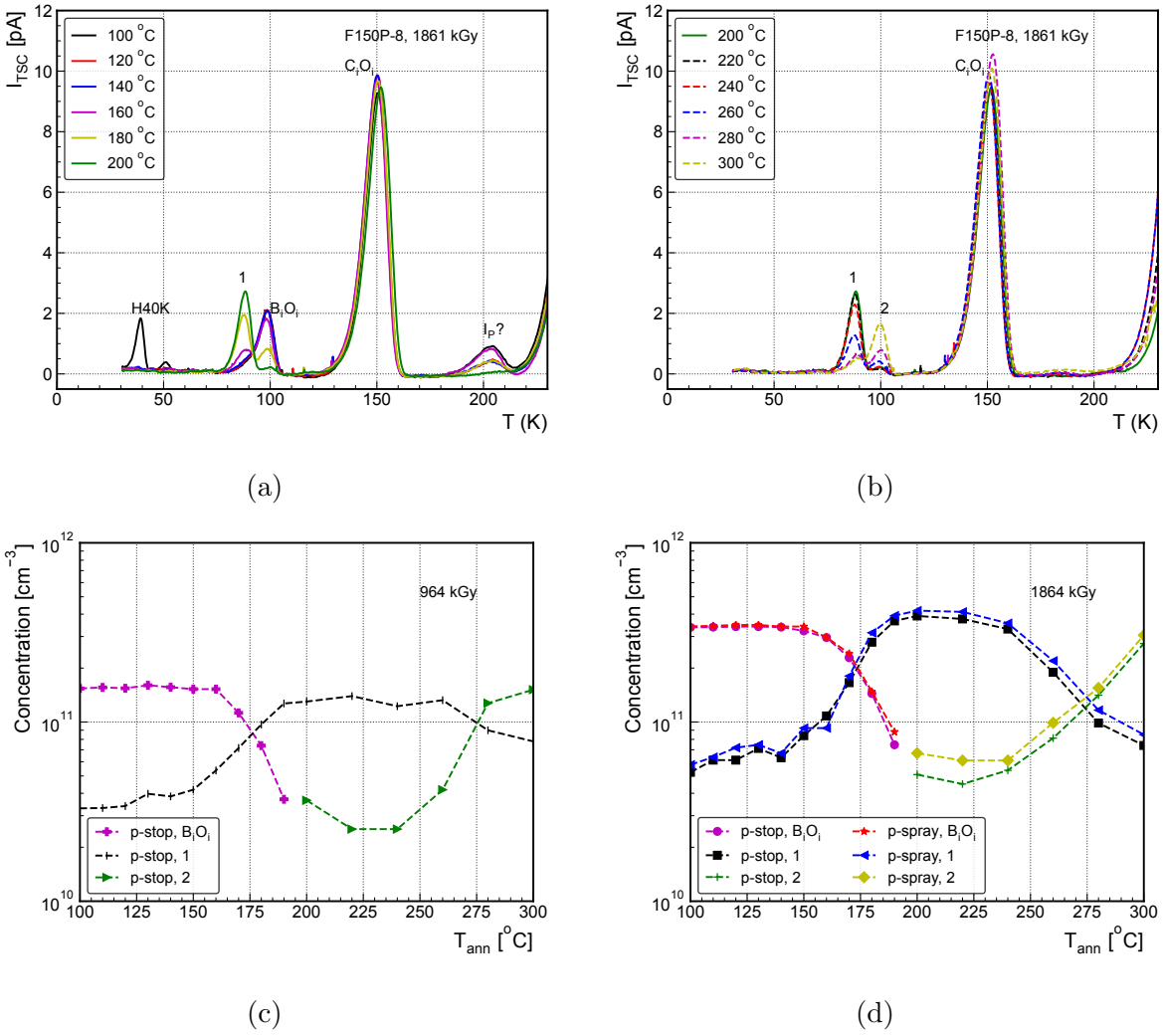

Figure 8.8: (a) TSC spectra for diode F150P-8 after isochronal annealing from 100 °C to 200 °C. (b) TSC spectra for diode F150P-8 after isochronal annealing from 200 °C to 300 °C. Measurement details for (a) and (b): Trap filling by forward current (I_{fill} = 1 mA) injection at T_{fill} = 30 K. The diode was irradiated with ^{60}Co-γ to a dose value of about D = 2 MGy, and the heating bias voltage was V_{bias} = -300 V. (c) Evolution of the defect concentration in diode F150P-7 as a function of annealing temperature T_{ann}. (d) Evolution of the defect concentration in diodes F150P-8 and F150Y-8 as a function of annealing temperature T_{ann}. Both (c) and (d) are determined from TSC measurements in the temperature range of 70 K to 110 K.

A further interesting observation is, that the decrease in the concentration of B_iO_i and I_p^* defects are accompanied by the formation of another center ($defect1$) of which concentration is growing up to about 200 °C (see Fig. 8.8a). After dissociation of B_iO_i defect, boron atom return on the substitutional site (B_s) and is recovering its acceptor character. This process is reflected in an increase of N_{eff} with twice the amount of the

dissociated B_iO_i donor. For the *p*-spray diode, the variation in the N_{eff} given in Fig. 8.8b is $[\Delta N_{eff}] = 7.25 \times 10^{11}$ cm^{-3} (between 140 °C and 200 °C). The total amount of dissociated B_iO_i defect for the same sample is $[B_iO_i] = 3.5 \times 10^{11}$ cm^{-3} (see Fig. 8.8d), almost a half of $[\Delta N_{eff}]$. Because the initial Boron doping is mostly restored during the dissociation of B_iO_i defect and considering the concentration of the newly formed $defect1$ (of 4.2×10^{11} cm^{-3}), we conclude that the Boron atom cannot be part of $defect1$.

The $defect1$ is stable up to about 240 °C (see Fig. 8.8b) when starts to transform in $defect2$ up to the limit of the used oven (300 °C). The variation in defect concentration is given in Fig. 8.8c and Fig. 8.8d. From TSC experiments with different applied bias voltages, no change in the position of the peak is found for defects 1 and 2. Also, no change in the N_{eff} values are determined during the annealing transformations occurring between 200 °C and 300 °C. This indicates that both defects (1 and 2) are in a neutral charge state at room temperature. In addition, experiments for 0 V filling at T_{fill} = 20 K and 40 K were performed. The defects 1 and 2 are both detected in this way (see Fig. 8.9), evidencing that they are acting as traps for holes.

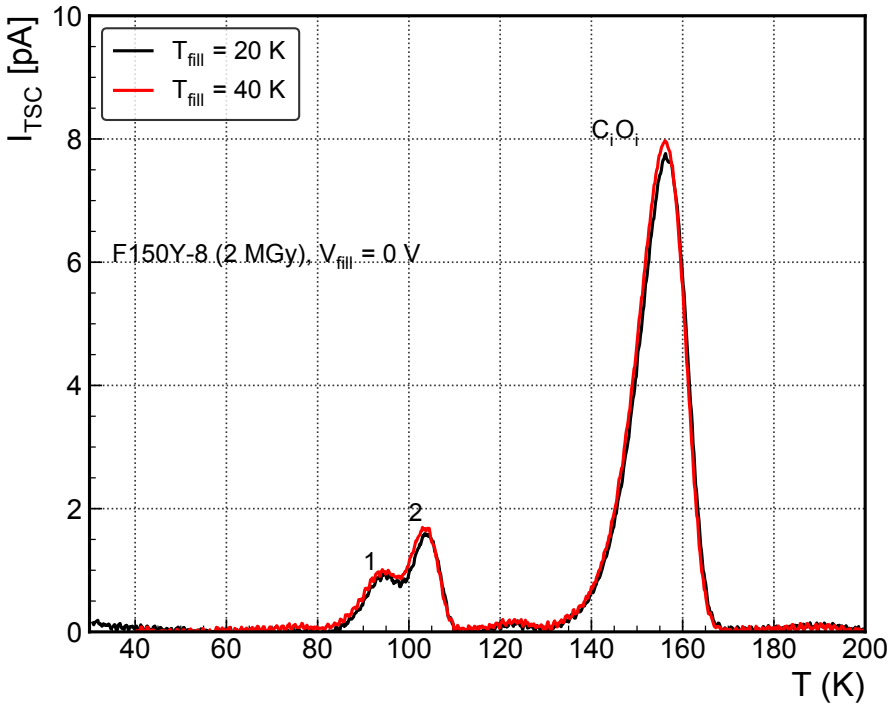

Figure 8.9: 0 V injection performed on diode F150P-8 after isochronal annealing at T_{ann} = 300 °C. Measurement details: T_{fill} = 20 and 40 K.

8.3.3 Surface effect

Contrary to the investigated *p*-spray diodes, the *p*-stop devices after high dose values (1 MGy and 2 MGy) show a frequency dependence of the C–V characteristics, an important source of errors when estimating N_{eff} depth profiles. This was shown previously for

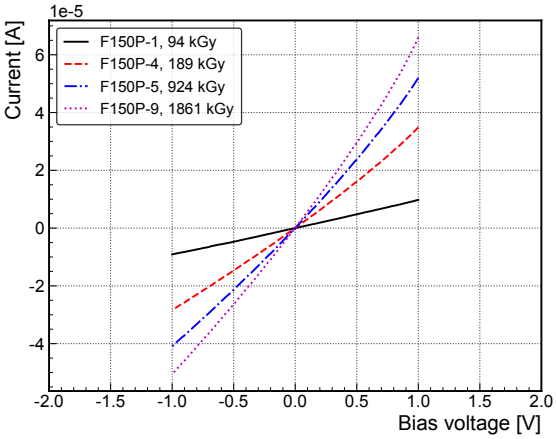

(a)

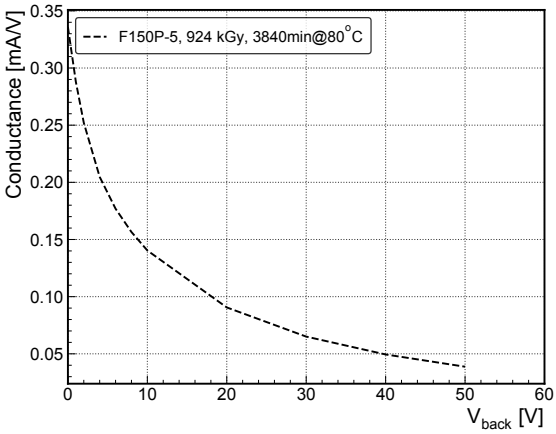

(b)

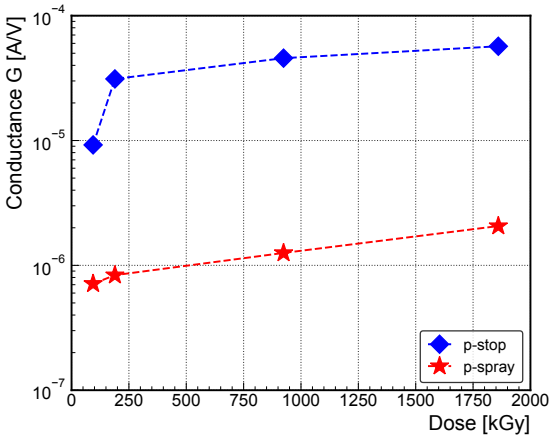

(c)

Figure 8.10: (a) Current measured on the pad with varies bias on the guard from -1 V to 1 V for *p*-stop diodes with different irradiation dose values, V_{back} = -10 V. (b) Conductance developed with bias on the backside while grounding the guard ring. (c) The development of G with dose, V_{back} = -10 V.

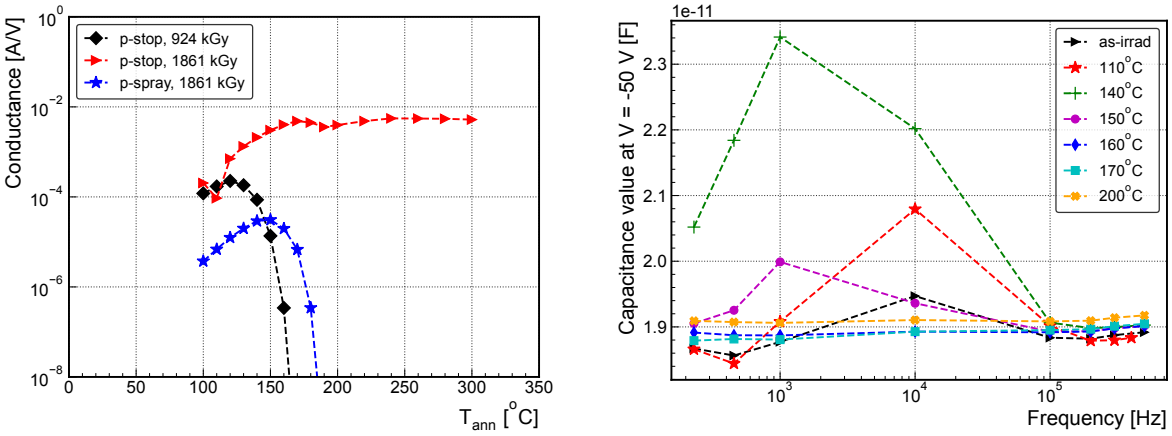

(a) (b)

Figure 8.11: (a) Development of surface conductance with T_{ann} at backside applied -10 V. (b) Capacitance value when applied V = -50 V vs frequency developed with annealing.

the 230 Hz $\sim$ 10 kHz frequency range [182]. As we will show further, the phenomena became more pronounced after high annealing temperatures. Also, the I–V characteristics change their behaviour, e.g. the pad current at low bias voltages became approximately zero while the current of the guard ring became large at zero voltage and decreases with increasing bias voltage. However, the same behaviours do not appear on the p-spray diodes. These findings led to the speculation that surface effects occurring between the guard ring and the pad area might be responsible for the above mentioned observations. In order to study such surface effects, the standard I–V setup was slightly modified compared to Fig. 8.1c and Fig. 8.1d. While the guard ring was connected to the ground via a voltage source, the pad was connected to a current meter. In addition, a second voltage source was connected to the backside of the diode (reverse bias V_{back}). With this setup, the current flow between the guard ring and the pad could be measured by varying the voltage of the guard ring in the range from -1 V to +1 V. At the same time, a reverse voltage was applied on the backside. As an example, Fig. 8.10a presents such surface I–V curves at a constant V_{back} = 10 V for several p-stop diodes irradiated to different dose values.

The slope of the surface current in the linear range (-0.5 V to +0.5 V) provides the surface conductance G, given by:

$$G = \frac{dI}{dV} \tag{8.10}$$

Figure 8.10b demonstrates the dependence of the conductance G versus V_{back}. The decrease of G with increasing V_{back} indicates a decrease in the charge carrier concentration near the surface. For $V_{\text{back}} \geq 50$ V the diode F150P-5 irradiated to 0.924 MGy becomes fully depleted. The dose dependence of the surface conductance is plotted in Fig. 8.10c,

for both, *p*-stop and *p*-spray diodes. There is more than one order of magnitude difference between the G values in the two types of diodes. This indicates that a much larger interface trap concentration exists in the *p*-stop diodes compared to the *p*-spray ones.

Isochronal annealing studies were performed for two *p*-stop diodes (F150P-7 (0.924 MGy), F150P-8 (1.861 MGy)) and one *p*-spray diode (F150Y-8 (1.861 MGy)).

The dependence of G on the annealing temperature T_{ann} is shown in Fig. 8.11a. For the 924 kGy irradiated diodes, the changes in G are observed first as an increase for annealing up to 120 °C and 150 °C, respectively, followed by a rapid decrease with increasing T_{ann}. At the same time, the conductance of the *p*-stop sample is much larger than that of the *p*-spray one. On the other hand, in the highly irradiated *p*-stop device, G increases up to about 120 °C and stays thereafter nearly constant up to the end of the annealing experimental, at the temperature of 300 °C. A frequency dependence in C–V measurements is only observed if G is larger than 3×10^{-6} or 2×10^{-6} A/V at V_{back} = 10 or 50 V, respectively. The frequency dependencies of the capacitance measured after annealing at different temperatures on F150P-7 *p*-stop diode are shown in Fig. 8.11b in the 230 Hz to 500 kHz frequency range. The capacitance values are taken for a reverse bias of 50 V, which is slightly below the full depletion voltage. As can be seen, the maximal capacitance value is observed for T_{ann} = 140 °C and a frequency of 1 kHz. From 160 °C on, the frequency dependence vanishes, in accordance with the corresponding very low conductance shown in Fig. 8.11a. It is worth noting that, above 100 kHz, the capacitance is constant for all the annealing temperatures. Measuring the capacitance in such a frequency-independent range is considered to be a safe procedure for performing the C–V measurements and extracting further the N_{eff} profiles. Under this assumption, the errors for all capacitance values at 500 kHz are below 4% for *p*-stop diodes with dose values below 1 MGy. Due to the conductance after 1.861 MGy doses, the capacitance of *p*-stop is not reliable anymore after annealing.

The errors in the determined N_{eff} in Fig. 8.7b caused by averaging range are around 1% (varying average ranges in between 60 µm and 120 µm). The main errors of N_{eff} are from the frequency-dependent C–V measurements, which will be discussed in detail in subsection 8.3.3.

Figure 8.10b demonstrates the dependence of the conductance G versus V_{back}. The decrease of G with increasing V_{back} means that the free charge carrier concentration near to the surface becomes smaller. For $V_{\mathrm{back}} \geq 50$ V the diode F150P-5 irradiated to 1 MGy becomes fully depleted. The dose dependence of the surface conductance is plotted in Fig. 8.10c for the *p*-stop as well as for the *p*-spray diodes. The difference between both types of diodes is more than one order of magnitude, indicating a much larger interface trap concentration in the *p*-stop diodes compared to the *p*-spray ones. An explanation of this difference cannot be given so far. Isochronal annealing studies were performed for two *p*-stop diodes (F150P-7 (1 MGy), F150P-8 (2 MGy)) and one *p*-spray diode (F150Y-8 (2 MGy)). In Fig. 8.11a the dependence of G on the annealing temperature

T_{ann} is shown. For the diodes F150P-7 and F150Y-8 an increase up to 120 °C or 150 °C is observed, followed by a rapid decrease with increasing T_{ann}. On the other hand, the highly irradiated p-stop device increases up to about 170 °C and stays thereafter nearly constant up to 300 °C. It is also obvious that the conductance of the p-stop sample is much larger compared to the p-spray one.

Finally, in Fig. 8.11b the frequency dependence of the capacitance from 230 Hz to 500 kHz is shown for the p-stop diode F150P-7 for different annealing temperatures. The capacitance values are taken at a bias voltage of -50 V, which is a bit below total depletion. As can be seen, the maximal capacitance value is observed for $T_{\text{ann}} = 140$ °C and a frequency of 1 kHz. Already at 160 °C the frequency dependence vanished corresponding with the very low conductance value in Fig. 8.11a. Above 100 kHz the capacitance is constant for all annealing steps. In general, when the capacitance is constant with changing frequency, which is assumed as a corrected value. Thus, the errors for C-V from surface current are given by the difference between 100 kHz and 500 kHz. Under this assumption, the errors for all capacitance values at 500 kHz are below 4% for p-stop diodes with dose values below 1 MGy. For $D = 2$ MGy, the capacitance of p-stop is not reliable after annealing. For C-V before annealing, the errors caused by the surface effect can be ignored if using the capacitance at 230 Hz.

8.4 Conclusion

The radiation damage of two types of silicon diodes (p-spray and p-stop), manufactured on p-type Fz-material, with a resistivity of about 4 kΩcm and exposed to ^{60}Co γ-ray at different dose values (0.1 MGy, 0.2 MGy, 1 MGy, and 2 MGy) was investigated in this study. I–V and C–V measurements were employed for studying the radiation-induced changes in the densities of leakage current (J_d) and effective space charge (N_{eff}). The results showed that with increasing the dose, N_{eff} decreases while J_d linearly increases, the latter exhibiting a similar trend to that of oxygen enriched n-type silicon irradiated with ^{60}Co γ-ray. In order to identify the γ-induced traps in the bulk of the samples, TSC measurements were performed on irradiated p-type diodes. The TSC spectra revealed the presence of defects, including H40K, VO, B_iO_i, C_iO_i, V_2, and the newly detected I_P^*. The results showed that all the concentrations of defects increased linearly with dose except the I_P^* that shows a quadratic dose dependence. The process of multi-phonon capture of holes by the C_iO_i defect was investigated by analyzing the corresponding TSC peak obtained after the filling of the defect was performed at different temperatures. The obtained results differ from those determined after irradiation with 1 MeV neutrons of n-type silicon diode, the capturing process on the C_iO_i defect being faster after irradiation with γ-rays. This is explained considering that there are additional potential barriers surrounding the disordered (clustered) regions produced by hadron which slow down the charge transport in the diodes.

To gain a better understanding of the defects' thermal stability, kinetics and their impact on the device properties, isochronal annealing experiments were performed in the 100 °C-300 °C temperature range. The TSC experiments revealed that C_iO_i complex is thermally stable up to the end of the isochronal annealing, performed up to 300 °C in our study. In contrast, the other radiation-induced defects change their concentrations during the thermal treatment. Thus, H40K anneals out at 120 °C while B_iO_i and I_P^* start to anneal out after annealing at 140 °C and the devices are recovering most of their initial doping. Two unidentified traps are detected to form during the annealing, labelled as $defect1$ and $defect2$. $defect1$ is forming during the treatment in the 140 °C-200 °C temperature range and transforms into $defect2$ after annealing at higher temperatures. Both defects were found to be hole traps and neutral charged at room temperature.

The results of the macroscopic measurements showed that the density of leakage current (J_d) measured in full depletion conditions (at V = -300 V) remains stable for annealing temperatures up to 200 °C, indicating that none of the annealed out defects has an influence on the measured current. In the 200 °C-300 °C temperature range of annealing, J_d increases up to 260 °C and then decreases. No evidence for bulk defects responsible for such behaviour was detected in TSC experiments. Variations of N_{eff} were observed only in the 150 °C-200 °C temperature annealing range, where the dissociation of the B_iO_i defect occurs and N_{eff} increases because the initial removed substitutional Boron is recovered. Depending on the isolation technique used for the fabrication of the two types of investigated diodes, different frequency dependences were evidenced, according not only to the irradiation dose but also to the isolation technique used for separating the pad from the guard ring. To further investigate this phenomenon, surface conductance (G) measurements were performed on different samples. The frequency dependence in C–V measurements is only observed if G was large than 3×10^{-6} or 2×10^{-6} A/V at $V_{\text{back}} = 10$ or 50 V, respectively. This is not the case for most of the irradiated p-spray diodes, apart from this highest dose of 1861 kGy after annealing at high temperature. For irradiated p-stop diodes, the value of G is consistently above this limit, but it can be decreased by annealing for D value below 1 MGy (F150P-7).

8.5 Additional Materials

8.5.1 I–V, C–V Before Irradiation

The I–V and C–V characteristics of diodes before irradiation are shown in Fig. 8.12. The current values measured before irradiation are around nA. Figure 8.12d shows that the C–V values are identical for all investigated diodes.

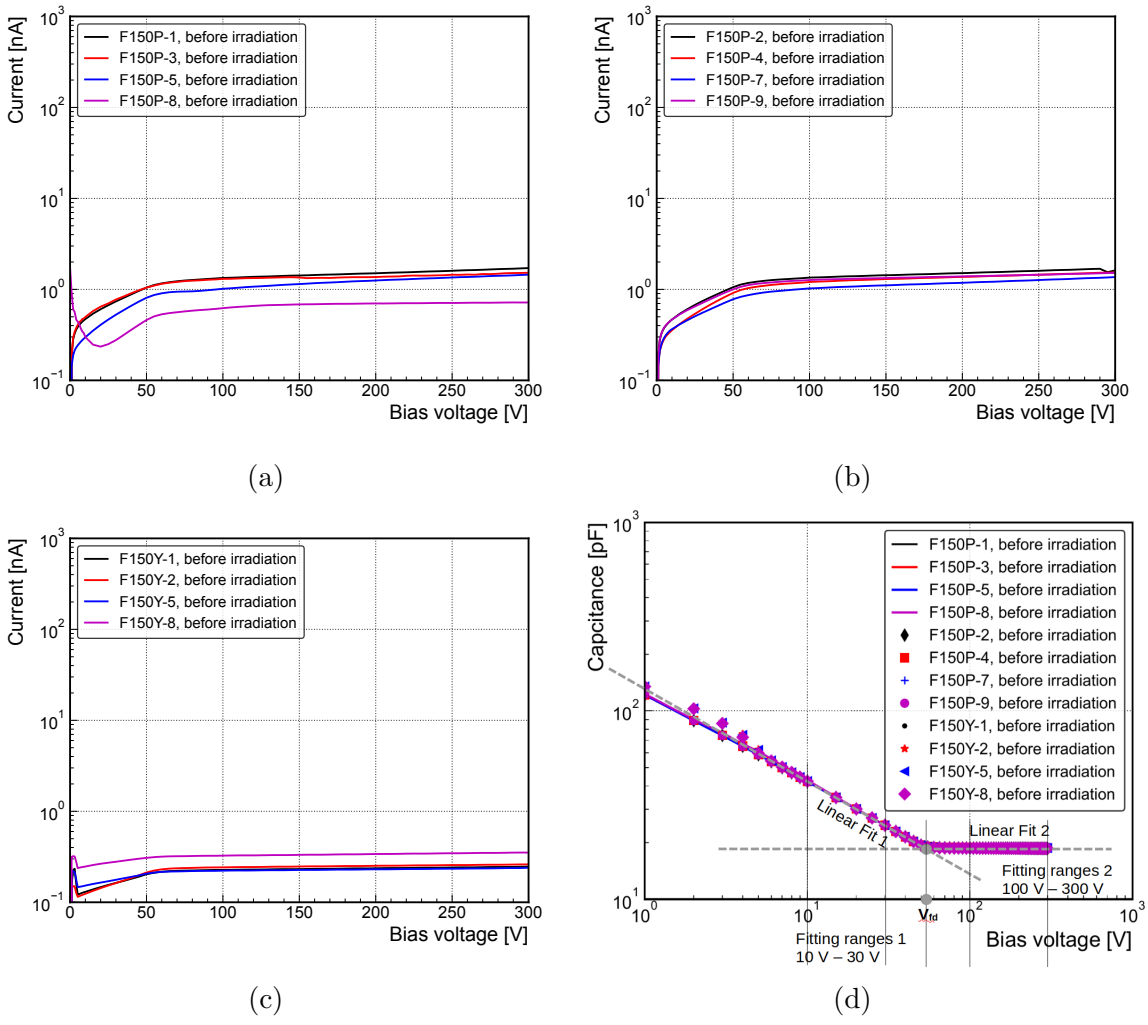

Figure 8.12: (a), (b) and (c) are current-voltage (I–V) characteristics of about 4 kΩ·cm diodes before irradiation. (d) C–V characteristics of about 4 kΩ·cm diodes before irradiation. The measurements corresponding to diodes were indicated in the legends. Measurements condition: $T = 20\,^{\circ}\mathrm{C}$, humidity $\leq 10\,\%$, $V_{\mathrm{AC}} = 0.5$ V and freq = 10 kHz.

8.5.2 I–V, C–V After Irradiation

The I–V and C–V characteristics of irradiated diodes are shown in Fig 8.13. The results presented in Fig. 8.13a-8.13d for p-stop diodes are similar to those presented in section 8.3 for p-stop diodes. However, the frequency-dependent C–V measurements only appeared

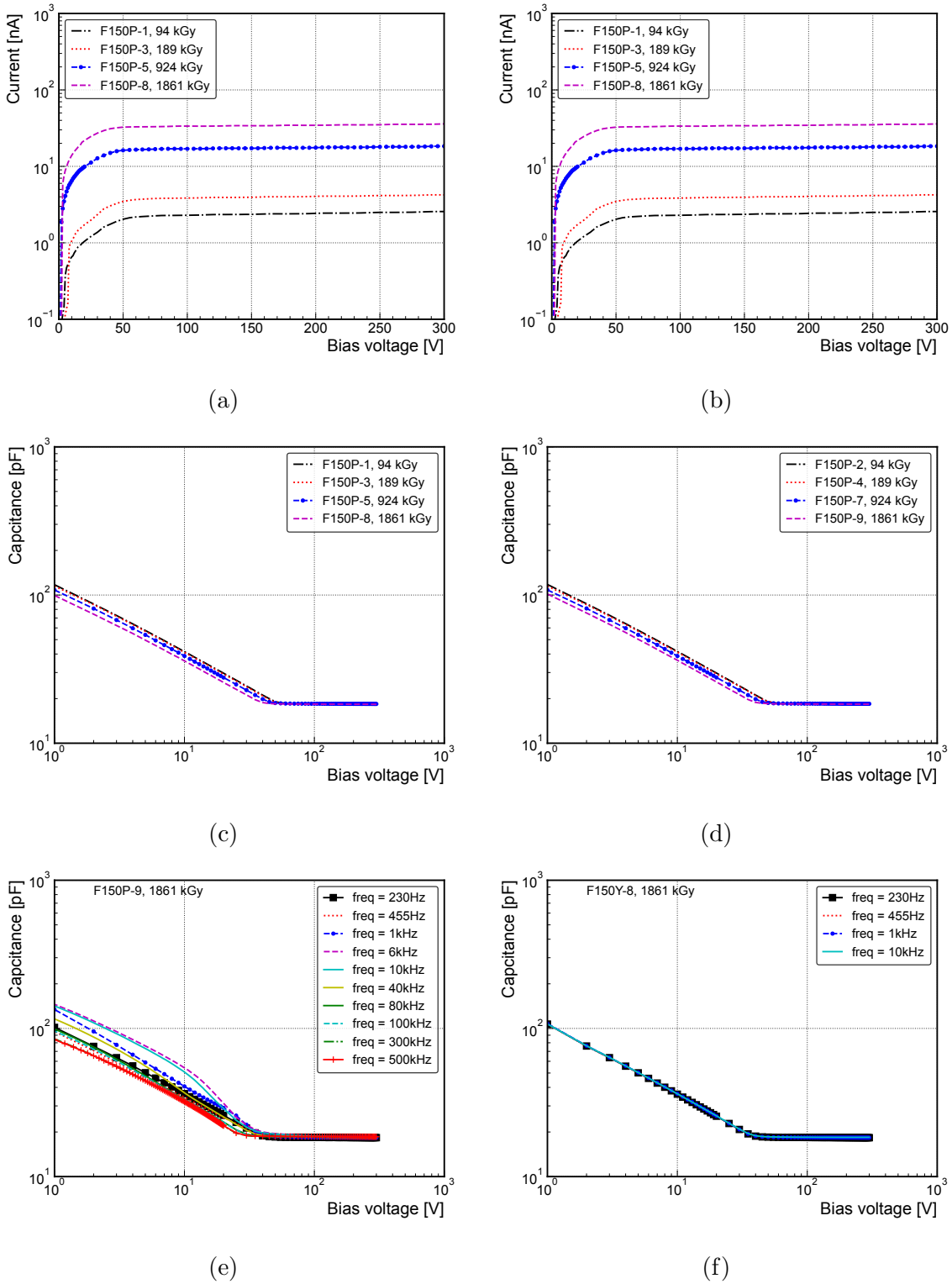

Figure 8.13: I-V and C-V characteristics of about 4 kΩ·cm diodes after irradiation. (a) and (b) are the I–V for all p-stop diodes as indicated in legends. (c) and (d) are the C–V for all p-stop diodes as indicated in legends. The investigated diodes irradiated with ^{60}Co-ray with $D \approx 0.1$, 0.2, 1, 2 MGy. (e) and (f) are the C–V with different freq performed F150P-9 and F150Y-8 after irradiation with $D \approx 2$ MGy. Measurements condition: $T = 20\,^{\circ}$C, humidity $\leq 10\,\%$, $V_{\mathrm{AC}} = 0.5$ V, freq = 230 Hz for (c) and (d). The frequencies of (e) and (f) are indicated in the legends.

on p-stop diodes, and not on p-spray diodes, after being irradiated with ^{60}Co γ-rays at a dose of 2 MGy, as shown in Fig. 8.13e and 8.13f.

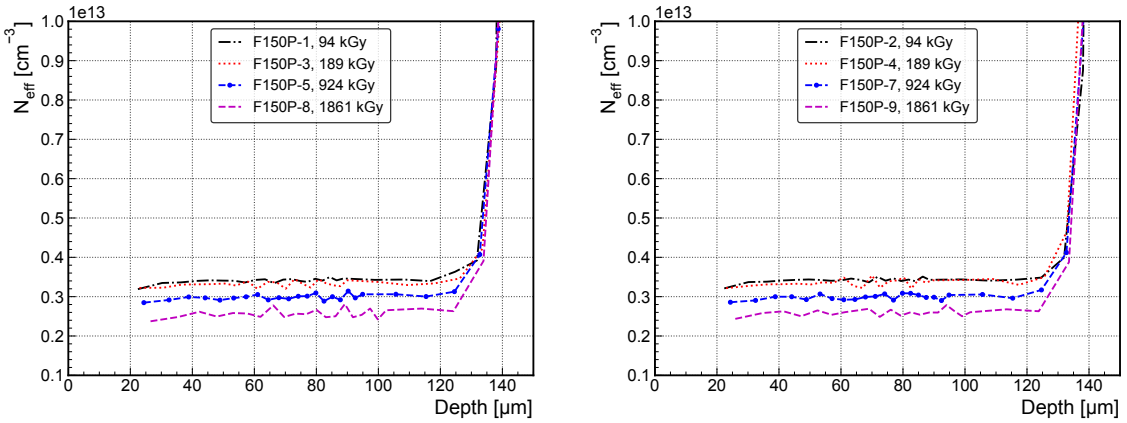

(a) (b)

Figure 8.14: N_{eff} profile of p-stop diodes irradiation with different D values. The data were evaluated from C-V measurements by using Eq. 8.1 and Eq. 8.2. (a) F150P-1, 3, 5 and 8. (b) F150P-2, 4, 7 and 9.

Table 8.5: V_{fd} and N_{eff} before and after irradiation

p-stop(label)	F150P-1	F150P-3	F150P-5	F150P-8
V_{fd} before irrad (V)	53.1 ± 0.8	52.8 ± 0.8	52.3 ± 0.7	51.8 ± 0.7
V_{fd} after irrad (V)	52.7 ± 0.4	52.0 ± 0.7	46.3 ± 0.5	40.1 ± 0.7
N_{eff} before irrad (10^{12} cm^{-3})	3.53 ± 0.02	3.54 ± 0.02	3.53 ± 0.01	3.50 ± 0.04
N_{eff} after irrad (10^{12} cm^{-3})	3.42 ± 0.07	3.32 ± 0.13	3.00 ± 0.14	2.59 ± 0.21
p-stop(label)	F150P-2	F150P-4	F150P-7	F150P-9
V_{fd} before irrad (V)	53.1 ± 0.8	52.2 ± 0.8	52.2 ± 0.8	52.9 ± 0.8
V_{fd} after irrad (V)	52.9 ± 0.6	51.1 ± 0.8	46.3 ± 0.8	40.2 ± 0.6
N_{eff} before irrad (10^{12} cm^{-3})	3.55 ± 0.02	3.54 ± 0.01	3.53 ± 0.01	3.55 ± 0.02
N_{eff} after irrad (10^{12} cm^{-3})	3.43 ± 0.08	3.37 ± 0.17	3.00 ± 0.09	2.61 ± 0.17
p-spray(label)	F150Y-1	F150Y-2	F150Y-5	F150Y-8
V_{fd} before irrad (V)	53.9 ± 0.5	53.7 ± 0.5	52.3 ± 0.5	53.0 ± 0.5
V_{fd} after irrad (V)	53.4 ± 0.6	52.6 ± 0.6	45.9 ± 0.7	38.7 ± 0.8
N_{eff} before irrad (10^{12} cm^{-3})	3.52 ± 0.02	3.51 ± 0.01	3.52 ± 0.02	3.52 ± 0.02
N_{eff} after irrad (10^{12} cm^{-3})	3.37 ± 0.03	3.31 ± 0.04	2.99 ± 0.06	2.50 ± 0.06

Fig. 8.14 presents the extracted N_{eff} profiles for all p-stop diodes after irradiation. With increasing D, the profiles are shifted to lower values similar to results measured on p-spray diodes. The obtained V_{fd} and N_{eff} were summarized in Table 8.5.

8.5.3 Annealing Studies on I–V, C–V

In addition to isochronal annealing, isothermal annealing was also performed on F150P-5 at 80 °C. The annealing times for measurements were 10, 30, 60, 90, 120, 240, 480, 975, 1920, and 3840 min.

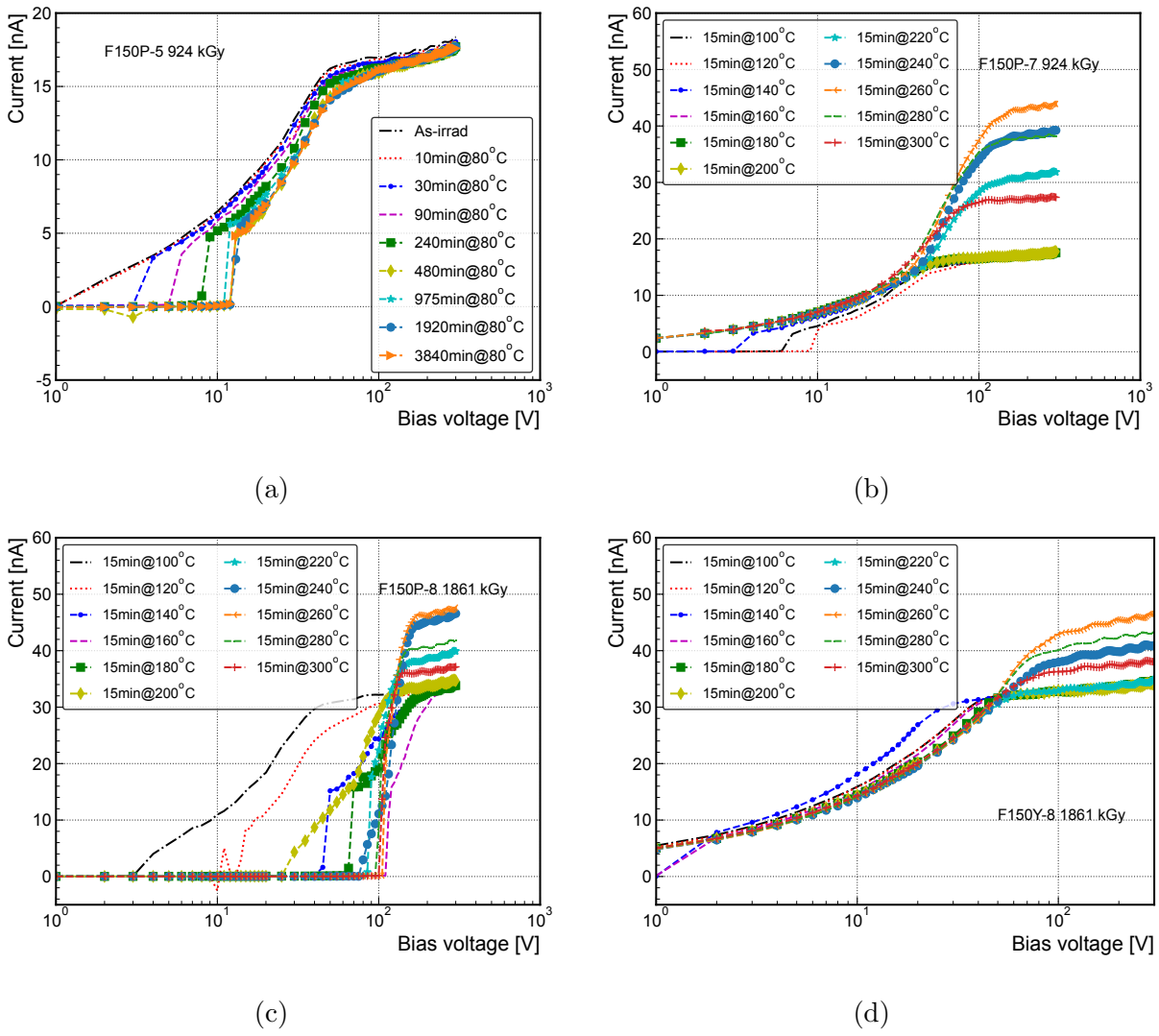

Figure 8.15: I-V characteristics for isothermal and isochronal annealing. (a) I-V curves of different isothermal annealing steps for diode F150P-5. I-V characteristics for different isochronal annealing steps were presented in (b) F150P-7, (c) F150P-8 and (d) F150Y-8.

The I–V characteristics for isothermal and isochronal annealing are presented in Fig. 8.15. The figure shows that lower current values ($I \leq 1 \times 10^{-11}$ A) appeared for V values below specific thresholds, which depend on the dose and annealing steps. These thresholds, denoted as V_{raise}, correspond to the points where the current suddenly increases, such as $V = 3$ V (30 min@80°C) and 5 V (90 min@80°C) in Fig. 8.15a. The changes in V_{raise} are due to variations in the surface conductance G. Higher G values increase the likelihood of current flowing to the guard ring instead of the pad, resulting in lower current values

for a given V. This observation can be further supported by comparing it with Fig. 8.11a and Fig. 8.17.

The C–V characteristics for isothermal and isochronal annealing are presented in Fig. 8.16. Due to the high G value for F150P-8 (see Fig. 8.16d), the C-V measurements are not reliable anymore. The changes in C-V for different annealing steps are negligible for F150P-5 under isothermal annealing. The measurements after isochronal annealing are presented in Fig. 8.16b and 8.16c, which are used to extract N_{eff} as presented in Fig. 8.7b.

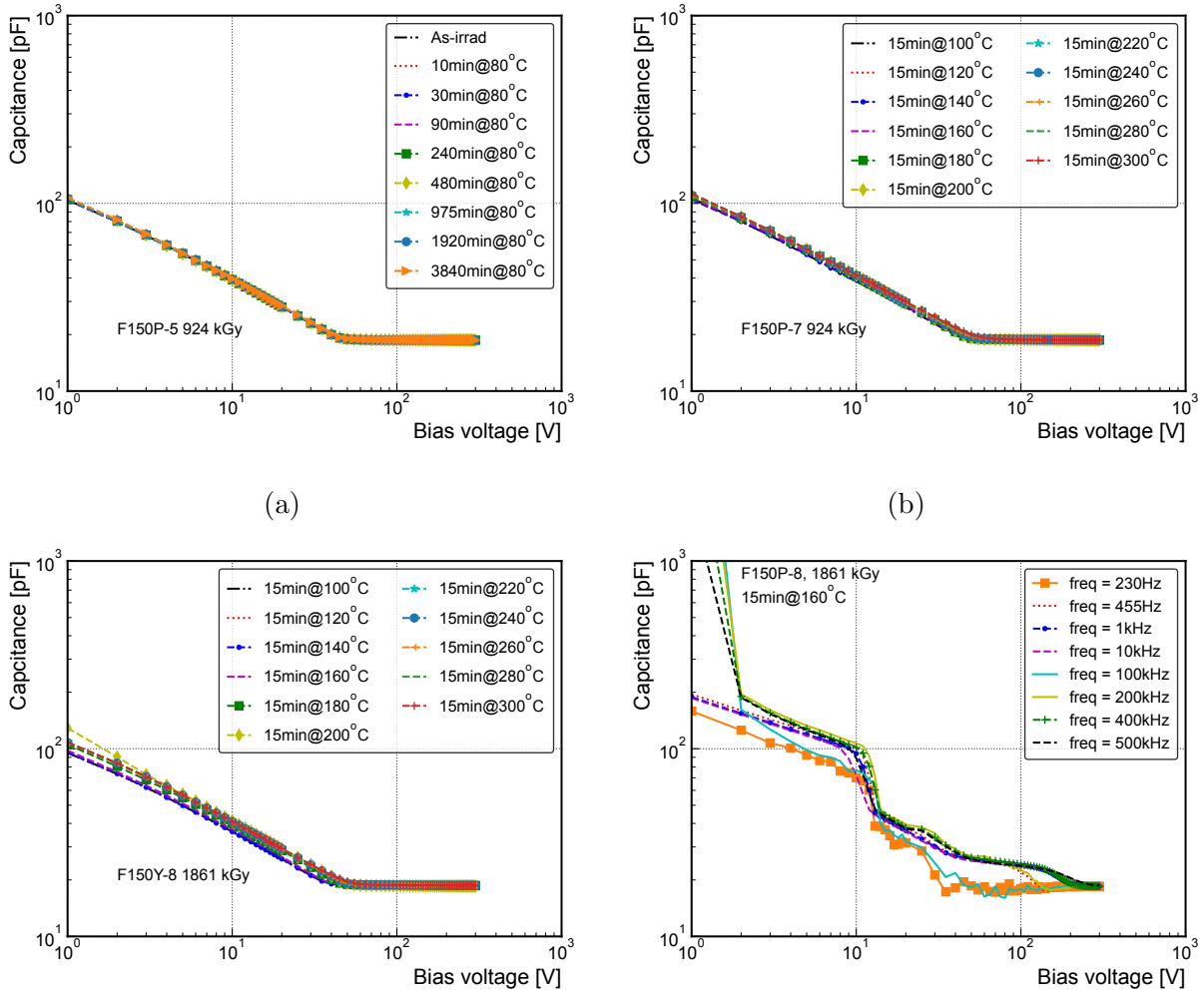

Figure 8.16: C-V characteristics for isothermal and isochronal annealing. (a) C-V curves of different isothermal annealing steps for diode F150P-5. C-V characteristics for different isochronal annealing steps were presented in (b) F150P-7 and (c) F150Y-8. freq = 500 kHz for (a)-(c). (d) C–V measurement with different frequencies on F150P-8 after isochronal annealing step 15min@160 °C.

8.5.4 Surface State

The evolution of G during isothermal annealing at 80 °C is presented in Fig. 8.17. It can be seen that G initially increased with annealing time up to a maximum value after

975 min, and then slightly decreased. This observation differs from the results reported in [89].

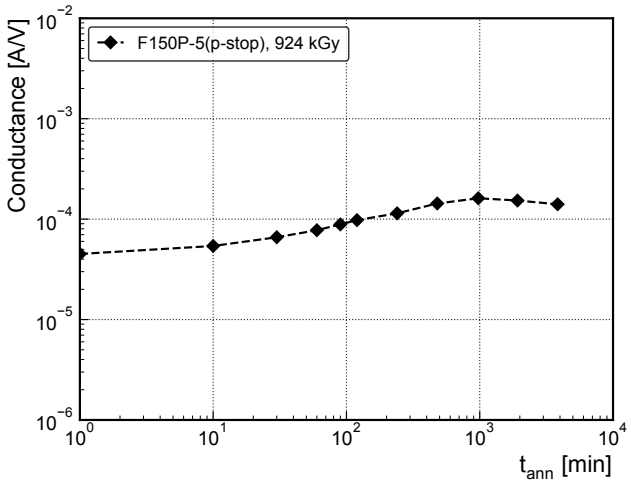

Figure 8.17: The development of G with annealing time t_{ann} for F150P-5 after 3840 min annealing at 80 °C, V_{back} = -10 V.

8.5.5 [B_iO_i] and N_{eff} vs Dose

The relationship between the development of [B_iO_i] and N_{eff} with respect to the fluence D is shown in Fig. 8.18. It can be observed that the decrease in N_{eff} is approximately twice the increase in [B_iO_i].

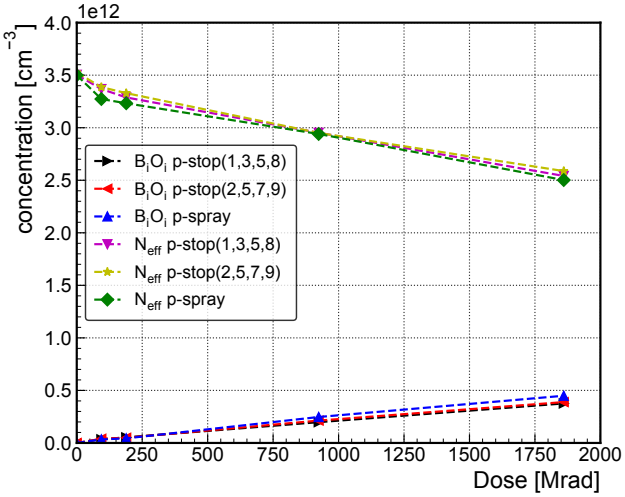

Figure 8.18: Evolution of the [B_iO_i] and N_{eff} as a function of dose value D.

8.5.6 $[C_iO_i]$ vs T_{fill} for Different D Value

Figure 8.19 shows the dependence of the C_iO_i concentration ($[C_iO_i]$) on the filling temperature (T_{fill}). As can be seen, $[C_iO_i]$ initially increases with T_{fill} and saturates at $T_{fill} \geq$ 60 K for dose values of 94 and 189 kGy. It increases to 80 K for a dose of 924 kGy.

In Fig. 8.19d, the curves calculated by feedback parameters were plotted together with the data, including the curve calculated by using parameters a and E_s given by [11].

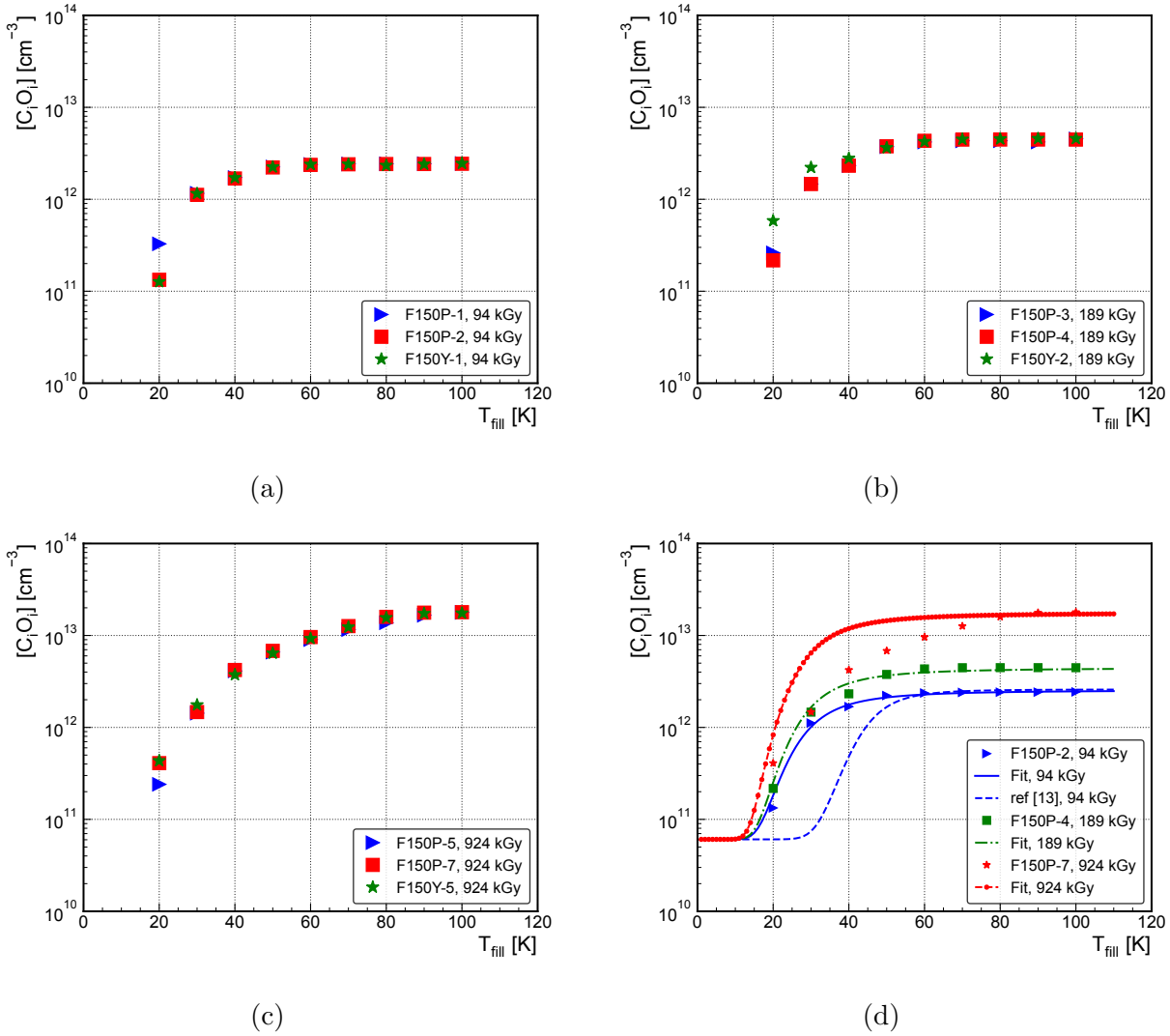

Figure 8.19: $[C_iO_i]$ vs T_{fill} extracted from TSC spectra with different T_{fill}. (a), (b) and (c) are the results extracted from the diodes irradiated by γ-ray with D = 0.1, 0.2, and 1 MGy, respectively. (d) The comparison between the data of $[C_iO_i]$ vs T_{fill} (F150P-2, F150P-4 and F150P-7) and the calculation by using feedback parameters a and E_s, including also the curve obtained by using parameters a and E_s given by [11].

8.5.7 TSC for Isothermal Annealing

Fig. 8.20a and 8.20b present TSC spectra for diode F150P-5 at different t_{ann}. It can be seen that H40K and E50K decrease with increasing t_{ann} and are eliminated when $t_{ann} \geq$ 240 min. The VO peak shows a decrease only for TSC measurements with $T_{fill} \leq$ 40K, and the maximum value of VO is stable with t_{ann}. B_iO_i, C_iO_i, and V_2 are stable with t_{ann}. [H40K], [E50K], and [I_P*] are summarized in Fig. 8.20c for different t_{ann} at 80 °C, while [B_iO_i], [C_iO_i], and [V_2] are presented in Fig. 8.20d as a function of t_{ann}. Comparing with the results presented in section 8.5.3, it can be concluded that the changes of H40K, E50K, and I_P* do not contribute to macroscopic properties.

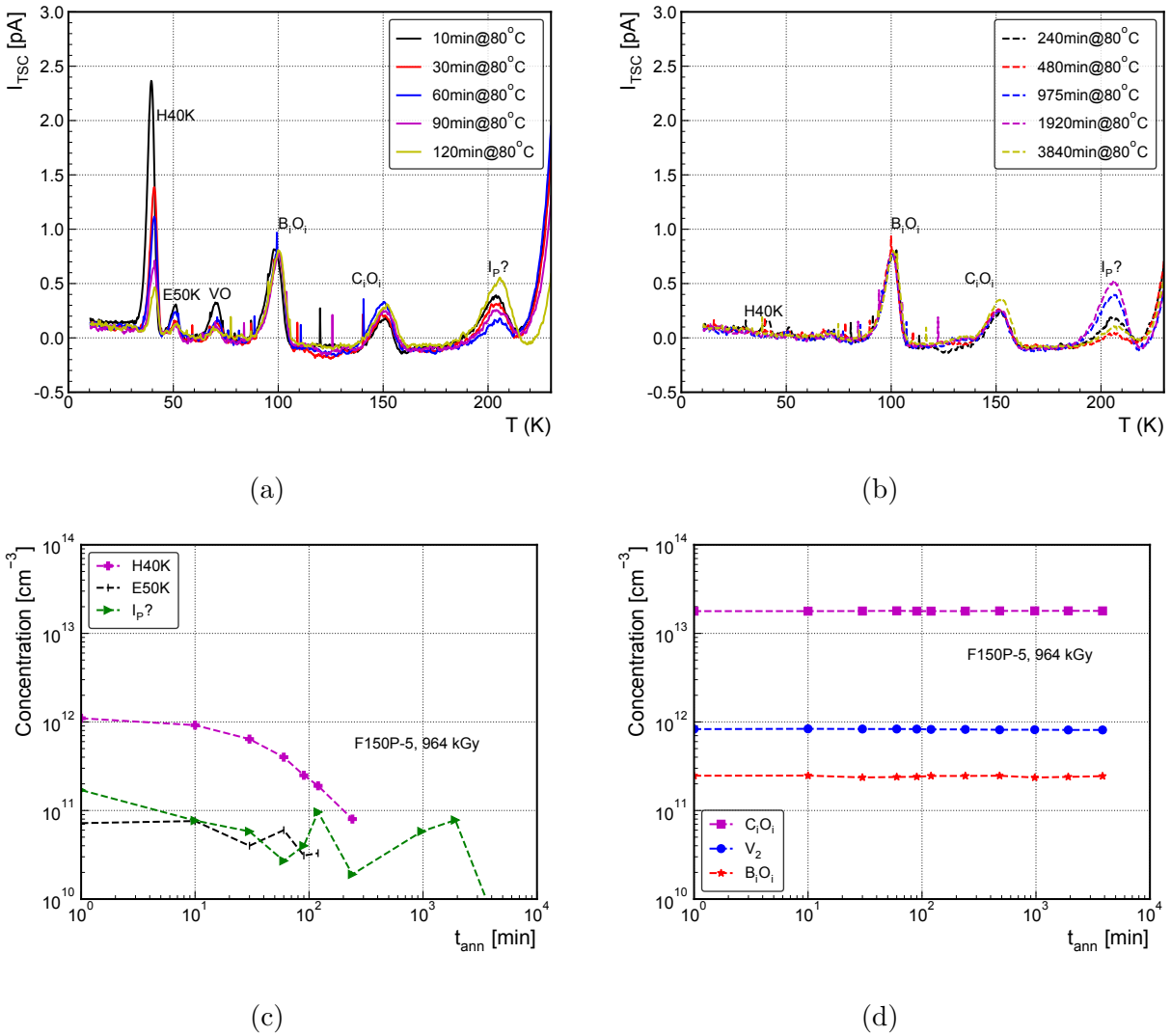

Figure 8.20: TSC spectra for diode F150P-5 after isothermal annealing at 80 °C. (a) t_{ann} = 10 to 120 min (b) t_{ann} = 240 to 3840 min. Measurement details for (a) and (b): Forward current (I_{fill} = 1 mA), T_{fill} = 10 K, V_{bias} = -200 V. (c) The development of [H40K], [E50K] and [I_P*] with t_{ann}. (d) The development of [C_iO_i], [V_2] and [B_iO_i] with t_{ann}.

8.5.8 TSC for Isochronal Annealing

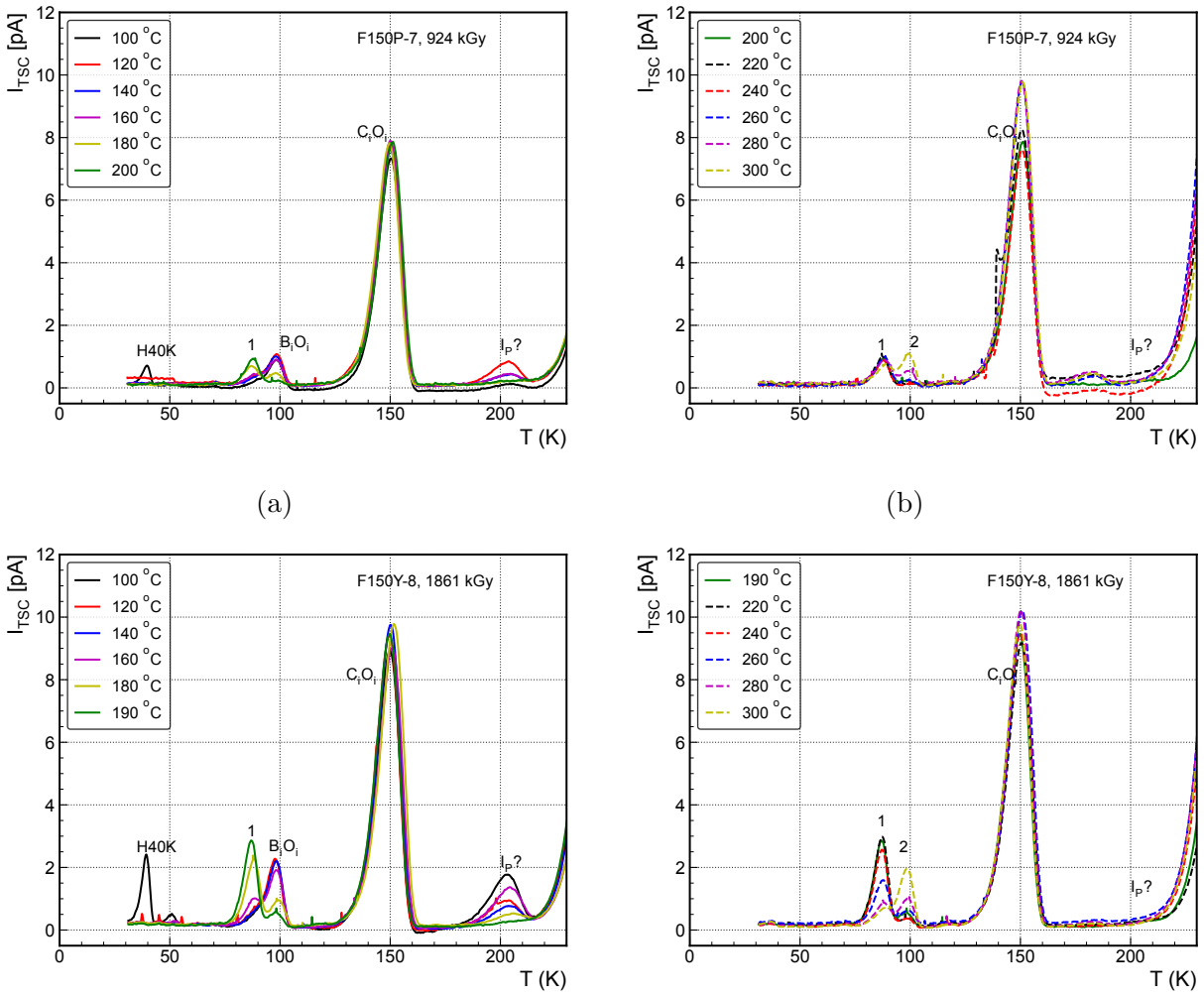

Figure 8.21: TSC spectra for diode after isochronal annealing from 100 °C to 300 °C. (a) From 100 °C to 200 °C and (b) From 200 °C to 300 °C for F150P-7. (c) From 100 °C to 190 °C and (d) From 190 °C to 300 °C for F150Y-8. Measurement details: Trap filling by forward current ($I_{\text{fill}} = 1$ mA) injection at $T_{\text{fill}} = 30$ K, $V_{\text{bias}} = -200$ V.

Figure 8.21 shows TSC spectra for F150P-7 and F150Y-8 after isochronal annealing at different temperatures, which are similar to F150P-8. The defect concentrations extracted for B_iO_i, peak 1, and peak 2 were plotted as a function of T_{ann} in Fig. 8.8.

Measurements for Peak 1 and 2

As mentioned in section 6.4, E_a can depend on the electric field if the defect is charged after emission. To investigate this, we performed TSC measurements with different V_{bias} for F150P-7 and F150P-8 after isochronal annealing at 170 °C and 300 °C, respectively. The TSC spectra with varying V_{bias} were presented in Fig. 8.25a and 8.25b for F150P-7

and F150P-8, respectively. As shown, except for B_iO_i, the Poole-Frenkel effect did not appear in other defects.

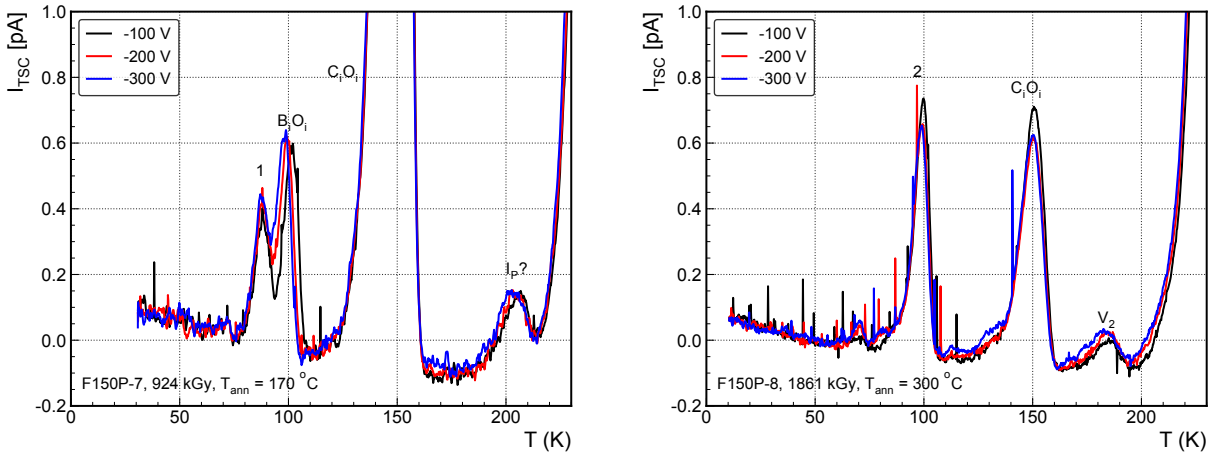

(a) (b)

Figure 8.22: (a) and (b) TSC spectra with forward bias injection, followed by heating up under different V_{bias} indicated in legends. (a) F150P-7 after isochronal annealing at T_{ann} = 170 °C. (b) F150P-8 after isochronal annealing at T_{ann} = 300 °C.

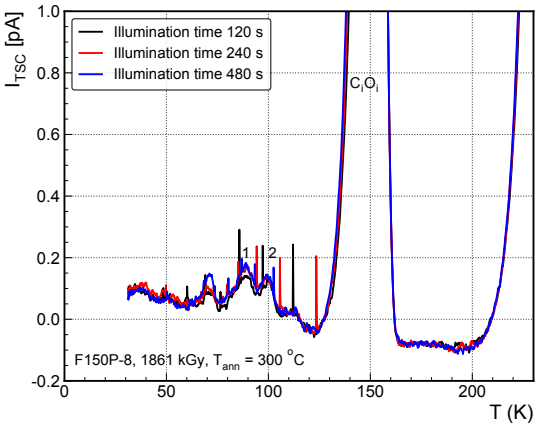

Figure 8.23: Light injection performed on diode F150P-8 after isochronal annealing at T_{ann} = 300 °C. Measurement details: Illumination time t_{fill} = 120, 240 and 480 s, V_{bias} = -200 V.

The light injection was performed on the diode F150Y-8 after 300 °C annealing. For this, a 520 nm wavelength light was used to illuminate the front side (n+) of an over-depleted diode at T_{fill} = 30 K. Since the absorption length of 520 nm light is roughly 1 μm [131, 132], it can be assumed that only holes are injected into the bulk of reverse biased illuminated diode. The result can be found in Fig. 8.23

$[C_iO_i]$, $[V_2]$ and $[I_p*]$ vs T_{ann}

The extracted $[C_iO_i]$, $[V_2]$, and $[I_p*]$ on F150P-7 were plotted as a function of T_{ann} in Fig. 8.24. Here, the $[C_iO_i]$ and $[V_2]$ were obtained from TSC measurements with T_{fill} = 100 K. As can be seen, both the C_iO_i and V_2 are stable up to 300 °C.

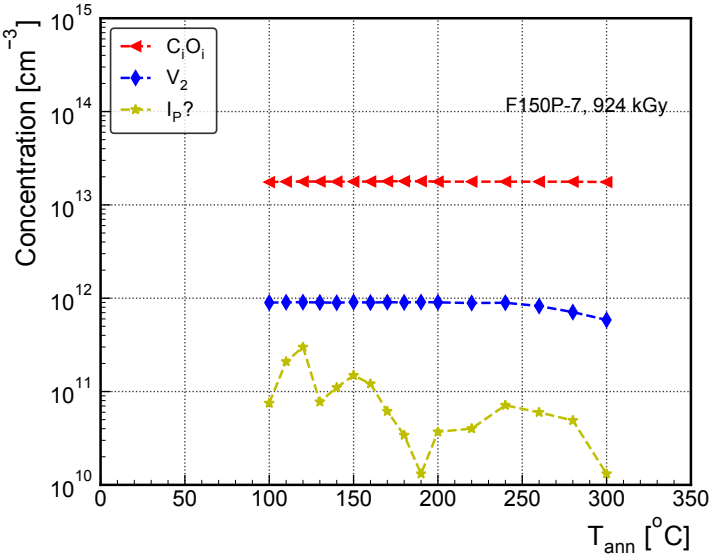

Figure 8.24: Evolution of the defect concentration in diode F150P-7 as a function of annealing temperature T_{ann}.

$\sigma_{n,p}$ for I_p*

In this work, $\sigma_{n,p}$ were determined by DLTS measurement as shown in Fig. 8.25.

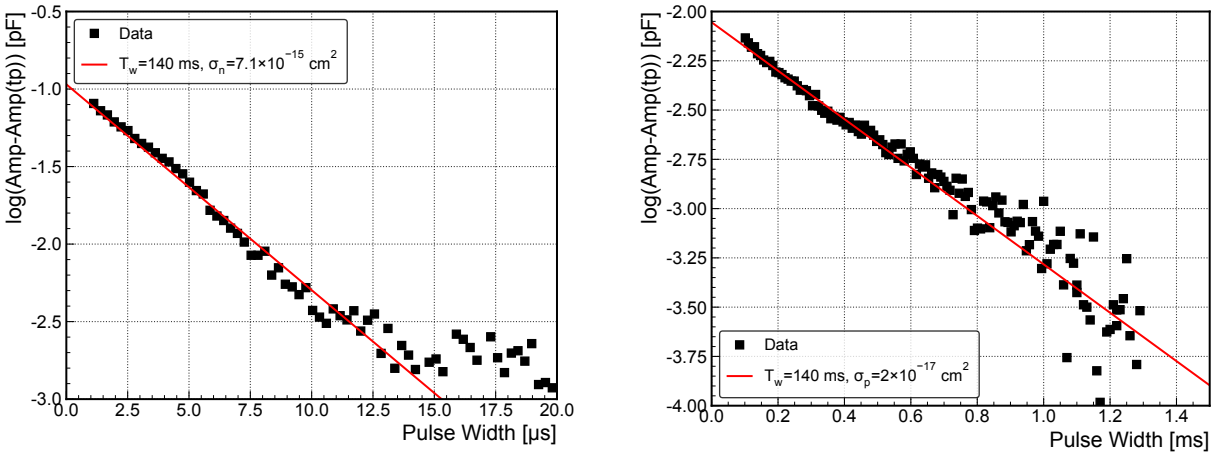

(a) (b)

Figure 8.25: (a) Pulse Width forward injection (for determining σ_n). (b) Pulse Width for determining the σ_p using a double pulse sequence: 1st with 20 µs forward injection with 1 V followed by a second one with -0.1 V of different duration.

9 Summary and Outlook

9.1 Summary

Silicon sensors for future particle physics and photon science detectors need to be resistant to radiation. For p-type sensors one of the main effects caused by radiation damage is the removal of substitutional boron, leading to a decrease of the initial doping concentration. The aim of this thesis was the systematic and detailed investigation of the boron removal effect in p-type silicon diodes. The boron removal effect had been introduced in detail in the previous chapters, which mainly involved the reduction of space charge density N_{eff} and is a dominant effect at lower irradiation fluence value. To investigate the boron removal effect in silicon sensors, the p-type silicon diodes containing EPI, Cz and FZ were investigated in detail after exposure to three different radiation sources (23 GeV protons, 5.5 MeV and ^{60}Co γ-ray). The work of this thesis was presented following the radiation sources:

In the first irradiation campaign, diodes of different resistivity were exposed to 23 GeV protons, with a fluence of $\Phi_{\text{p}} = 7 \times 10^{13}$ cm^{-2}. Within this group, it was investigated that the diodes with the same carbon concentration [C_{s}] of 2×10^{15} cm^{-3} and oxygen concentration [O_{i}] of 1×10^{17} cm^{-3}, but different boron doping concentrations [B_{s}] of 6.24×10^{12}, 4.53×10^{13}, 1.97×10^{14}, and 1.37×10^{15} cm^{-3}.

In a second campaign was exposed to 5.5 MeV electrons, with a fluence ranging from $\Phi_{\text{e}^-} = 1 \times 10^{15}$ cm^{-2} to $\Phi_{\text{e}^-} = 6 \times 10^{15}$ cm^{-2}. In this campaign, it was investigated that the diodes with the same boron doping concentration [B_{s}] of 1.37×10^{15} cm^{-3} and oxygen concentration [O_{i}] of 1.5×10^{17} cm^{-3}, but different carbon concentrations [C_{s}] of 2×10^{15} (EPI-diodes) and 3×10^{16} (Cz-diodes) cm^{-3}.

In a third campaign, high resistivity FZ silicon diodes were exposed to ^{60}Co gamma-ray irradiation, with doses ranging from $D = 0.1$ MGy to $D = 2$ MGy. Within this campaign, it was investigated that the diodes with the same boron doping concentration [B_{s}] of 3.5×10^{12} cm^{-3}, carbon concentration [C_{s}] of 2×10^{15} cm^{-3}, and oxygen concentration [O_{i}] of 1×10^{17} cm^{-3}.

Both macroscopic and microscopic measurements were performed to study the effects of irradiation on these diodes.

9.1.1 Macroscopic Properties

The macroscopic properties are the properties contributed by all electrically active microscopic defects at specific temperatures (normally around room temperature).

Space Charge Density at Room Temperature (Boron Removal Effect)

The observed decreases in N_{eff} with increasing fluence or dose were consistent across all irradiated diodes, indicating a common trend. This decrease is mainly attributed to the boron removal effect. However, it should be noted that this assumption does not hold for two high-resistivity EPI-diodes with resistivities of 2 k$\Omega \cdot$ cm and 250 $\Omega \cdot$ cm, which were irradiated with 23 GeV protons, as shown in Fig. 6.20.

In these particular diodes, most of the initial boron concentration ($[\mathrm{B_s}]$) was removed, which suggests that other factors contribute to the observed changes in N_{eff}. The irradiation with hadrons in these cases induced the formation of cluster-related defects, which also influences the space charge density (N_{eff}).

Except for the two high-resistivity EPI-diodes mentioned earlier, several conclusions can be drawn from the overall analysis of the results:

a) The change of N_{eff} is quite small after isothermal annealing at 80 °C for different annealing time t_{ann}, which correlates with the nearly constant concentration of the $\mathrm{B_iO_i}$ defect.

b) For 23 GeV proton irradiation, the increase of N_{eff} at temperatures above 150 °C correlates with the annealing-out of $\mathrm{B_iO_i}$ where the change of N_{eff} is about two times the change of $\mathrm{B_iO_i}$, indicating that most the $\mathrm{B_i}$ resulted from the dissociation of the $\mathrm{B_iO_i}$ donor defect returns to substitutional sites, regaining the acceptor character of the boron dopant.

c) For 5.5 MeV electron and ^{60}Co γ-ray irradiation, the N_{eff} decreases nearly linear with increasing fluence Φ_{eq} or dose D. By comparing the boron removal rate resulting from C–V measurements with the result by accounting twice the value of the $\mathrm{B_iO_i}$ introduction rate $g_{\mathrm{B_iO_i}}$ due to the donor character of the defect, a good agreement is obtained.

d) In the case of 5.5 MeV electron irradiation on Cz- and EPI-diodes, a significant decrease in N_{eff} was observed in EPI-diodes compared to Cz-diodes, despite being irradiated with the same fluence. This difference can be attributed to the higher carbon concentration in Cz-diodes, which leads to a reduction in $[\mathrm{B_iO_i}]$. The presence of higher carbon levels influences the boron removal process, thereby affecting the space charge density.

e) For ^{60}Co γ-ray irradiation, the isochronal annealing shows similar behaviour on N_{eff} compared to 23 GeV proton irradiation. However, N_{eff} returns back to 98%

for a dose of 1 MGy and 95% for a dose of 2 MGy of the initial value of about 3.5×10^{12} cm^{-3} after an annealing temperature of $T_{\text{ann}} > 200\,^{\circ}$C. This few percents difference at $T_{\text{ann}} \geq 200\,^{\circ}$C might be due to the fact that some of the boron atoms after dissociation of the B_iO_i will form other boron related defects like the B_iC_s.

Leakage Current

The increase in leakage current is caused by the increase in the concentration of the deep generation center after irradiation. While the boron removal effect is not responsible for the observed increases in leakage current after irradiation, some interesting results from the I–V measurements are observed:

a) Compared with 23 GeV proton irradiation, the obtained current-related damage parameter α is much smaller in 5.5 MeV electron irradiation, indicating that the increase of the leakage current caused by low energy electrons is substantially less than that caused by hadrons. Also, the change of the mean value of current density J_d with annealing time at 80 °C is strongly suppressed compared with hadron irradiated devices indicating that the irradiation with low energy electrons creates less current generation centers and more stable defects

b) For p-type FZ-diodes with ^{60}Co γ-ray irradiation, J_d linearly increased with dose and exhibited a trend similar to that of n-type silicon enriched with oxygen.

9.1.2 Microscopic Defects

The B_iO_i defect

The main focus of this work is on the defect B_iO_i, which is an electron trap with a positive charge at room temperature. It was found that B_iO_i predominantly contributes to the changes in N_{eff} for all investigated diodes, except for the 2 k$\Omega \cdot$ cm and 250 $\Omega \cdot$ cm diodes irradiated with 23 GeV protons.

In addition to these general observations, several other important informations about B_iO_i were obtained following different irradiation experiments:

a) For 23 GeV proton irradiation, the zero field activation energy $E_{a0} \approx 0.27$ eV of the B_iO_i was evaluated by using the 3-D Poole Frenkel effect. The generation rate of B_iO_i ($g_{B_iO_i}(N_{\text{eff},\,0})$) is presented together with data of other groups and compared with a defect kinetics model [21], [86]. It is shown that $g_{B_iO_i}$ increases with the initial doping up to some 1×10^{14} cm^{-3} and tends to saturation for higher values.

b) For 5.5 MeV electron irradiation, the TS-Cap method was used on non-fully depleted diodes to extract $[B_iO_i]$. The introduction rate of B_iO_i is much smaller in Cz than in EPI material, of 0.63 cm^{-1} compared with 1.75 cm^{-1}, the opposite is happening

for C_iO_i. This can be explained by the higher carbon concentration in Cz-diodes compare to EPI-diodes. Also, a 2 times large B_iO_i introduction rate was obtained compared to 23 GeV proton irradiation.

c) For ^{60}Co γ-ray irradiation, during isochronal annealing and with the decrease of the B_iO_i a new defect with a lower temperature of the peak maximum (defect 1) is forming and growing up to about 200 °C. For temperatures higher than 200 °C defect 1 is stable up to about 250 °C and during the decay a further defect 2 is formed and grows up to the limit of the used oven (300 °C). The defect 2 might be assigned to the B_iC_s defect.

The C_iO_i defect

The boron removal effect is strongly influenced by the presence of carbon in the material, which mainly forms the defect C_iO_i a well-known hole trap and neutral at room temperature.

After irradiation of EPI-diodes with 23 GeV protons it was observed that the concentrations of $[C_iO_i]$ decreases from 4.2×10^{13} cm^{-3} to 2.8×10^{13} cm^{-3} with an increase of the corresponding initial boron concentration from 6.24×10^{12} cm^{-3} to 1.37×10^{15} cm^{-3}.

For the diodes with same resistivity irradiated by 5.5 MeV electrons with same the fluence value, the less $[C_iO_i]$ was observed on EPI diodes with carbon concentration of 2×10^{15} cm^{-3} comparing to the Cz diodes with carbon concentration of 3×10^{16} cm^{-3}.

These observations indicate an opposite trend compared to the development of $[B_iO_i]$ with respect to $[C_s]$ and $[B_s]$. This is the reason why carbon co-implantation can enhance the radiation hardness of LGADs.

Electron Traps

Besides B_iO_i, other electron traps were also observed after irradiation, including:

a) **E30K** ($E_a = E_C - 0.079$ eV, $\sigma_n = 1.68 \times 10^{-14}$ cm^{-2}), which was observed in the 23 GeV proton-irradiated diodes. This defect exhibits a clear Poole-Frenkel effect, suggesting a positive charge at room temperature and its possible involvement in the annealing-related changes in N_{eff} for $T_{\text{ann}} < 150$ °C.

b) **E50K** ($E_a = E_C - 0.11$ eV, $\sigma_n = 5.4 \times 10^{-15}$ cm^{-2}) was exclusively observed in ^{60}Co γ-ray irradiated diodes, and its concentration was found to be very small.

c) **VO** ($E_a = E_C - 0.16$ eV, $\sigma_n = 6.1 \times 10^{-15}$ cm^{-2}), which was observed only in high resistivity diodes after irradiation, but did not contribute to the changes in N_{eff}.

d) $\mathbf{V_2^{-/o}}$ ($E_a = E_C - 0.429$ eV, $\sigma_n = 1.5 \times 10^{-15}$ cm^{-2}), which was observed only in diodes with resistivity higher than 10 $\Omega \cdot$ cm after irradiation, and did not contribute to the changes in N_{eff}.

Hole Traps

Besides the C_iO_i, some other hole traps were also observed after irradiation.

a) **H40K** ($E_a = E_V + 0.11$ eV, $\sigma_p = 4.3 \times 10^{-15}$ cm^{-2}) was observed in all lower boron-doped diodes, such as 2 k$\Omega \cdot$cm (EPI 12-74) and 250 $\Omega \cdot$cm (EPI 09-73), after 23GeV proton irradiation, as well as in all ^{60}Co gamma-ray-irradiated diodes. This defect exhibited a decrease in concentration during isothermal annealing at 80 °C, and its contribution to N_{eff} was not observed.

b) **H140K** ($E_a = E_V + 0.36$ eV, $\sigma_p = 2.5 \times 10^{-15}$ cm^{-2}) and **H152K** ($E_a = E_V + 0.42$ eV, $\sigma_p = 2.3 \times 10^{-14}$ cm^{-2}) were exclusively observed in the 23 GeV proton-irradiated diodes. These defects are negatively charged at RT and exhibit the Poole-Frankel effect, which means they contribute to N_{eff}. However, only in the 2 k$\Omega \cdot$cm EPI 12-74 diode, their concentrations is comparable to $[B_iO_i]$. It is possible that for higher fluences, they may play a more significant role.

9.2 Outlook

9.2.1 Question

All questions had been mentioned in chapter 6-8. The main two questions in this work are related to 1) TSC measurement and 2) The electrical properties of some defects.

TSC Method

As discussed in chapter 5, the measured currents during heating up include conduction, displacement, and diffusion currents. In the TSC method, the focus is on the conduction and diffusion currents, as they are the dominant contributions. This assumption is valid for diodes that are fully depleted during the heating up.

For diodes that cannot be fully depleted, this work takes into account the error in the extracted defect concentration by considering the depleted layer. However, it is important to note that the equation used for this correction is only applicable when the space charge density changes are homogeneously distributed in the bulk during heating up, and it does not account for the diffusion current. Furthermore, in diodes with thicker non-depleted regions, negative currents can be observed [183].

Consequently, the critical question for TSC measurement is how the electrically active defects in the depleted and non-depleted regions contributed to the TSC signal.

Defects

The main focus of this work is to investigate boron-related defects and their impact on the space charge density in the semiconductor material. One of the prominent boron-

related defects studied is B_iO_i, which has been found to have a strong influence on the space charge density. However, there are other defects, such as the X-defect, defect 1, and defect 2, which are still uncertain whether these defects are directly related to boron or if they have any boron-related origin.

9.2.2 New Project in the Frame of the RD50 Collaboration

To improve the radiation hardness of LGADs (Low-Gain Avalanche Diodes), institutions in the RD50 Collaboration: the National Institute of Materials Physics (NIMP), European Organization for Nuclear Research (CERN), Forschungsinstitut für Mikrosensorik GmbH (CiS), Jožef Stefan Institute (JSI), Universität Hamburg (UHH), Instituto Nazionale di Fisica Nucleare (INFN-Torino), and Vilnius University, has proposed further investigation on the acceptor removal effect.

The main objective of this project is to gain a better understanding of the acceptor removal effect and to develop parameterizations for different levels of B, C, and O impurities and irradiation fluences. The goal is to find suitable defect engineering solutions that can enhance the radiation hardness of the gain layers in LGADs.

In this project, diodes with resistivity ranging from 15 to 1.5 $\Omega \cdot$ cm will be investigated. Additionally, the compensation for substitutional phosphorus impurities will also be included in the investigation. By studying the acceptor removal effect and its relationship with impurity content, irradiation fluences, and compensation techniques, this project aims to provide valuable insights and guidelines for optimizing the design and fabrication of radiation-hard LGADs.

Appendix A: Chapter 6

Detailed information about other diodes can be found in Table 1, including the EPI 06-72 diodes which are identical to the EPI 06-71 diodes in terms of resistivity, area, and thickness, and were irradiated with the same fluence of 23 GeV protons. The EPI 06-73 and 06-74 diodes have similar physical and geometric parameters to the EPI 06-71 and 06-72 diodes but were irradiated with different fluences. The investigation also included a Czochralski silicon diode (Cz 03-300).

The extracted values of V_{fd} and N_{eff} were summarized in Table 2 before annealing including the diodes presented in Table 6.1 and Table 1, where the included N_{eff} is the mean value in the ranges presented in Fig. 6.2b.

Table 1: Device information (* 1 MeV neutron equivalent fluence)

Label	EPI 06-72	EPI 06-73	EPI 06-74	Cz 03-300
$N_{\mathrm{eff},0}$ (cm^{-3})	1.97×10^{14}	1.97×10^{14}	1.97×10^{14}	1.05×10^{14}
Initial resistivity ($\Omega \cdot \mathrm{cm}$)	≈50	≈50	≈50	≈250
Proton fluence Φ_{p} (cm^{-2})	7×10^{13}	5×10^{13}	5×10^{13}	7×10^{13}
Fluence value Φ_{eq} (cm^{-2})*	4.3×10^{13}	2.5×10^{13}	2.5×10^{13}	4.3×10^{13}
Area A (cm^2)	0.06927	0.06927	0.06927	0.06927
Thickness d (µm)	50	50	50	350

Table 2: V_{fd} and N_{eff} before and after irradiation

label	EPI 12-74	EPI 09-73	EPI 06-71	EPI 01-73
V_{fd} before irrad (V)	∼ 10	∼ 76.0	∼ 330	-
V_{fd} after irrad (V)	4.4 ± 0.3	18.1 ± 0.8	166.7 ± 6.0	-
$N_{\mathrm{eff},0}$ (10^{12} cm^{-3})	6.24	45.3	197	1370
N_{eff} after irrad (10^{12} cm^{-3})	2.01 ± 0.7	10.8 ± 1	101.8 ± 6	1010 ± 10
label	EPI 06-72	EPI 06-73	EPI 06-74	Cz 03-300
V_{fd} before irrad (V)	∼ 330	∼ 330	∼ 330	-
V_{fd} after irrad (V)	172.1 ± 4	271.9 ± 17	300.1 ± 12	-
$N_{\mathrm{eff},0}$ (10^{12} cm^{-3})	197	197	197	105
N_{eff} after irrad (10^{12} cm^{-3})	102.6 ± 2.5	162.1 ± 10	179.4 ± 7	82.3 ± 1.5

Bibliography

[1] M. Moll, "Displacement Damage in Silicon Detectors for High Energy Physics," *IEEE Transactions on Nuclear Science*, vol. 65, no. 8, pp. 1561–1582, 2018.

[2] G. Kramberger *et al.*, "Silicon detectors with 3-D electrode arrays: fabrication and initial test results," *J. Instrum*, vol. 10, no. 7, p. P07006, 2015.

[3] M. Ferrero *et al.*, "Radiation resistant LGAD design," *Nucl. Instrum. Methods Phys. Res. A*, vol. 919, pp. 16–26, 2019.

[4] A. Affolder *et al.*, "Charge collection studies in irradiated HV-CMOS particle detectors," *J. Instrum*, vol. 11, no. 04, p. P04007, 2016.

[5] E. Cavallaro *et al.*, "Studies of irradiated AMS H35 CMOS detectors for the ATLAS tracker upgrade," *J. Instrum*, vol. 12, no. 01, p. C01074, 2017.

[6] B. Hiti *et al.*, "Charge collection properties in an irradiated pixel sensor built in a thick-film HV-SOI process," *J. Instrum*, vol. 12, no. 10, p. P10020, 2017.

[7] I. Mandić *et al.*, "Neutron irradiation test of depleted CMOS pixel detector prototypes," *J. Instrum*, vol. 12, no. 02, p. P02021, 2017.

[8] B. Hiti *et al.*, "Charge collection in irradiated HV-CMOS detectors," *Nucl. Instrum. Methods Phys. Res. A*, vol. 924, pp. 214–218, 2019.

[9] I. Mandić *et al.*, "E-TCT measurements with passive CMOS pixel detectors on RD50-MPW1 chips from LFoundry," in *33th RD50 Workshop*, 2018.

[10] R. Wunstorf, *Systematische Untersuchungen zur Strahlenresistenz von Silizium-Detektoren für die Verwendung in Hochenergiephysik Experimenten.* PhD thesis, Universität Hamburg, 1992.

[11] M. Moll, *Radiation damage in silicon particle detectors: Microscopic defects and macroscopic properties.* PhD thesis, Universität Hamburg, 1999.

[12] H. Feick, *Radiation tolerance of silicon particle detectors for high-energy physics experiments.* PhD thesis, Universität Hamburg, 1997.

[13] A. Junkes, *Influence of radiation induced defect clusters on silicon particle detectors.* PhD thesis, Universität Hamburg, 2011.

[14] R. Radu, E. Fretwurst, R. Klanner, G. Lindström and I. Pintilie, "Radiation damage in n-type silicon diodes after electron irradiation with energies between 1.5 MeV and 15 MeV," *Nucl. Instrum. Methods Phys. Res. A*, vol. 730, pp. 84–90, 2013.

[15] P. M. Mooney, L. J. Cheng, M. Süli, J. D. Gerson and J. W. Corbett, "Defect energy levels in boron-doped silicon irradiated with 1-MeV electrons," *Phys. Rev. B*, vol. 15, no. 0, pp. 3836–3843, 1977.

[16] I. Pintilie, E. Fretwurst and G. Lindström, "Cluster related hole traps with enhanced-field-emission the source for long term annealing in hadron irradiated Si diodes," *Appl. Phys. Lett*, vol. 92, no. 2, p. 024101, 2008.

[17] K. A. Abdullin, B. Mukashev and Y. V. Gorelkinskii, "Metastable oxygen-silicon interstitial complex in crystalline silicon," *Semicond. Sci. Technol*, vol. 11, no. 11, p. 1696, 1996.

[18] I. Pintilie, G. Lindström, A. Junkes and E. Fretwurst, "Radiation-induced point- and cluster-related defects with strong impact on damage properties of silicon detectors," *Nucl. Instrum. Methods Phys. Res. A*, vol. 611, no. 1, pp. 52–68, 2009.

[19] J. Coutinho *et al.*, "Electronic and dynamical properties of the silicon trivacancy," *Phys. Rev. B*, vol. 86, no. 13, p. 174101, 2012.

[20] L. C. Kimerling, M. T. Asom, J. L. Benton, P. J. Drevinsky and C. E. Caefer, "Interstitial Defect Reactions in Silicon," in *Defects in Semiconductors 15*, pp. 141–150, 1989.

[21] L. F. Makarenko *et al.*, "Formation of a Bistable Interstitial Complex in Irradiated p-Type Silicon," *Phys. Status Solidi (A)*, vol. 216, no. 17, p. 1900354, 2019.

[22] C. Besleaga *et al.*, "Bistability of the BiOi complex and its implications on evaluating the "acceptor removal" process in p-type silicon," *Nucl. Instrum. Methods Phys. Res. A*, vol. 1017, p. 165809, 2014.

[23] C. Liao *et al.*, "The Boron–Oxygen (B_iO_i) Defect Complex Induced by Irradiation With 23 Gev Protons in p-Type Epitaxial Silicon Diodes," *IEEE Trans. Nucl. Sci*, vol. 69, no. 3, pp. 576–586, 2022.

[24] A. Hallén, N. Keskitalo, F. Masszi and V. Nágl, "Lifetime in proton irradiated silicon," *J. Appl. Phys*, vol. 79, no. 8, pp. 3906–3914, 1996.

[25] *https://www.indiamart.com/proddetail/silica-quartz-stone-20276543155.html.*

[26] *https://smallcaps.com.au/australia-the-lucky-country-in-silica-sand-race/.*

[27] *https://www.winfredint.com/.*

[28] *https://www.pv-magazine.com/2018/10/25/ingot-wafer-prices-dropping-market-momentum-needed/.*

[29] *https://en.wikipedia.org/wiki/Monocrystalline-silicon.*

[30] W. von-Ammon and H. Herzer, "The production and availability of high resistivity silicon for detector application," *Nucl. Instrum. Methods Phys. Res. A*, vol. 226, no. 1, pp. 94–102, 1984.

[31] J. Czochralski, "Ein neues Verfahren zur Messung der Kristallisationsgeschwindigkeit der Metalle," *Zeitschrift für Physikalische Chemie*, vol. 92U, no. 1, pp. 219–221, 1918.

[32] G. K. Teal, M. Sparks and E. Buehler, "Growth of Germanium Single Crystals Containing p-n Junctions," *Phys. Rev*, vol. 81, p. 637, 1951.

[33] C. P. Ewels, *Density functional modelling of point defects in semiconductors.* PhD thesis, University of Exeter, 1997.

[34] W. Lin, "The incorporation of oxygen into silicon crystals," in *Semicond*, pp. 9–52, 1994.

[35] S. M. Sze, *Semiconductor devices: physics and technology.* John wiley & sons, 2008.

[36] O. Madelung and M. Schulz, *Numerical data and functional relationships in Science and technology.* New York, Springer Verlag, 1990.

[37] H. Föll, *Electronic Materials.* University of Kiel, 2019.

[38] W. Zulehner, "Czochralski growth of silicon," *J. Cryst. Growth*, vol. 65, no. 1, pp. 189–213, 1983.

[39] R. W. Series and K. G. Barraclough, "Control of carbon in Czochralski silicon crystals," *J. Cryst. Growth*, vol. 63, no. 1, pp. 219–221, 1983.

[40] W. Kaiser, H. L. Frisch and H. Reiss, "Mechanism of the Formation of Donor States in Heat-Treated Silicon," *Phys. Rev*, vol. 112, no. 0, pp. 1546–1554, 1958.

[41] J. Michel and L. C. Kimerling, "Electrical properties of oxygen in silicon," in *Semicond*, pp. 251–287, 1994.

[42] D. Åberg, B. G. Svensson, T. Hallberg and J. L. Lindström, "Kinetic study of oxygen dimer and thermal donor formation in silicon," *Phys. Rev. B*, vol. 58, no. 0, pp. 12944–12951, 1998.

[43] W. Götz, G. Pensl and W. Zulehner, "Observation of five additional thermal donor species TD12 to TD16 and of regrowth of thermal donors at initial stages of the new oxygen donor formation in Czochralski-grown silicon," *Phys. Rev. B*, vol. 46, no. 0, pp. 4312–4315, 1992.

[44] S. D. Brotherton and P. Bradley, "Defect production and lifetime control in electron and γ-irradiated silicon," *J. Appl. Phys*, vol. 53, no. 8, pp. 5720–5732, 1982.

[45] G. D. Watkins and J. W. Corbett, "Defects in Irradiated Silicon. I. Electron Spin Resonance of the Si-*A* Center," *Phys. Rev*, vol. 121, no. 0, pp. 1001–1014, 1961.

[46] W. Von-Ammon *et al.*, "Application of magnetic fields in industrial growth of silicon single crystals," in *The 15th Riga and 6th PAMIR Conf. on Fundamental and Applied MHD.- Riga*, pp. 41–54, 2005.

[47] C. Wang, H. Zhang, T. H. Wang and T. F. Ciszek, "A continuous Czochralski silicon crystal growth system," *J. Cryst. Growth*, vol. 250, no. 1, pp. 209–214, 2003.

[48] H. C. Theuerer, "Method of processing semiconductive materials," Oct. 23 1962. US Patent 3,060,123.

[49] *Neutron Transmutation Doping of Silicon at Research Reactors.* No. 1681 in TECDOC Series, Vienna: INTERNATIONAL ATOMIC ENERGY AGENCY, 2012.

[50] G. K. Celler and S. Cristoloveanu, "Frontiers of silicon-on-insulator," *J. Appl. Phys*, vol. 93, no. 9, pp. 4955–4978, 2003.

[51] D. M. Hansen and T. F. Kuech, "Epitaxial technology for integrated circuit manufacturing," in *Encyclopedia of Physical Science and Technology (Third Edition)* (R. A. Meyers, ed.), pp. 641–652, New York: Academic Press, 2003.

[52] I. Pintilie, M. Buda, E. Fretwurst, G. Lindström and J. Stahl, "Stable radiation-induced donor generation and its influence on the radiation tolerance of silicon diodes," *Nucl. Instrum. Methods Phys. Res. A*, vol. 556, no. 1, pp. 197–208, 2006.

[53] E. Schrödinger, "An Undulatory Theory of the Mechanics of Atoms and Molecules," *Phys. Rev*, vol. 28, no. 6, pp. 1049–1070, 1926.

[54] F. Bloch, "Über die quantenmechanik der elektronen in kristallgittern," *Zeitschrift für physik*, vol. 52, no. 7, pp. 555–600, 1929.

[55] J. C. Slater and G. F. Koster, "Simplified LCAO Method for the Periodic Potential Problem," *Phys. Rev*, vol. 94, no. 0, pp. 1498–1524, 1954.

[56] M. L. Cohen and T. K. Bergstresser, "Band Structures and Pseudopotential Form Factors for Fourteen Semiconductors of the Diamond and Zinc-blende Structures," *Phys. Rev*, vol. 141, no. 0, pp. 789–796, 1966.

[57] M. M. William, *Pseudopotential-Derived Band Structure of Silicon*. GitHub, 2015.

[58] W. Shockley, *Electrons and Holes in Semiconductors: With Applications to Transistor Electronics*. Van Nostrand, 1950.

[59] M. A. Green, "Intrinsic concentration, effective densities of states, and effective mass in silicon," *J. Appl. Phys*, vol. 67, no. 6, pp. 2944–2954, 1990.

[60] D. M. Caughey and R. E. Thomas, "Carrier mobilities in silicon empirically related to doping and field," *Proceedings of the IEEE*, vol. 55, no. 12, pp. 2192–2193, 1967.

[61] W. Shockley and W. T. Read, "Statistics of the Recombinations of Holes and Electrons," *Phys. Rev*, vol. 87, no. 0, pp. 835–842, 1952.

[62] Z. Li, "New BNL 3D-Trench electrode Si detectors for radiation hard detectors for sLHC and for X-ray applications," *Nucl. Instrum. Methods Phys. Res. A*, vol. 658, no. 1, pp. 90–97, 2011.

[63] M. Liu, S. Lu and Z. Li, "Theoretical bases of hypothetical sphere-electrode detectors and practical near-sphere-electrode (semisphere-electrode and near-semisphere-electrode) detectors," *J PHYS D APPL PHYS*, vol. 54, no. 4, p. 045101, 2020.

[64] C. Liao, M. Liu, Y. Zhang, J. Zhao and Z. Li, "Designs and electric properties studied of 3D trench electrode Si detector with adjustable central collection electrode," *AIP Advances*, vol. 8, no. 7, 2018.

[65] J. Schwandt and R. Klanner, "On the weighting field of irradiated silicon detectors," *Nucl. Instrum. Methods Phys. Res. A*, vol. 942, p. 162418, 2019.

[66] D. M. Fleetwood, "$1/f$ noise and defects in microelectronic materials and devices," *IEEE Trans. Nucl. Sci*, vol. 62, no. 4, pp. 1462–1486, 2015.

[67] Z. Li and H. W. Kraner, "Studies of frequency dependent CV characteristics of neutron irradiated p^+-n silicon detectors," *IEEE Trans. Nucl. Sci*, vol. 38, no. 2, pp. 244–250, 1991.

[68] A. Owens, *Semiconductor radiation detectors*. CRC Press, 2019.

[69] S. Ramo, "Currents induced by electron motion," *Proceedings of the IRE*, vol. 9, no. 9, pp. 584–585, 1939.

[70] G. Cavalleri, E. Gatti, G. Fabri and V. Svelto, "Extension of Ramo's theorem as applied to induced charge in semiconductor detectors," *Nucl. Instrum. Methods Phys. Res. A*, vol. 92, no. 1, pp. 137–140, 1971.

[71] G. Cavalleri, E. Gatti, G. Fabri and V. Svelto, "Signal evaluation in multielectrode radiation detectors by means of a time dependent weighting vector," *Nucl. Instrum. Methods Phys. Res. A*, vol. 193, no. 3, pp. 651–653, 1982.

[72] W. Riegler, "An application of extensions of the Ramo-Shockley theorem to signals in silicon sensors," *Nucl. Instrum. Methods Phys. Res. A*, vol. 940, pp. 453–461, 2019.

[73] T. J. Brodbeck *et al.*, "A new method of carrier trapping time measurement," *Nucl. Instrum. Methods Phys. Res. A*, vol. 455, no. 3, pp. 645–655, 2000.

[74] G. L. Bayatian *et al.*, "CMS Physics: Technical Design Report Volume 1: Detector Performance and Software," tech. rep., CERN-LHCC-2006-001, CMS-TDR-8-1, CERN-LHCC-2006-001, CMS-TDR-8-1, 2006.

[75] F. Feindt, *Silicon Pixel Sensors in the Inner Tracking System of the CMS Experiment*. PhD thesis, Universität Hamburg, 2021.

[76] S. Seidel, "Silicon strip and pixel detectors for particle physics experiments," *Phys. Rep*, vol. 828, pp. 1–34, 2019.

[77] D. Bortoletto, "How and why silicon sensors are becoming more and more intelligent?," *J. Instrum*, vol. 10, 2015.

[78] S. I. Parker, C. J. Kenney and J. Segal, "3D—A proposed new architecture for solid-state radiation detectors," *Nucl. Instrum. Methods Phys. Res. A*, vol. 395, no. 3, pp. 328–343, 1997.

[79] C. Kenney, S. Parker, J. Segal and C. Storment, "Silicon detectors with 3-D electrode arrays: fabrication and initial test results," *IEEE Trans. Nucl. Sci*, vol. 46, no. 4, pp. 1224–1236, 1999.

[80] G. D. Betta and M. Povoli, "Progress in 3D silicon radiation detectors," *Front. in Phys.*, vol. 10, p. 927690, 2022.

[81] N. Otte *et al.*, "The SiPM—A new photon detector for PET," *Nucl. Phys. B-Proceedings Supplements*, vol. 150, pp. 417–420, 2006.

[82] E. Garutti and Yu. Musienko, "Radiation damage of SiPMs," *Nucl. Instrum. Meth. A*, vol. 926, pp. 69–84, 2019.

[83] F. Sefkow, F. Simon and CALICE Collaboration, "A highly granular SiPM-on-tile calorimeter prototype," in *Journal of Physics: Conference Series*, p. 012012, 2019.

[84] R. Agishev *et al.*, "Lidar with SiPM: Some capabilities and limitations in real environment," *Opt. Laser Technol*, vol. 49, pp. 86–90, 2013.

[85] Hamamatsu Photonics K.K, *https://www.hamamatsu.com/*, 2023.

[86] M. Moll, "Acceptor removal – Displacement damage effects involving the shallow acceptor doping of p-type silicon devices," *PoS*, vol. Vertex2019, p. 027, 2020.

[87] E. M. Donegani, *Energy-Dependent Proton Damage in Silicon*. PhD thesis, Universität Hamburg, 2017.

[88] J. M. Benedetto and H. E. Boesch, "The Relationship between ^{60}Co and 10-keV X-Ray Damage in MOS Devices," *IEEE Trans. Nucl. Sci*, vol. 33, no. 6, pp. 1317–1323, 1986.

[89] J. Zhang, *X-ray Radiation Damage Studies and Design of a Silicon Pixel Sensor for Science at the XFEL*. PhD thesis, Universität Hamburg, 2013.

[90] D. M. Fleetwood and R. D. Schrimpf, *Defects in microelectronic materials and devices*. CRC press, 2008.

[91] V. A. J. V. Lint, *Mechanisms of Radiation Effects in Electronic Materials*. Wiley, 1980.

[92] C. Leroy and G. Rancoita, Pier, *Principles of Radiation Interaction in Matter and Detection*. WORLD SCIENTIFIC, 4th ed., 2016.

[93] Y. Shi, D. X. Shen, F. M. Wu and K. J. Cheng, "A numerical study of cluster center formation in neutron-irradiated silicon," *J. Appl. Phys*, vol. 67, no. 2, pp. 1116–1118, 1990.

[94] M. S. Lazo, D. M. Woodall and P. J. McDaniel, "Silicon and silicon dioxide neutron damage functions," in *Proc. Fast Burt React. Workshop*, vol. 1, pp. 49–54, 1986.

[95] M. Huhtinen and P. A. Aarnio, "Pion induced displacement damage in silicon devices," *Nucl. Instrum. Methods Phys. Res. A*, vol. 335, no. 3, pp. 580–582, 1993.

[96] A. Vasilescu *et al.*, "The NIEL scaling hypothesis applied to neutron spectra of irradiation facilities and in the ATLAS and CMS SCT," *ROSE= TN*, pp. 97–2, 1997.

[97] P. J. Griffin, J. G. Kelly, T. F. Luera and J. VanDenburg, "SNL RML recommended dosimetry cross section compendium," tech. rep., Sandia National Labs., Albuquerque, NM (United States), 1993.

[98] A. Y. Konobeyev, Y. A. Korovin and V. N. Sosnin, "Neutron displacement cross-sections for structural materials below 800 MeV," *J. Nucl. Mater*, vol. 186, no. 2, pp. 117–130, 1992.

[99] G. P. Summers, E. A. Burke, P. Shapiro, S. R. Messenger and R. J. Walters, "Damage correlations in semiconductors exposed to gamma, electron and proton radiations," *IEEE Trans. Nucl. Sci*, vol. 40, no. 6, pp. 1372–1379, 1993.

[100] I. Pintilie, E. Fretwurst, G. Lindström and J. Stahl, "Second-order generation of point defects in gamma-irradiated float-zone silicon, an explanation for 'type inversion'," *Appl. Phys. Lett*, vol. 82, no. 13, pp. 2169–2171, 2003.

[101] J. Adey, R. Jones and P. R. Briddon, "Formation of BiOi, BiCs, and BiBsHi defects in e-irradiated or ion-implanted silicon containing boron," *Appl. Phys. Lett*, vol. 83, no. 4, pp. 665–667, 2003.

[102] G. D. Watkins and J. W. Corbett, "Defects in Irradiated Silicon: Electron Paramagnetic Resonance and Electron-Nuclear Double Resonance of the Si-E Center," *Phys. Rev.*, vol. 134, pp. A1359–A1377, 1964.

[103] I. Pintilie, E. Fretwurst, G. Lindström, and J. Stahl, "Results on defects induced by ^{60}Co γ irradiation in standard and oxygen-enriched silicon," *Nucl. Instrum. Methods Phys. Res. A*, vol. 514, no. 1, pp. 18–24, 2003.

[104] J. Lindström *et al.*, "Interaction between self-interstitials and the oxygen dimer in silicon," *Physica B: Condensed Matter*, vol. 308-310, pp. 284–289, 2001. International Conference on Defects in Semiconductors.

[105] B. R. Gossick, "Disordered regions in semiconductors bombarded by fast neutrons," *J. Appl. Phys*, vol. 30, no. 8, pp. 1214–1218, 2004.

[106] A. Scheinemann and A. Schenk, "TCAD-based DLTS simulation for analysis of extended defects," *Phys. Status Solidi (A)*, vol. 211, no. 1, pp. 136–142, 2014.

[107] E. M. Donegani *et al.*, "Study of point-and cluster-defects in radiation-damaged silicon," *Nucl. Instrum. Methods Phys. Res. A*, vol. 898, pp. 15–23, 2018.

[108] G. Davies *et al.*, "Radiation damage in silicon exposed to high-energy protons," *Phys. Rev. B*, vol. 73, no. 10, p. 165202, 2006.

[109] T. R. Waite, "Theoretical Treatment of the Kinetics of Diffusion-Limited Reactions," *Phys. Rev*, vol. 107, no. 0, pp. 463–470, 1957.

[110] B. G. Svensson and J. L. Lindström, "Kinetic study of the 830- and 889-cm^{-1} infrared bands during annealing of irradiated silicon," *Phys. Rev. B*, vol. 34, no. 0, pp. 8709–8717, 1986.

[111] Provided by Prof. Dr. Erika Guratti in private correspondence, 2022.

[112] Y. Gurimskaya *et al.*, "Acceptor removal in silicon pad diodes with different resistivities," in *presented at the 31st RD50 Workshop, CERN, Geneva, Switzerland*, 2017.

[113] V. Eremin, E. Verbitskaya and Z. Li, "The origin of double peak electric field distribution in heavily irradiated silicon detectors," *Nucl. Instrum. Methods Phys. Res. A*, vol. 476, no. 3, pp. 556–564, 2002.

[114] J. Schwandt *et al.*, "A new model for the TCAD simulation of the silicon damage by high fluence proton irradiation," in *Proceedings of NSS/MIC 2018*, pp. 1–3.

[115] Z. Li, "Radiation damage effects in Si materials and detectors and rad-hard Si detectors for SLHC," *J. Instrum*, vol. 4, no. 3, p. P03011, 2009.

[116] E. Verbitskaya *et al.*, "The effect of charge collection recovery in silicon p–n junction detectors irradiated by different particles," *Nucl. Instrum. Methods Phys. Res. A*, vol. 514, no. 1, pp. 47–61, 2003.

[117] V. Radeka, "Low-Noise Techniques in Detectors," *Annu. Rev. Nucl*, vol. 38, no. 1, pp. 217–277, 1988.

[118] Z. Li and H. W. Kraner, "Modeling and simulation of charge collection properties for neutron irradiated silicon detectors," *Nucl. Phys. B - Proceedings Supplements*, vol. 32, no. 32, pp. 398–409, 1993.

[119] M. Moll *et al.*, "Recent advances in the development of radiation tolerant silicon detectors for the Super-LHC," *Detectors and Experimental Techniques*, pp. 101–110, 2010.

[120] Z. Galloway *et al.*, "Properties of HPK UFSD after neutron irradiation up to 6e15 n/cm2," *Nucl. Instrum. Methods Phys. Res. A*, vol. 940, pp. 19–29, 2019.

[121] M. Glaser *et al.*, "New irradiation zones at the CERN-PS," *Nucl. Instrum. Methods Phys. Res. A*, vol. 426, no. 1, pp. 72–77, 1999.

[122] M. Glaser, F. Ravotti and M. Moll, "Dosimetry Assessments in the Irradiation Facilities at the CERN-PS Accelerator," *IEEE Trans. Nucl. Sci*, vol. 53, no. 4, pp. 2016–2022, 2006.

[123] E. León-Florián, C. Leroy and C. Furetta, "Particle fluence measurements by activation technique for radiation damage studies," tech. rep., CERN, 1995.

[124] L. F. Makarenko, M. Moll, F. P. Korshunov and S. B. Lastovski, "Reactions of interstitial carbon with impurities in silicon particle detectors," *J. Appl. Phys*, vol. 101, no. 11, 2007.

[125] M. Roguljic *et al.*, "Low dose rate ^{60}Co facility in Zagreb," *PoS*, vol. Vertex2019, p. 066, 2020.

[126] Keithley, *User's Manual*. Model 6517B Electrometer, 2020.

[127] Agilent, *User's Manual*. Agilent E4980A LCR meter, 2020.

[128] T. Kuphaldt, "Lessons In Electric Circuits, Volume II–AC," 2007.

[129] B. Dezillie *et al.*, "Improved neutron radiation hardness for Si detectors: application of low resistivity starting material and/or manipulation of N_{eff} by selective filling of radiation-induced traps at low temperatures," *IEEE Trans. Nucl. Sci*, vol. 46, no. 3, pp. 221–227, 1999.

[130] C. T. Sah, L. Forbes, L. L. Rosier and A. F. Tasch, "Thermal and optical emission and capture rates and cross sections of electrons and holes at imperfection centers in semiconductors from photo and dark junction current and capacitance experiments," *Solid State Electron*, vol. 13, no. 6, pp. 759–788, 1970.

[131] W. C. Dash and R. Newman, "Intrinsic Optical Absorption in Single-Crystal Germanium and Silicon at 77 K and 300 K," *Phys. Rev*, vol. 99, no. 0, pp. 1151–1155, 1955.

[132] R. Braunstein, A. R. Moore and F. Herman, "Intrinsic Optical Absorption in Germanium-Silicon Alloys," *Phys. Rev*, vol. 109, no. 0, pp. 695–710, 1958.

[133] I. Pintilie, L. Pintilie, M. Moll, E. Fretwurst and G. Lindström, "Thermally stimulated current method applied on diodes with high concentration of deep trapping levels," *Appl. Phys. Lett*, vol. 78, no. 4, pp. 550–552, 2001.

[134] M. G. Buehler, "Impurity centers in PN junctions determined from shifts in the thermally stimulated current and capacitance response with heating rate," *Solid State Electron*, vol. 15, no. 1, pp. 69–79, 1972.

[135] J. Frenkel, "On Pre-Breakdown Phenomena in Insulators and Electronic Semi-Conductors," *Phys. Rev*, vol. 54, no. 0, pp. 647–648, 1938.

[136] J. L. Hartke, "The Three-Dimensional Poole-Frenkel Effect," *J. Appl. Phys*, vol. 39, no. 10, pp. 4871–4873, 2003.

[137] G. A. M. Hurkx, D. B. M. Klaassen and M. P. G. Knuvers, "A new recombination model for device simulation including tunneling," *IEEE Trans. Electron Devices*, vol. 39, no. 2, pp. 331–338, 1992.

[138] C. Zener, "A theory of the electrical breakdown of solid dielectrics," *Proc. R. Soc*, vol. 145, no. 855, pp. 523–529, 1934.

[139] A. G. Chynoweth, W. L. Feldmann and R. A. Logan, "Excess tunnel current in silicon Esaki junctions," *Phys. Rev*, vol. 121, no. 3, p. 684, 1961.

[140] F. Hurkx, H. L. Peek, J. W. Slotboom, and R. A. Windgassen, "Anomalous behavior of surface leakage currents in heavily doped gated-diodes," *IEEE Transactions on Electron Devices*, vol. 40, no. 12, pp. 2273–2281, 1993.

[141] R. Fleming, C. Seager, D. Lang, E. Bielejec, and J. Campbell, "Defect-driven gain bistability in neutron damaged, silicon bipolar transistors," *Appl. Phys. Lett*, vol. 90, no. 17, p. 172105, 2007.

[142] I. Pintilie, E. Fretwurst, G. Lindström and J. Stahl, "Close to midgap trapping level in ^{60}Co gamma irradiated silicon detectors," *Appl. Phys. Lett*, vol. 81, no. 1, pp. 165–167, 2002.

[143] Institute of Electronic Materials Technology (ITME), . Warsaw, Poland.

[144] CiS Forschungsinstitut für Mikrosensork GmbH, . Erfurt, Germany.

[145] P. Allport *et al.*, "Experimental determination of proton hardness factors at several irradiation facilities," *J. Instrum*, vol. 14, no. 12, p. P12004, 2019.

[146] E. Fretwurst *et al.*, "Determination of the p-spray profile for n+p silicon sensors using a MOSFET," *Nucl. Instrum. Methods Phys. Res. A*, vol. 866, pp. 140–149, 2017.

[147] L. Tsetseris, R. D. Schrimpf, D. M. Fleetwood, R. Pease, and S. T. Pantelides, "Common origin for enhanced low-dose-rate sensitivity and bias temperature instability under negative bias," *IEEE Trans. Nucl. Sci*, vol. 52, no. 6, pp. 2265–2271, 2005.

[148] T. Zundel and J. Weber, "Dissociation energies of shallow-acceptor-hydrogen pairs in silicon," *Phys. Rev. B*, vol. 39, pp. 13549–13552, 1989.

[149] T. Zundel and J. Weber, "Boron reactivation kinetics in hydrogenated silicon after annealing in the dark or under illumination," *Phys. Rev. B*, vol. 43, pp. 4361–4372, 1991.

[150] L. Makarenko, F. Korshunov, S. Lastovskii, and N. Zamyatin, "Detection of hydrogen impurity in silicon radiation detectors," *Semiconductors*, vol. 37, pp. 611–615, 2003.

[151] O. Feklisova, N. Yarykin, E. Yakimov, and J. Weber, "On the nature of hydrogen-related centers in p-type irradiated silicon," *Physica B Condens. Matter*, vol. 308-310, pp. 210–212, 2001. International Conference on Defects in Semiconductors.

[152] C. Liao *et al.*, "The boron-oxygen (B_iO_i) defect complex induced by irradiation with 23 GeV protons in p-type epitaxial silicon diodes," in *37th RD50 Workshop*, 2020.

[153] L. F. Makarenko *et al.*, "Formation and annealing of boron-oxygen defects in irradiated silicon and silicon-germanium n+–p structures," *AIP Conference Proceedings*, vol. 1583, no. 1, pp. 123–126, 2014.

[154] A. Khan *et al.*, "Role of the impurities in production rates of radiation-induced defects in silicon materials and solar cells," *J. Appl. Phys*, vol. 90, no. 3, pp. 1170–1178, 2001.

[155] O. Feklisova, N. Yarykin, and J. Weber, "Annealing kinetics of boron-containing centers in electron-irradiated silicon," *Semiconductors*, vol. 47, pp. 228–231, 2013.

[156] A. Himmerlich *et al.*, "Defect investigations of electron irradiated p-type Si sensors," in *37th RD50 Workshop*, 2020.

[157] I. Pintilie *et al.*, "Structural, compositional and defect studies on hadron irradiated B-doped silicon diodes," in *37th RD50 Workshop*, 2020.

[158] L. Vines *et al.*, "Formation and origin of the dominating electron trap in irradiated *p*-type silicon," *Phys. Rev. B*, vol. 78, p. 085205, 2008.

[159] C. Liao *et al.*, "Investigation of the Boron removal effect induced by 5.5 MeV electrons on highly doped EPI- and Cz-silicon," *arXiv:2306.14736*, 2023.

[160] A. Himmerlich *et al.*, "Defect characterization studies on irradiated boron-doped silicon pad diodes and Low Gain Avalanche Detectors," *Nucl. Instrum. Methods Phys. Res. A*, vol. 1048, p. 167977, 2023.

[161] L. F. Makarenko, S. B. Lastovskii, H. S. Yakushevich, M. Moll, and I. Pintilie, "Effect of electron injection on defect reactions in irradiated silicon containing boron, carbon, and oxygen," *J. Appl. Phys*, vol. 123, no. 16.

[162] I. Jun, W. Kim, and R. Evans, "Electron Nonionizing Energy Loss for Device Applications," *IEEE Trans. Nucl. Sci*, vol. 56, no. 6, pp. 3229–3235, 2009.

[163] R. Radu *et al.*, "Investigation of point and extended defects in electron irradiated silicon—Dependence on the particle energy," *J. Appl. Phys*, vol. 117, no. 16, 2015.

[164] M. Moll, E. Fretwurst, and G. Lindström, "Leakage current of hadron irradiated silicon detectors – material dependence," *Nucl. Instrum. Methods Phys. Res. A*, vol. 426, no. 1, pp. 87–93, 1999.

[165] M. Moll, E. Fretwurst, M. Kuhnke and G. Lindström, "Relation between microscopic defects and macroscopic changes in silicon detector properties after hadron irradiation," *Nucl. Instrum. Methods Phys. Res. B*, vol. 186, no. 1, pp. 100–110, 2002.

[166] C. Liao *et al.*, "Investigation of high resistivity p-type FZ silicon diodes after ^{60}Co γ-irradiation," *arXiv:2306.15336*, 2023.

[167] C. Möller and K. Lauer, "Light-induced degradation in indium-doped silicon," *Phys. Status Solidi - Rapid Res. Lett*, vol. 7, no. 7, pp. 461–464, 2013.

[168] K. Lauer, C. Möller, C. Teßmann, D. Schulze and N. V. Abrosimov, "Activation energies of the InSi-Sii defect transitions obtained by carrier lifetime measurements," *Phys. Status Solidi C*, vol. 14, no. 5, p. 1600033, 2017.

[169] Y. Gurimskaya *et al.*, "Radiation damage in p-type EPI silicon pad diodes irradiated with protons and neutrons," *Nucl. Instrum. Methods Phys. Res. A*, vol. 958, p. 162221, 2020.

[170] C. Liao *et al.*, "Investigation of the B_iO_i defect in EPI and Cz silicon diodes using Thermally Stimulated Current (TSC) and Thermally Stimulated Capacitance (TSCap)," in *39th RD50 Workshop*, 2021.

[171] J. H. Cahn, "Irradiation damage in germanium and silicon due to electrons and gamma rays," *J. Appl. Phys*, vol. 30, no. 8, pp. 1310–1316, 1959.

[172] J. Schwandt *et al.*, "CMS Pixel detector development for the HL-LHC," *Nucl. Instrum. Methods Phys. Res. A*, vol. 924, pp. 59–63, 2019.

[173] Tracker Group of the CMS Collaboration, "Evaluation of HPK n^+-p planar pixel sensors for the CMS Phase-2 upgrade," *arXiv preprint*, 2022.

[174] E. Fretwurst *et al.*, "Bulk damage effects in standard and oxygen-enriched silicon detectors induced by ^{60}Co-gamma radiation," *Nucl. Instrum. Methods Phys. Res. A*, vol. 514, no. 1, pp. 1–8, 2003.

[175] R. Radu, *Bulk radiation damage in silicon: from point defects to clusters.* PhD thesis, University of Bucharest, 2015.

[176] I. Pintilie *et al.*, "Second-order generation of point defects in highly irradiated float zone silicon — annealing studies," *Physica B Condens. Matter*, vol. 340-342, pp. 578–582, 2003.

[177] A. Chilingarov, "Temperature dependence of the current generated in Si bulk," *J. Instrum*, vol. 8, no. 10, p. P10003, 2013.

[178] P. Bräunlich, *Thermally stimulated relaxation in solids*, vol. 37. 1979. section 2.5.

[179] B. G. Svensson, B. Mohadjeri, A. Hallén, J. H. Svensson and J. W. Corbett, "Divacancy acceptor levels in ion-irradiated silicon," *Phys. Rev. B*, vol. 43, pp. 2292–2298, 1991.

[180] E. V. Monakhov *et al.*, "Ion mass effect on vacancy-related deep levels in Si induced by ion implantation," *Phys. Rev. B*, vol. 65, p. 245201, 2002.

[181] P. J. Drevinsky, C. E. Caefer, S. P. Tobin, J. C. Mikkelsen and L. C. Kimerling, "Influence of Oxygen and Boron on Defect Production in Irradiated Silicon," *MRS Online Proceedings Library (OPL)*, vol. 104, p. 167, 1987.

[182] C. Liao *et al.*, "Investigation of high resistivity p-type FZ silicon diodes after ^{60}Co-γ irradiation," in *40th RD50 Workshop*, 2022.

[183] S. Niels *et al.*, "Defect spectroscopy on 23 GeV Proton-Irradiated CZ Pad Diodes," in *presented at the 42st RD50 Workshop, Tivat, Montenegro, Switzerland*, 2017.

Acknowledgements

I would like to express my sincere gratitude to all the individuals who have been part of my journey. Firstly, I am immensely grateful to my supervisor, Prof. Dr. Erika Garutti, for providing and supporting me with the invaluable opportunity to work in the Detector Lab at Universität Hamburg. Her guidance and support have been instrumental in shaping this research. I would also like to extend my thanks to Dr. Jörn Schwandt for generously sharing his personal library, which included valuable books and references that greatly enriched my work. Additionally, I am indebted to Prof. Dr. Robert Klanner for his critical insights and valuable comments on my research.

A special paragraph is dedicated to expressing my deepest gratitude to Dr. Eckhart Fretwurst. Your continuous education, training, discussions, and insightful suggestions have been indispensable in the completion of this work. As an 85-year-old researcher, your unwavering dedication to science has not only inspired me but has also taught me the true essence of being a scholar. This experience will remain a cherished treasure throughout my life. I am grateful not only for the knowledge I have gained from you but also for the unwavering spirit and determination I have learned from you.

I am sincerely grateful to my group members, Peter Buhmann and Stephan Martens, for their invaluable assistance in improving the experimental setup. Dr. Annika Vauth's support and guidance have been immensely helpful. I also want to thank Carman Villalba, Bianca Raciti, Lukas Eikelmann, and Jack Rolph for their companionship, cultural exchange, and support throughout my journey.

I am deeply grateful to Dr. Michael Moll and Dr. Ioana Pintilie for their invaluable suggestions and assistance in revising my papers. Dr. Michael Moll's thesis was instrumental in completing my work, and his guidance has been crucial throughout my research journey. I extend my sincere appreciation to Dr. Ioana Pintilie for her insightful comments and meticulous revisions, which greatly improved the quality of my research. I would like to thank Prof. Dr. Leonid Makarenko for providing me with electron-irradiated diodes and assisting me during the submission process of the electron paper, contributing significantly to the progress of my research. Special thanks go to Dr. Yana Gurimskaya and Dr. Anja Himmerlich for their engaging discussions, valuable insights, and support in reviewing my papers throughout the project.

I am grateful to my master supervisor Prof. Dr. Li Zheng (李正) for supporting my Ph.D application at Universität Hamburg and for teaching me the fundamental knowledge of silicon detectors. His valuable suggestions on my work, even while I was in Hamburg,

have been invaluable.

I would like to express my gratitude to the friends I met in Hamburg: Dr. Li Xinyang (李新阳), Dr. Ma Shuailing (马帅领), Dr. Wu Xie (谢武), and Dr. Wang Cody (王科迪) for the enjoyable times we shared over drinks. To Dr. Gu Yikun (顾易坤), Dr. Sun Xiao (孙笑), Xiao Cao (小草), Qiu Qiu (秋秋), Liu Xin (刘鑫) and Dr. Han Yubo (韩雨孛), thank you for the wonderful moments spent cooking, watching movies, and listening to music together. Dr. Li Chufeng (李楚峰), Dr. Wang Zhengjun (王政军), and Dr. Yang Guang (杨光), thank you for the enjoyable basketball sessions. Special thanks to Dr. Zhang Jin (张晋) and Dr. Ran Kunlin (冉坤林) for our engaging discussions on particle physics and enjoyable basketball time.

I would like to express my heartfelt appreciation to my friends in China: Prof. Dr. Guo Jian (郭剑), Dr. Zhang Wei (张伟), Dr. Cao Hongshuai (曹洪帅), and Dr. Yao Honghao (姚洪浩) for engaging in stimulating discussions and exchanging ideas in the field of material science. I am grateful for the inspiration provided by Tang Lipeng (唐立鹏), Wang Zhengyu (王振宇), Yang Shuo (杨硕), Cai Xin (蔡兴), Shang Lei (尚磊), Xiang Wuliang (向武良), Hu Huan (胡欢), Chen Qi (陈琦), Xiang Wendong (向文东), and all my friends in China. Your support has been invaluable in helping me navigate through challenging times.

Most importantly, I would like to extend my heartfelt appreciation to my parents and family. Their unwavering support and encouragement have been the driving force behind the completion of this thesis. Their love, understanding, and sacrifices have provided me with the strength and motivation to overcome challenges and pursue my goals.